

ANA CECÍLIA PONTES RODRIGUES

Effect of nanoparticulate copper, zirconia and graphite:  
contribution to the friction coefficient and transfer layer formation in dry  
sliding tests with interfacial media addition

São Paulo

2019

ANA CECÍLIA PONTES RODRIGUES

Effect of nanoparticulate copper, zirconia and graphite:  
contribution to the friction coefficient and transfer layer formation in dry  
sliding tests with interfacial media addition

PhD Thesis submitted to the  
Polytechnic School of the University  
of São Paulo to obtain the title of  
Doctor in Science.

São Paulo

2019

ANA CECÍLIA PONTES RODRIGUES

Effect of nanoparticulate copper, zirconia and graphite:  
contribution to the friction coefficient and transfer layer formation in dry  
sliding tests with interfacial media addition

PhD Thesis submitted to the  
Polytechnic School of the University  
of São Paulo to obtain the title of  
Doctor in Science.

Concentration Area: Metallurgy and  
Materials.

Supervisor: Prof. Dr. Cesar  
Roberto Farias de Azevedo

São Paulo

2019

I authorize total and partial reproduction and divulgation of this work, by any conventional or electronic mean, for the purpose of study of research, as long as the source is cited.

Este exemplar foi revisado e alterado em relação à versão original, sob responsabilidade única do autor e com a anuência de seu orientador.

São Paulo, 28 de Maio de 2019

Assinatura do autor

Assinatura do orientador

### Catálogo-na-publicação

Rodrigues, Ana Cecília Pontes

Effect of nanoparticulate copper, zirconia and graphite: contribution to the friction coefficient and transfer layer formation in dry sliding tests with interfacial media addition / A.C.P. Rodrigues. -- versão corr. -- São Paulo, 2019.

148 p.

Tese (Doutorado) - Escola Politécnica da Universidade de São Paulo. Departamento de Engenharia Metalúrgica e de Materiais.

1. Tribology 2. Transfer layer 3. Friction Materials 4. FIB characterization 5. TEM characterization I. Universidade de São Paulo. Escola Politécnica. Departamento de Engenharia Metalúrgica e de Materiais II. t.

To my dearest Quentin Lamour,

To my beloved parents, Cecília and Iram,

## ACKNOWLEDGMENTS

I would like to extend my sincere and heartfelt gratitude to Prof. Cesar Roberto de Farias Azevedo. For being an admirable supervisor during my long path through becoming a researcher. For becoming a dear friend, a part of my life, and for sharing his exceptionally humanist vision of this world.

I would like to express my gratitude to all my official and un-official co-supervisors at BAM and IPT. To Dr. Werner Österle, for the most valuable guidance on the multi-scale cosmos within the transfer layer formation, and for welcoming me at BAM in 2015. To Dr. Thomas Gradt for allowing me to perform all tribotests of this work under his kind and thoughtful co-supervision. To Dr. Taeko Yonamine Fukuhara, for teaching and sharing so much knowledge on FIB characterization and for always trusting me. To Dr. Catia Fredericci, for supporting me when necessary.

I would like to greatly acknowledge my colleagues at BAM. To Dr. Ilona Dörfel, for all the TEM results in this work. To Dr. Pedro Portella, that helped me on the adaptation process in Berlin. To Christian Wolter, Nicole Wollschläger, René Hesse, Olaf Berndes, Geraldine Theiler and Matthias Heidrich, for the imperative contribution of each of them to this thesis.

To the colleagues at IPT, to Juliana Flor and Fabiano Raymundo dos Santos, for the great help during the characterization time.

To LAMFI (Laboratory for Material Analysis with Ion Beams) for the PIXE analysis in this work. To Dr. Cleber Rodrigues, for all the thoughtfulness and patience.

I would like to thank heartily the delightful staff of the Metallurgical and Materials Engineering Department (PMT) at the University of São Paulo that helped on this doctoral journey: Suellen Alves, Rubens Carvalho, Rafael Maia, Veríssimo, Maria Cristina dos Santos, and Gilberto Martins.

To CAPES, this work was financed in part by the Coordenação de Aperfeiçoamento de Pessoal de Nível superior – Brasil (CAPES) – Finance code 001. The visiting scholar period at BAM (Bundesanstalt für Materialforschung und –prüfung) was also sponsored by CAPES, Brazil (99999.006285/2015-05).

To FIPT (Fundação de Apoio ao Instituto de Pesquisas Tecnológicas do Estado de São Paulo) for the grant from the Novos Talentos program and to the IPT (Instituto de Pesquisas Tecnológicas do Estado de São Paulo), for all the support offered.

To my dearest friends, for easing the way. To Arthur Nishikawa and Achim Feller, for the foremost necessary assistance with Python. To Dany Michel Centeno, Camila Conegundes, Leidy Hernández, Juan Ignacio Pereira, Cesar Yuji Narita, Marcelo Rojas and Roberto Spoglianti de Souza, for the contribution of each of you to this work. To Anna Turriani, Ana Marincek, Ricardo Januário, Mariama Camara, Paula Nunes and Maíra Sasso, for all the dancing, breathing and decluttering of the mind.

To my beloved parents Cecília e Iram, this all started with you. Thank you for raising, educating me and for always supporting unconditionally all my decisions.

To my dearest Quentin Lamour, for the daily care and the solid partnership throughout these years, for making my personal project our common project: «Nous serons ce que nous ferons ensemble»<sup>[1]</sup>.

## ABSTRACT

Copper is present in brake pads in the form of fibres, though its suppression from pads' formulations is already a trend compared to the suppression of asbestos in the 1980's. As a contribution to this challenging *scenario*, this work investigated the behaviour of mixture additions containing copper, zirconia, graphite and magnetite in dry sliding tribotests. Pin-on-disc tribotests with interfacial media addition were performed in order to contribute on the mission of understanding how Cu, graphite and ZrO<sub>2</sub> particles act on the oxide transfer layer formation on dry sliding conditions. Thus describing some of the tribological properties that a possible replacement for copper in brake pads should mimic. Tests were performed at 23°C in air, 400°C in air and 400°C in N<sub>2</sub>. Nanoparticulate Cu, ZrO<sub>2</sub> and micron-sized graphite were mixed in a Fe<sub>3</sub>O<sub>4</sub> based-matrix. The ZrO<sub>2</sub> particles were incorporated to the mixtures by two mixing methods: manual mixing and high-energy ball milling. This study sought to explain the coefficient of friction (CoF) behaviour of these additions individually, as well as together, by correlating the CoF with comprehensive characterization of the oxide transfer layer. The transfer layer was characterized by means of scanning electron microscopy (SEM), Focused Ion Beam (FIB) and Transmission electron microscopy. Graphite containing mixtures displayed low average CoF values (0.23 to 0.31) due to selective transfer of graphite films to the first bodies' tribosurfaces. Copper formed agglomerates and patches within the oxide transfer layer that were responsible for raising the CoF values at 23°C and acted as soft copper films at 400°C. The nanoparticulate addition of ZrO<sub>2</sub> in the manual mixtures prevented the formation of Cu patches and larger agglomerates, promoting the formation of a smooth and compact oxide tribolayer, though graphite's selective transfer was still observed.

Keywords: Tribology, Transfer layer, Friction Materials, FIB characterization, TEM characterization

## RESUMO

O cobre está presente em pastilhas de freio na forma de fibras e sua eliminação das formulações de pastilhas já é comparável aos esforços para a eliminação do amianto dos freios nos anos 1980's. Para contribuir nessa missão, esse trabalho investigou o comportamento, em ensaios tribológicos sem lubrificação com adição de misturas de cobre, zircônia, grafite e magnetita. Foram realizados ensaios pino x disco com adição de meio interfacial com o objetivo de contribuir na descrição da atuação do Cu, grafite e partículas de  $ZrO_2$  na formação de uma camada de óxido compacta em condições sem lubrificação. De forma a descrever propriedades tribológicas relevantes que um possível substituto do cobre deve mimetizar nas pastilhas de freio. Os ensaios foram realizados a 23°C em ar, 400°C em ar e 400°C em  $N_2$ . Nanopartículas de Cu,  $ZrO_2$  (50 nm) e grafite micrométrico (20  $\mu m$ ) foram misturados em uma base de  $Fe_3O_4$  nanoparticulado. As partículas de  $ZrO_2$  foram incorporadas às misturas, por dois métodos distintos, mistura manual, e moagem de bolas de alta energia. Este estudo procurou explicar os resultados de coeficiente de atrito (CoF) dessas adições, individualmente bem como em conjunto, correlacionando os resultados de coeficiente de atrito à extensa caracterização da camada de transferência. Esta última foi caracterizada por meio de microscopia eletrônica de varredura (SEM), feixe de íons focalizado (FIB) e microscopia eletrônica de transmissão (TEM). As misturas contendo grafite apresentaram os menores valores médios de CoF (0.23 to 0.31) devido à presença de filmes contínuos de grafite na camada de transferência. A adição de cobre formou aglomerados e placas na camada de transferência, que foram responsáveis tanto pelo aumento do CoF a 23°C, e agiram como filmes moles de cobre a 400°C. A adição de  $ZrO_2$  em misturas manuais preveniu a formação de aglomerados de Cu, auxiliando na formação de uma camada mais compacta, no entanto, não foi suficiente para prevenir a formação de filmes de grafite.

Palavras Chave: Tribologia, Camada de Transferência, Materiais de atrito, Caracterização por FIB, Caracterização por TEM.

## FIGURES' LIST

Figure 1 Kato's pin-on-disc methodology, showing the particulate interfacial media supply <sup>[17]</sup> .....	10
Figure 2 Schematic diagram of a cross-section showing the third body layer in Österle et al. (2009) pin-on-disc tribotest results <sup>[26]</sup> . ....	12
Figure 3 Topographic examination of disc surface after tribotest for the condition Cu20m and respective XEDS mapping results. a) Secondary electron image showing the presence of flat continuous surfaces (see arrows) as well as loose debris and wear marks. b) XEDS mapping for Fe is inhomogeneous, showing a higher Fe content on the upper left corner of the figure. c) O XEDS mapping indicating higher O content in regions with loose particles deposit (region 1) as well as smoother surfaces (region 2). d) XEDS mapping for Cu inhomogeneous, showing a higher Cu content on the lower right corner of the figure <sup>[62]</sup> . ....	16
Figure 4 a) and b) FIB cross-section on the pin surface after tribotesting with no interfacial media addition. It is possible to observe the plastically deformed layer under the Pt deposition as well as the presence of particulate debris on the left image and a thin continuous layer on the image to the right. Additionally, the pin microstructure shows the presence of a plastically deformed region (~ 3 µm) near the tribosurface <sup>[61]</sup> . ....	17
Figure 5 FIB cross-section of the disc surface after tribotesting with addition of 400 µm copper (Cu400m). a) A plastically deformed layer of approximately 2 µm may be seen under the Pt deposition. Arrow 1 points to the presence of wear debris at the asperity valley, whereas arrow 2 points to a thin grey continuous compact oxide layer at the asperity peak <sup>[62]</sup> .....	17

Figure 6 Copper aggregates as received SEM-SEI. a) Copper particles in micron-sized agglomerates. b) Detail from copper agglomerates.....	19
Figure 7 Graphite cathode chips as received SEM-SEI. a) Graphite particles in micron-sized distribution. b) Detail from graphite particle.....	20
Figure 8 Schematic presentation of the pin-on-disc tribometer used in this study. (Image kindly provided by Dr. Thomas Gradt).....	23
Figure 9 a) Pt cap deposition prior to FIB cutting, tilt of 52 ° (SEI); b) FIB cross section surface view; c) FIB cross section observed with the electrons beam (SEM-SEI); d) FIB cross section observed with the Ga ions beam (SIM-SEI).....	25
Figure 10 Ternary (Cu-graphite-Fe <sub>3</sub> O <sub>4</sub> ) MM mixture. Morphological characterization of the addition: a) before mixing with pestle and mortar; b) after mixing for 4 minutes with pestle and mortar. ....	26
Figure 11 Quaternary (ZrO <sub>2</sub> -Cu-graphite-Fe <sub>3</sub> O <sub>4</sub> ) BM mixture. Morphological characterization. Ball mixed for: a) 30 minutes; b) 90 minutes; c) 3 hours; d) Zr EDS elemental mapping of the 3 hour ball milled mixture. ....	27
Figure 12 - Quaternary (ZrO <sub>2</sub> -Cu-graphite-Fe <sub>3</sub> O <sub>4</sub> ) BM mixture. a) TEM Bright field image; b) C EDS elemental mapping; c) O EDS elemental mapping; d) Cu EDS elemental mapping; f) Zr EDS mapping. ....	28
Figure 13 - Quaternary (ZrO <sub>2</sub> -Cu-graphite-Fe <sub>3</sub> O <sub>4</sub> ) BM mixture: a) TEM image showing the particles size in the agglomerates range in size from 10 to 80 nm. b) HR-TEM image, the detail shows the graphite curved lattice structure inside the particles agglomerates.....	29
Figure 14 Quaternary (ZrO <sub>2</sub> -Cu-graphite-Fe <sub>3</sub> O <sub>4</sub> ) BM mixture. TEM image showing the particles size in the agglomerates ranges from 10 to 60 nm. ....	29

Figure 15 Summary of the average values of the CoF of all investigated mixtures, in terms of conditions tested. ....30

Figure 16 Disc, pure Fe<sub>3</sub>O<sub>4</sub>. Macrograph for system tested at: a) 23°C in air (CoF~0.46); b) 400°C in air (CoF~0.60). ....32

Figure 17 Pin, pure Fe<sub>3</sub>O<sub>4</sub> tested at 23°C in air, FIB cross-section. The depth of plastically deformed layer ranges from 3 to 8 μm. The depth of the transfer layer is approximately 4 μm and shows cracks within. The arrow points to metallic debris trapped within the transfer layer. A compact oxide transfer layer is visible between layers of the metallic first body (see circle). (CoF~0.46). ....33

Figure 18 Pin, pure magnetite (Fe<sub>3</sub>O<sub>4</sub>) at 400°C in air, FIB cross-section. The depth of plastically deformed layer is ranges from 2 to 5 μm. The depth of the transfer layer varies from 0.5 to 5 μm and shows cracks within it. A metallic debris is visible trapped within the transfer layer (see arrow) (CoF ~ 0.60). ....34

Figure 19 Pin, binary (graphite-Fe<sub>3</sub>O<sub>4</sub>) MM mixture tested at 23°C in air: a) SEM topographical and compositional examination of the tribosurface, BEI (CoF ~0.23). 37

Figure 20 Disc, binary (graphite -Fe<sub>3</sub>O<sub>4</sub>) MM mixture tested at 23°C in air, FIB cross-section. The depth of plastically deformed layer is approximately 5 μm. The depth of the compact transfer layer is approximately 1.5 μm. A ~10 μm long crack is visible throughout the transfer layer. The arrow points to a carbon-rich film, 8 μm long, within the transfer layer (CoF ~0.23). ....38

Figure 21 Pin, binary (graphite -Fe<sub>3</sub>O<sub>4</sub>) MM mixture tested at 23°C in air, FIB cross-section. The depth of plastically deformed layer ranges approximately from 0.5 to 3 μm. Sub-superficial crack in the plastically deformed layer accompanies metallic debris (see arrows). The depth of the coarse-grained transfer layer is just under 3 μm. Cracks and discontinuities are visible within the transfer layer. (CoF ~0.23). ....39

Figure 22 Pin, binary (graphite -Fe<sub>3</sub>O<sub>4</sub>) MM mixture tested at 400°C in N<sub>2</sub>, FIB cross-section. The depth of plastically deformed layer is approximately 0.5. The depth of the compact transfer layer is just under 5 μm. Cracks and discontinuities are visible within the transfer layer. The arrows point to C-rich regions (CoF ~0.46). .....40

Figure 23 Pin, binary (graphite-Fe<sub>3</sub>O<sub>4</sub>) MM mixture tested at 400°C in N<sub>2</sub>, Detail of FIB cross-section in Figure 22. A 8 μm crack is visible within the compact smooth transfer layer. The ellipse comprises a less compact region of the transfer layer. The arrows point to C-rich regions (CoF ~0.46). .....41

Figure 24 - Disc, binary (6%Cu -Fe<sub>3</sub>O<sub>4</sub>) MM mixture tested at 23°C in air. a) FIB cross-section. The plastically deformed layer is not visible. The depth of the transfer layer is over 10 μm. Cracks are visible within the transfer layer. b) Cu EDS mapping on the same area, but performed in a different instrument. (CoF ~0.55).....45

Figure 25 - Disc, binary (6%Cu -Fe<sub>3</sub>O<sub>4</sub>) MM mixture tested at 23°C in air. a) FIB cross-section. The plastically deformed layer ranges from 1 to 2 μm. The depth of the transfer layer varies from 1 to 2 μm. Cracks and discontinuities are visible within the transfer layer. b) Cu EDS mapping on the same area but performed in a different instrument. (CoF ~0.55). .....46

Figure 26 Pin, binary (15%Cu -Fe<sub>3</sub>O<sub>4</sub>) MM mixture tested at 23°C in air, FIB cross-section. The depth of plastically deformed layer is approximately 0.5 μm. The depth of the compact transfer layer is approximately 4 μm. Cracks and discontinuities are visible within the transfer layer. (CoF ~0.65). .....47

Figure 27 Pin, binary (15%Cu -Fe<sub>3</sub>O<sub>4</sub>) MM mixture tested at 23°C in air, Detail of FIB cross-section in Figure 26. The depth of plastically deformed layer is approximately 0.5 μm. The depth of the compact transfer layer is approximately 4 μm. Cracks and discontinuities are visible within. (CoF ~0.65). .....47

Figure 28 - Disc, binary (6%Cu-Fe<sub>3</sub>O<sub>4</sub>) MM mixture tested at 23°C in air. (a) STEM, bright field image from a tribosurface lamella; (b) Fe EDS elemental mapping; (c) Cu EDS elemental mapping; (CoF ~0.55).....48

Figure 29 Disc, binary (15%Cu -Fe<sub>3</sub>O<sub>4</sub>) MM mixture tested at 400°C in N<sub>2</sub>. FIB cross-section. The plastically deformed layer ranges between 4 to 7 μm. The depth of the transfer layer is approximately 2 to 5 μm thick. Cracks and scarce discontinuities (see arrow) are visible amid the compact smooth transfer layer. (CoF ~0.51). .....49

Figure 30 - Disc, binary (15%Cu -Fe<sub>3</sub>O<sub>4</sub>) MM mixture tested at 400°C in N<sub>2</sub>. a) FIB cross-section. The depth of the transfer layer varies from 5 to 7.5 μm. Cracks and discontinuities are visible within the transfer layer. The rectangle shows the region where the EDS mapping was performed; b) Fe EDS mapping on the same area. c) Cu EDS mapping on the same area. (CoF ~0.51). .....50

Figure 31 - Disc, binary (15%Cu-Fe<sub>3</sub>O<sub>4</sub>) MM mixture tested at 400°C in N<sub>2</sub>. (a) STEM, bright field image from a tribosurface lamella; (b) Layered EDS elemental mapping combining C, Fe and Cu maps; (CoF ~0.51).....51

Figure 32 Disc, binary (15%Cu-Fe<sub>3</sub>O<sub>4</sub>) MM mixture tested at 400°C in N<sub>2</sub>. HREM image from a Cu-rich area near the tribosurface (encircled in red) (CoF ~0.51). .....51

Figure 33 Pin, binary (6%Cu -Fe<sub>3</sub>O<sub>4</sub>) MM mixture tested at 400°C in air, FIB cross-section. The depth of plastically deformed layer is approximately 5 μm. The depth of the compact, smooth transfer layer varies from 1 to 2 μm. Cracks are visible within the transfer layer. (CoF ~0.57). .....52

Figure 34 Pin, binary (15%Cu -Fe<sub>3</sub>O<sub>4</sub>) MM mixture tested at 400°C in air. a) FIB cross-section. The plastically deformed layer is over 10 μm thick. The compact oxide transfer layer is smooth and varies between 1 to 3 μm and thickness and contours a plastically

deformed region of the steel, keeping it from detaching from the tribolayer. b) Cu EDS mapping on the same area showing Cu-rich micro-agglomerates (CoF ~0.51). .....53

Figure 35 Pin, binary (15%Cu -Fe<sub>3</sub>O<sub>4</sub>) MM mixture tested at 400°C in air. a) FIB cross-section. The plastically deformed layer is over 5 μm. The depth of the transfer layer is approximately 3 μm thick. Longitudinal cracks are visible within the compact smooth, yet discontinuous transfer layer. b) Cu EDS mapping on the same area showing Cu presence throughout the transfer layer, with greater presence in a lower stripe (see arrow) (CoF ~0.51).....54

Figure 36 Disc, ternary (Cu-graphite-Fe<sub>3</sub>O<sub>4</sub>) MM mixture tested at 23°C in air. a) FIB cross-section. The plastically deformed layer is approximately 3 μm. The depth of the transfer layer ranges from 0.5 to 1 μm. Cracks and discontinuities are visible within the transfer layer. The rectangle shows the region where the EDS mapping was performed; b) Fe EDS mapping on the same area. c) Cu EDS mapping on the same area. (CoF ~0.23).....57

Figure 37 - Disc, ternary (Cu-graphite-Fe<sub>3</sub>O<sub>4</sub>) MM mixture tested at 23°C in air. (a) STEM, bright field image from a tribosurface lamella; (b) Fe, Cu and O EDS elemental mapping. (CoF ~0.23). .....58

Figure 38 - Disc, ternary (Cu-graphite-Fe<sub>3</sub>O<sub>4</sub>) MM mixture tested at 23°C in air. TEM image from a C-rich area near the tribosurface (CoF ~0.23).....58

Figure 39 Pin, ternary (Cu-graphite-Fe<sub>3</sub>O<sub>4</sub>) MM mixture tested at 400°C in N<sub>2</sub>. SEM-SEI topographical examination of the tribosurface. C-rich region on transfer layer (encircled). (CoF ~0.46). .....59

Figure 40 Pin, ternary (Cu-graphite-Fe<sub>3</sub>O<sub>4</sub>) MM mixture tested at 400°C in N<sub>2</sub>. FIB cross-section performed over C-rich region in Figure 39 (see circle). The plastically deformed layer varies between 2 and 5 μm thick with the presence of a sub-superficial

crack (see arrow). The depth of the coarse-grained transfer layer ranges from 1 to 3  $\mu\text{m}$  and with the presence of longitudinal cracks. (CoF  $\sim 0.46$ ).....60

Figure 41 Pin, ternary (Cu- graphite- $\text{Fe}_3\text{O}_4$ ) MM mixture tested at  $400^\circ\text{C}$  in air. FIB cross-section. The plastically deformed layer is approximately 5  $\mu\text{m}$  thick. The depth of the compact smooth transfer layer ranges from 0.5 to 1  $\mu\text{m}$  (CoF  $\sim 0.55$ ). .....61

Figure 42 Pin, ternary (Cu- $\text{ZrO}_2$ - $\text{Fe}_3\text{O}_4$ ) BM mixture tested at  $23^\circ\text{C}$  in air, FIB cross-section. The depth of plastically deformed layer is approximately 10  $\mu\text{m}$  and the thickness of the compact transfer layer is approximately 1 to 3  $\mu\text{m}$  (CoF  $\sim 0.62$ ). .....63

Figure 43 Pin, ternary (Cu- $\text{ZrO}_2$ - $\text{Fe}_3\text{O}_4$ ) BM mixture tested at  $23^\circ\text{C}$  in air, detail of the FIB cross-section showed in Figure 42. The depth of plastically deformed layer is approximately 10  $\mu\text{m}$  and the thickness of the compact transfer layer is approximately 1 to 3  $\mu\text{m}$  (CoF  $\sim 0.62$ ). .....64

Figure 44 Pin, ternary (Cu- $\text{ZrO}_2$ - $\text{Fe}_3\text{O}_4$ ) BM mixture tested at  $400^\circ\text{C}$  in  $\text{N}_2$ , FIB cross-section. The depth of plastically deformed layer is approximately 10  $\mu\text{m}$ , but the ferritic-pearlitic microstructure is comparatively less elongated than the one observed at  $23^\circ\text{C}$ . The depth of the compact transfer layer varies from 5 to 10  $\mu\text{m}$  and do not show any cracks. The arrows point at Zr-rich microsized particles. Metal debris is visible trapped within the transfer layer (CoF  $\sim 0.55$ ). .....65

Figure 45 Pin, ternary (Cu- $\text{ZrO}_2$ - $\text{Fe}_3\text{O}_4$ ) BM mixture tested at  $400^\circ\text{C}$  in  $\text{N}_2$ , FIB cross-section. A multi-layered structure of plastically deformed steel between compact oxide transfer layers is visible. The depth of the main superficial compact transfer layer varies from 5 to 9  $\mu\text{m}$  with the presence of a few cracks. The arrows point at Zr-rich sized particles. (CoF  $\sim 0.55$ ).....66

Figure 46 Pin, quaternary (Cu-graphite- $\text{ZrO}_2$ - $\text{Fe}_3\text{O}_4$ ) MM mixture tested at  $23^\circ\text{C}$  in air. FIB cross-section. The depth of the plastically deformed layer is over 5  $\mu\text{m}$ . The square

points at a smooth and compact transfer layer region, while the ellipse points at layer of plastically deformed steel trapped within transfer layer deposits (CoF ~0.31).....69

Figure 47 Pin, quaternary (Cu-graphite-ZrO<sub>2</sub>-Fe<sub>3</sub>O<sub>4</sub>) MM mixture tested at 23°C in air. (a) STEM, bright field image from a tribosurface lamella; (b) C EDS elemental mapping; (c) O EDS elemental mapping; (d) Cu EDS elemental mapping (CoF ~0.31). .....70

Figure 48 Pin, quaternary (Cu-graphite-ZrO<sub>2</sub>-Fe<sub>3</sub>O<sub>4</sub>) MM mixture tested at 23°C in air. TEM image from a tribosurface lamella: a) Region of a homogeneously mixed tribolayer featuring a thin layer graphite in the tribofilm microstructure (see arrow); b) Presence of a layer of graphite films between other particles (see arrow (CoF ~0.31). .....71

Figure 49 Pin, quaternary (Cu-graphite-ZrO<sub>2</sub>-Fe<sub>3</sub>O<sub>4</sub>) MM mixture tested at 23°C in air. (a) TEM image from a tribosurface lamella (b) STEM, bright field image from the third body trapped between the first body's steel layers (CoF ~0.53).....72

Figure 50 Pin, quaternary (Cu-graphite-ZrO<sub>2</sub>-Fe<sub>3</sub>O<sub>4</sub>) MM mixture tested at 23°C in air. (a) STEM, dark field image from a tribosurface lamella; (b) Zr EDS elemental mapping; (c) Cu EDS elemental mapping; (CoF ~0.53).....72

Figure 51 Pin, quaternary (Cu-graphite-ZrO<sub>2</sub>-Fe<sub>3</sub>O<sub>4</sub>) MM mixture tested at 400°C in air. FIB cross-section. The depth of the plastically deformed layer is ~ 5 μm thick, and the thickness of the compact smooth transfer ranges from 0.5 to 3.5 μm thick. The arrows show a sub-micron sized particle within the transfer layer (CoF ~0.56). .....73

Figure 52 Pin, quaternary (Cu-graphite-ZrO<sub>2</sub>-Fe<sub>3</sub>O<sub>4</sub>) MM mixture tested at 400°C in N<sub>2</sub>. FIB cross-section. The depth of the plastically deformed layer is ~ 5 μm thick, and the thickness of the transfer layer ranges from 0.5 to 3.5 μm thick, lacking compaction. (CoF ~0.56). .....74

Figure 53 Disc, quaternary  $ZrO_2$ -Cu-graphite- $Fe_3O_4$  BM mixture tested at 23°C in air. FIB cross-section. The tribosintered transfer layer ranges from 1.5 to 5  $\mu m$  thick. The plastically deformed layer ranges from 1.5 to 7  $\mu m$  in thickness. Metallic debris are visible within the transfer layer (arrows), alongside with longitudinal cracks and discontinuities. Zr-rich particles are identified with circles. (CoF  $\sim 0.54$ ). .....75

Figure 54 Pin, quaternary ( $ZrO_2$ -Cu-graphite- $Fe_3O_4$ ) BM mixture tested at 23°C in air. FIB cross-section. The plastically deformed layer is over 10  $\mu m$  thick. Compact smooth patches of oxide transfer layer are visible and are approximately 2  $\mu m$  thick. The arrow points to a discontinuity within the microstructure, and the presence of trapped oxide third body inside the tribologically transformed layer. (CoF  $\sim 0.54$ ).....76

Figure 55 Pin, quaternary ( $ZrO_2$ -Cu-graphite- $Fe_3O_4$ ) BM mixture tested at 23°C in air. SEM-BEI image. The arrows point at Zr-rich particles (0.54). .....77

Figure 56 Pin, quaternary ( $ZrO_2$ -Cu-graphite- $Fe_3O_4$ ) BM mixture tested at 23°C in air. FIB cross-section. The plastically deformed layer is approximately 5  $\mu m$  thick. A Zr-rich inclusion is encrusted at the tribosurface. (CoF  $\sim 0.54$ ). .....78

Figure 57 Pin, quaternary (Cu-graphite- $ZrO_2$ - $Fe_3O_4$ ) BM mixture tested at 400°C in  $N_2$ , FIB cross-section. The depth of the plastically deformed layer ranges from 2 to 5  $\mu m$ , and the thickness of the compact transfer layer is  $\sim 3.5 \mu m$  thick. The arrows point at Zr-rich areas, A region of the tribofilm is sandwiched by the plastically deformed region (CoF  $\sim 0.53$ ). .....79

Figure 58 A) Pin, quaternary (Cu-graphite- $ZrO_2$ - $Fe_3O_4$ ) BM mixture tested at 400°C in air, FIB cross-section. The depth of the plastically deformed zone ranges from 2 to 3  $\mu m$ , while the thickness of the compact transfer layer is between 1 and 3  $\mu m$  thick and compact. The arrows point Zr-rich areas, while the circles show discontinuities in the transfer layer (CoF  $\sim 0.74$ ). .....80

Figure 59 Pin, quaternary (Cu-graphite-ZrO<sub>2</sub>-Fe<sub>3</sub>O<sub>4</sub>) BM mixture tested at 400°C in air. (a) STEM, bright field image from a tribosurface lamella; (b) C EDS elemental mapping; (c) O EDS elemental mapping; (d) Cu EDS elemental mapping (CoF ~0.53). .....81

Figure 60 Pin, quaternary (Cu-graphite-ZrO<sub>2</sub>-Fe<sub>3</sub>O<sub>4</sub>) BM mixture tested at 400°C in air. TEM image from a tribosurface lamella. (a) Cu-rich area, Cu nanoparticles near the sample surface; (b) Graphite fibres amid the tribofilm (see arrows) (CoF ~0.53). .....82

Figure 61 Pin, quaternary (Cu-graphite-ZrO<sub>2</sub>-Fe<sub>3</sub>O<sub>4</sub>) BM mixture tested at 400°C in air. a) Energy filtered SAED pattern; b) EDS spectrum for the same area. The pattern and spectrum confirm the presence of magnetite and hematite crystallographic phases.83

Figure 62 Schematic illustration of the oxide transfer layer with copper patches presence typically observed in Cu containing systems tested at 23°C. ....95

Figure 63 Schematic illustration of the oxide transfer layer with copper film presence typically observed in Cu containing systems tested at 400°C. ....97

Figure 64 Schematic illustration of the oxide transfer layer with graphite film presence typically observed in graphite containing systems tested at 23°C. ....98

Figure 65 Schematic illustration of the oxide transfer layer of the MM quaternary system, with graphite film presence, nano-sized copper agglomerates and ZrO<sub>2</sub> particles. ....101

Figure 66 Schematic illustration of the oxide transfer layer of the BM quaternary system, with nano-seized graphite and copper, alongside with ZrO<sub>2</sub> particles from the ball mill grinding media. ....102

## TABLES' LIST

Table 1 Mixing processes.....	20
Table 2 Investigated mixtures and conditions.....	22
Table 3 Average CoF values for the pure Fe <sub>3</sub> O <sub>4</sub> conditions.....	31
Table 4 Results summary for the pure Fe <sub>3</sub> O <sub>4</sub> conditions.....	35
Table 5 Average friction coefficient values for the binary graphite-Fe <sub>3</sub> O <sub>4</sub> conditions.....	36
Table 6 Results summary for the graphite-Fe <sub>3</sub> O <sub>4</sub> conditions.....	43
Table 7 Average friction coefficient values for the binary Cu-Fe <sub>3</sub> O <sub>4</sub> conditions.....	44
Table 8 Results summary for the binary MM Cu-Fe <sub>3</sub> O <sub>4</sub> conditions.....	55
Table 9 Average CoF values for the ternary Cu-graphite-Fe <sub>3</sub> O <sub>4</sub> conditions.....	56
Table 10 Results summary for the MM ternary Cu-graphite-Fe <sub>3</sub> O <sub>4</sub> conditions.....	62
Table 11 Average CoF values for the ternary ZrO <sub>2</sub> -Cu-Fe <sub>3</sub> O <sub>4</sub> conditions.....	63
Table 12 Results summary for the BM ternary Cu- ZrO <sub>2</sub> -Fe <sub>3</sub> O <sub>4</sub> conditions.....	67
Table 13 Average friction coefficient values for the quaternary ZrO <sub>2</sub> -Cu-graphite-Fe <sub>3</sub> O <sub>4</sub> conditions.....	68
Table 14 Results summary for the quaternary ZrO <sub>2</sub> -Cu-graphite-Fe <sub>3</sub> O <sub>4</sub> conditions.....	85
Table 15 Results Summary.....	90

## INDEX

1	Introduction .....	1
2	Objectives .....	3
3	Bibliographic review .....	4
3.1	Tribosystem.....	4
3.2	Automotive brake system .....	5
3.2.1	Disc Brake .....	5
3.2.2	Copper in brake pads .....	6
3.2.3	Graphite in brake pads.....	7
3.2.4	Abrasive in brake pads .....	7
3.2.5	Copper free brake pads and novel materials .....	8
3.3	Pin-on-disc tribotest to analyse the automotive brake tribological system .....	9
3.3.1	Kato's tribotests .....	9
3.3.2	Tribofilm microstructural characterization .....	11
3.4	Previous tribotests and tribosurfaces microstructural characterization from author.....	15
4	Materials and methods.....	19
4.1	Interfacial media additions .....	19
4.2	Tribotests.....	23
4.3	Characterization .....	24
5	Results.....	26
5.1	Mixture characterization.....	26
5.2	Overview of the friction coefficient results.....	30
5.3	Pure Fe <sub>3</sub> O <sub>4</sub> system .....	31
5.3.1	Characterization of the pure Fe <sub>3</sub> O <sub>4</sub> system.....	31
5.3.2	Results summary for the pure Fe <sub>3</sub> O <sub>4</sub> system .....	35
5.4	Binary graphite-Fe <sub>3</sub> O <sub>4</sub> system .....	36
5.4.1	Characterization of the MM binary graphite-Fe <sub>3</sub> O <sub>4</sub> system.....	37
5.4.2	Results summary for the MM binary graphite-Fe <sub>3</sub> O <sub>4</sub> system .....	42
5.5	Binary Cu-Fe <sub>3</sub> O <sub>4</sub> systems.....	44
5.5.1	Characterization of the MM binary Cu-Fe <sub>3</sub> O <sub>4</sub> system .....	45
5.5.2	Results summary for the MM binary Cu-Fe <sub>3</sub> O <sub>4</sub> system.....	54

5.6	Ternary Cu-graphite-Fe <sub>3</sub> O <sub>4</sub> system.....	56
5.6.1	Characterization of the MM ternary Cu-graphite-Fe <sub>3</sub> O <sub>4</sub> system.....	57
5.6.2	Results summary for the MM ternary Cu-graphite-Fe <sub>3</sub> O <sub>4</sub> system.....	62
5.7	Ternary ZrO <sub>2</sub> - Cu-Fe <sub>3</sub> O <sub>4</sub> system.....	63
5.7.1	Characterization of the BM ternary ZrO <sub>2</sub> - Cu-Fe <sub>3</sub> O <sub>4</sub> mixture.....	63
5.7.2	Results summary for the ternary Cu-ZrO <sub>2</sub> -Fe <sub>3</sub> O <sub>4</sub> system.....	66
5.8	Quaternary ZrO <sub>2</sub> -Cu-graphite-Fe <sub>3</sub> O <sub>4</sub> systems.....	68
5.8.1	Quaternary MM ZrO <sub>2</sub> - Cu-graphite-Fe <sub>3</sub> O <sub>4</sub> mixture .....	69
5.8.2	Quaternary BM ZrO <sub>2</sub> - Cu-graphite-Fe <sub>3</sub> O <sub>4</sub> mixture characterization .....	75
5.8.3	Results summary for the quaternary ZrO <sub>2</sub> -Cu-graphite-Fe <sub>3</sub> O <sub>4</sub> system.....	83
5.9	Results Summary.....	86
6	Discussion .....	91
6.1	Parameters acting in the transfer layer and friction coefficient.....	92
6.1.1	Effect of temperature.....	93
6.1.2	Effect of atmosphere.....	94
6.1.3	Effect of copper addition.....	95
6.1.4	Effect of graphite addition .....	98
6.1.5	Effect of ZrO <sub>2</sub> particles .....	101
6.1.6	Effect of high-energy ball milling .....	102
6.1.7	Final considerations .....	104
7	Conclusions .....	105
8	Future Work Suggestions .....	106
9	References.....	107
	Annex 1.....	116
	Annex 2.....	118
	Annex 3.....	123
	Annex 4.....	130
	Annex 5.....	137
	Annex 6.....	140

## 1 INTRODUCTION

The word tribology comes from the Greek τριβ (tribos) literally meaning “to rub”. Friction, wear and lubrication have been studied for hundreds of years now, but the term tribology emerged only in 1965, when H. P. Jost presented a report in which he estimated the amount of possible savings if tribological principles were applied to the British industry [2].

While earlier tribological research concentrated on friction and lubrication, Dowson (1979) stated that wear would dominate not only the latter half of the 20<sup>th</sup> century but also much of the 21<sup>st</sup> century [3]. Considering brake friction materials, a major concern on airborne emissions from brake wear, its harmfulness to human health and environment are now at the centre of brake development efforts.

In the early 80's, asbestos-free brake materials were starting to be adopted in the USA, Europe and Japan. From that point on, as anticipated by Jacko et al. (1984) friction materials would need to withstand environmental standards, higher service temperatures and present higher performance to produce lighter brakes with reduced aerodynamic drag coefficient [4].

For the past decades, copper has been at the spotlight of environmental and human health concerns. It is present in automotive brake pads in the form of fibres. Its amount usually varies between 10 to 20 wt.%. The use of Cu in the brake pad composition was commonly justified by its good thermal conductivity properties, though it was reported to cause excessive wear on cast iron [5]. On the short term, however, the amount of Cu in brake pads must be reduced in developed countries, as a measure to mitigate copper airborne emission.

The characterization of the copper particles emission from brake pads confirmed its potential harmful effects. The wear of copper fibres produces ultrafine particulate airborne that may easily enter the respiratory tract. [6–8]. Nevertheless, its replacement in the brake pad composition is a trend comparable to the suppression of asbestos in brake materials three decades ago.

The suppressing of the Cu in the brake pad composition is rather challenging for brake pad manufacturers. The desired friction coefficient (CoF) value for braking

systems ranges between 0.35 and 0.5, depending on the type of vehicle. Brake pads' composition is also a complex topic especially when it comes to the behaviour of each ingredient. Confidentiality and empirical methodology seem to be a common ground for the development of new friction materials in braking system industry [9, 10].

Recent efforts on developing Cu-free brake pads favour the improvement of existing fillers and fibres over the addition of a novel friction material to replace copper fibres [11]. Among the possibilities are the use of thermo-graphite [12], conductive Rockwool fibres [11], environmentally friendly geo-polymer and natural hemp fibres [13], natural fibres and titanate [14]. In addition, the improvement of these fillers mixing methods is also proposed as a possible path to Cu suppression [15].

This study assesses the behaviour of third body mixtures composed by micron-sized graphite, nanoparticulate copper and zirconium oxide amid a magnetite matrix; the contribution of these additions on forming an oxide, compact and smooth transfer layer. The use of a magnetite matrix intends to approximate the third body composition to those characterized in real braking applications [16]. Additionally, this work investigates the effect of the aforementioned additions to the friction coefficient behaviour. Kato's pin-on-disc tribotests with interfacial media addition were performed at 23°C and 400°, in air and N<sub>2</sub> as a simplified method to simulate the third body produced during braking [17-19].

## 2 OBJECTIVES

The main objective of this work was to investigate the influence of interfacial media additions (copper, graphite and ZrO<sub>2</sub> particles amid a Fe<sub>3</sub>O<sub>4</sub> based-matrix) on the CoF behaviour and on the transfer layer formation. Thus, describing how Cu, graphite and ZrO<sub>2</sub> particles act on dry sliding conditions, and establishing a correlation between these friction materials. Lastly, this should help to reveal properties that are unique to copper and how zirconia and graphite could play a role on the suppression of copper in brake pads.

To assess this matter, this study sought to explain the CoF behaviour with the characterization results of the transfer layers, observed by means of SEM, FIB and TEM techniques.

Tribotests with different mixtures of copper, graphite and zirconia in a magnetite based-matrix allowed to investigate the effects of each of these additions individually, alongside with the synergetic effects, that are nevertheless important in friction materials.

Tribotests were performed at two different temperatures (23°C and 400°C) to assess the temperature effect on the CoF behaviour and on the transfer layer formation of the aforementioned mixtures. In addition, two atmospheres (air and N<sub>2</sub>) were applied to the tribotests, in an effort to isolate possible effects of oxidation of these mixtures components at 400°C. Lastly, two mixing methods (manually mixing and high-energy ball milling) were used to incorporate ZrO<sub>2</sub> particles, thus allowing the observation of the effects of these methods on the transfer layer formation.

### 3 BIBLIOGRAPHIC REVIEW

#### 3.1 Tribosystem

We all know the story of Newton asleep under an apple tree, when an apple fell on his head. He woke up, and established “the Laws of Gravity”. As Tribologists, we may well ask whether, had Newton slipped on a banana skin, that would have led to his recognition of the importance of force transference between two surfaces in relative motion, from which the concept of tribology might have been born 300 years ago. Alas, bananas were not available (in Britain) in the 17th century, and this recognition therefore had to wait until 1966 when, on March 9, 1966, the word and concept of tribology were first enunciated to an unsuspecting world in a report of a Committee of the British Department (Ministry) of Education and Science [2].

On the second half of the 20th century, static and kinetic forces were recognized as material and system dependents, and the term “tribological system” was initially used to define a complex variety of parameters and *phenomena* that control friction coefficient and the systems’ properties [20].

The tribological system approach became a modern tool for the use and interpretation of friction data in modelling friction; developing friction-moderator materials; friction test methods and machinery design [5].

The friction coefficient is a convenient way of characterizing the movement resistance between surfaces, though it is neither a material’s property nor a constant. Friction and wear are responses of a tribological system, and must be correlated in each of the system’s contact state. This is useful for understanding wear mechanisms, confirming materials’ tribological characteristics, and for describing the phenomenon in terms of: roughness, hardness, ductility, oxide film, reaction layer and adhesive transfer [21, 22].

In a tribosystem, the interaction between the first bodies occurs in various hierarchical levels, and several physical processes may act. Lubrication theories may be used to study the interaction whether the lubricating regime is adequate to promote

complete separation between surfaces. However, if there is no sufficient lubrication in order to separate the first bodies, the solids characteristic and surface structures, as well as those of third bodies, shall act. This is the case for dry sliding systems and thus the lubrication theories may not be directly applied.

According to Godet (1984), in the dry sliding condition the friction coefficient is controlled by a third-body, which differs in microstructure and composition from the first bodies of the tribopair [23]. The third-body separates these first bodies and transmits the mechanical load between them. The good performance of a frictional brake system depends on the formation of a friction layer or third body, which is developed during friction [24].

## **3.2 Automotive brake system**

### **3.2.1 Disc Brake**

The main objective of a braking system is to convert kinetical energy from a movable part into heat. There are two basic available brakes for vehicles: disc brakes and drum brakes.

The disc brake consists of a rotor that spins with the wheels and two pads, the latter, during braking, exert braking torque as they are pressed against the disc connected to the wheels, the friction against the pads, as well as the friction between tires and ground, thus reducing the automobile's speed.

The heat generated by the sliding interface is initially dissipated by conduction through several of the brake's components. The discs are typically made of cast iron, while pads may be manufactured with several combinations of constituents, but are essentially made of four macro components: a matrix, reinforcement fibres, load and friction additives. The matrix is usually composed of a polymer based resin, whereas the fibres are either of metal, glass, carbon or ceramics, conferring mechanical resistance. The load is partially used to reduce costs and to enhance properties such as squealing mitigation and thermal properties. Additives to control wear and the friction coefficient may consist of solid lubricants, oxides, metallic sulphides or metallic silicate [7, 10].

Friction materials for braking application differ in many respects from most other tribomaterials, as they are designed to show a stable, higher than lubricated

coefficient of friction, without seizing during service. The coefficient of friction (CoF) is one of the most important properties of a brake system. A good value for the friction coefficient in brakes varies between 0.35 and 0.50, and should remain within those values regardless of pressure, temperature or humidity [25, 26].

### 3.2.2 Copper in brake pads

Copper is present in brake pads in the form of fibres. This presence of copper fibres in the microstructure of the brake pads is often explained based on its capacity to ensure good thermal conductivity to the component [8, 27]. The details of material composition, microstructure and processing of brake pads, however, are usually under strict industrial confidentiality and new developments usually mix several ingredients together without isolating the behaviour of each ingredient within the recipe. These developments are still predominantly based on past experience and empirical methods [9, 28].

The wear of brake pads is responsible for releasing Cu particles to the environment. About 35 to 50% of these debris are reported to become airborne and there is a widespread awareness towards the reported harmful effects of these debris to the environment and human health [29–31].

While up to 50% of the copper debris are reported to become airborne, Denier van der Gon et al. (2007) showed that the use of copper in automotive brake pads may be responsible for up to 70% of the emissions of Cu nanoparticles to the atmosphere [8].

Kukutschová et al. (2011) investigated the granulometry of the particle's emission during the use of a semi-metallic automotive brake lining. They detected the emission of nanosized particles as low as 20 nm during the use of a semi-metallic automotive brake lining [6, 32, 33].

In the United States, laws have stated a relevant reduction of copper used in brake pads. Until 2020, brake pads shall contain below 0.5 wt. % of Cu, as prior investigation confirmed the existence of a correlation between the exposure to Cu particulate pollution and pulmonary toxicity and mutagenicity [34–36].

Though the effects of copper particles to human health have been comprehensively studied in the past decade, the effects of copper debris on the composition of the tribofilm and, as result, on the friction coefficient is yet to be

unveiled. In order to minimize and suppress the use of copper in the brake pad composition, it is important to define the frictional contribution of the copper third body present at the braking tribosystem.

### 3.2.3 Graphite in brake pads

Solid lubricants are used in brakes and are responsible for providing a constant CoF between 0.3–0.5 [16]. The amount of solid lubricant was reported to influence important properties in braking: friction stability, fade resistance, anti-fade, and wear of grey iron discs [37].

Graphite with another “soft metal” is the most common combination, and has been shown as responsible for producing smooth sliding behaviour [12, 16]. The lubricity of graphite, what Savage (1948) [38] described as the “slipperiness”, depends on whether the graphite is natural or synthetic [39], adsorbed moisture [38], crystallinity, particle size [40].

### 3.2.4 Abrasive in brake pads

Jang and Kim (2000) investigated the effects of solid lubricants with abrasive inclusions. They concluded that by varying the amount of zircon in relation to antimony trisulphide, the abrasive particles were responsible for a friction film removal on the disc surface and an increase on the torque variation [41]. Indeed, one and a half decade before, Sasada et al. (1984), observed that abrasives may remove wear debris when adhesive wear mechanisms take place due to particles smaller than a critical size [42].

Moreover, abrasives are usually used in commercial brake, and consists on Zr, Si, Mg, Cr, Si compounds like zircon, quartz, alumina, chromate and magnesia. High hardness inorganic particles may be used as abrasives in brake friction materials in order to eliminate pyrolysed ingredients in the tribosurfaces [43]. Regarding abrasive particles size, in non-steel friction materials, coarse quartz ( $\text{SiO}_2$ ) and zircon ( $\text{ZrSiO}_4$ ) particles were reported to produce better friction stability and severe disc wear; whereas fine abrasive particles were found to be responsible for partially removing the transfer layer and therefore, for producing friction instability [44, 45].

In semi-metallic friction materials, Matějka et al. concluded that fixed silicon carbide particles were responsible for raising the friction coefficient's stability but also

for high disc wear <sup>[46]</sup>. Abrasive particles (~ 200 µm in size) were reported by Lazim et al. <sup>[47]</sup> to promote a change on the effective contact area, promoting smooth sliding and reducing considerably the squeal level <sup>[47]</sup>. In this sense, Kchaou et al. <sup>[48]</sup> showed that sand embedment contributed to the reduction of the CoF and the squeal noise. This friction coefficient decrease was explained by Kim et al. <sup>[49]</sup> as due to the blunting of the abrasive particles and their clogging by the wear <sup>[49]</sup>.

### 3.2.5 Copper free brake pads and novel materials

[...] the application of tribology, and especially of green tribology can provide a breathing space which would enable scientists and technologists to find solutions to these, mankind's crucial problems and allow time for them to be implemented by governments, organizations and indeed everyone operating in this important field. Consequently, this important—albeit limited—breathing space may be extremely valuable to all working for the survival of life as we know it. However, the ultimate key is science and its application. Tribology—especially green tribology can and—I am confident—will play its part to assist and give time for science to achieve the required solutions and for policy makers to implement them. (JOST, 2009 apud NOSONOVSKY AND BHUSHAN, 2010) <sup>[50]</sup>.

Green tribology was the term coined by Jost in 2009 to define the study and science of tribological aspects to develop and improve tribosystems, considering their effects on human health and the environment <sup>[51]</sup>.

Nosonovsky and Bhushan (2010) suggested borrowing ideas from Green Chemistry to evaluate the impacts of tribological technologies with quantitative metrics <sup>[50]</sup>. In this sense, the suppression of copper alongside with the overall improvement of brake pads, considering environmental aspects, is a clear challenge within the green tribology field.

Straffelini et al. (2015) reported the existence of copper-free brake pad formulations<sup>[52–54]</sup> available in patents <sup>[55]</sup>. As copper suppression becomes a reality, the final answers to this challenge reveal, once more, the industrial secrecy aspect of brake materials development.

### **3.3 Pin-on-disc tribotest to analyse the automotive brake tribological system**

As a metallic surface slides against another metallic surface, the transition from severe wear regime to mild wear regime is often observed. Severe and moderate regimes are, according to Sasada (1984), subcategories of adhesive wear. On the severe wear regime, the central mechanism is the adhesive wear, and the transition to mild wear happens as a thin oxide layer is formed on the interface, preventing direct metal-metal contact [17, 42, 56] .

Performing dry sliding pin-on-disc tribotests is a simplified yet suitable methodology to evaluate the aforementioned transition and to simulate the formation of the third body oxide layer on the tribosurfaces.

#### **3.3.1 Kato's tribotests**

Materials selection of tribosystems components may benefit from the use of Kato's tribotest methodology (2003, 2007, 2008), pin-on-disc tribotests with interfacial media addition<sup>[17-19]</sup>. They consists of a simple and useful way to compare and investigate the friction behaviour of an artificial third body friction layer. Kato et al. studied the formation of a compact oxide layer on the tribosurfaces by adding several different oxide particles to the disc track. Figure 1 displays schematically Kato's pin-on-disc methodology <sup>[17]</sup>.

Kato et al. showed exogenous interfacial media added to pin-on-disc tribotest and was able to promote rapid severe to mild wear transition explained by an early formation of an oxide protective tribofilms <sup>[17-19]</sup>. The experiment consisted of a pin-on-disc rig and exogenous interfacial media was added, from 0.1 to 0.5 g, to a machined track on the disc surface. The applied load ranged from 10 to 50 N at the sliding speed of 0.05 m/s.

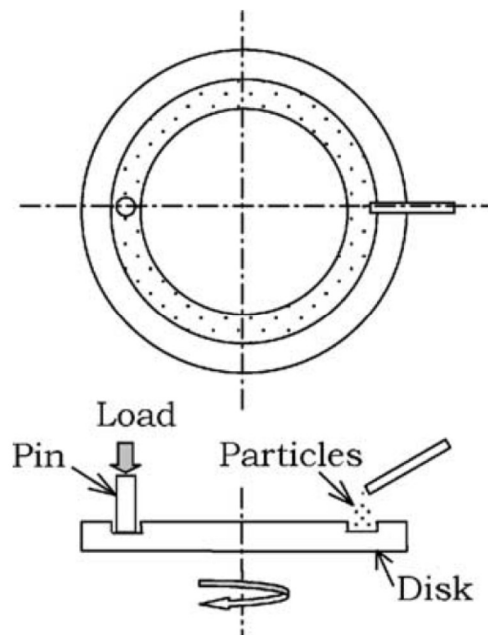


Figure 1 Kato's pin-on-disc methodology, showing the particulate interfacial media supply [17].

Kato et al. studied the effects of supply of fine oxide particles, such as  $\text{Fe}_2\text{O}_3$ ,  $\text{SnO}_2$ ,  $\text{CuO}$  and  $\text{Bi}_2\text{O}_3$ , on rubbing steel surfaces on severe–mild wear transition [18, 19]. For the  $\text{Fe}_2\text{O}_3$  addition, the sliding distance to this transition decreased and the relative area of oxide films increased more sharply when finer particles were supplied, suggesting that these fine particles were more easily sintered on the wear surface and incorporated into the tribofilm. Though in these Kato's works the conclusion uses the tribofilm formation in its discussion, it is not always shown, but only cited by the results of tribofilm early characterization in Jiang et al. [57].

The severe to mild wear transition may also alter the particles morphology, and therefore the nature of the transfer layer. However, according to Hiratsuka and Muramoto [56], “moderate particles” are found on the severe wear regime and “severe particles” are found on the mild wear regime. That is explained as the small particles go through oxidization becoming “moderates”, but when removed from the surface, the transition to mild wear regime may not occur. Furthermore, when the speed is increased, the distance also increases for the severe to mild wear transition to occur, showing that the formation of “moderate particles” is time dependent [56].

The flow of these particulate third body within the tribolayer was defined by Berthier (2001) [58]. His definition of internal source flow is used to name the detachment of particles due to STTs (superficial tribological transformations), sub-superficial cracking and creation of bounds; whereas the addition of artificial interfacial media is defined by Berthier (2001) as the external source flow  $Q_s^e$  [58].

According to Dmitriev and Österle [59], the use of Cu in brake compositions may in fact be explained by its ability to provide smooth sliding conditions and reducing noise generation at elevated temperatures. Through movable cellular automata (MCA) modelling, they indicated that tribofilms containing up to 10 wt.% of “soft” Cu mixed with Fe<sub>3</sub>O<sub>4</sub> (magnetite) particles provided the stabilization of smooth sliding. According to the authors, this stabilization was caused by the formation of a granular layer of mechanically mixed materials from the friction layers. Particles of recrystallized copper in the friction layer would provide a lubricating effect similar to graphite. The modelling results on the effect of graphite mixed with Fe<sub>3</sub>O<sub>4</sub> on the CoF have been experimentally confirmed, but the role of “soft” copper on the CoF was yet to be confirmed [60]. Previous investigations from this author indicated pure Cu addition actually increased the CoF during pin-on-disc testing at room temperature [61, 62].

### 3.3.2 Tribofilm microstructural characterization

The formation of a friction layer, or third-body developed during friction, is an important factor for ensuring the performance of frictional brake systems. Blau and McLaughlin (2003) observed the presence of friction-induced heterogeneous films, ranging from about 0.5 to 5 µm thick, on the surfaces of friction brakes and they pointed out that these deposits were responsible for the stabilization of the frictional behaviour [24]. Eriksson et al. (2001) observed that the formation of a film in braking systems was possible due to the support granted by primary *plateaus*, such as metal fibres found in the composition of brake pads [25].

Österle et al. (2009) carried out pin-on-disc tribotests with pins made from brake pad materials. They concluded that during braking, the tribosurfaces are separated by a third body, and that this third body layer is the major responsible for the friction response. Moreover, the third body consisted mostly of a nanocrystalline matrix of wear debris that went through comminution (see figure 2). The coarse wear particles featured the tendency to be ejected from the contact [26].

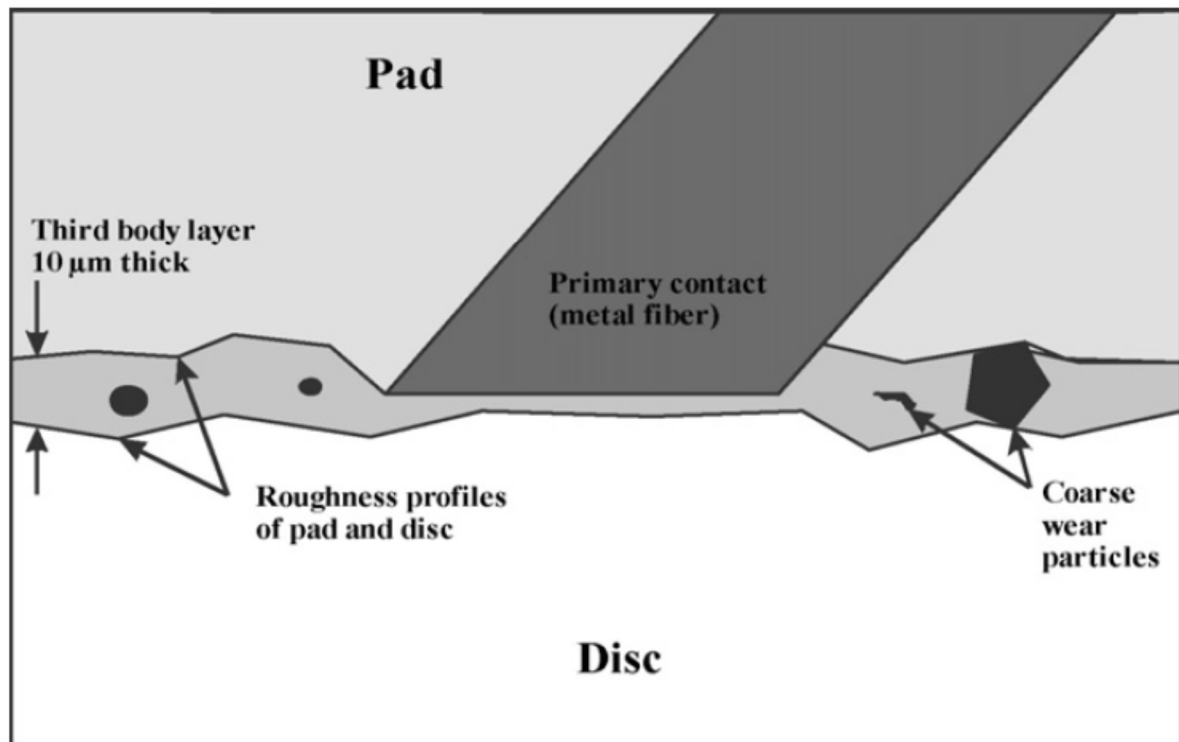


Figure 2 Schematic diagram of a cross-section showing the third body layer in Österle et al. (2009) pin-on-disc tribotest results [26].

Tribofilms in braking materials have been characterized for decades now. In the late 70's, Libsch and Rhee (1978) [63] observed that a mix of debris from pad and rotor formed tribofilms and the reduction of iron and graphite grain sizes. A plastically deformed layer was also shown in their study. A comprehensive characterization of this third-body and transfer layers started over a decade ago with the studies of Österle and Urban (2006) [64] on the role of the microstructure and third body on friction properties of brake materials, showing the presence of several nanocrystalline oxide phases on the tribosurfaces for different compositions of the brake pad tribosystems. By characterizing the transfer layers, it was possible to observe the nanocrystalline microstructure of the third-body on the tribosurfaces [29, 64, 65]. They concluded that besides mechanical mixing, oxidation is also responsible for the production of wear debris and the formation of the friction layer. They suggested one focus for further studies was to work out differences of friction layer formation for selecting new pad material formulations to fulfil the environmental criteria [64].

Concerning materials characterization of brake components, iron oxide is commonly among the sampled wear debris of brake commercial materials. Several studies reported the presence of iron and iron oxide within the debris, as well as the presence of copper transferred from the brake pads to the brake disc [65–68]. Further investigation showed the iron oxide within the wear particles is mostly composed of magnetite ( $\text{Fe}_3\text{O}_4$ ) [64, 69], and that obtaining smooth sliding conditions requires mixing magnetite with the other pad constituents [70].

The presence of metallic copper within the wear debris was reported by several studies. Copper oxide on the other hand, was rarely found [26, 65, 69, 71–73]. In that sense, Österle and Dmitriev (2016) stated [16] and showed by the use of computational models [27, 59, 60, 70, 74–76] that soft metallic particles may adopt the function of solid lubricants like graphite or metal sulphides. More recently, Straffelini et al. (2015) [55] reviewed the past efforts on unveiling how copper acts on the transfer layers. They showed copper was reported to promote the formation of compacted transfer layers in the pad's surface [13, 71, 76]. Composite brake pads with copper powder loads were reported by Kumar and Bijwe (2013) to form a film on the pad's surface [77].

Mosleh et al. (2004) showed the distribution of brake debris has nano and microsized particles, the nanoscale particles have higher concentrations of Fe, O and C [68]. Once again, the product of brake wear consists basically of iron oxide agglomerates. The disc debris are more likely to form sub-micron wear particles, while pads form micron-sized wear debris, Cu debris included. Österle and Dmitriev (2016) [16] considered that the micron-sized particles represent the early stages of pad wear. Roubicek et al. (2008) showed also the presence of nanocrystalline particles within the third body [78].

Temperature has also been reported to play a role on the tribological characteristics. Jacko (1978) showed that the wear increases with the rise of temperature. He also observed a black tribofilm, probably consisting of magnetite mixed with carbonaceous material [79]. A decade later, this tribofilm was found to be continuously formed by the compaction of wear debris, and sheared on both counter bodies. [80]

By the use of drag tests at elevated temperatures, Cho et al. (2005) obtained transfer layers of 10 to 50  $\mu\text{m}$  thick. Such thick layers are not very common in practice,

but in this study solid lubricants were found to impact the transfer layer thickness and provide smoother sliding without much impact on the CoF [43].

Moreover, on the use of solid lubricants, EDS-maps from Yin and Yan (2007) shows greater material transfer from the use of formulations with addition of solid lubricants. The transferred layer was probably responsible for the stabilization of the friction coefficient and led to a reduction in wear. [81]. Österle and Urban (2006) have also shown that Fe-constituents within the third body were mixed with solid lubricants on the nanometer scale [64]. As a result, a nanocrystalline third body composed of a magnetite matrix with embedded graphite nanocrystals is formed [82]. Kato had already pointed out that tribo-elements softer than the matrix may form a soft layer on the counter surface and thus decrease wear rates, while moderate hardness tribo-elements such as Al, Cu, Ni, Fe may lead to severe plastic deformation resulting on larger wear rates and the destruction of this protective transfer layer.

Focused ion beam (FIB) and transmission electron microscopy (TEM) characterization were able to show a plastically deformed layer below the tribofilm at the disc surfaces [61, 62, 70, 78, 82]. Österle et al. (2014) explained low friction cases by the protection of the steel first bodies by a third body film, the destruction of this film, however, would lead to higher friction and severe plastic deformation of the steel substrate [83]. Roubicek et al. (2008) results showed a zone of severe plastic deformation of commercial non-asbestos brake lining and iron brake. In their work, a thin discontinuous layer was observed, partially covering the tribosurface [78].

Österle and Dmitriev (2016) observed nanocrystalline  $\text{Fe}_3\text{O}_4$  as the main third body matrix formed during multiple braking events, alongside with nanoparticles of graphite and other soft ingredients, as well as submicron-sized abrasives such as  $\text{ZrO}_2$  or  $\text{Al}_2\text{O}_3$ . Leading to their description of the third body structure as: “A certain amount of soft nanoinclusions ( $d < 10$  nm) and some bigger hard inclusions (50–100 nm) homogeneously distributed in an agglomerate of brittle oxide nanoparticles” [16].

### **3.4 Previous tribotests and tribosurfaces microstructural characterization from author**

Previous works from Rodrigues et al. (2015), investigated by means of Kato's pin-on-disc tribotest, the effect of adding Cu particles with different particle sizes on the CoF and microstructure of the pins' and discs' tribologically transformed surface (TTS) using pin-on-disc tribotest (steel against steel). They compared the effects of Cu addition with other systems (with addition of graphite and magnetite as interfacial media and without any addition).

The particulate copper, for all three granulometries, did not show a behaviour comparable to the solid lubricant (graphite) tested, and for all copper additions, the friction coefficient increased with the decrease of the particle size <sup>[61]</sup>.

The cross-sections of the pins were examined in a dual beam FIB-SEM microscope to study the formation of transfer layers and third body and to investigate the microstructural changes near the tribosurfaces (to a depth of approximately 15  $\mu\text{m}$ ). Furthermore, the addition of copper powder to the pin-on-disc test was able to form a transfer layer with the presence of oxygen, as showed by EDS, suggesting that there was the formation of oxide third body. EDS mapping was able to find the presence of copper on pin surfaces of the systems with copper particulate addition with particle size of 20  $\mu\text{m}$  (see figure 3) and 50 nm <sup>[61, 62]</sup>.

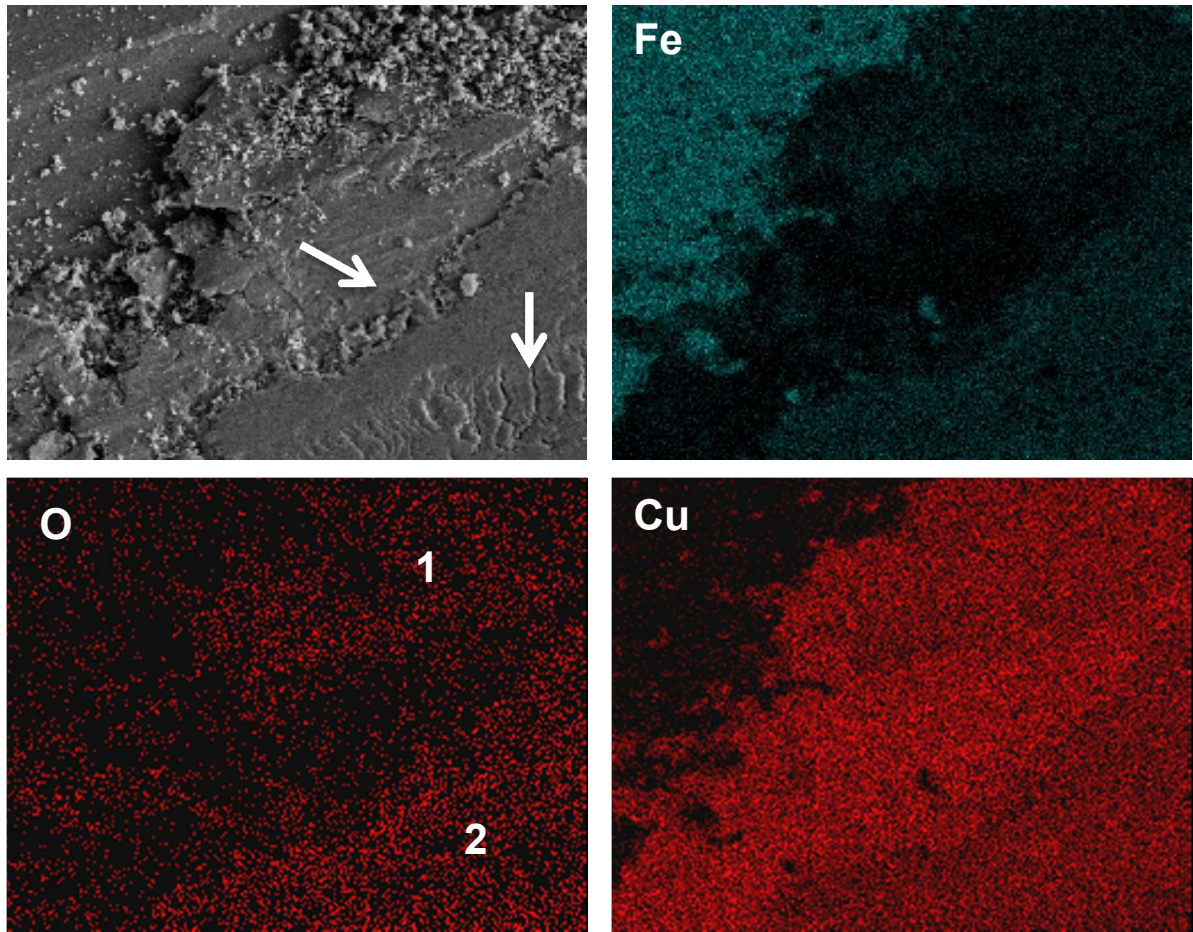


Figure 3 Topographic examination of disc surface after tribotest for the condition Cu20m and respective XEDS mapping results. a) Secondary electron image showing the presence of flat continuous surfaces (see arrows) as well as loose debris and wear marks. b) XEDS mapping for Fe is inhomogeneous, showing a higher Fe content on the upper left corner of the figure. c) O XEDS mapping indicating higher O content in regions with loose particles deposit (region 1) as well as smoother surfaces (region 2). d) XEDS mapping for Cu inhomogeneous, showing a higher Cu content on the lower right corner of the figure [62].

FIB characterization showed debris on the surfaces formed compact and continuous oxide layer observed only for the systems with copper particulate addition with granulometry of 400  $\mu\text{m}$  (figures 4 and 5), and on the condition with no interfacial media addition, 10 N of applied normal load. For the systems with copper particulate addition with granulometry of 20  $\mu\text{m}$  and 50 nm, debris on the tribosurface were able to go through oxidation and some degree of sintering, but they were not able to form a compact film for 10 N of applied normal load [61, 62].

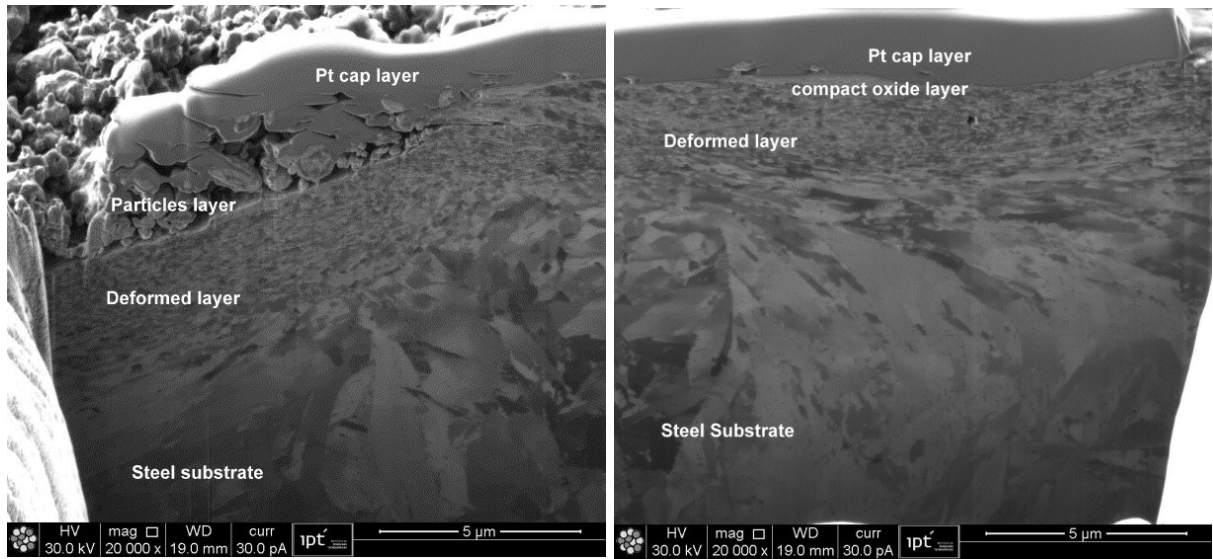


Figure 4 a) and b) FIB cross-section on the pin surface after tribotesting with no interfacial media addition. It is possible to observe the plastically deformed layer under the Pt deposition as well as the presence of particulate debris on the left image and a thin continuous layer on the image to the right. Additionally, the pin microstructure shows the presence of a plastically deformed region ( $\sim 3 \mu\text{m}$ ) near the tribosurface [61].

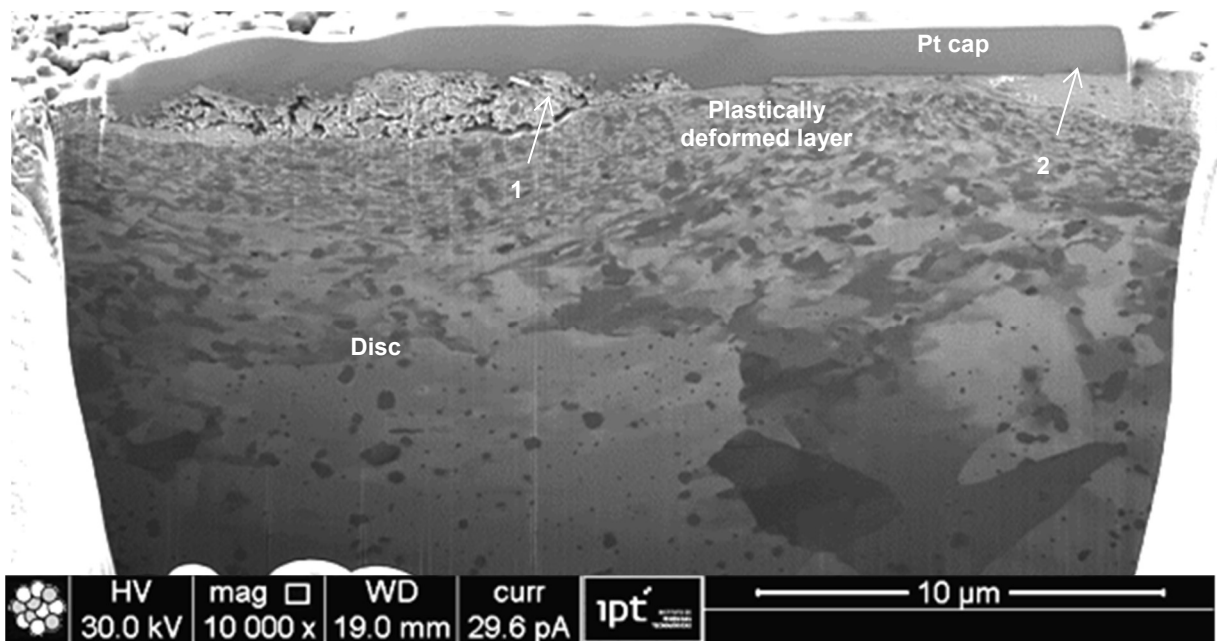


Figure 5 FIB cross-section of the disc surface after tribotesting with addition of  $400 \mu\text{m}$  copper (Cu400m). a) A plastically deformed layer of approximately  $2 \mu\text{m}$  may be seen under the Pt deposition. Arrow 1 points to the presence of wear debris at the asperity valley, whereas arrow 2 points to a thin grey continuous compact oxide layer at the asperity peak [62]

The present study is a step further, using pin-on-disc tribotests to investigate the formation of oxide transfer layer on the surface of the first bodies. The use of third body mixtures composed of nanoparticulate copper, magnetite, graphite and zirconium oxide enhanced the tribofilm model. Furthermore, high temperature tests were incorporated to the previous studies parameters as well as the use of nitrogen atmosphere. The resulting transfer layers were observed by means of scanning and transmission electron microscopy alongside with focused ion beam characterization.

## 4 MATERIALS AND METHODS

### 4.1 Interfacial media additions

Dry powders of nanocrystalline aggregates of magnetite, copper and graphite were used in the present investigation. The interfacial media additions consisted of different mixtures of these particles. Copper and iron oxide nanopowders (50 nm) were purchased from Sigma Aldrich and the graphite cathode chips (25  $\mu\text{m}$ ) were donated by Comercial de Peças de Grafite S.A.. Figure 6 and Figure 7 show copper and graphite particles as received, prior to the tribotests and mixing process.

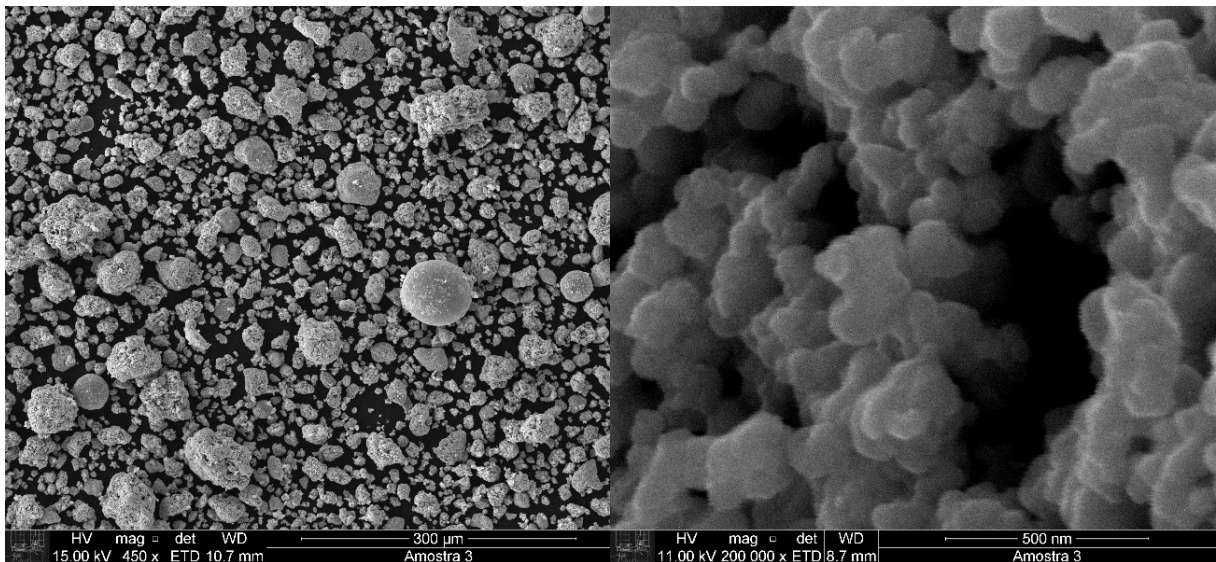


Figure 6 Copper aggregates as received SEM-SEI. a) Copper particles in micron-sized agglomerates. b) Detail from copper agglomerates.

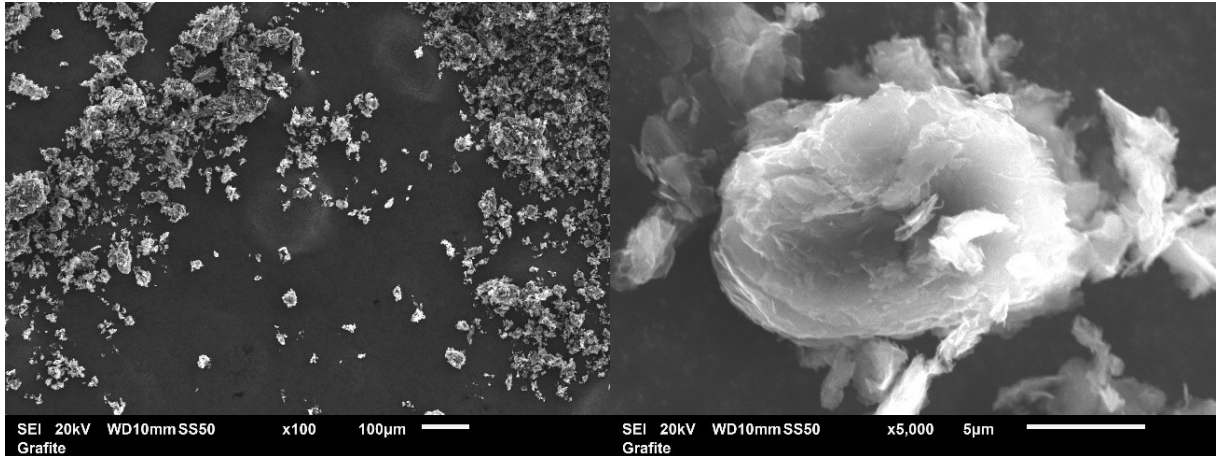


Figure 7 Graphite cathode chips as received SEM-SEI. a) Graphite particles in micron-sized distribution. b) Detail from graphite particle.

Magnetite was used as the main mixture matrix component, over 85% in volume, because of its already cited presence as main wear debris in several previous brake's characterization studies [64–70]. And because experimental and modelling results have showed and proposed explanations on why smooth sliding is achieved with friction coefficient values of at least 0.35 when magnetite is mixed with soft particles [73].

By seeking to achieve homogeneous mixtures, different mixing methods were employed, and the terms used to define the mixing processes are described in the table 1.

Table 1 Mixing processes.

<b>Acronym</b>	<b>Mixing process</b>	<b>Description</b>
MM	Manual mixing.	The powders were mixed for 4 minutes by the use of pestle and mortar.
BM	High-energy ball milling.	The powders were mixed for 3h (with sampling after 15 min, 30 min, 1h30min) in a 2L high-energy ball mill at ZoZ company in Olpe, Germany. ZrO <sub>2</sub> balls were used as grinding media.

MM mixtures were prepared by means of pestle and mortar during 4 minutes at 23°C, whereas BM mixtures were prepared at 23°C by a 2L high-energy ball mill at ZoZ company (Olpe, Germany) for 3 h using ZrO<sub>2</sub> balls as grinding media. As consequence, BM condition contain a relevant amount of ZrO<sub>2</sub> in the final interfacial mixtures. The percentages of ZrO<sub>2</sub> in the BM mixtures were quantified by means of Particle-Induced X-ray Emission (PIXE) analysis as described by Silva et al. [84].

The interfacial media mixtures were divided in six main groups (see below) and table 2 shows the compositions investigated (all percentages are in volume):

- Pure Fe<sub>3</sub>O<sub>4</sub>.
- Binary graphite-magnetite mixtures: 15 % in volume of graphite cathode chips mixed with nanoparticulate magnetite (Fe<sub>3</sub>O<sub>4</sub>).
- Binary copper-magnetite mixtures: 6 and 15% in volume of nanoparticulate Cu mixed with nanoparticulate magnetite (Fe<sub>3</sub>O<sub>4</sub>).
- Ternary graphite-copper-magnetite mixtures: 7.5% Cu + 7.5% graphite + with nanoparticulate magnetite (Fe<sub>3</sub>O<sub>4</sub>).
- Ternary ZrO<sub>2</sub>-Cu-magnetite mixtures: 8% Cu + 3% ZrO<sub>2</sub> mixed with nanoparticulate Fe<sub>3</sub>O<sub>4</sub>.
- Quaternary ZrO<sub>2</sub>-graphite-Cu-magnetite: 6% Cu + 6% graphite + 4% ZrO<sub>2</sub> and 7.5% Cu + 7.5% graphite + 1%ZrO<sub>2</sub>, both mixed with nanoparticulate Fe<sub>3</sub>O<sub>4</sub>

Table 2 Investigated mixtures and conditions

	Mixture (Systems)	Composition (vol.%)	Mixing method	Temp.	Atm.
<b>Pure Magnetite</b>	(Fe <sub>3</sub> O <sub>4</sub> )	100% Fe <sub>3</sub> O <sub>4</sub>	none	23°C	Air
			none	400°C	Air
<b>Binary</b>	(Cu-Fe <sub>3</sub> O <sub>4</sub> )	94% Fe <sub>3</sub> O <sub>4</sub> + 6% Cu	MM	23°C	Air
			MM	400°C	Air
			MM	400°C	N <sub>2</sub>
			MM	23°C	Air
			MM	400°C	Air
			MM	400°C	N <sub>2</sub>
	(graphite-Fe <sub>3</sub> O <sub>4</sub> )	85% Fe <sub>3</sub> O <sub>4</sub> + 15% C	MM	23°C	Air
			MM	400°C	Air
			MM	400°C	N <sub>2</sub>
			MM	400°C	N <sub>2</sub>
<b>Ternary</b>	(Cu-graphite-Fe <sub>3</sub> O <sub>4</sub> )	85% Fe <sub>3</sub> O <sub>4</sub> + 7.5% C + 7.5%Cu	MM	23°C	Air
			MM	400°C	Air
			MM	400°C	N <sub>2</sub>
	(ZrO <sub>2</sub> -Cu-Fe <sub>3</sub> O <sub>4</sub> )	89% Fe <sub>3</sub> O <sub>4</sub> + 8% Cu + 3% ZrO <sub>2</sub>	BM	23°C	Air
			BM	400°C	N <sub>2</sub>
			BM	400°C	N <sub>2</sub>
<b>Quaternary</b>	(ZrO <sub>2</sub> -Cu-graphite-Fe <sub>3</sub> O <sub>4</sub> )	84% Fe <sub>3</sub> O <sub>4</sub> + 6%Cu + 6% C+ 4% ZrO <sub>2</sub>	BM	23°C	Air
			BM	400°C	Air
			BM	400°C	N <sub>2</sub>
			MM	23°C	Air
			MM	400°C	Air
			MM	400°C	N <sub>2</sub>

## 4.2 Tribotests

Two different test rigs were used for the tribotests. The tribometer referred to as WZ is a commercial pin-on-disc tribometer of the WAZAU-SST type, and may only be used for testing in ambient air. It features a maximum applicable load of 2000 N and a maximum rotational speed of 3000 rpm. The normal force is applied to the support of the disc by means of an adjustable spring. The other rig, a high-vacuum tribometer referred to as VT1 is used for testing in inert atmosphere and wider range of temperatures (the sample can be cooled to -80 or heated to 500°C). The samples are mounted inside a vacuum chamber, which may be evacuated to a residual pressure of  $10^{-5}$  mbar. The drive allows a rotational speed up to 3000 rpm, corresponding to a maximum sliding velocity of  $7 \text{ ms}^{-1}$ . Both tribometers, WZ and VT1, provide a test rig with a stationary disc and a rotating pin that rubs against the disc (see Figure 8). The discs presented a 65 mm diameter.

The mixtures were tested at 23°C in air, 400°C in air and 400°C in  $\text{N}_2$  atmosphere using pin-on-disc tribotest with steel counter bodies.

Pin-on-disc tribotests used DIN St52 ferritic-pearlitic steel for the pins ( $293 \pm 9$  HV) and discs ( $198 \pm 4$  HV). The interfacial media (mass of 0.1g) was added to the machined track on the disc's surface before the start of the tribotest.



Figure 8 Schematic presentation of the pin-on-disc tribometer used in this study. (Image kindly provided by Dr. Thomas Gradt).

The duration of the tribotest was 60 minutes using a normal load of 20 N and speed of 0.05 m/s at either  $23 \pm 2^\circ\text{C}$  or  $400^\circ\text{C}$  in air (relative humidity  $40 \pm 5\%$ ) and  $\text{N}_2$  dry atmosphere. The evolution of the CoF was recorded for each condition during tribotest. The curves were plotted with a Python routine that, in the case of the WZ tribometer, calculated a “smooth” average CoF curve based on a moving average box (by convolution). The CoF evolution curves are presented in the Annex. The average values of the CoF and their standard deviations were calculated by Origin software using all CoF values within the time interval from 0 to 3600 s.

### 4.3 Characterization

The ability of these mixtures to form a tribofilm was investigated by microstructural characterization - SEM (scanning electron microscopy) associated with FIB (*focused ion beam*), EDS (energy dispersive X-ray spectroscopy) and EDS mapping techniques - using dual beam FEI Quanta 3D FEG microscope and single beam Strata 100xp FIB. Furthermore, the incorporation of  $\text{ZrO}_2$  to the BM mixtures was quantified by means of Particle-Induced X-ray Emission (PIXE) analysis with external beam as described by Silva et al.<sup>[84]</sup>.

For each group of mixtures, a series of FIB cuts were performed to the discs' and pins' tribosurfaces. FIB cross-sections used the principle of the ion beam milling and deposition technique. FIB systems can provide a high milling and deposition rate of the order of  $1 \text{ mm}^3 \text{ nC}^{-1}$  <sup>[85]</sup>. The FIB cuts were performed similarly to the cross-sections described in <sup>[26, 69, 74, 86]</sup>. That is, a platinum cap of up to  $30 \times 2 \times 2 \mu\text{m}$  was deposited by FIB-induced chemical vapour deposition on the samples surface, resulting on a protective layer of solid Pt cap as visible in Figure 9-a. Material removal was carried out by FIB milling, with Ga ions to create a clean observable cross-section (see Figure 9-b) without damaging the third body layer adhered to the tribosurface. Figures 9-c and 9-d present images generated by secondary electrons (SE) produced from the beams interaction with the cross-section surface, figure 9-c shows a scanning electron microscopy (SEM) while figure 9-d presents the scanning ion microscopy (SIM) the electrons beam and the ions beam. Ions present lower range in matter in comparison to electrons, therefore, SE produced in SIM carry information only from the surface <sup>[85]</sup>. According to Volkert and Minor (2007), ion beams offer generally lower resolution than electron beams, but the contrast observed at SIM features stronger

channelling from crystals than SEM imaging [87]. The FIB cross-sections presented in this work were all performed by SIM, in order to reveal compaction and microstructural information of the third body layer in more detail than the SEM image is able to deliver.

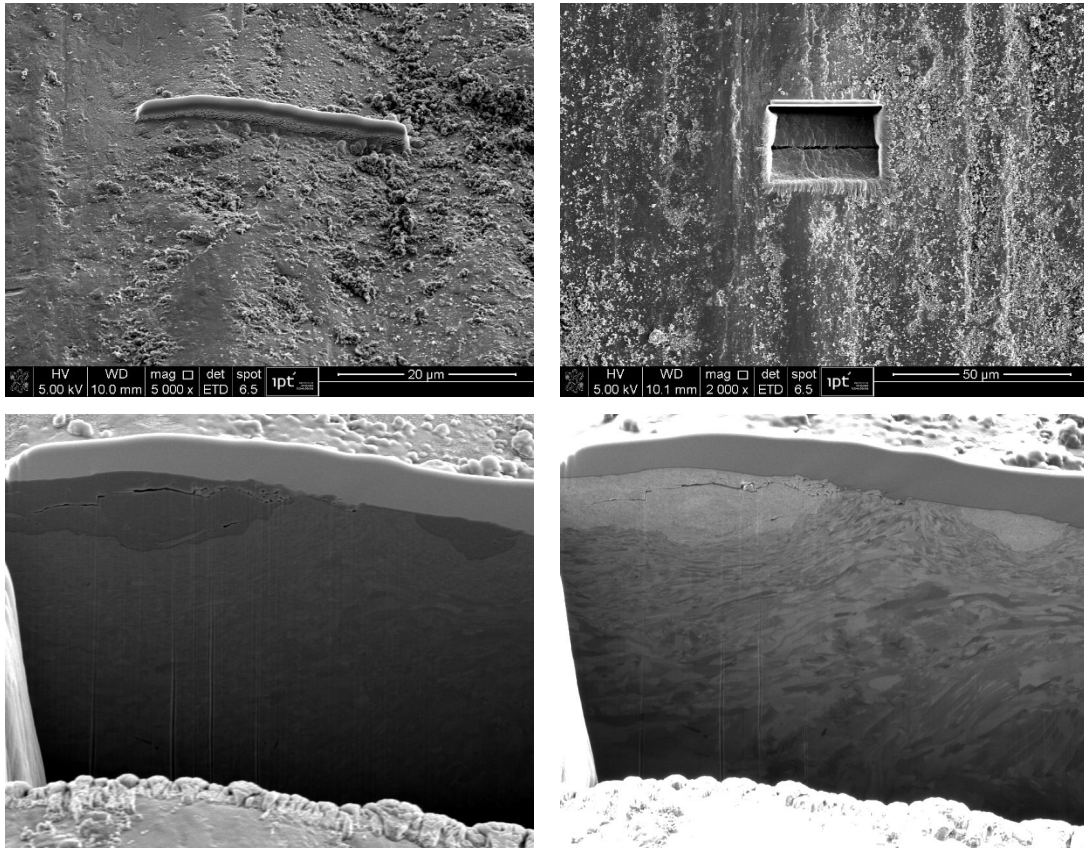


Figure 9 a) Pt cap deposition prior to FIB cutting, tilt of 52 ° (SEI); b) FIB cross section surface view; c) FIB cross section observed with the electrons beam (SEM-SEI); d) FIB cross section observed with the Ga ions beam (SIM-SEI).

For a few chosen conditions, transmission electron microscopy was carried out in a TEM/STEM JEOL JEM 2200FS (field emission gun (FEG), 200 kV, ultra-high resolution (UHR) pole piece, in-column energy filter). In addition, it is equipped with a liquid N<sub>2</sub> free energy dispersive X-ray SDD an ASTAR system for scanning nano-beam electron diffraction including the ACOM software for calculations of phase and orientation maps. Lastly, this TEM is equipped with a DigiScan device for STEM, two dark-field detectors as well as a bright field detector and a 1 k slow-scan CCD camera. The preparation of the TEM lamellae was as described by Österle and Urban (2006) [64].

## 5 RESULTS

### 5.1 Mixture characterization

Two mixing methods were performed in this study: manually mixing (MM) and high-energy ball milling (BM). Mixtures performed with each of the two methods were characterized to assess their morphology and degree of homogenization.

Figure 10 shows the MM ternary (Cu-graphite-Fe<sub>3</sub>O<sub>4</sub>) mixture before (figure 10-a) and after (figure 10-b) the 4 minutes mixing with pestle and mortar. The result of crushing the mixture manually with pestle and mortar was enough to break the bigger agglomerates apart, and therefore obtain sub-micron sized granulometry. This simple pestle and mortar 4 minute step became part of the tribotest preparation routine just as important as cleaning the first bodies prior to the test.

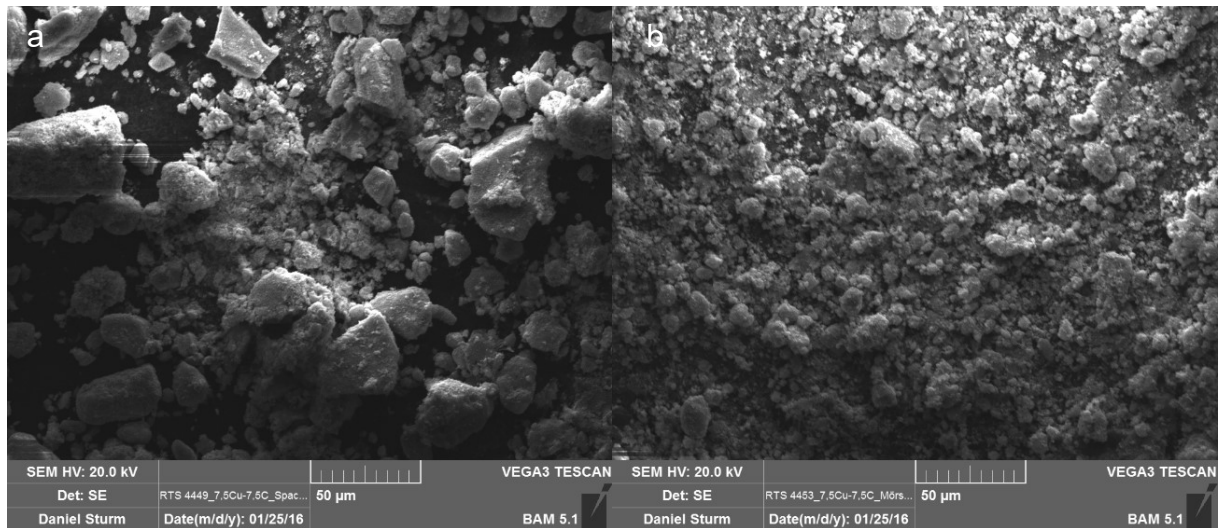


Figure 10 Ternary (Cu-graphite-Fe<sub>3</sub>O<sub>4</sub>) MM mixture. Morphological characterization of the addition: a) before mixing with pestle and mortar; b) after mixing for 4 minutes with pestle and mortar.

Figure 11 shows the morphological characterization of the BM quaternary (ZrO<sub>2</sub>-Cu-graphite-Fe<sub>3</sub>O<sub>4</sub>) mixture sampled after 30 min, 90 min and 3 hours of milling, alongside with the Zr XEDS mapping for the 3 hours milled mixture used as addition. The mixtures milled during 30 and 90 minutes (figures 10-a and b) present sub-micron sized granulometry and similar appearance between them. Moreover, they look also similar to the mixed media with pestle and mortar (Figure 10-b). Figure 11-c shows ball milling for 3 hours seems to have formed larger agglomerates during the longer milling

process. Furthermore, Zr-rich particles are observable in the Zr EDS elemental mapping (Figure 11-d). The Zr-rich particles are present throughout the mixture, as well as in the larger agglomerate visible on the bottom left side (see arrow), the presence of Zr confirms the incorporation of  $ZrO_2$  from the grinding media used on the milling process.

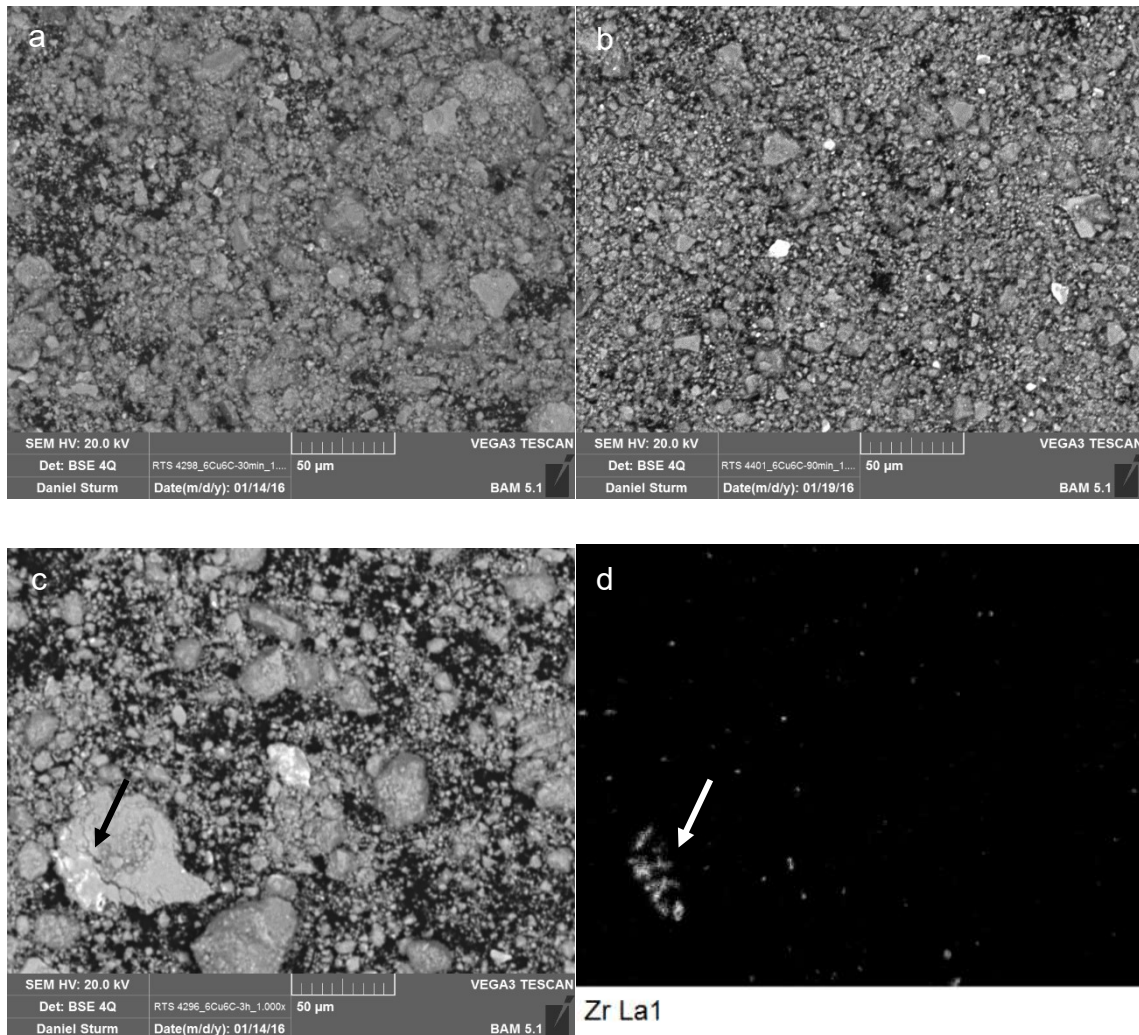


Figure 11 Quaternary ( $ZrO_2$ -Cu-graphite- $Fe_3O_4$ ) BM mixture. Morphological characterization. Ball mixed for: a) 30 minutes; b) 90 minutes; c) 3 hours; d) Zr EDS elemental mapping of the 3 hour ball milled mixture.

A BM quaternary ( $ZrO_2$ -Cu-graphite- $Fe_3O_4$ ) mixture sample was analysed by means of TEM. Figure 12-a shows a bright field TEM image of the BM quaternary ( $ZrO_2$ -Cu-graphite- $Fe_3O_4$ ) mixture. Figure 12-b to 12-f feature the EDS elemental mapping for C, O, Fe, Cu and Zr respectively. C, O, Fe and Cu are visible in the whole

sample. Thus, indicating carbon and copper are homogeneously distributed throughout the mixture.

Figure 12-e suggests copper is present in the form of nanoparticles. Zirconia particles, introduced during ball milling with  $ZrO_2$  balls, are not homogeneously distributed to the nanometre scale (see Figure 12-f), but appear as larger sub-micron particles.

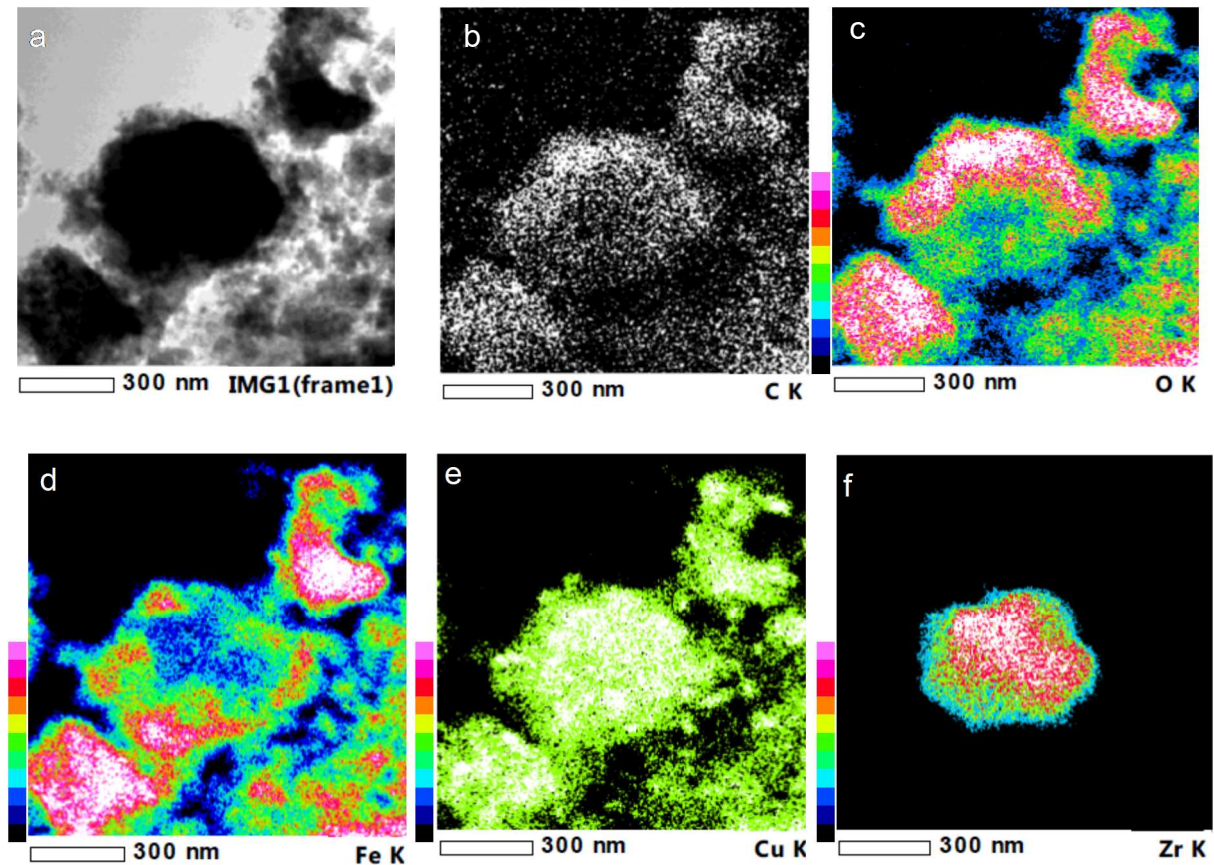


Figure 12 - Quaternary ( $ZrO_2$ -Cu-graphite- $Fe_3O_4$ ) BM mixture. a) TEM Bright field image; b) C EDS elemental mapping; c) O EDS elemental mapping; d) Cu EDS elemental mapping; f) Zr EDS mapping.

Figure 13-a shows a TEM image of the mixture's nanoparticles, varying from 10 to 80 nm in size. Figure 13-b shows the graphite structure detail, in high resolution TEM (HR-TEM) from a region in Figure 13-a (see arrows). Copper nanoparticles are not resolved by HR-TEM because of their smaller lattice planes spacing, in comparison to graphite.

Figure 14 shows the TEM image of agglomerates of particles that vary from 10 to 60 nm in size.

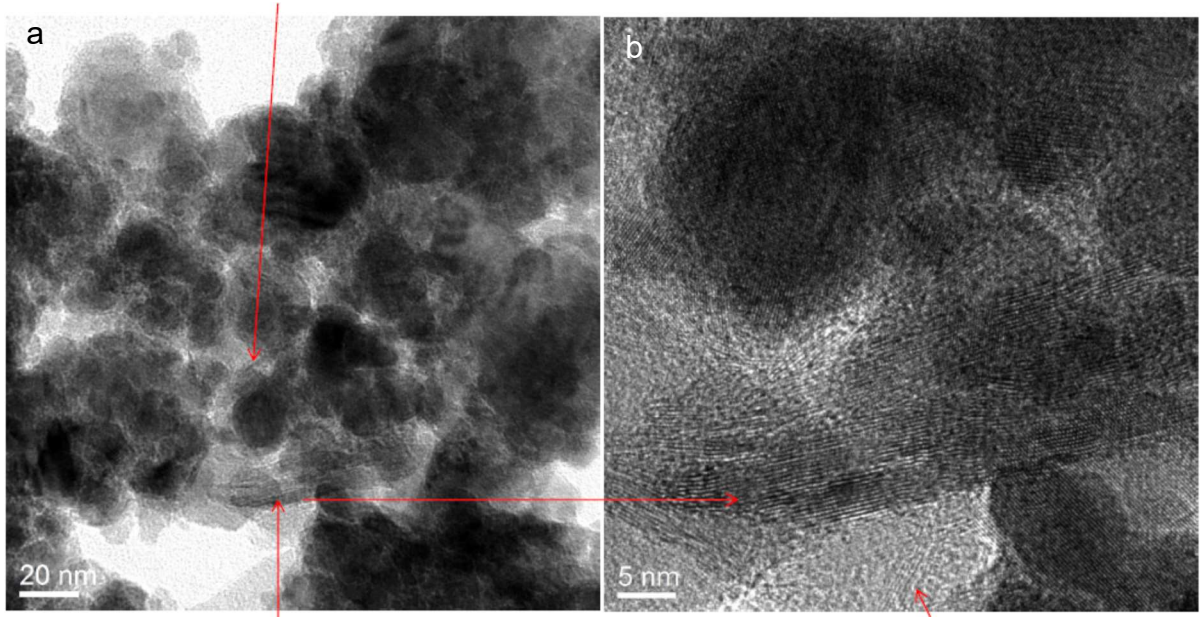


Figure 13 - Quaternary ( $ZrO_2$ -Cu-graphite- $Fe_3O_4$ ) BM mixture: a) TEM image showing the particles size in the agglomerates range in size from 10 to 80 nm. b) HR-TEM image, the detail shows the graphite curved lattice structure inside the particles agglomerates.

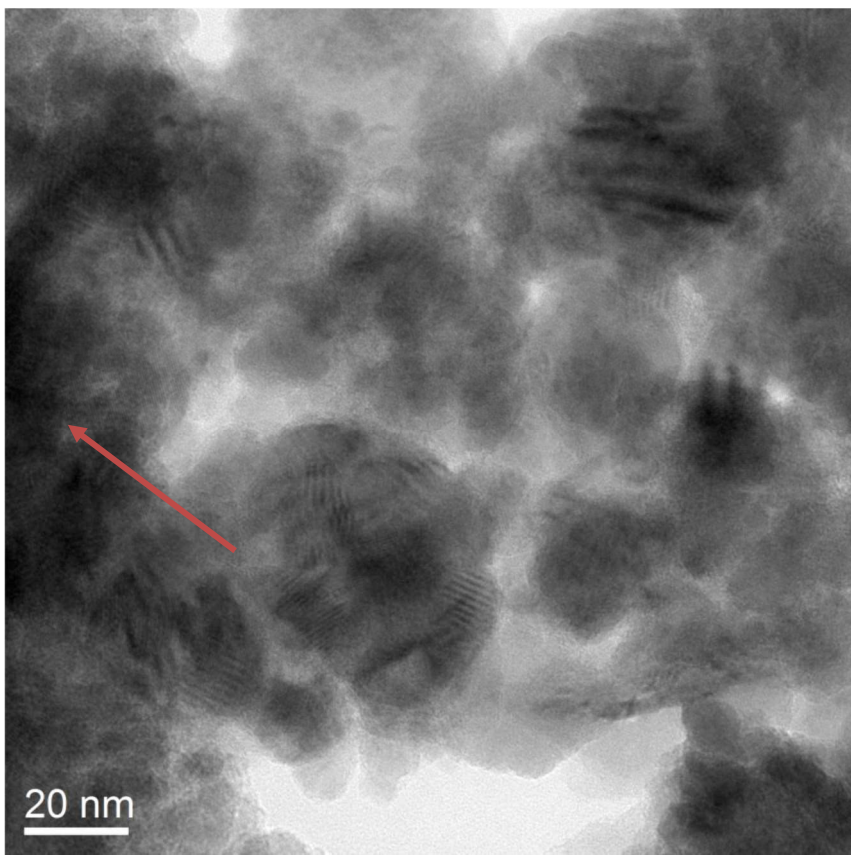


Figure 14 Quaternary ( $ZrO_2$ -Cu-graphite- $Fe_3O_4$ ) BM mixture. TEM image showing the particles size in the agglomerates ranges from 10 to 60 nm.

## 5.2 Overview of the friction coefficient results

For each condition herein studied, an average CoF value was calculated with the tribotests acquired CoF data. An overview of all systems and respective conditions is presented in figure 15. The tribotest evolution curve for each condition is presented in the Annexes 1 to 6. The results for each system displayed in Table 2 will be described individually and compared between them in the end of the results section.

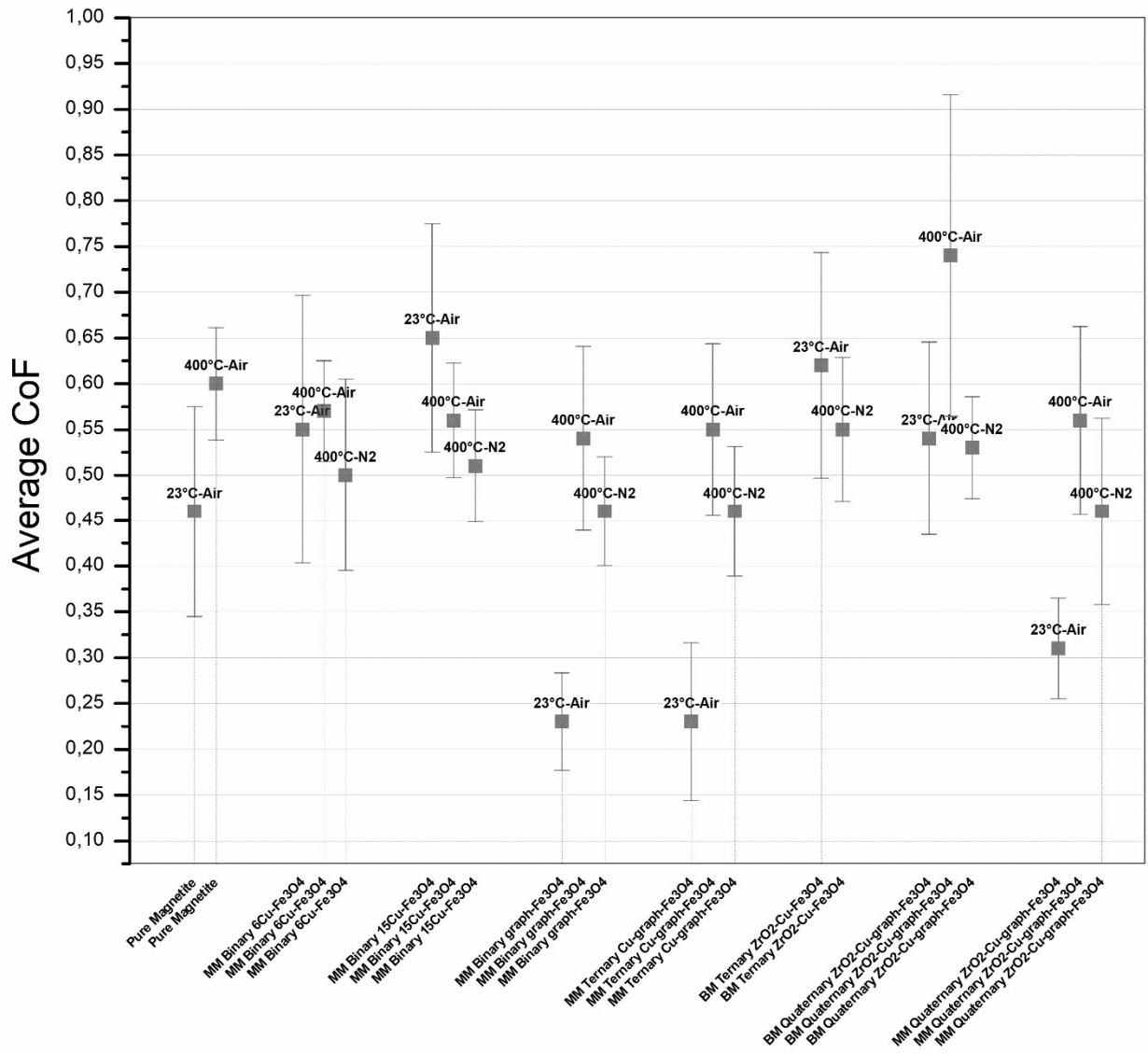


Figure 15 Summary of the average values of the CoF of all investigated mixtures, in terms of conditions tested.

### 5.3 Pure Fe<sub>3</sub>O<sub>4</sub> system

The pure Fe<sub>3</sub>O<sub>4</sub> system was tested in two conditions: 23°C in air and 400°C in air. The average CoF values for these conditions and their standard deviation are presented in Table 3.

The average CoF value obtained for pure Fe<sub>3</sub>O<sub>4</sub> system tested at 23°C in air differed from the same system tested at 400°C in air, rising the average CoF value from 0.46 to 0.60, respectively (see Table 3). The evolution curves for both conditions, 23° and 400°C in air show stable average curves, with the presence of a few peaks for the pure Fe<sub>3</sub>O<sub>4</sub> tested at room temperature (see Annex 1). At 400°C in air, the evolution curves for tribotests present extremely stable CoF without the presence of peaks (see Annex 1).

Table 3 Average CoF values for the pure Fe<sub>3</sub>O<sub>4</sub> conditions.

	Mixture (Systems)	Composition (vol.%)	Mixing method	Temp.	Atm.	Average CoF	Standard Deviation	Tribotest repetitions
<b>Pure Magnetite</b>	(Fe <sub>3</sub> O <sub>4</sub> )	100% Fe <sub>3</sub> O <sub>4</sub>	none	23°C	Air	0.46	0.12	3
			none	400°C	Air	0.60	0.06	3

#### 5.3.1 Characterization of the pure Fe<sub>3</sub>O<sub>4</sub> system

Figure 16 shows macrographs of the pure magnetite system tested at 23° in air and 400°C in air (Figure 16-a and Figure 16-b, respectively). The pure magnetite interfacial media addition in Figure 16-a remained black, whereas tests carried out at 400 °C in air (Figure 16-b), display a change in the colour of the magnetite addition, black to a brownish red, with some reminiscent regions of black transfer layer. Magnetite at 400°C is not a stable form of iron oxide and its partial transformation to hematite is thermodynamically favourable at this temperature. The change of colour observed for tests performed at 400 °C in air suggests magnetite transformed, at least partially, to hematite at this condition. This hypothesis will be further investigated by means of selected area electron diffraction (SAED) in further sections.

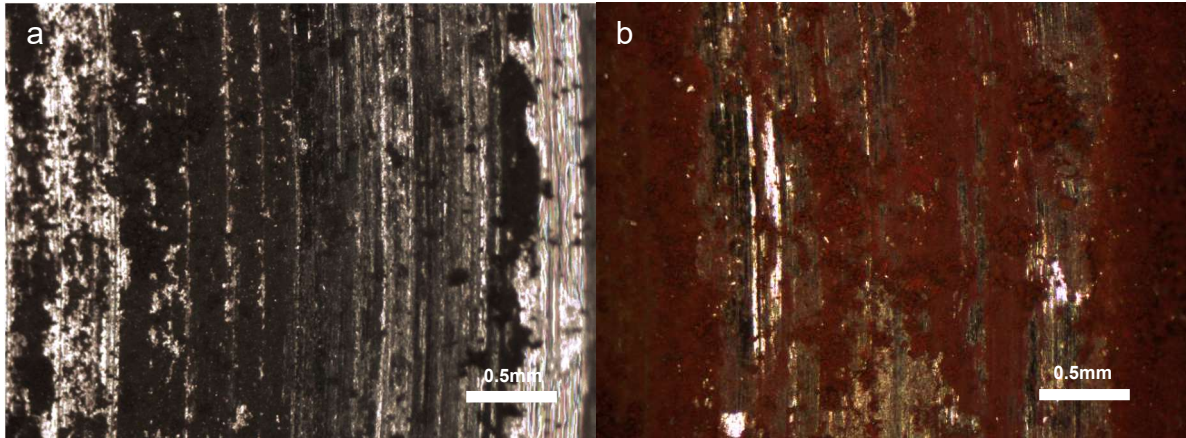


Figure 16 Disc, pure  $\text{Fe}_3\text{O}_4$ . Macrograph for system tested at: a)  $23^\circ\text{C}$  in air ( $\text{CoF}\sim 0.46$ ); b)  $400^\circ\text{C}$  in air ( $\text{CoF}\sim 0.60$ ).

Figure 17 presents a FIB cross-section of the pin's surface tested at  $23^\circ\text{C}$  in air with pure  $\text{Fe}_3\text{O}_4$  addition. The transfer layer ranges is approximately  $4\ \mu\text{m}$  thick. The tribolayer is a compact powder agglomerate, with the presence of a longitudinal crack. The arrow points metallic debris, indicating material detachment from the first body's tribologically transformed surface (TTS), which was further trapped within the transfer layer. A compact oxide transfer layer is visible between layers of the metallic first body (see circle). This region is smoother than the oxide transfer layer at the pin's surface and does not show the agglomerate aspect. The depth of the plastically deformed layer varies from  $3$  to  $5\ \mu\text{m}$  in thickness.



Figure 17 Pin, pure  $\text{Fe}_3\text{O}_4$  tested at  $23^\circ\text{C}$  in air, FIB cross-section. The depth of plastically deformed layer ranges from 3 to  $8\ \mu\text{m}$ . The depth of the transfer layer is approximately  $4\ \mu\text{m}$  and shows cracks within. The arrow points to metallic debris trapped within the transfer layer. A compact oxide transfer layer is visible between layers of the metallic first body (see circle). ( $\text{CoF}\sim 0.46$ ).

Figure 18 features a FIB cross-section of the pin's surface tested at  $400^\circ\text{C}$  in air with pure  $\text{Fe}_3\text{O}_4$  addition. The transfer layer displays a compact powder agglomerate region that is approximately  $0.5\ \mu\text{m}$  thick, and a very smooth compact region of approximately  $5\ \mu\text{m}$  thick. Cracks are visible within both transfer layer regions. The arrow shows a metallic debris, detached from the first body's tribologically transformed surface (TTS), and trapped within the transfer layer. The depth of the plastically deformed layer varies from 2 to  $5\ \mu\text{m}$  in thickness. Lastly, the magnetite matrix of the transfer layer went probably through oxidation and transformed into hematite.

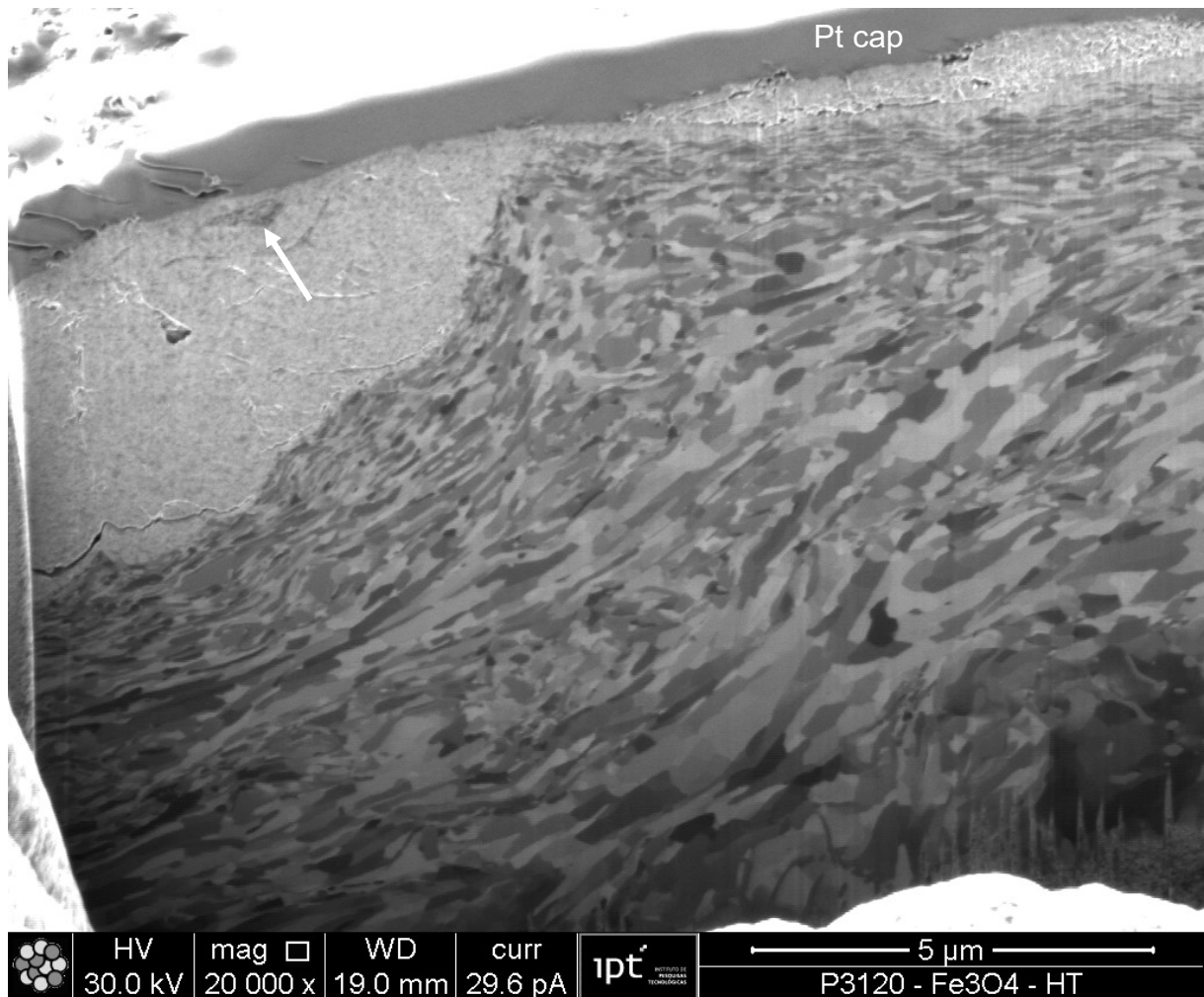


Figure 18 Pin, pure magnetite ( $\text{Fe}_3\text{O}_4$ ) at  $400^\circ\text{C}$  in air, FIB cross-section. The depth of plastically deformed layer is ranges from 2 to 5  $\mu\text{m}$ . The depth of the transfer layer varies from 0.5 to 5  $\mu\text{m}$  and shows cracks within it. A metallic debris is visible trapped within the transfer layer (see arrow) ( $\text{CoF} \sim 0.60$ ).

### 5.3.2 Results summary for the pure Fe<sub>3</sub>O<sub>4</sub> system

Table 4 presents the results summary for the pure Fe<sub>3</sub>O<sub>4</sub> system. The increase of testing temperature from 23°C to 400°C resulted in the increase of the average CoF value, from 0.46 to 0.60. Both conditions showed similar stability of the CoF evolution curves (see Annex 1). The transfer layers for both conditions compact and smooth, though the condition tested at 400°C in air shows a smoother oxide transfer layer, in comparison to the condition tested at 23° in air (see figures 16 and 17). Lastly, the probable phase transformation, magnetite to hematite, was the major difference observed between tribotests performed with pure Fe<sub>3</sub>O<sub>4</sub> at 23°C in air and at 400°. CoF values obtained during the tribotesting of pure magnetite were compared with values of hematite additions pin-on-disc tribological tests in air [88]. The values obtained for pure hematite were around 0.52 for tests at 23 °C and approximately 0.58 for tests at 400°C [88]. These results suggest magnetite's was responsible for raising the CoF value at 400°C (see Figure 16). The examination of this hematite presence, will be presented further in this work, for other mixtures in a Fe<sub>3</sub>O<sub>4</sub> matrix.

Table 4 Results summary for the pure Fe<sub>3</sub>O<sub>4</sub> conditions

Result	Pure Fe <sub>3</sub> O <sub>4</sub>	
	23°C in air	400° in air
Average CoF value	0.46	0.60
CoF evolution	Stable	Stable
Transfer layer thickness	~ 4 μm*	0.5 to 5 μm*
Transfer layer compaction	Compact yet coarse-grained*	Compact and smooth*
Probable magnetite-hematite partial transformation	No	Yes

\* Result observed in one cross-section.

## 5.4 Binary graphite-Fe<sub>3</sub>O<sub>4</sub> system

MM Binary graphite-Fe<sub>3</sub>O<sub>4</sub> system was tested in three conditions: 23°C in air, 400°C in N<sub>2</sub> and 400°C in air. The average CoF values for these conditions and their standard deviation are presented in table 5.

The average values of CoF results for the binary graphite-Fe<sub>3</sub>O<sub>4</sub> system, manually mixed, tested at 23°C in air diverged from the same system tested at 400°C in air, rising the average CoF value from 0.23 to 0.54 respectively (see table 5). Tests performed at 23° in air with binary graphite-Fe<sub>3</sub>O<sub>4</sub> mixture presented lower CoF than the one observed for pure Fe<sub>3</sub>O<sub>4</sub> in the same temperature and atmosphere condition. Whereas for tests performed at 400°C in air, the average CoF was slightly lower the value obtained for pure Fe<sub>3</sub>O<sub>4</sub> in the same condition. Tribotests performed at 400°C in N<sub>2</sub> showed a decrease in the average CoF value (0.46) in comparison to tests performed at 400°C in air. The evolution curves for the condition at 23° in air showed stable average curves, whereas the condition tested at 400°C in air features less stable CoF curves, with the presence of peaks (see Annex 2).

Table 5 Average friction coefficient values for the binary graphite-Fe<sub>3</sub>O<sub>4</sub> conditions.

	Mixture (Systems)	Composition (vol.%)	Mixing method	Temp.	Atm.	Average CoF	Standard Deviation	Tribotest repetitions
<b>Binary graphite- Fe<sub>3</sub>O<sub>4</sub></b>	(graphite-Fe <sub>3</sub> O <sub>4</sub> )	85% Fe <sub>3</sub> O <sub>4</sub> + 15% C	MM	23°C	Air	0.23	0.05	6
			MM	400°C	Air	0.54	0.10	7
			MM	400°C	N <sub>2</sub>	0.46	0.06	3

#### 5.4.1 Characterization of the MM binary graphite-Fe<sub>3</sub>O<sub>4</sub> system

The interfacial media addition the binary graphite-Fe<sub>3</sub>O<sub>4</sub> system tested at 23°C in air remained black whereas the interfacial media addition of the same system tested at 400° in air, changed from black to brown after tribotesting, similarly to the pure magnetite addition displayed in figure 15.

Figure 19 features a topographic image from the pin's tribosurface, tested at **23°C in air**. Arrows point to a darker transfer layer area that differ from the overall grey transfer layer in the rest of the image. EDS showed that these darker portions are C-rich, demonstrating a lack of homogenization of the third body single powders within the transfer layer.

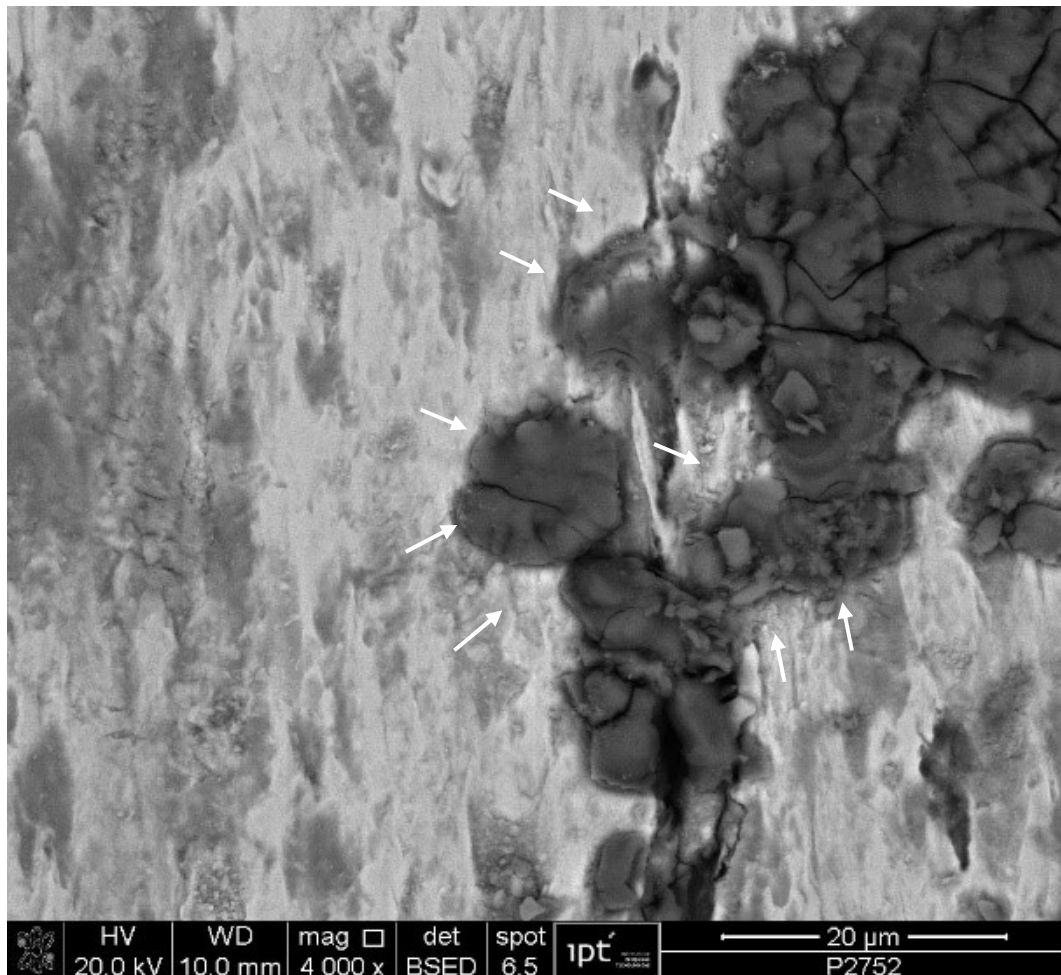


Figure 19 Pin, binary (graphite-Fe<sub>3</sub>O<sub>4</sub>) MM mixture tested at 23°C in air: a) SEM topographical and compositional examination of the tribosurface, BEI (CoF ~0.23).

Figures 20 and 21 show FIB cross-sections of disc's and pin's tribosurfaces, respectively, tested at **23°C in air** with binary graphite-Fe<sub>3</sub>O<sub>4</sub> addition.

Figure 20 presents a thin (~ 1.5 μm thick) transfer layer adhered to the tribosurface alongside a plastically deformed layer of over 5 μm thick. EDS elemental mapping showed the presence of a carbon-rich layer near the surface (see arrow). Moreover, the transfer layer is compact but coarse grained. A 7 μm longitudinal crack is visible within the transfer layer.

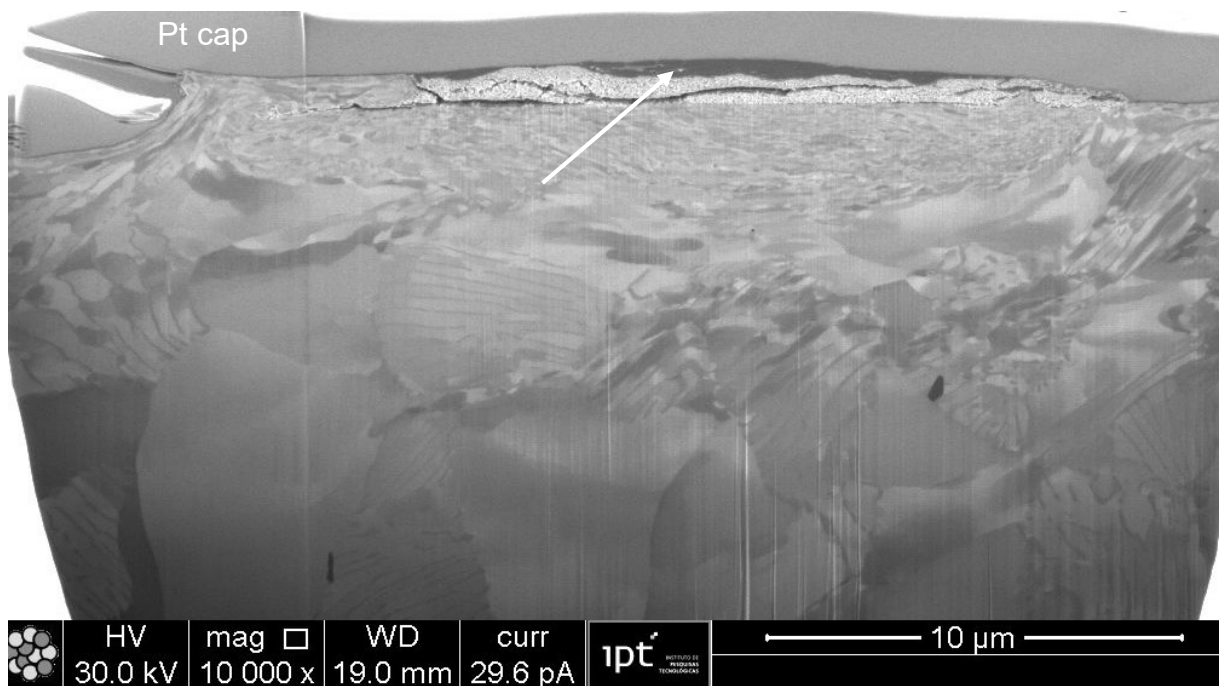


Figure 20 Disc, binary (graphite -Fe<sub>3</sub>O<sub>4</sub>) MM mixture tested at 23°C in air, FIB cross-section. The depth of plastically deformed layer is approximately 5 μm. The depth of the compact transfer layer is approximately 1.5 μm. A ~10 μm long crack is visible throughout the transfer layer. The arrow points to a carbon-rich film, 8 μm long, within the transfer layer (CoF ~0.23).

Figure 21 displays a plastically deformed layer of the pin's surface varying from approximately 0.5 to 3  $\mu\text{m}$  in thickness with the presence of sub-superficial cracks and metallic debris (see arrows). The oxide transfer layer is coarse-grained and just under 3  $\mu\text{m}$ . Longitudinal cracks are observable within it.

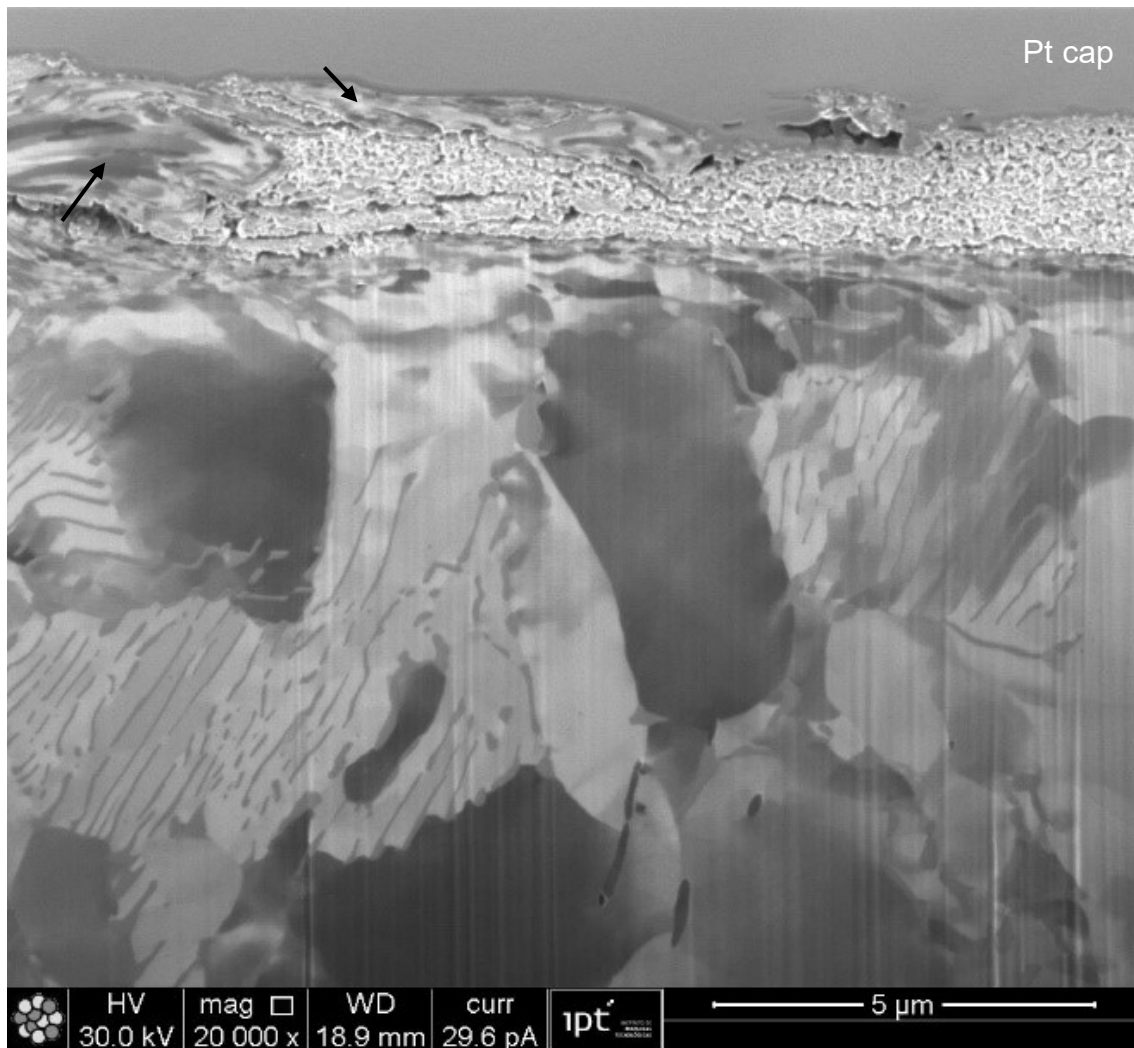


Figure 21 Pin, binary (graphite - $\text{Fe}_3\text{O}_4$ ) MM mixture tested at 23°C in air, FIB cross-section. The depth of plastically deformed layer ranges approximately from 0.5 to 3  $\mu\text{m}$ . Sub-superficial crack in the plastically deformed layer accompanies metallic debris (see arrows). The depth of the coarse-grained transfer layer is just under 3  $\mu\text{m}$ . Cracks and discontinuities are visible within the transfer layer. (CoF  $\sim$ 0.23).

Figure 22 and Figure 23 feature FIB cross-sections of the pin's tribosurface tested at **400°C in N<sub>2</sub>** with binary graphite-Fe<sub>3</sub>O<sub>4</sub> addition.

Figure 22 presents a very thin (~ 0.5 μm thick) plastically deformed layer. The oxide transfer layer is compact, predominantly smooth and is just under 3 μm thick. EDS elemental mapping showed the presence of carbon-rich regions under 1 μm in length (see arrows). Figure 23 features the same FIB cross-section in detail. The ellipse comprises a less compact region within the mostly smooth transfer layer. The arrows point to C-rich regions, indicating lack of homogenization of the manually mixed third body addition.

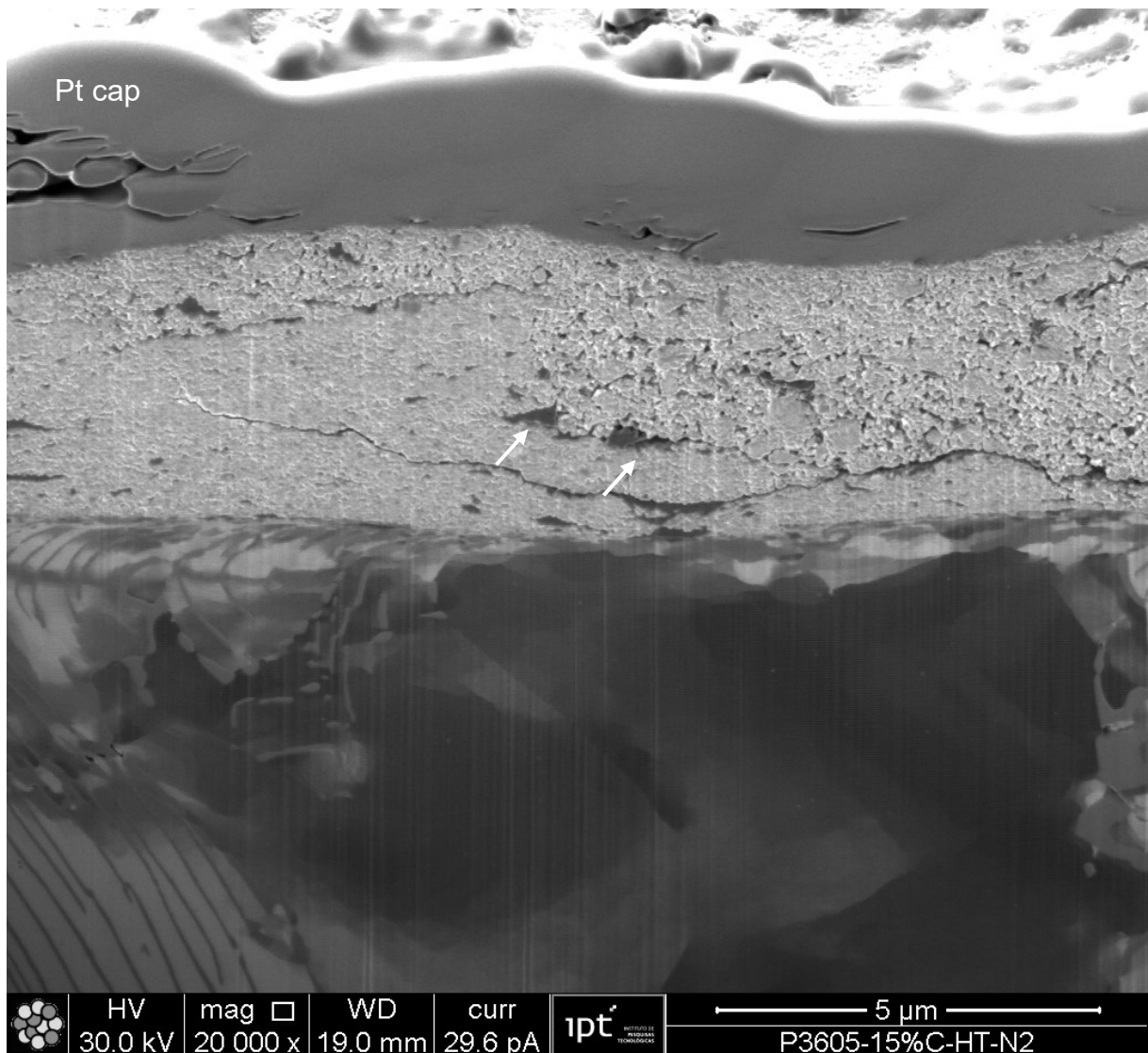


Figure 22 Pin, binary (graphite -Fe<sub>3</sub>O<sub>4</sub>) MM mixture tested at 400°C in N<sub>2</sub>, FIB cross-section. The depth of plastically deformed layer is approximately 0.5. The depth of the compact transfer layer is just under 5 μm. Cracks and discontinuities are visible within the transfer layer. The arrows point to C-rich regions (CoF ~0.46).

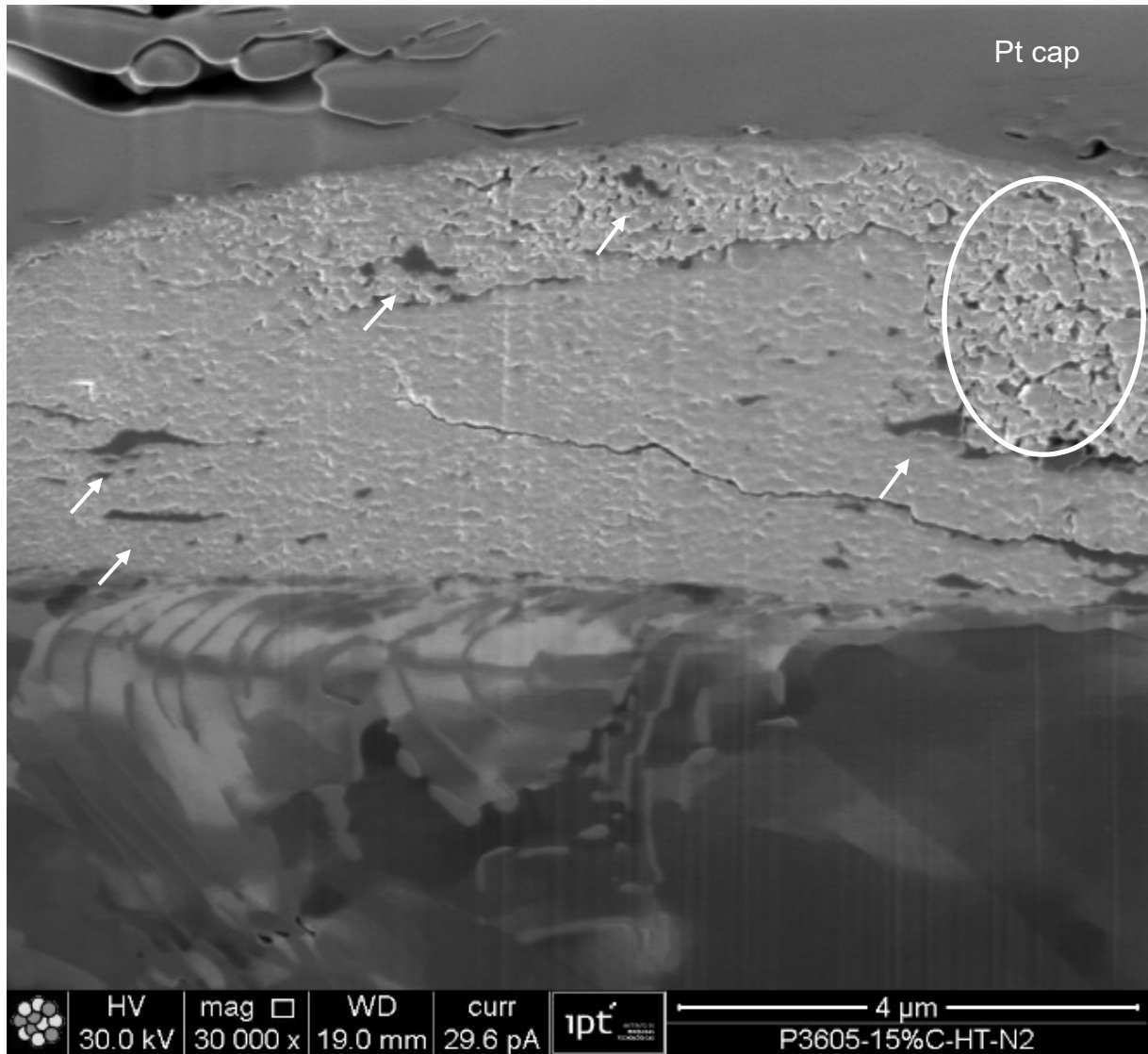


Figure 23 Pin, binary (graphite- $\text{Fe}_3\text{O}_4$ ) MM mixture tested at  $400^\circ\text{C}$  in  $\text{N}_2$ , Detail of FIB cross-section in Figure 22. A  $8\ \mu\text{m}$  crack is visible within the compact smooth transfer layer. The ellipse comprises a less compact region of the transfer layer. The arrows point to C-rich regions (CoF  $\sim 0.46$ ).

#### 5.4.2 Results summary for the MM binary graphite-Fe<sub>3</sub>O<sub>4</sub> system

Table 6 presents the results summary for the binary graphite-Fe<sub>3</sub>O<sub>4</sub> system. The increase of testing temperature from 23°C to 400°C rose the average CoF value, from 0.23 to 0.54. The use of N<sub>2</sub> atmosphere decreased the CoF value at 400°C from 0.54 to 0.46, in comparison to the tribotests performed in air. A possible explanation for this behaviour is the loss of lubricity that graphite experiences under vacuum. By increasing the temperature, the humidity that produces surfaces of low cohesion is withdrawn from graphite, thus making the graphite fibres to seize upon a moving plate, as described by Savage (1948) <sup>[38]</sup>. Sliney (1982) also showed that graphite is serviceable in air up to 350°C <sup>[89]</sup>. The tribotest nominal temperature of 400°C is probably lower than the flash temperature at the tribosurfaces contact.

Magnetite-hematite transformation was only observed for this system tested at 400°C in air. Increasing the temperature, from 23 to 400°C rose the instability within the CoF evolution curves, resulting on curves with greater presence of peaks and less stable for the binary graphite-Fe<sub>3</sub>O<sub>4</sub> system tested at 400°C in air. The partial transformation of magnetite to hematite was most likely responsible for the higher CoF values at 400°C in air, as well as the aforementioned lack of stability of the CoF evolution curve.

For all three conditions, the oxide transfer layer was compact, featuring a less compact structure at 23°C in air (see Figure 21) and smoother layer with greater compaction at 400°C in air (see Figures 22 and 23). Furthermore, carbon-rich films were visible on the tribosurface and amid the oxide transfer layer (see Figures 19 to 23). The formation of metallic debris, (see Figure 21) did not raise the CoF value by creating metallic contact within the tribolayer. Suggesting the lubricating effect of graphite films observed on the tribosurfaces was dominant for this system.

Table 6 Results summary for the graphite-Fe<sub>3</sub>O<sub>4</sub> conditions

Result	Graphite-Fe <sub>3</sub> O <sub>4</sub>		
	23°C in air	400° in air	400° in N <sub>2</sub>
<b>Average CoF value</b>	0.23	0.54	0.46
<b>CoF evolution</b>	Stable	Less stable, presence of peaks	Stable
<b>Transfer layer thickness</b>	1.5 to 3 μm**	N.C.	~ 5 μm*
<b>Transfer layer homogenization</b>	No	No	No
<b>Transfer layer compaction</b>	Less compact**	N.C.	Compact and mostly smooth*
<b>Probable magnetite-hematite transformation</b>	No	Yes	No
<b>Presence of C-rich regions</b>	Yes, continuous layer.	N.C.	Yes

\* Result observed in one cross-section. \*\* Result compiled from 2 cross-sections. N.C. = not characterized by FIB.

## 5.5 Binary Cu-Fe<sub>3</sub>O<sub>4</sub> systems

Two MM Binary Cu-Fe<sub>3</sub>O<sub>4</sub> systems, 6%Cu-Fe<sub>3</sub>O<sub>4</sub> and 15%Cu-Fe<sub>3</sub>O<sub>4</sub>, were tested in three conditions: 23°C in air, 400°C in N<sub>2</sub> and 400°C in air. The average CoF values for these conditions and their standard deviation are presented in Table 7. Both systems differed in CoF values only for condition tested at 23° in air. Conditions tested at 400°C in air and N<sub>2</sub> produced practically equal results. Moreover, the characterization of these systems were also very similar. Therefore, both 6%Cu-Fe<sub>3</sub>O<sub>4</sub> and 15%Cu-Fe<sub>3</sub>O<sub>4</sub> systems shall be presented as a general MM Binary Cu-Fe<sub>3</sub>O<sub>4</sub> system.

Table 7 Average friction coefficient values for the binary Cu-Fe<sub>3</sub>O<sub>4</sub> conditions.

	Mixture (Systems)	Composition (vol.%)	Mixing method	Temp.	Atm.	Average CoF	Standard Deviation	Tribotest repetitions
<b>Binary Cu-Fe<sub>3</sub>O<sub>4</sub></b>	(6%Cu-Fe <sub>3</sub> O <sub>4</sub> )	94% Fe <sub>3</sub> O <sub>4</sub> + 6% Cu	MM	23°C	Air	0.55	0.15	4
			MM	400°C	Air	0.57	0.06	3
			MM	400°C	N <sub>2</sub>	0.50	0.11	4
	(15%Cu-Fe <sub>3</sub> O <sub>4</sub> )	85% Fe <sub>3</sub> O <sub>4</sub> + 15% Cu	MM	23°C	Air	0.65	0.13	6
			MM	400°C	Air	0.56	0.06	3
			MM	400°C	N <sub>2</sub>	0.51	0.06	3

For tests performed at 23°C in air, the 6%Cu-Fe<sub>3</sub>O<sub>4</sub> system showed slightly lower average CoF value (0.55) than that observed for the 15%Cu-Fe<sub>3</sub>O<sub>4</sub> (0.65) system tested in the same condition. Nevertheless, this difference cannot be considered significant, considering the standard deviation. The evolution curves for both systems, 6% Cu-Fe<sub>3</sub>O<sub>4</sub> and 15%Cu-Fe<sub>3</sub>O<sub>4</sub>, tested at 23° in air have an unstable behaviour, with the presence of peaks (see Annex 3). Moreover, the third body addition remained black for both systems at 23°C in air.

Both binary Cu-Fe<sub>3</sub>O<sub>4</sub> systems produced equal results for conditions tested at 400°C in air (0.57 and 0.56) and 400°C in N<sub>2</sub> (0.50 and 0.51). The third body addition changed from black to brown for both systems tested at 400°C in air, similarly to pure magnetite tested at 400°C in air (see Figure 16). Moreover, the 6%Cu-Fe<sub>3</sub>O<sub>4</sub> system tested at 400°C in air presented stable CoF evolution curves, whereas the 15%Cu-Fe<sub>3</sub>O<sub>4</sub> for the same condition, presented unstable CoF curves (see Annex 3).

Tribotesting both binary Cu-Fe<sub>3</sub>O<sub>4</sub> systems tested at 400°C in N<sub>2</sub> produced similar results regarding third body colour and CoF curves stability. For both systems

at this condition, the third body addition remained black after tribotesting. CoF evolution curves for both Cu-Fe<sub>3</sub>O<sub>4</sub> systems, tested at 400°C in N<sub>2</sub>, presented peaks and instabilities (see Annex 3).

### 5.5.1 Characterization of the MM binary Cu-Fe<sub>3</sub>O<sub>4</sub> system

Figure 24 and Figure 25 present FIB cross-sections of the same disc after testing at **23°C in air**, with the MM binary 6%Cu-Fe<sub>3</sub>O<sub>4</sub> addition. Figure 24-a presents a thick transfer layer (~ 10 µm) adhered to the tribosurface. The transfer layer is coarse-grained and lacks compaction. Cracks, mostly longitudinal, are visible throughout the transfer layer. The disc's steel microstructure is not observable in this image. The copper distribution is not uniform along the cross-section of the tribofilm, indicating the presence of micro-agglomerates of Cu (from 0.5 µm to 3 µm) within the thick transfer layer (see Figure 24-b).

Figure 25 features the presence of a plastically deformed layer (~ 3 µm of depth) in the disc, while the oxide transfer layer adhered to the tribosurface lacks compaction. Cracks and discontinuities are visible within the coarse-grained transfer layer. It is approximately 3 µm thick. EDS mapping shows the presence of micro-agglomerates of Cu of approximately 0.5 µm and a Cu-rich region, with a main axis approximately 10 µm long, see Figure 25-b).

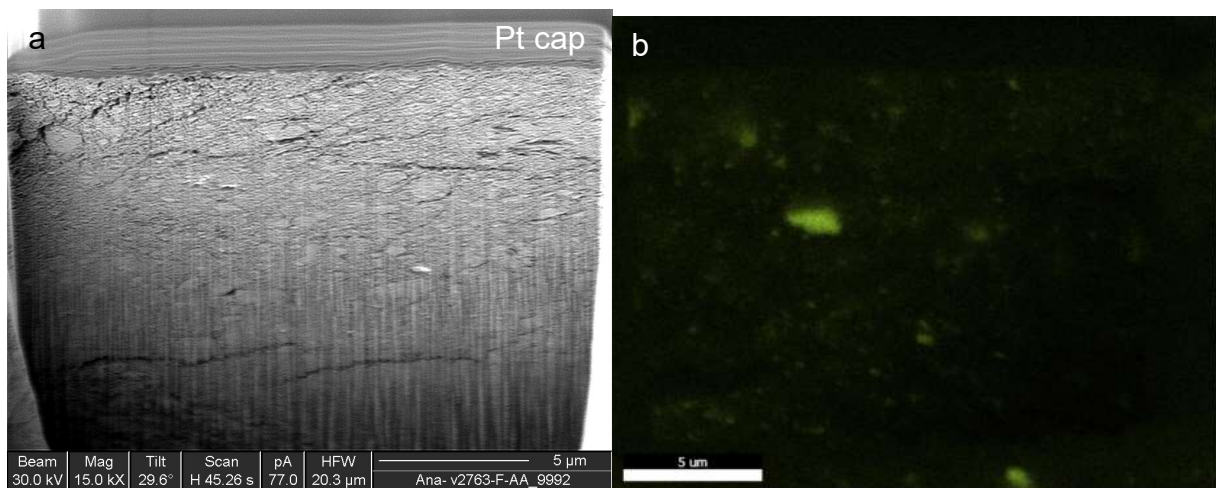


Figure 24 - Disc, binary (6%Cu -Fe<sub>3</sub>O<sub>4</sub>) MM mixture tested at 23°C in air. a) FIB cross-section. The plastically deformed layer is not visible. The depth of the transfer layer is over 10 µm. Cracks are visible within the transfer layer. b) Cu EDS mapping on the same area, but performed in a different instrument. (CoF ~0.55).

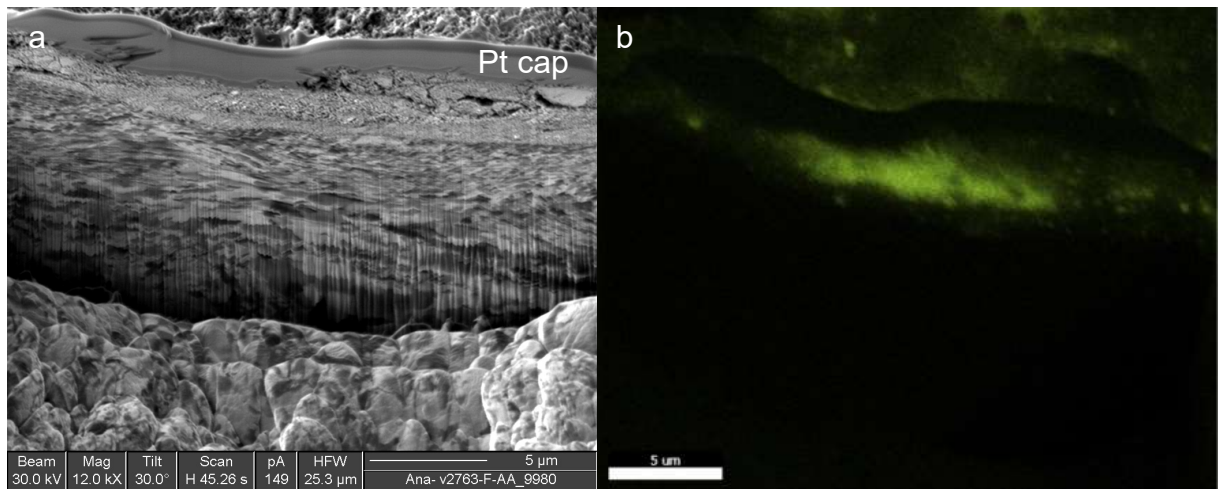


Figure 25 - Disc, binary (6%Cu -Fe<sub>3</sub>O<sub>4</sub>) MM mixture tested at 23°C in air. a) FIB cross-section. The plastically deformed layer ranges from 1 to 2 μm. The depth of the transfer layer varies from 1 to 2 μm. Cracks and discontinuities are visible within the transfer layer. b) Cu EDS mapping on the same area but performed in a different instrument. (CoF ~0.55).

Figures 26 and 27 feature FIB cross-sections of the pin's tribosurface tested at 23°C in air with binary MM 15%Cu-Fe<sub>3</sub>O<sub>4</sub> addition.

Figure 26 presents a very thin (~ 0.5 μm thick) plastically deformed layer. The oxide transfer layer is compact, but predominantly coarse-grained and is approximately 4 μm thick. Figure 27 features the same FIB cross-section in detail. The crack within the transfer layer is resolved in this image, featuring a very thin oxide transfer layer attached to the pin's metallic surface. Moreover, the coarse-grained aspect is also better resolved showing the discontinuities within the transfer layer are similar to pores.

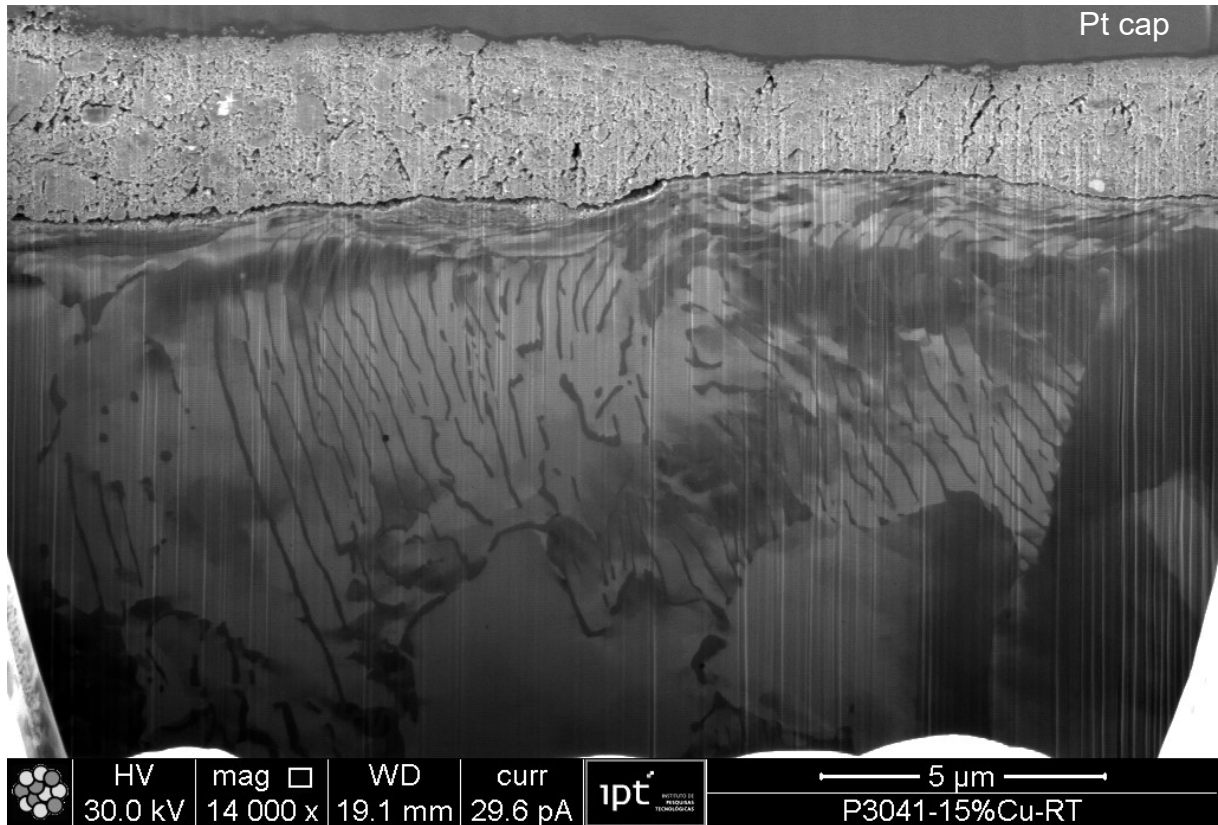


Figure 26 Pin, binary (15%Cu -Fe<sub>3</sub>O<sub>4</sub>) MM mixture tested at 23°C in air, FIB cross-section. The depth of plastically deformed layer is approximately 0.5 µm. The depth of the compact transfer layer is approximately 4 µm. Cracks and discontinuities are visible within the transfer layer. (CoF ~0.65).

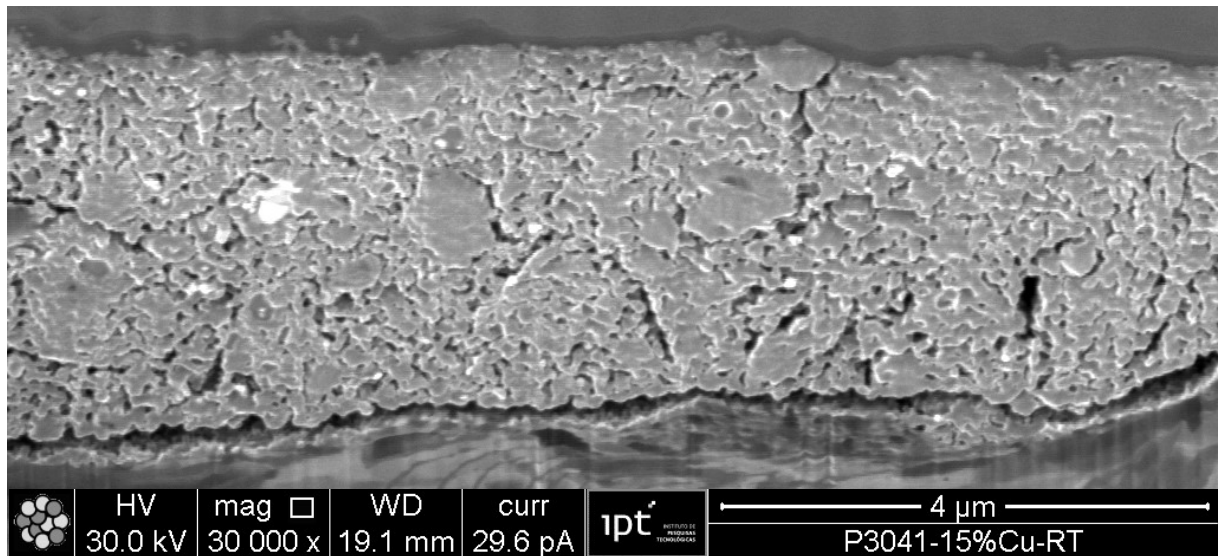


Figure 27 Pin, binary (15%Cu -Fe<sub>3</sub>O<sub>4</sub>) MM mixture tested at 23°C in air, Detail of FIB cross-section in Figure 26. The depth of plastically deformed layer is approximately 0.5 µm. The depth of the compact transfer layer is approximately 4 µm. Cracks and discontinuities are visible within. (CoF ~0.65).

TEM characterization was employed to resolve the Cu agglomerates within the oxide transfer layer. Figure 28-a shows a bright field image of the binary 6%Cu-Fe<sub>3</sub>O<sub>4</sub> system tested at 23°C in air. Figure 28-b and 28-c show the Fe EDS and Cu EDS mapping, respectively. Fe is homogeneously present in most regions of the layer, a depleted in Cu-rich regions (see figure 28-c). The presence of copper micro-agglomerates in form of patches are visible in figure 28-c.

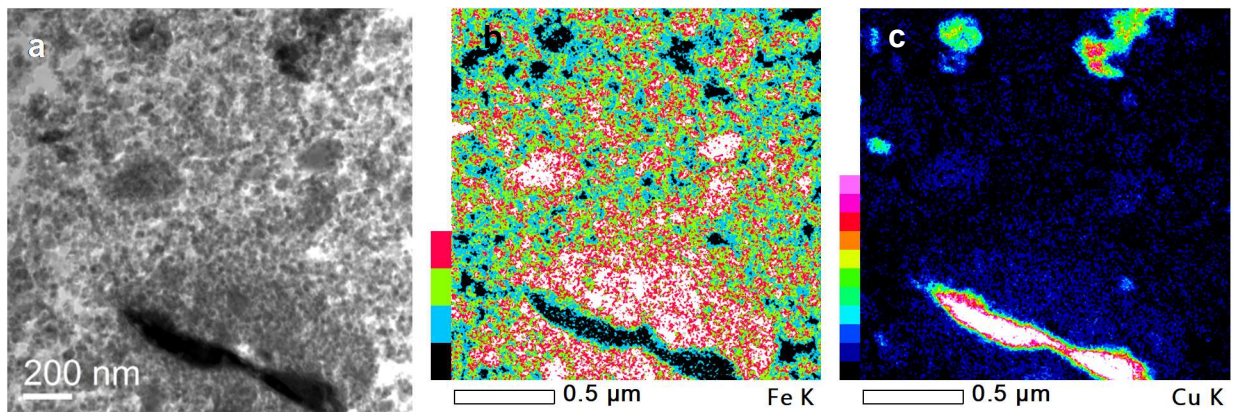


Figure 28 - Disc, binary (6%Cu-Fe<sub>3</sub>O<sub>4</sub>) MM mixture tested at 23°C in air. (a) STEM, bright field image from a tribosurface lamella; (b) Fe EDS elemental mapping; (c) Cu EDS elemental mapping; (CoF ~0.55).

Figure 29 shows a FIB cross-section for the disc's tribosurface tested at **400°C in N<sub>2</sub>** with the binary MM 15%Cu-Fe<sub>3</sub>O<sub>4</sub> addition. The plastically deformed layer observable in the disc's surface ranges from 4 to 10 μm (see Figure 29). The oxide transfer layer is also compact smooth, ranging from 2 to 5 μm in thickness. Some cracks are visible within the transfer layer. An arrow points to the presence of some scarce discontinuities in a less compact area of the transfer layer. Moreover, Figure 29 features the presence of interfacial addition trapped within the disc's plastically deformed layer. This suggests the third body filled a space created by the detachment of the tribologically transformed surface (TTS), followed by the covering the oxide layer by the TTS.

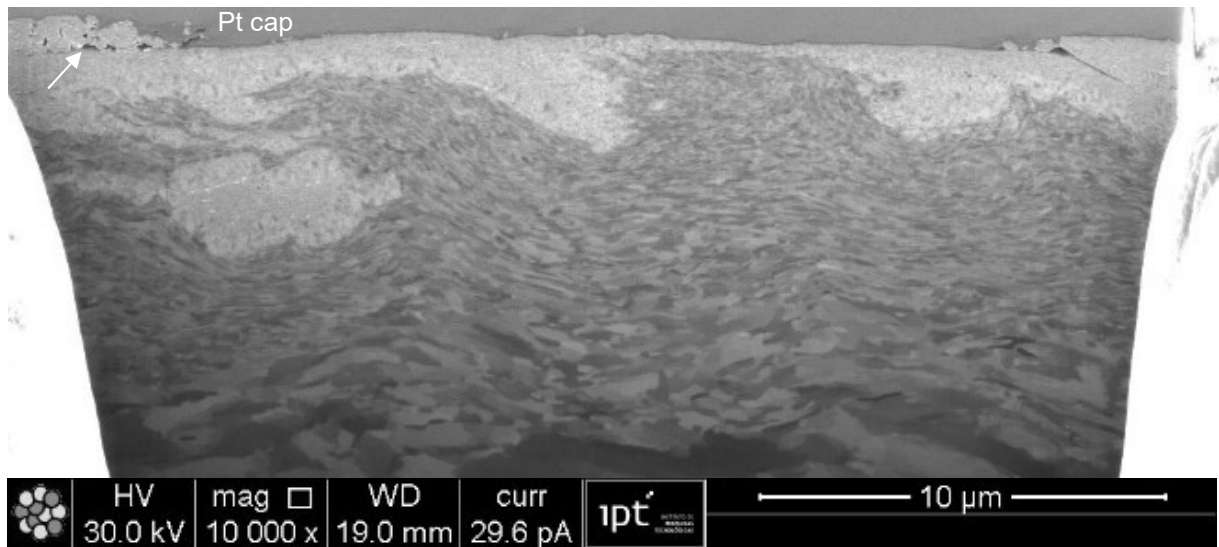


Figure 29 Disc, binary (15%Cu -Fe<sub>3</sub>O<sub>4</sub>) MM mixture tested at 400°C in N<sub>2</sub>. FIB cross-section. The plastically deformed layer ranges between 4 to 7 μm. The depth of the transfer layer is approximately 2 to 5 μm thick. Cracks and scarce discontinuities (see arrow) are visible amid the compact smooth transfer layer. (CoF ~0.51).

Figure 30 displays a FIB cross-sections and EDS elemental mapping of the disc after testing at 400°C in N<sub>2</sub>, with the MM binary 15%Cu-Fe<sub>3</sub>O<sub>4</sub> addition. Figure 30-a shows an oxide transfer layer (~ 5 to 7.5 μm thick) adhered to the surface of the first body. The plastically deformed layer is not well resolved in this image. The Fe EDS mapping is presented in Figure 30-b, and it shows a homogeneous distribution of Fe. Figure 30-c features the Cu EDS mapping, indicating the presence of larger clusters of Cu in which Fe is underrepresented. Additionally, Cu submicron-agglomerates are visible throughout the transfer layer.

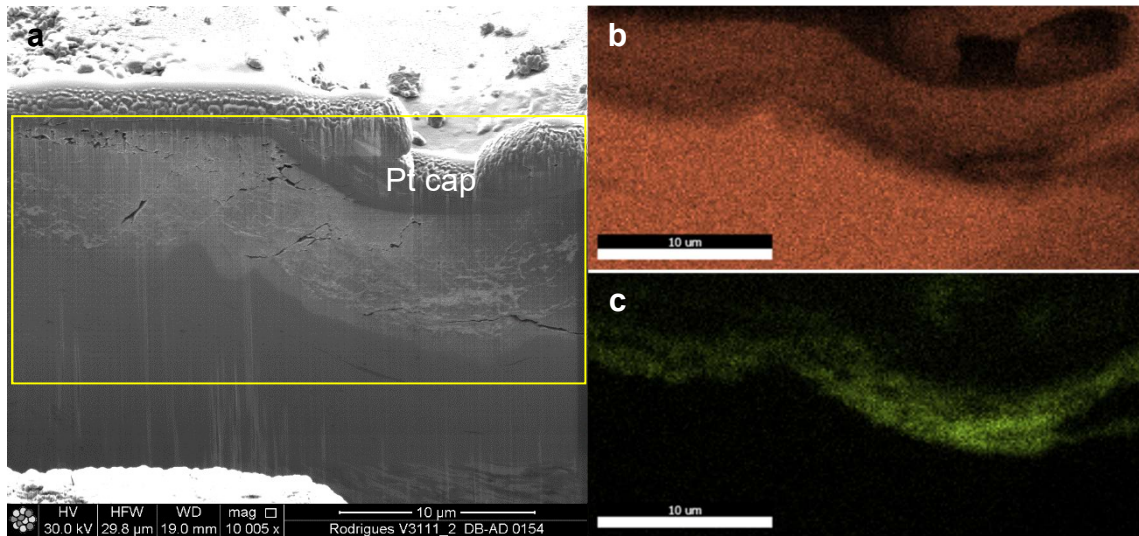


Figure 30 - Disc, binary (15%Cu -Fe<sub>3</sub>O<sub>4</sub>) MM mixture tested at 400°C in N<sub>2</sub>. a) FIB cross-section. The depth of the transfer layer varies from 5 to 7.5 µm. Cracks and discontinuities are visible within the transfer layer. The rectangle shows the region where the EDS mapping was performed; b) Fe EDS mapping on the same area. c) Cu EDS mapping on the same area. (CoF ~0.51).

Figure 30-a shows a TEM bright field image of the disc's transfer layer after testing at 400°C in N<sub>2</sub>, with the MM binary 15%Cu-Fe<sub>3</sub>O<sub>4</sub> addition. Figures 30-b shows the layered C, Fe and Cu EDS mapping. There is a clear separation between Cu and Fe-rich areas in the transfer layer, indicating the presence of submicron-agglomerates of Cu. Additional presence of nanoparticles of Cu was observed throughout the transfer layer. Furthermore, Figure 32 shows a high-resolution electron microscopy (HREM) image of a continuous Cu-rich region near the tribosurface (encircled in red). The clear separation between nanocrystalline Cu and the Fe-rich areas remains visible at this scale.

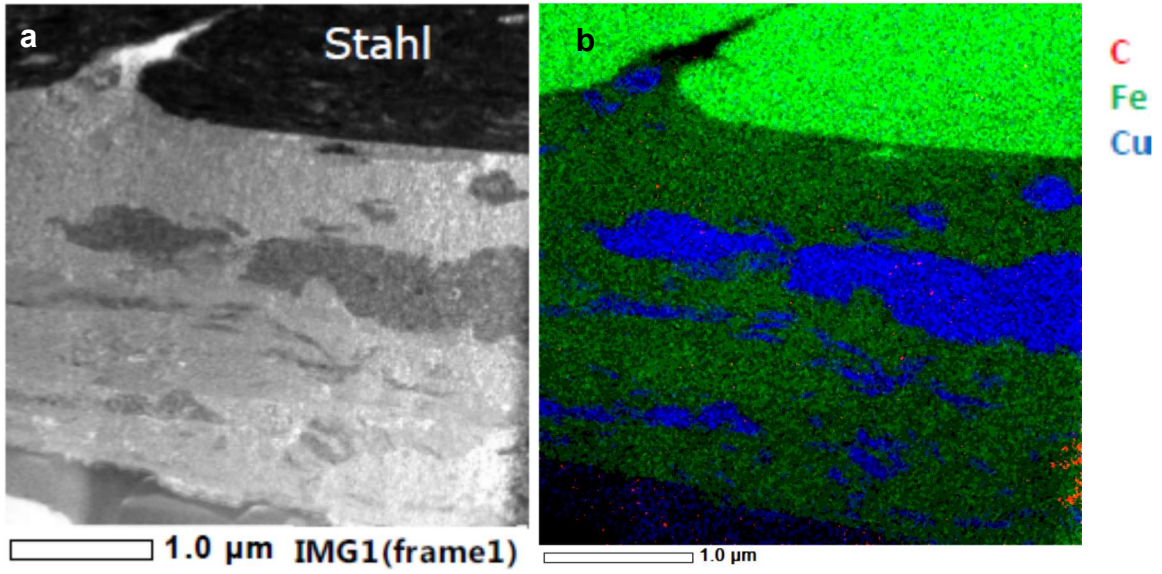


Figure 31 - Disc, binary (15%Cu-Fe<sub>3</sub>O<sub>4</sub>) MM mixture tested at 400°C in N<sub>2</sub>. (a) STEM, bright field image from a tribosurface lamella; (b) Layered EDS elemental mapping combining C, Fe and Cu maps; (CoF ~0.51).

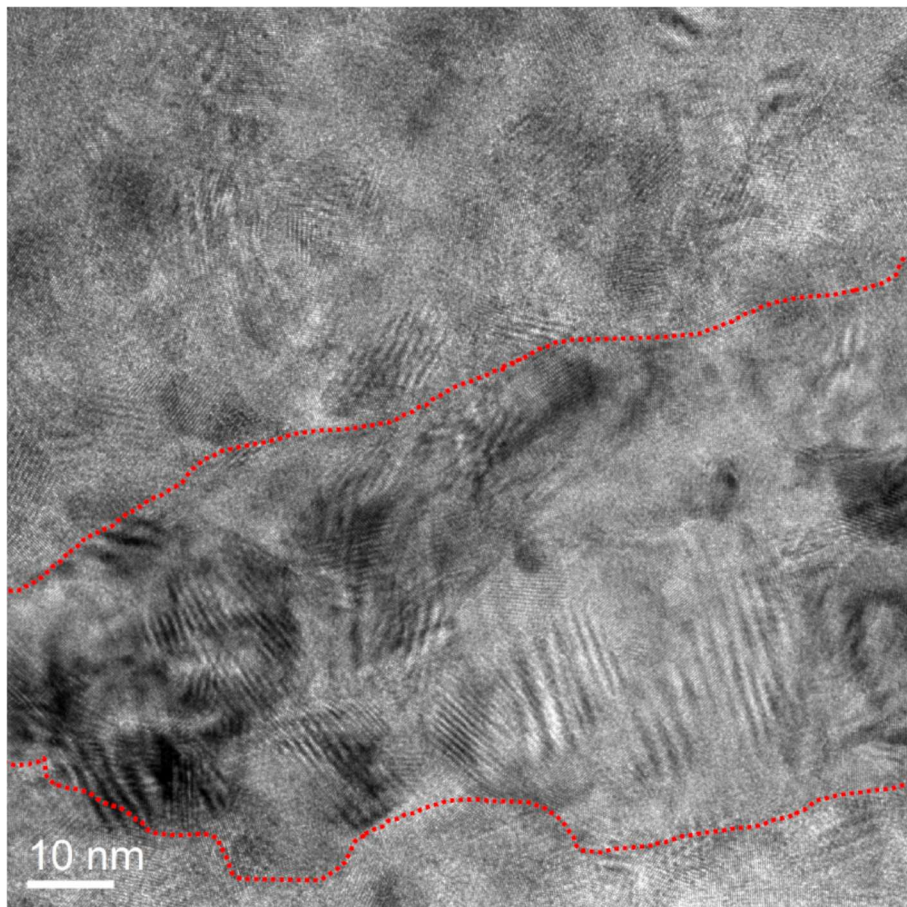


Figure 32 Disc, binary (15%Cu-Fe<sub>3</sub>O<sub>4</sub>) MM mixture tested at 400°C in N<sub>2</sub>. HREM image from a Cu-rich area near the tribosurface (encircled in red) (CoF ~0.51).

Figure 33 features a FIB cross-section of the pin's tribosurface tested at **400°C in air** with binary 6%Cu-Fe<sub>3</sub>O<sub>4</sub> addition. The oxide transfer layer is compact and smooth. It varies from 1 to 2 μm in thickness and some cracks are visible within it. The pin's plastically deformed layer is approximately 5 μm.

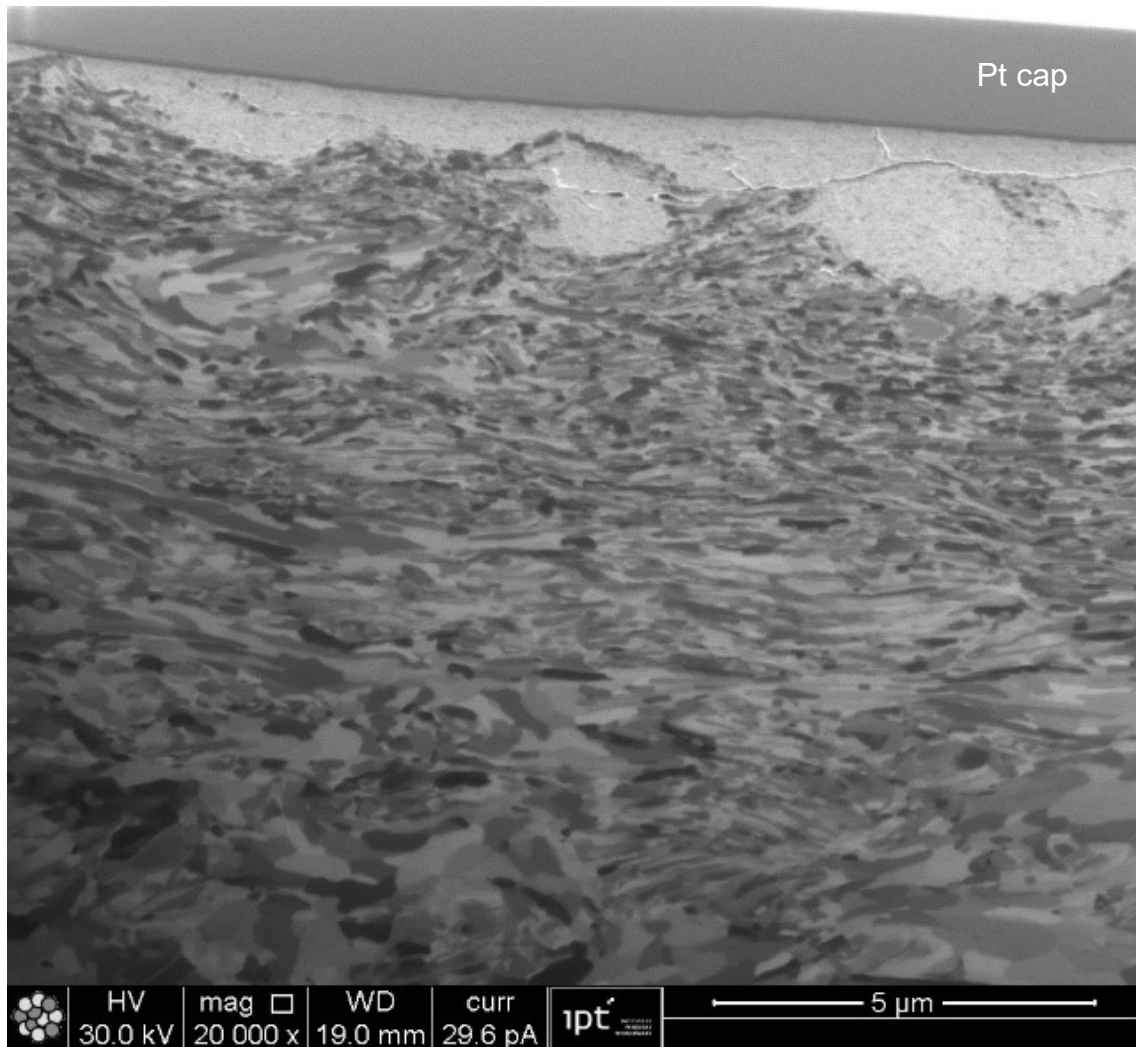


Figure 33 Pin, binary (6%Cu -Fe<sub>3</sub>O<sub>4</sub>) MM mixture tested at 400°C in air, FIB cross-section. The depth of plastically deformed layer is approximately 5 μm. The depth of the compact, smooth transfer layer varies from 1 to 2 μm. Cracks are visible within the transfer layer. (CoF ~0.57).

Figure 34 presents a FIB cross-section of the pin's tribosurface tested at 400°C in air, with the binary MM 15%Cu-Fe<sub>3</sub>O<sub>4</sub> addition. Figure 34-a features a plastically deformed steel debris of over 10 μm. Furthermore, the compact oxide transfer layer holds it at the tribolayer and prevents this large steel debris from detaching from the tribosurface. The compact oxide transfer layer is smooth and varies between 1 to 3 μm in thickness. Figure 34-b shows the Cu EDS mapping on the same area, and displays Cu-rich micro-agglomerates

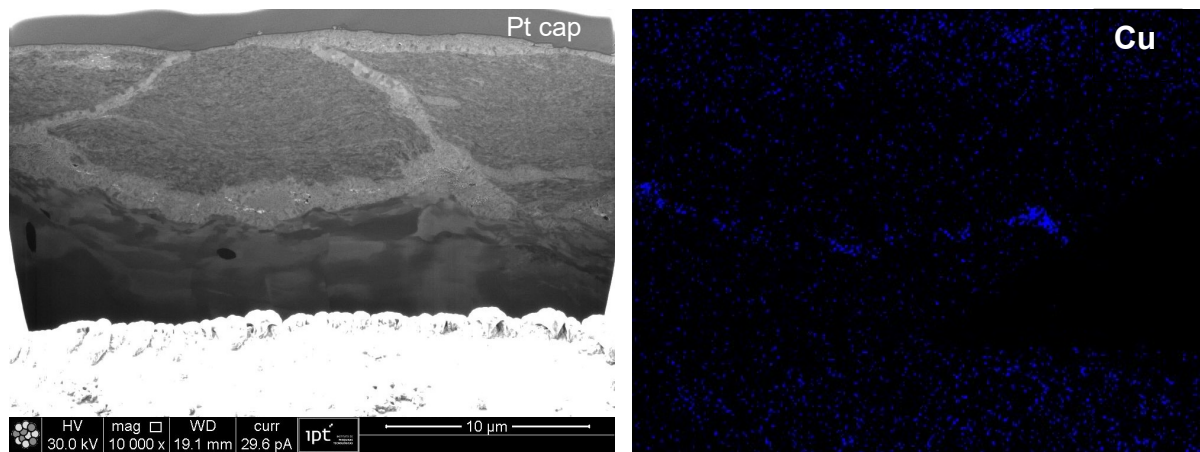


Figure 34 Pin, binary (15%Cu -Fe<sub>3</sub>O<sub>4</sub>) MM mixture tested at 400°C in air. a) FIB cross-section. The plastically deformed layer is over 10 μm thick. The compact oxide transfer layer is smooth and varies between 1 to 3 μm and thickness and contours a plastically deformed region of the steel, keeping it from detaching from the tribolayer. b) Cu EDS mapping on the same area showing Cu-rich micro-agglomerates (CoF ~0.51).

Figure 35 features a FIB cross-sections for pin's and disc's tribosurfaces tested at 400°C in air with the binary MM 15%Cu-Fe<sub>3</sub>O<sub>4</sub> addition. A plastically deformed layer of over 5 μm is observable on the pin's surface in figure 35-a. The transfer layer is compact and smooth, showing some longitudinal cracks. It is approximately 5 μm thick. Figure 35-b presents Cu EDS elemental mapping for the same cross-section. Cu appears throughout the transfer layer.

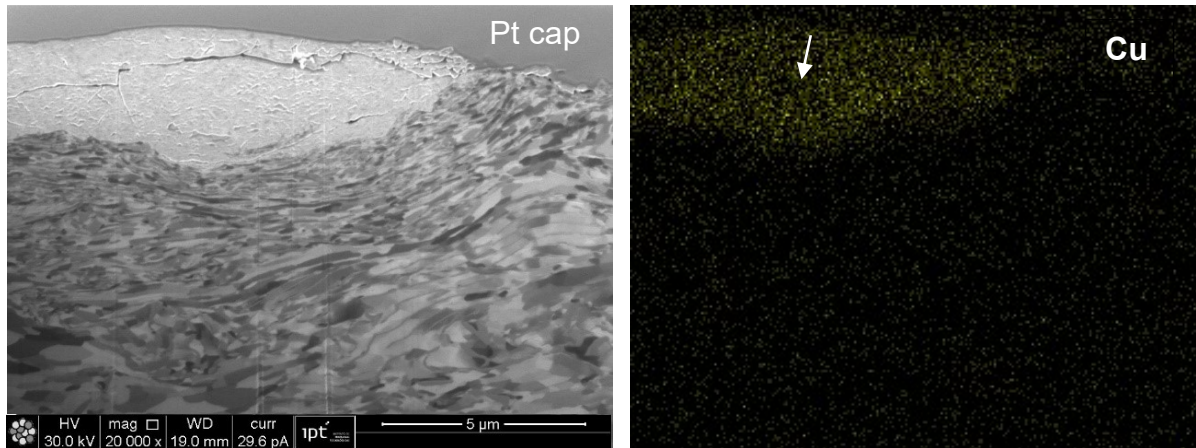


Figure 35 Pin, binary (15%Cu -Fe<sub>3</sub>O<sub>4</sub>) MM mixture tested at 400°C in air. a) FIB cross-section. The plastically deformed layer is over 5 μm. The depth of the transfer layer is approximately 3 μm thick. Longitudinal cracks are visible within the compact smooth, yet discontinuous transfer layer. b) Cu EDS mapping on the same area showing Cu presence throughout the transfer layer, with greater presence in a lower stripe (see arrow) (CoF ~0.51).

### 5.5.2 Results summary for the MM binary Cu-Fe<sub>3</sub>O<sub>4</sub> system

The similarity of results obtained for both 6%Cu- Fe<sub>3</sub>O<sub>4</sub> and 15%Cu-Fe<sub>3</sub>O<sub>4</sub> allowed the results summaries to be condensed as one MM binary Cu-Fe<sub>3</sub>O<sub>4</sub> system without losing any relevant information. Table 8 presents the aforementioned condensed summary.

The average values of CoF results of the investigated binary MM Cu-Fe<sub>3</sub>O<sub>4</sub> systems, tested at 23°C in air were statistically higher than the one obtained for pure Fe<sub>3</sub>O<sub>4</sub> in the same condition. Whereas for tests performed at 400°C in air, the binary MM Cu-Fe<sub>3</sub>O<sub>4</sub> produced lower CoF values than those obtained for pure Fe<sub>3</sub>O<sub>4</sub> at the same condition. Squealing noise was present during tribotesting for all temperature and atmosphere conditions. While the obtained CoF evolution curves were rather unstable, with the presence of peaks.

The use of N<sub>2</sub> atmosphere at 400°C lowered the CoF values in comparison with tests performed at 400°C in air and those performed at 23° in air.

Tests performed at 23°C in air produced oxide transfer layers that lacked in compaction and displayed a coarse-grained aspect (see figures 25 to 27). Whereas testing at 400°C, regardless of the atmosphere used, promoted a greater compaction

of the transfer layer, showing smoother transfer layers in comparison with the conditions tested 23°C in air (see figures 29, 30 and 33 to 35).

Additionally, EDS elemental mapping performed in FIB cross-sections and TEM lamellae showed a lack of homogenization of the transfer layer, featuring coarse Cu-clusters and microscale Cu-agglomerates (see figures 24, 25, 28, 30 to 32, 34 and 35).

These results suggest, at 400°C, recrystallization took place among the Cu patches, forming a ductile copper film as described by Kumar and Bijwe<sup>[77]</sup>. This result corroborates the choice of “soft” copper properties, on the modelling of tribolayer formation developed by Dmitriev and Österle<sup>[27, 60]</sup>. In tribotests performed at 400°C in air, the CoF rising effect of magnetite-hematite transformation was probably minimized by the presence of soft copper for the 6%Cu- Fe<sub>3</sub>O<sub>4</sub> system, and clearly overcome for the 15%Cu-Fe<sub>3</sub>O<sub>4</sub> system. Endorsing that copper may have a lubricating behaviour at greater temperatures, as it decreases the CoF values for the condition with greater Cu content, at 400°C.

Table 8 Results summary for the binary MM Cu-Fe<sub>3</sub>O<sub>4</sub> conditions

Result	Cu-Fe <sub>3</sub> O <sub>4</sub>		
	23°C in air	400° in air	400° in N <sub>2</sub>
Average CoF value	0.55 to 0.65	~0.56	~0.50
CoF evolution	Unstable, with the presence of peaks	Unstable, with the presence of peaks	Unstable, with the presence of peaks
Transfer layer thickness	1 to 10 µm*	1 to 2 µm**	2 to 7.5 µm**
Transfer layer homogenization	No	No	No
Transfer layer compaction	Lacks compaction*	Compact and smooth**	Compact and smooth**
Probable magnetite-hematite transformation	No	Yes	No
Presence of Cu-patches/agglomerates	Yes	Yes	Yes

\* Result compiled from 3 cross-sections. \*\* Result compiled from 2 cross-sections.

## 5.6 Ternary Cu-graphite-Fe<sub>3</sub>O<sub>4</sub> system

A MM ternary Cu-graphite-Fe<sub>3</sub>O<sub>4</sub> system was tested in three conditions: 23°C in air, 400°C in N<sub>2</sub> and 400°C in air. The average CoF values for these conditions and their standard deviation are presented in table 9.

Table 9 Average CoF values for the ternary Cu-graphite-Fe<sub>3</sub>O<sub>4</sub> conditions.

	Mixture (Systems)	Composition (vol.%)	Mixing method	Temp.	Atm.	Average CoF	Standard Deviation	Tribotest repetitions
<b>Ternary</b>	(Cu-graphite-Fe <sub>3</sub> O <sub>4</sub> )	85% Fe <sub>3</sub> O <sub>4</sub> +	MM	23°C	Air	0.23	0.09	11
		7.5% C +	MM	400°C	Air	0.55	0.09	4
		7.5%Cu	MM	400°C	N <sub>2</sub>	0.46	0.07	6

The average CoF value for the ternary MM Cu-graphite-Fe<sub>3</sub>O<sub>4</sub> system, manually mixed, tested at 23°C in air was significantly lower than the same system tested at 400°C in air, 0.23 and 0.55 respectively. Performing the tests at 400°C in N<sub>2</sub> atmosphere lowered the average CoF value, from 0.55 to 0.46, in comparison to tests performed at 400°C in air. (see Table 9). These results are practically equal to those obtained for the binary MM graphite-Fe<sub>3</sub>O<sub>4</sub> system in these conditions. Tests performed at 23° in air with ternary MM Cu-graphite-Fe<sub>3</sub>O<sub>4</sub> mixture presented lower CoF than the one observed for pure Fe<sub>3</sub>O<sub>4</sub> in the same temperature and atmosphere condition. Whereas for tests performed at 400°C in air, the average CoF was slightly lower the value obtained for pure Fe<sub>3</sub>O<sub>4</sub> in the same condition. The evolution curves for the condition at 23° in air showed unstable average curves with the presence of higher peaks. The condition tested at 400°C in air featured less peaks but had an unstable aspect as well. Moreover, the ternary stable CoF curves, with the presence of peaks (see Annex 2). Furthermore, tribotests performed at 400°C in N<sub>2</sub> presented a more stable evolution curve, without the peaks observed in the other two conditions for this system.

### 5.6.1 Characterization of the MM ternary Cu-graphite-Fe<sub>3</sub>O<sub>4</sub> system

Figure 35 displays a FIB cross-section and EDS elemental mapping of the disc after testing at **23°C in air**, with the MM binary 15%Cu-Fe<sub>3</sub>O<sub>4</sub> addition. Figure 35-a shows the presence of a plastically deformed region, approximately 3 μm thick. The transfer oxide layer varies from 0.5 to 1 μm in thickness. The corresponding EDS maps (see figures 35-b and 35-c) show the distribution of Fe and Cu in the transfer layer. Fe is present throughout the transfer layer. A Cu is present in agglomerates within the transfer layer.

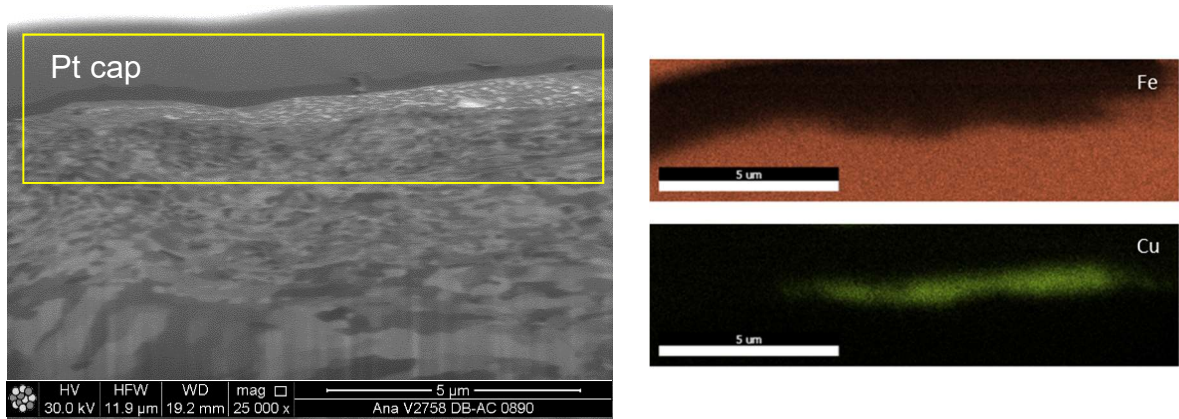


Figure 36 Disc, ternary (Cu-graphite-Fe<sub>3</sub>O<sub>4</sub>) MM mixture tested at 23°C in air. a) FIB cross-section. The plastically deformed layer is approximately 3 μm. The depth of the transfer layer ranges from 0.5 to 1 μm. Cracks and discontinuities are visible within the transfer layer. The rectangle shows the region where the EDS mapping was performed; b) Fe EDS mapping on the same area. c) Cu EDS mapping on the same area. (CoF ~0.23).

Figure 36-a shows a STEM bright field image of the disc's transfer layer after testing at 23°C in air, with the MM ternary Cu-graphite- Fe<sub>3</sub>O<sub>4</sub> addition. Patches are visible within the transfer layer. The Cu, C and Fe EDS mapping in Figure 36-b, confirms these patches (100 to 300 nm long), are mainly composed of Cu. Moreover, a carbon deposit is observable near the tribosurface.

Figure 37 features a TEM image of the disc's transfer layer after testing at 23°C in air, with the MM ternary Cu-graphite-Fe<sub>3</sub>O<sub>4</sub> addition. A carbon-rich region, characterized as graphite is shown on the right side of the image.

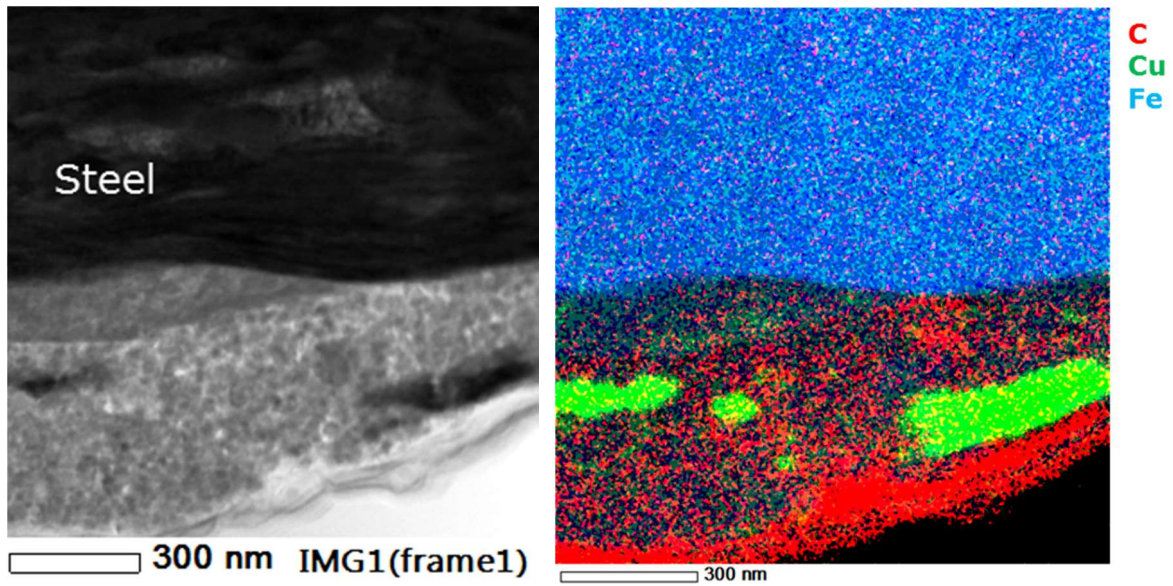


Figure 37 - Disc, ternary (Cu-graphite-Fe<sub>3</sub>O<sub>4</sub>) MM mixture tested at 23°C in air. (a) STEM, bright field image from a tribosurface lamella; (b) Fe, Cu and O EDS elemental mapping. (CoF ~0.23).

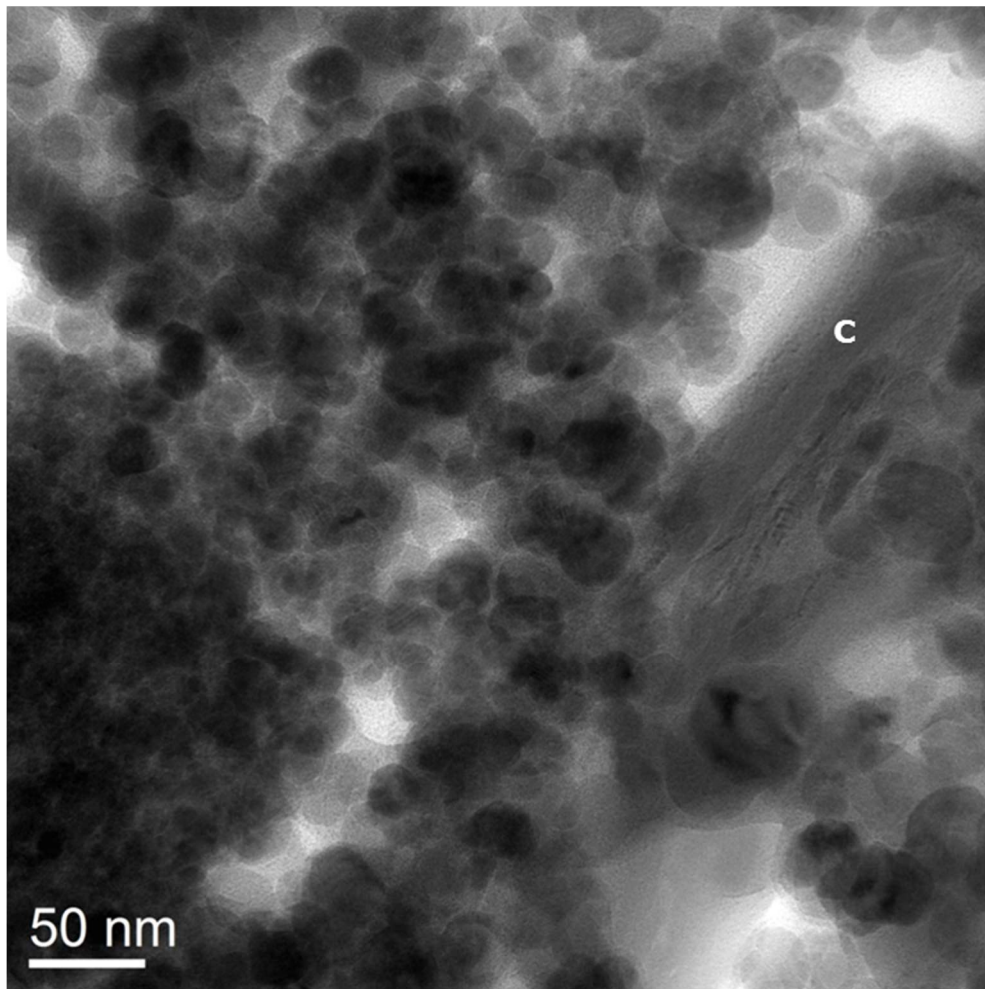


Figure 38 - Disc, ternary (Cu-graphite-Fe<sub>3</sub>O<sub>4</sub>) MM mixture tested at 23°C in air. TEM image from a C-rich area near the tribosurface (CoF ~0.23).

Figure 38 exhibits a SEM-SEI topographical examination of the pin's tribosurface tested at **400°C in N<sub>2</sub>** with the ternary (Cu-graphite-Fe<sub>3</sub>O<sub>4</sub>) MM addition. EDS confirmed a C-rich region (see ellipse) on the compact transfer layer. Figure 39 discloses a cross-section performed on the C-rich region is presented in figure 38. The plastically deformed layer varies between 2 and 5 μm thick with the presence of a sub-superficial crack (see arrow). The transfer layer is compact, however coarse-grained and ranges in thickness from 1 to 3 μm. Longitudinal cracks in the transfer layer are visible just above the pin's surface. (CoF ~0.46).

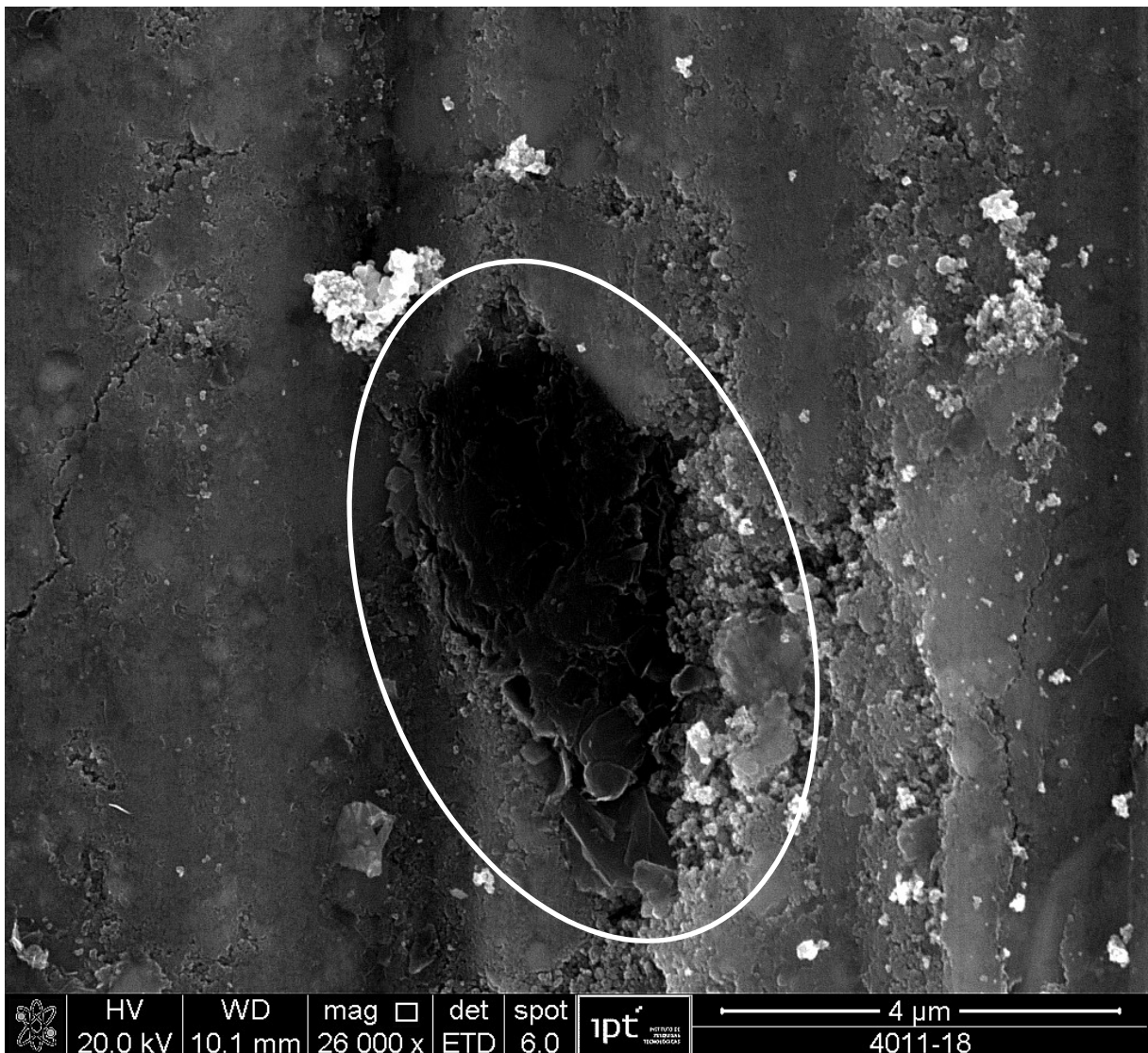


Figure 39 Pin, ternary (Cu-graphite-Fe<sub>3</sub>O<sub>4</sub>) MM mixture tested at 400°C in N<sub>2</sub>. SEM-SEI topographical examination of the tribosurface. C-rich region on transfer layer (encircled). (CoF ~0.46).

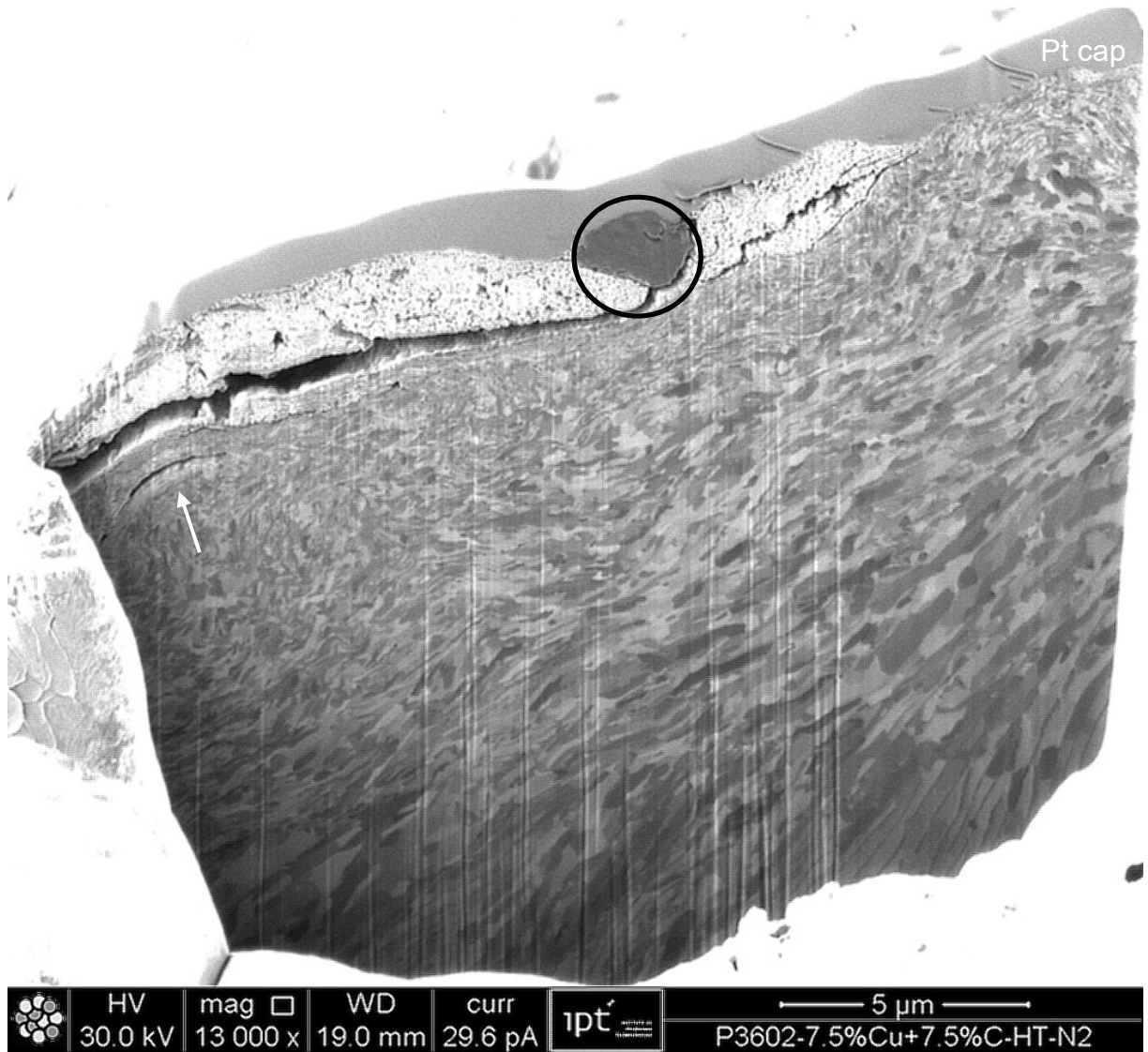


Figure 40 Pin, ternary (Cu-graphite- $\text{Fe}_3\text{O}_4$ ) MM mixture tested at  $400^\circ\text{C}$  in  $\text{N}_2$ . FIB cross-section performed over C-rich region in Figure 39 (see circle). The plastically deformed layer varies between 2 and  $5\ \mu\text{m}$  thick with the presence of a sub-superficial crack (see arrow). The depth of the coarse-grained transfer layer ranges from 1 to  $3\ \mu\text{m}$  and with the presence of longitudinal cracks. (CoF  $\sim 0.46$ ).

Figure 40 features a FIB cross-section of the pin's tribosurface tested at  **$400^\circ\text{C}$  in air** with the ternary (Cu- graphite- $\text{Fe}_3\text{O}_4$ ) MM addition. The oxide transfer layer is compact and smooth and continuous. It varies from  $0.5$  to  $1\ \mu\text{m}$ . The pin's plastically deformed layer is over  $5\ \mu\text{m}$ .

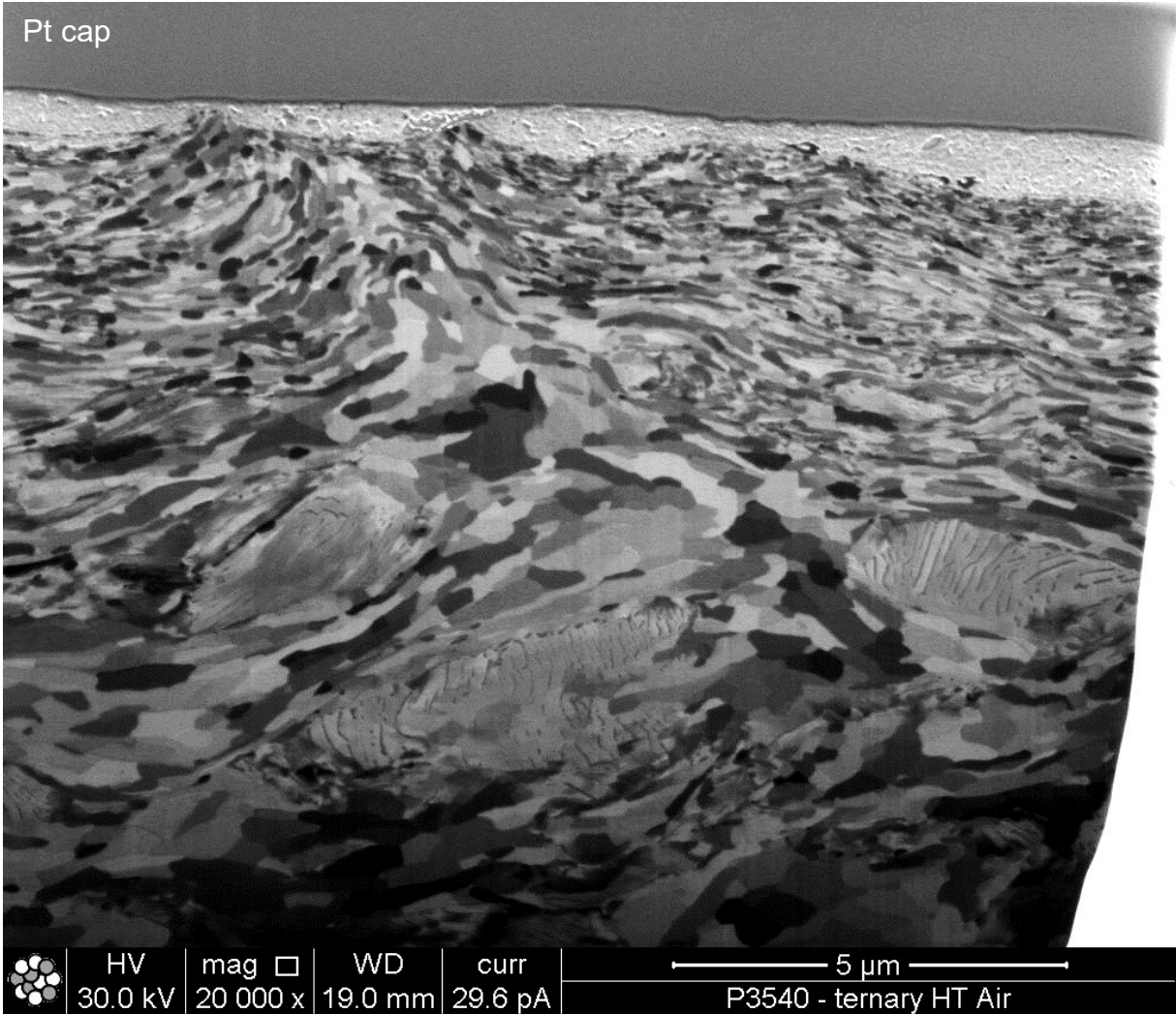


Figure 41 Pin, ternary (Cu- graphite- $\text{Fe}_3\text{O}_4$ ) MM mixture tested at 400°C in air. FIB cross-section. The plastically deformed layer is approximately 5  $\mu\text{m}$  thick. The depth of the compact smooth transfer layer ranges from 0.5 to 1  $\mu\text{m}$  (CoF ~0.55).

### 5.6.2 Results summary for the MM ternary Cu-graphite-Fe<sub>3</sub>O<sub>4</sub> system

The ternary MM Cu-graphite-Fe<sub>3</sub>O<sub>4</sub> system produced average CoF values nearly identical to those obtained with the binary MM graphite-Fe<sub>3</sub>O<sub>4</sub> system. Suggesting graphite controlled the friction behaviour in this system. Table 10 presents the results summary for this system.

Varying the temperature, from 23°C to 400°C, increased the average CoF value. The use of N<sub>2</sub> atmosphere at 400°C decreased the CoF from 0.55 to 0.46 in comparison with tests at 400°C in air.

The oxide transfer layer was compact, but coarse-grained for condition tested at 23°C in air. Moreover, it showed the presence of copper patches and graphite film deposits within the transfer layer (see Figure 36, Figure 37 and Figure 38). Furthermore, the coarse-grained aspect was also observed amid the transfer layers of condition tested at 400°C in N<sub>2</sub> (see Figure 40). Whereas the transfer layer of condition tested at 400°C in air was compact and smooth (see Figure 41).

Table 10 Results summary for the MM ternary Cu-graphite-Fe<sub>3</sub>O<sub>4</sub> conditions

Result	Cu-graphite-Fe <sub>3</sub> O <sub>4</sub>		
	23°C in air	400° in air	400° in N <sub>2</sub>
Average CoF value	0.23	0.55	0.46
CoF evolution	Unstable with peaks	Unstable, few peaks	Stable
Transfer layer thickness	0.5 to 1 µm*	1 to 3 µm*	0.5 to 1 µm*
Transfer layer homogenization	No	-	No
Transfer layer compaction	Compact, yet coarse-grained*	Compact, yet coarse-grained*	Compact and smooth*
Magnetite-hematite transformation	No	Yes	No
Presence of Cu-patches/agglomerates	Yes	N.A.	Yes
Presence of C-rich regions	Yes	N.A.	Yes

\* Result obtained from 1 cross-section. N.A. = not available

## 5.7 Ternary ZrO<sub>2</sub>- Cu-Fe<sub>3</sub>O<sub>4</sub> system

The average CoF values of the investigated BM and MM ternary ZrO<sub>2</sub>-Cu-Fe<sub>3</sub>O<sub>4</sub> systems tested at 23°C in air and 400°C in N<sub>2</sub> did not differ significantly. Table 11 shows a summary of the average CoF results for these systems.

Table 11 Average CoF values for the ternary ZrO<sub>2</sub>-Cu-Fe<sub>3</sub>O<sub>4</sub> conditions.

Mixture (Systems)	Composition (vol.%)	Mixing method	Temp.	Atm.	Average CoF	Standard Deviation	Tribotest repetitions
(ZrO <sub>2</sub> -Cu-Fe <sub>3</sub> O <sub>4</sub> )	89% Fe <sub>3</sub> O <sub>4</sub> + 8%Cu + 3%ZrO <sub>2</sub>	BM	23°C	Air	0.62	0.12	5
		BM	400°C	N <sub>2</sub>	0.55	0.07	3

### 5.7.1 Characterization of the BM ternary ZrO<sub>2</sub>- Cu-Fe<sub>3</sub>O<sub>4</sub> mixture

Figures 42 and 43 present FIB cross-sections of the pin's tribosurface tested at **23°C in air** with ternary BM (Cu-ZrO<sub>2</sub>-Fe<sub>3</sub>O<sub>4</sub>) addition. Figure 41 features a very thick, over 10 µm, plastically deformed layer. The oxide transfer layer shows a compact strip, with the presence of a less compact third body layer above it, ranging from 1 to 3 µm thick. Figure 43 shows the same FIB cross-section in detail. The thin compact and smooth transfer layer is visible just under a coarse-grained deposit on the surface. This transfer layer's coarse-grained aspect better resolved in this image, showing the similarity of these discontinuities to pores formed by powder sintering.

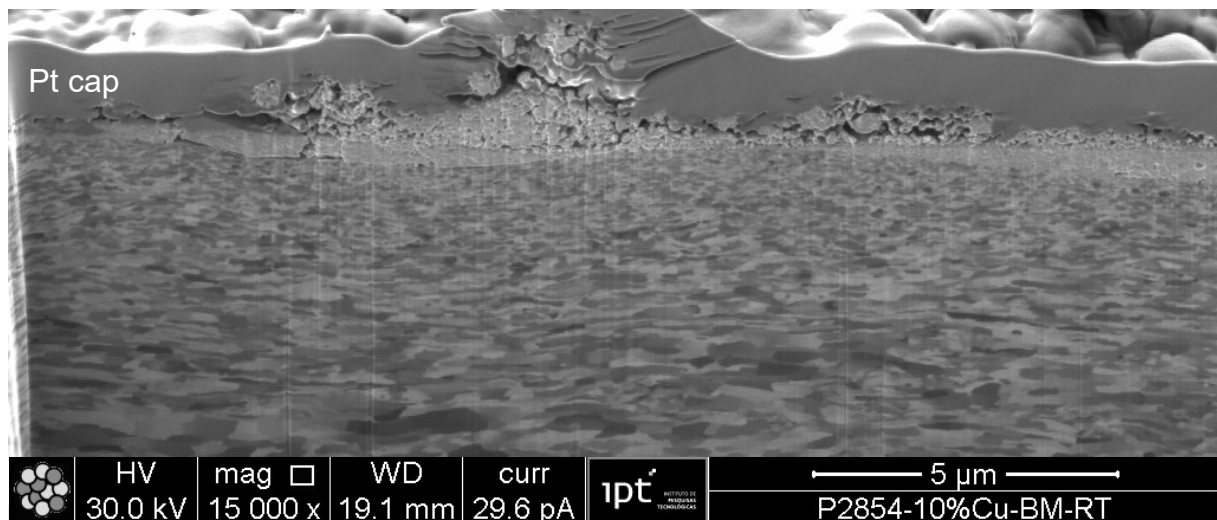


Figure 42 Pin, ternary (Cu-ZrO<sub>2</sub>-Fe<sub>3</sub>O<sub>4</sub>) BM mixture tested at 23°C in air, FIB cross-section. The depth of plastically deformed layer is approximately 10 µm and the thickness of the compact transfer layer is approximately 1 to 3 µm (CoF ~0.62).

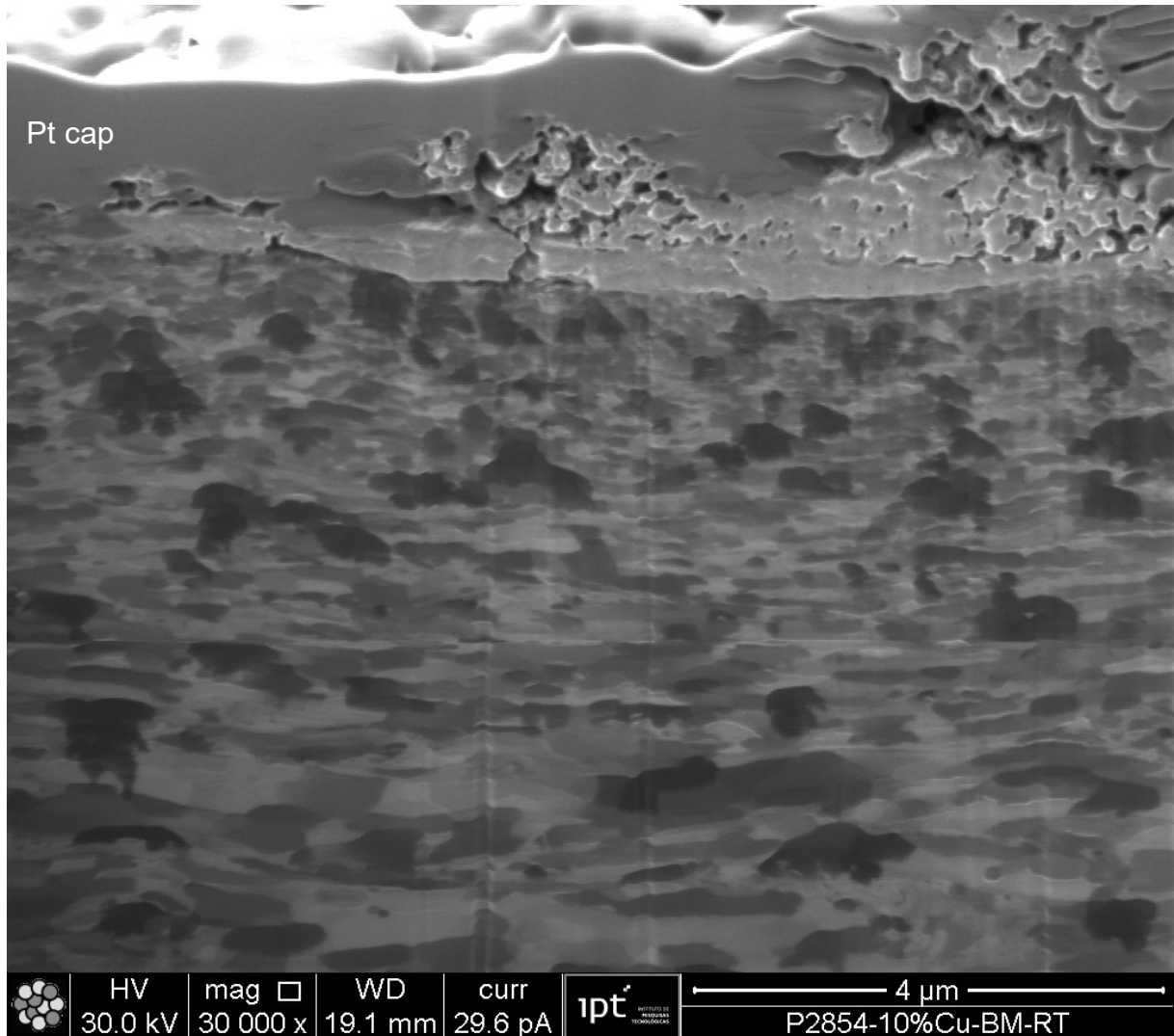


Figure 43 Pin, ternary (Cu-ZrO<sub>2</sub>-Fe<sub>3</sub>O<sub>4</sub>) BM mixture tested at 23°C in air, detail of the FIB cross-section showed in Figure 42. The depth of plastically deformed layer is approximately 10 μm and the thickness of the compact transfer layer is approximately 1 to 3 μm (CoF ~0.62).

FIB cross-section of the ternary Cu-ZrO<sub>2</sub>-Fe<sub>3</sub>O<sub>4</sub> BM mixtures tested at 400°C in N<sub>2</sub> is presented in Figure 44. The condition features a plastically deformed layer of approximately 10 μm. The oxide layer ranges from 5 to 10 μm in thickness. EDS microanalysis confirmed the sub-micron sized particles are Zr-rich (see arrows) sub-micron particles.

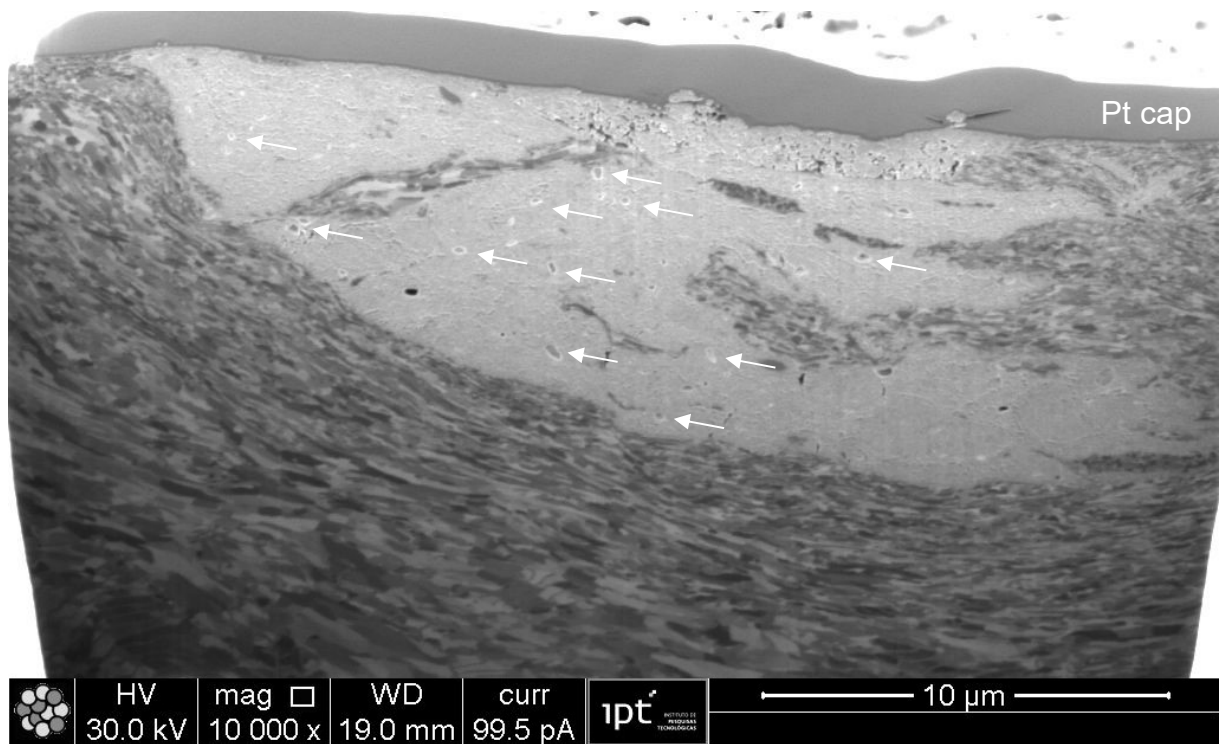


Figure 44 Pin, ternary (Cu-ZrO<sub>2</sub>-Fe<sub>3</sub>O<sub>4</sub>) BM mixture tested at 400°C in N<sub>2</sub>, FIB cross-section. The depth of plastically deformed layer is approximately 10 μm, but the ferritic-pearlitic microstructure is comparatively less elongated than the one observed at 23°C. The depth of the compact transfer layer varies from 5 to 10 μm and do not show any cracks. The arrows point at Zr-rich microsized particles. Metal debris is visible trapped within the transfer layer (CoF ~0.55).

A FIB cross-section of the ternary Cu-ZrO<sub>2</sub>-Fe<sub>3</sub>O<sub>4</sub> BM mixtures tested at 400°C in N<sub>2</sub> is displayed in Figure 45. The condition features a multi-layered structure of plastically deformed layers in between compact oxide transfer layers. The main oxide layer adhered to the tribosurface, ranges from 5 to 9 μm in thickness. EDS microanalysis confirmed the sub-micron sized particles are Zr-rich (see arrows) sub-micron particles.

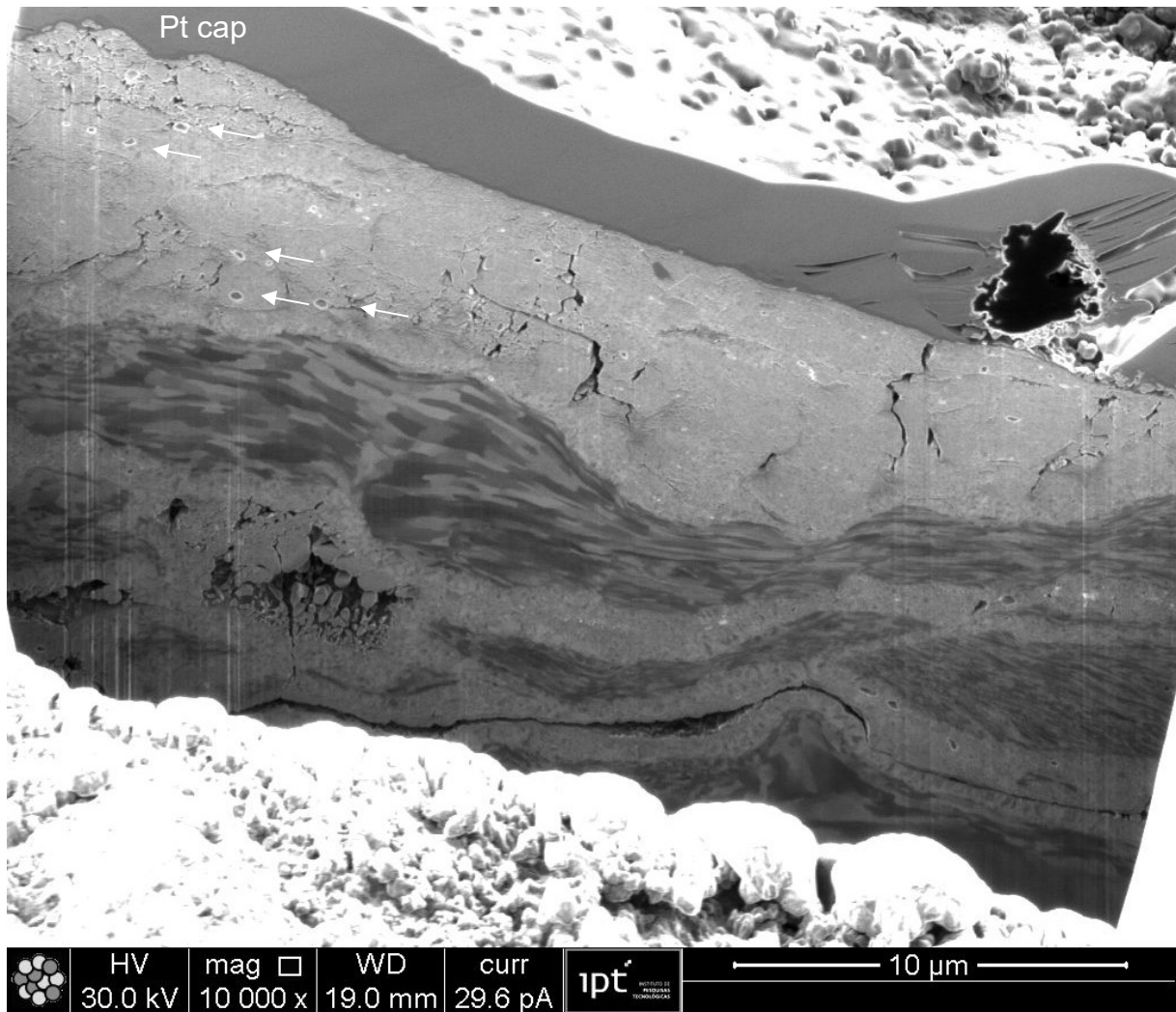


Figure 45 Pin, ternary (Cu-ZrO<sub>2</sub>-Fe<sub>3</sub>O<sub>4</sub>) BM mixture tested at 400°C in N<sub>2</sub>, FIB cross-section. A multi-layered structure of plastically deformed steel between compact oxide transfer layers is visible. The depth of the main superficial compact transfer layer varies from 5 to 9 μm with the presence of a few cracks. The arrows point at Zr-rich sized particles. (CoF ~0.55).

### 5.7.2 Results summary for the ternary Cu-ZrO<sub>2</sub>-Fe<sub>3</sub>O<sub>4</sub> system

Tests with the BM ternary Cu-ZrO<sub>2</sub>-Fe<sub>3</sub>O<sub>4</sub> mixture, performed in at 400°C in N<sub>2</sub>, produced slightly lower CoF average values in comparison to tribotests performed at 23°C in air Table 11. These results are comparable to those observed for the MM binary Cu- Fe<sub>3</sub>O<sub>4</sub> systems tested at the same conditions.

The increase in temperature under an inert atmosphere, was able to isolate aspects of metallic copper's behaviour within the tribolayer. Thus, indicating copper acted as "soft copper" at 400°C.

FIB cross-sections performed to the BM ternary (Cu-ZrO<sub>2</sub>-Fe<sub>3</sub>O<sub>4</sub>) showed the presence of compact smooth oxide layers for condition tested at 23°C in air (see Figure 42 and Figure 43). Whereas the cross-sections for both tribotests at 400°C in air and N<sub>2</sub> showed thick (over 5 µm) smooth compact oxide transfer layers (see Figure 44 and Figure 45). Moreover, EDS elemental mapping confirmed the presence of sub-micron Zr-rich particles within the oxide transfer layer.

The presence of ZrO<sub>2</sub> particles incorporated to the mixture, has most likely played a role on the slight increase of the average CoF value at 400°C in N<sub>2</sub> (0.55) in comparison with the MM binary Cu- Fe<sub>3</sub>O<sub>4</sub> systems (approximately 0.50). This possible effect will be further investigated in the quaternary system section.

Table 12 Results summary for the BM ternary Cu- ZrO<sub>2</sub>-Fe<sub>3</sub>O<sub>4</sub> conditions

Result	BM Cu-ZrO <sub>2</sub> -Fe <sub>3</sub> O <sub>4</sub>	
	23°C in air	400° in N <sub>2</sub>
Average CoF value	0.62	0.55
CoF evolution	unstable	unstable
Transfer layer thickness	1 to 3 µm*	5 to 10 µm**
Transfer layer homogenization	N.A	N.A
Transfer layer compaction	Compact, yet coarse-grained*	Compact and smooth**
Probable magnetite-hematite transformation	No	No
Presence of Cu-patches/agglomerates	N.A	N.A
Presence of C-rich films	N.A	N.A
Presence of Zr-rich particles	N.A	Yes

\* Result obtained from 1 cross-section. \*\*Result compiled from 2 cross-sections. N.A. = not available.

## 5.8 Quaternary ZrO<sub>2</sub>-Cu-graphite-Fe<sub>3</sub>O<sub>4</sub> systems

Table 13 shows a summary for of the average CoF values and standard deviation for the quaternary ZrO<sub>2</sub>-Cu-graphite-Fe<sub>3</sub>O<sub>4</sub> systems, tested each in three conditions: 23°C in air, 400°C in air and 400°C in N<sub>2</sub>.

Table 13 Average friction coefficient values for the quaternary ZrO<sub>2</sub>-Cu-graphite-Fe<sub>3</sub>O<sub>4</sub> conditions.

	Mixture (Systems)	Composition (vol.%)	Mixing method	Temp.	Atm.	Average CoF	Standard Deviation	Tribotest repetitions
<b>Quaternary</b>	(ZrO <sub>2</sub> -Cu-graphite-Fe <sub>3</sub> O <sub>4</sub> )	84% Fe <sub>3</sub> O <sub>4</sub> +	BM	23°C	Air	0.54	0.11	9
		6%Cu + 6%	BM	400°C	Air	0.74	0.18	9
		C+ 4% ZrO <sub>2</sub>	BM	400°C	N <sub>2</sub>	0.53	0.06	3
		84% Fe <sub>3</sub> O <sub>4</sub> +	MM	23°C	Air	0.31	0.06	5
		7.5% C +	MM	400°C	Air	0.56	0.11	3
		7.5%Cu + 1%ZrO <sub>2</sub>	MM	400°C	N <sub>2</sub>	0.46	0.10	3

As a rule, the average values of the CoF of the tribotests performed at 23°C in air, 0.54 (BM) and 0.31 (MM), were comparatively lower than the CoF values observed for tribotests performed at 400°C in air, 0.74 (BM) and 0.56 (MM). Additionally, tribotests performed at 400°C in N<sub>2</sub> featured lower average CoF values, 0.53 (BM) and 0.46 (MM), when compared to the results of the tribotests of the quaternary mixtures at 400°C in air, 0.74 (BM) and 0.56 (MM). The BM mixture tested at 400°C in N<sub>2</sub> showed a decrease in the average value of the CoF from 0,74 to 0.53, when compared to the BM quaternary mixtures tested at 400°C in air. Furthermore, the MM quaternary mixture tested at 400°C in N<sub>2</sub> showed an increase (0.56) of the CoF, when compared to the MM ZrO<sub>2</sub>-Cu-graphite-Fe<sub>3</sub>O<sub>4</sub> mixtures tested at 23°C in air (0.31).

Lastly, the average CoF results for the quaternary ZrO<sub>2</sub>-Cu-graphite-Fe<sub>3</sub>O<sub>4</sub> BM addition were always higher than those observed for the ZrO<sub>2</sub>-Cu-graphite-Fe<sub>3</sub>O<sub>4</sub> MM addition for each condition.

### 5.8.1 Quaternary MM ZrO<sub>2</sub>- Cu-graphite-Fe<sub>3</sub>O<sub>4</sub> mixture

Figure 46 presents a FIB cross-section of the pin's surface tested at **23°C in air** with the addition of the quaternary ZrO<sub>2</sub>-Cu-graphite-Fe<sub>3</sub>O<sub>4</sub> MM mixture. The transfer layer ranges from 0.5 to 2 μm in thickness. The central region of the tribolayer displays a compact smooth oxide region (see rectangle), while the rest of the transfer layer features several particle agglomerates, forming a coarse-grained transfer layer. The elliptic area shows a layer of the metallic microstructure from the first body trapped in the transfer layer. Sub-superficial cracks are visible throughout the transfer layer. The presence of a plastically deformed layer (~2 μm) accompanies the shape of the oxide layer's (see arrows).

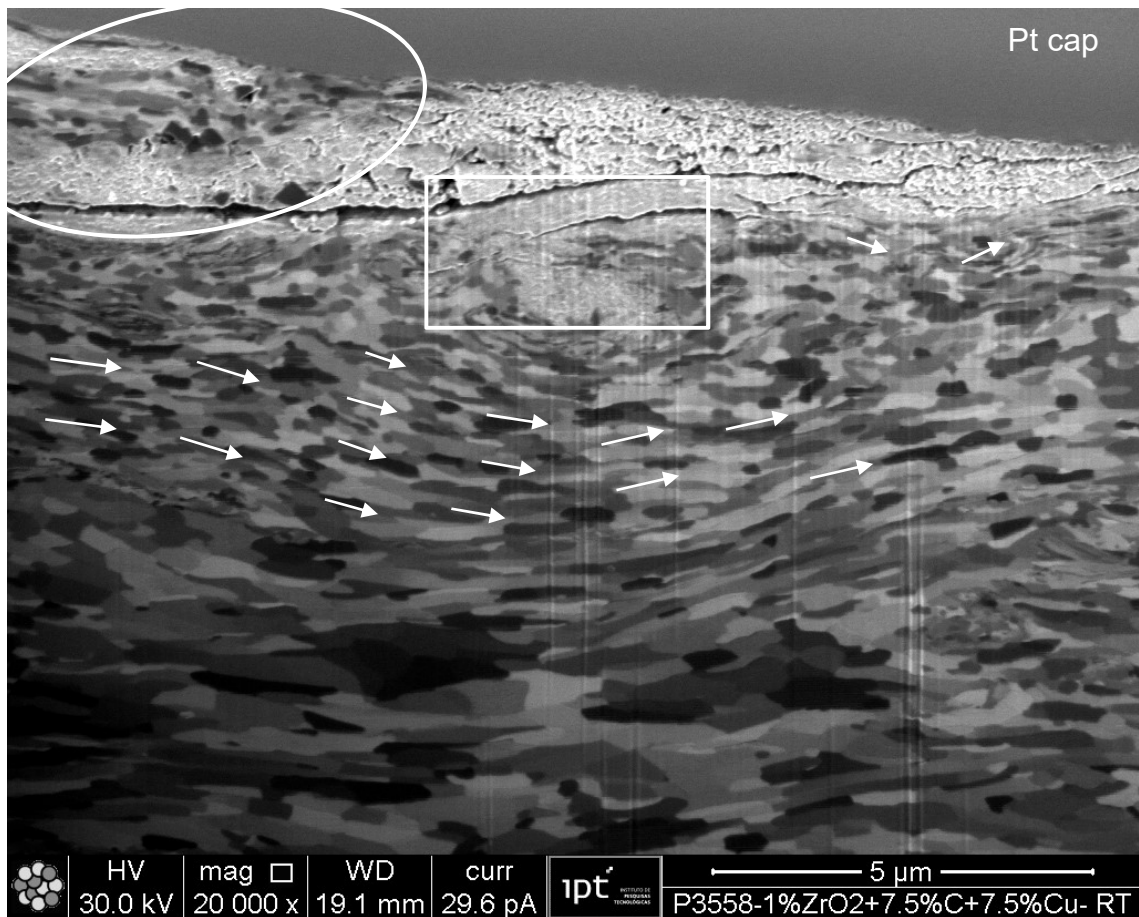


Figure 46 Pin, quaternary (Cu-graphite-ZrO<sub>2</sub>-Fe<sub>3</sub>O<sub>4</sub>) MM mixture tested at 23°C in air. FIB cross-section. The depth of the plastically deformed layer is over 5 μm. The square points at a smooth and compact transfer layer region, while the ellipse points at layer of plastically deformed steel trapped within transfer layer deposits (CoF ~0.31).

Figure 47-a shows a STEM bright field image of the transfer layer taken from the pin's surface tested at 23°C in air with the quaternary Cu-graphite-ZrO<sub>2</sub>-Fe<sub>3</sub>O<sub>4</sub> MM addition. Figure 47-b shows the C EDS elemental mapping, where C-rich layers, in the probably graphite lamellae are visible near the surface and within the transfer layer (see arrows). For these C-rich regions, Figures 47-c and 476-d show that these areas are depleted in O, and Cu, respectively. The Cu EDS elemental mapping in Figure 47-d shows the presence of Cu is somewhat homogeneous, and does not display the presence of patches within the transfer layer.

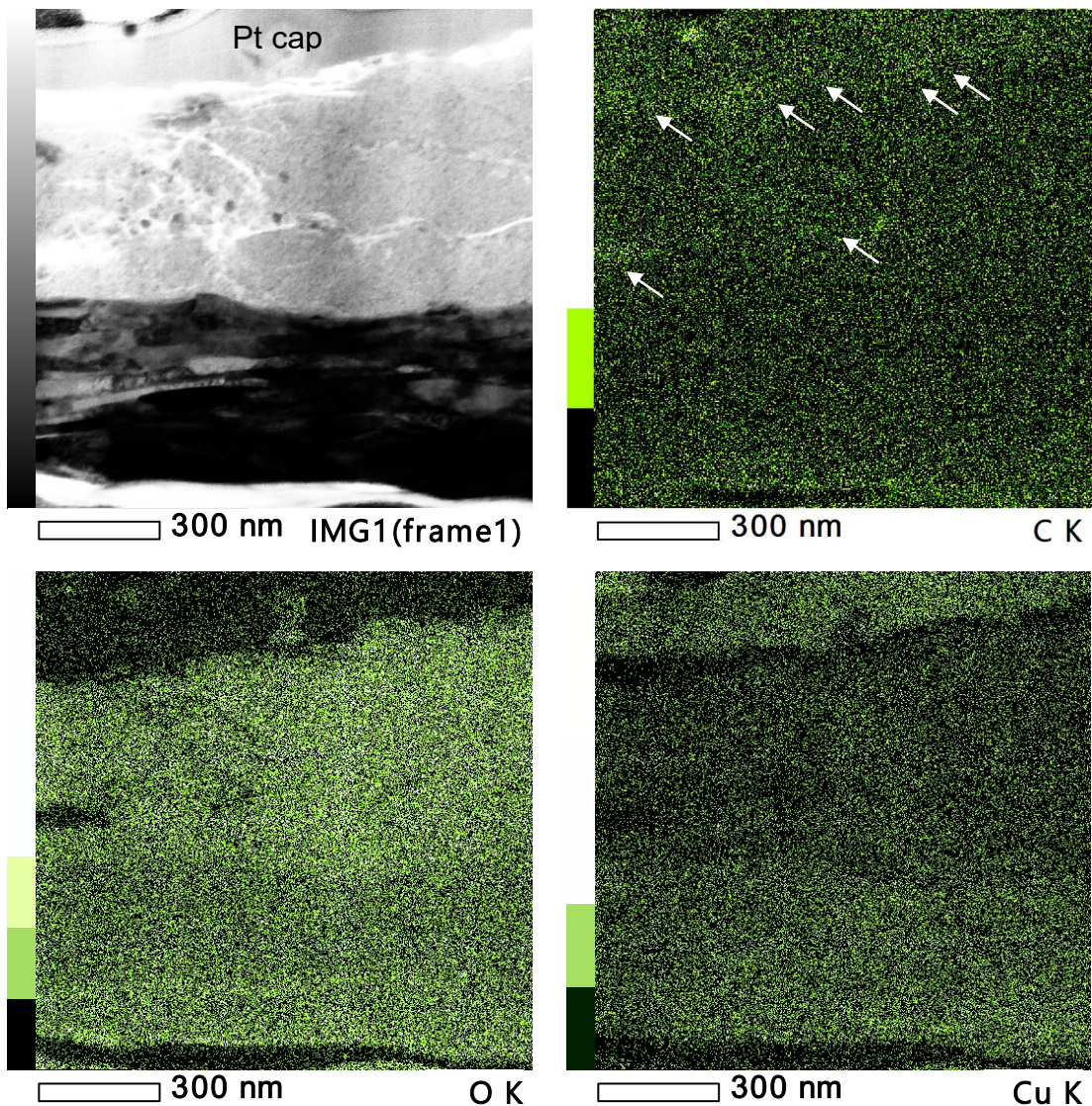


Figure 47 Pin, quaternary (Cu-graphite-ZrO<sub>2</sub>-Fe<sub>3</sub>O<sub>4</sub>) MM mixture tested at 23°C in air. (a) STEM, bright field image from a tribosurface lamella; (b) C EDS elemental mapping; (c) O EDS elemental mapping; (d) Cu EDS elemental mapping (CoF ~0.31).

Figure 48 features two TEM images of an area from Figure 47, that is, the pin tested with the addition of the quaternary Cu-graphite-ZrO<sub>2</sub>-Fe<sub>3</sub>O<sub>4</sub> MM mixture at 23°C in air. Figure 48-a displays a large area of a homogeneously mixed tribolayer, with a graphite layer near the surface (see arrow), which coincides with one of the C-rich areas shown in figure 47-b. Figure 48-b features another region of the tribofilm with the presence of fibre-like graphite (see arrow), which also coincides with one of the C-rich areas shown in Figure 47-b.

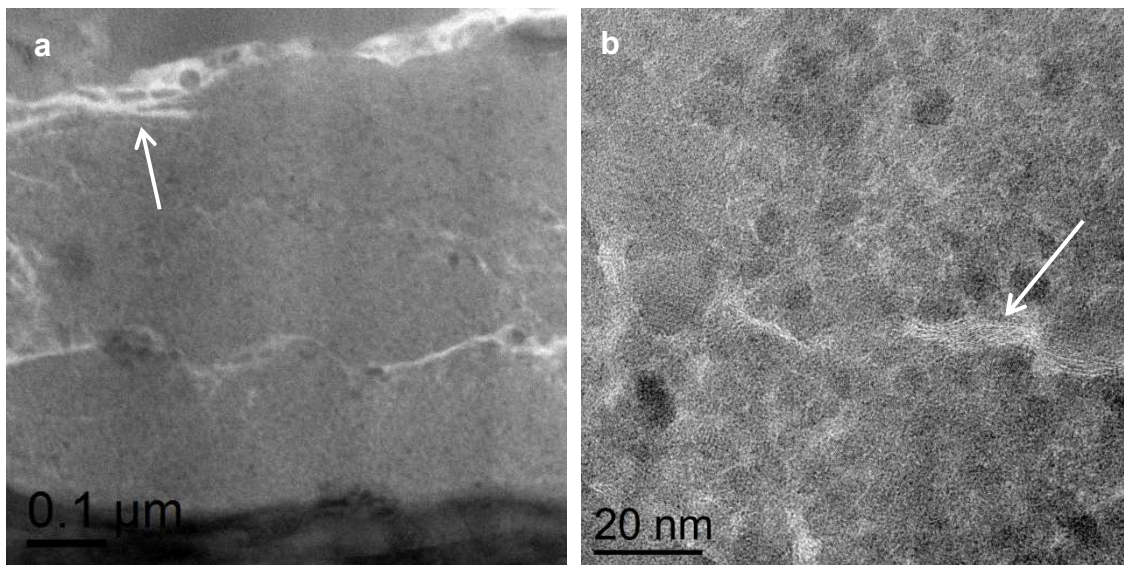


Figure 48 Pin, quaternary (Cu-graphite-ZrO<sub>2</sub>-Fe<sub>3</sub>O<sub>4</sub>) MM mixture tested at 23°C in air. TEM image from a tribosurface lamella: a) Region of a homogeneously mixed tribolayer featuring a thin layer graphite in the tribofilm microstructure (see arrow); b) Presence of a layer of graphite films between other particles (see arrow (CoF ~0.31)).

Figure 49-a features a TEM image from the pin's tribolayer tested with the addition of the quaternary Cu-graphite-ZrO<sub>2</sub>-Fe<sub>3</sub>O<sub>4</sub> MM mixture at 23°C in air. A third body oxide deposit is trapped within the pin's steel surface and a metallic debris about to detach from the tribolayer. Figure 49-b features the STEM bright field image from the trapped third body, the third body is not homogenised. Figure 49 displays the STEM dark field image for the same region and the EDS spectrum images for the green rectangle. Figures 50-a and 50-b display Zr-rich and Cu-rich nanoparticle agglomerates within the third body.

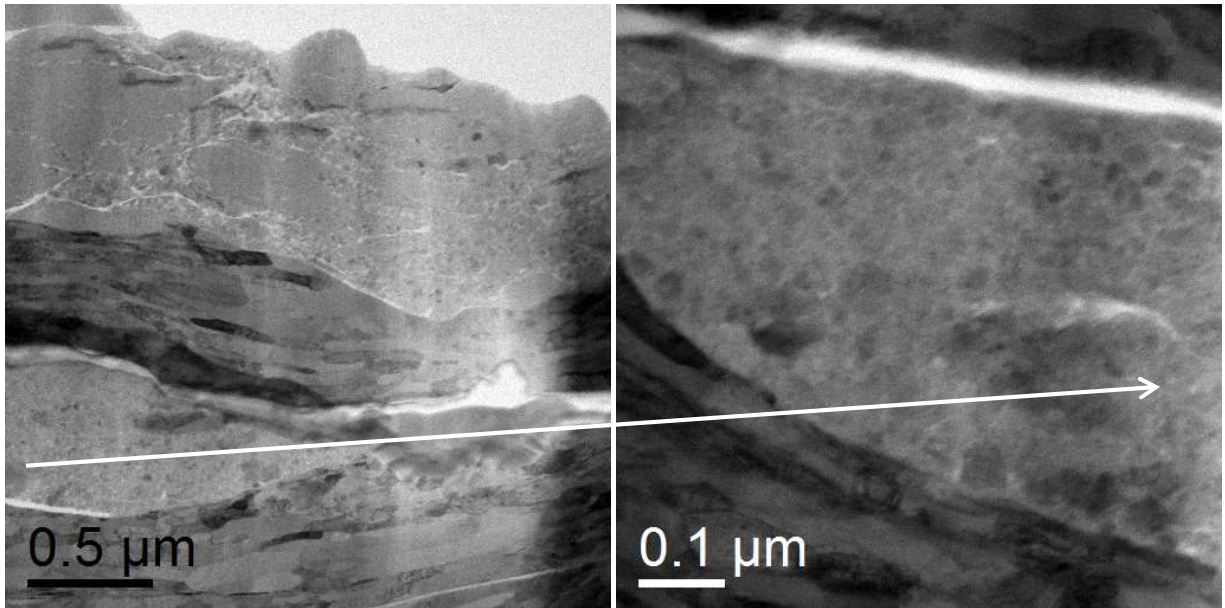


Figure 49 Pin, quaternary (Cu-graphite-ZrO<sub>2</sub>-Fe<sub>3</sub>O<sub>4</sub>) MM mixture tested at 23°C in air. (a) TEM image from a tribosurface lamella (b) STEM, bright field image from the third body trapped between the first body's steel layers (CoF ~0.53).

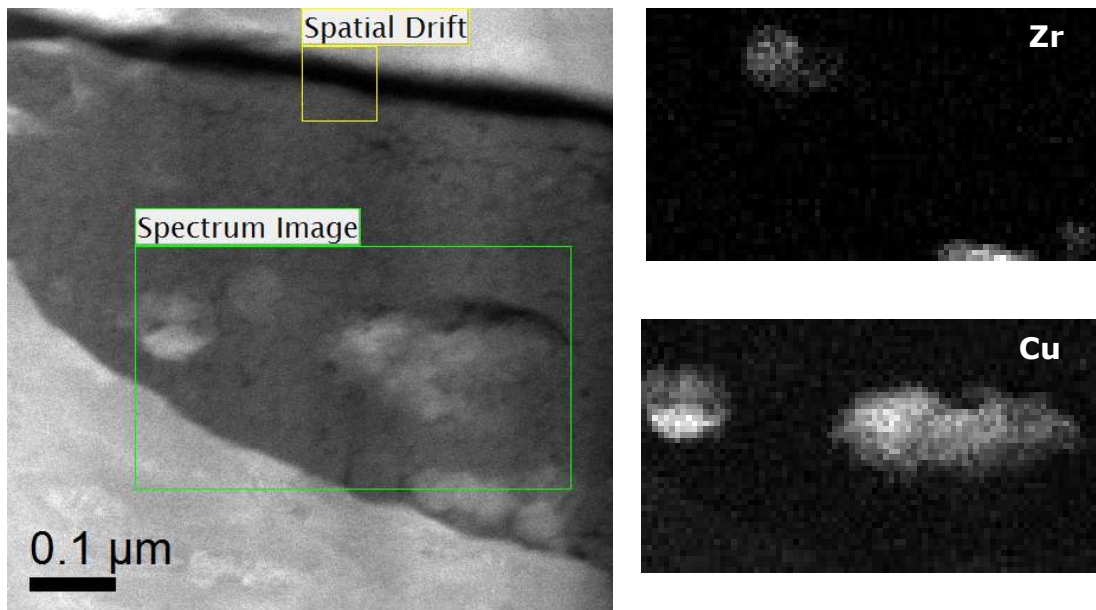


Figure 50 Pin, quaternary (Cu-graphite-ZrO<sub>2</sub>-Fe<sub>3</sub>O<sub>4</sub>) MM mixture tested at 23°C in air. (a) STEM, dark field image from a tribosurface lamella; (b) Zr EDS elemental mapping; (c) Cu EDS elemental mapping; (CoF ~0.53).

Figures 51 and 52 present FIB cross-sections of the pin's surface after testing with the addition of the quaternary Cu-graphite-ZrO<sub>2</sub>-Fe<sub>3</sub>O<sub>4</sub> MM mixture at 400°C in air and at 400°C in N<sub>2</sub>, respectively. The thickness of the interfacial media observable ranges from 0.5 to 3.5 μm for both images. Figure 51 displays compact smooth oxide layer, with the presence of Zr-rich particles (see arrows). Figure 52 shows lack of compaction within the tribolayer. The presence of a plastically deformed layer (~5 μm) accompanies both images.

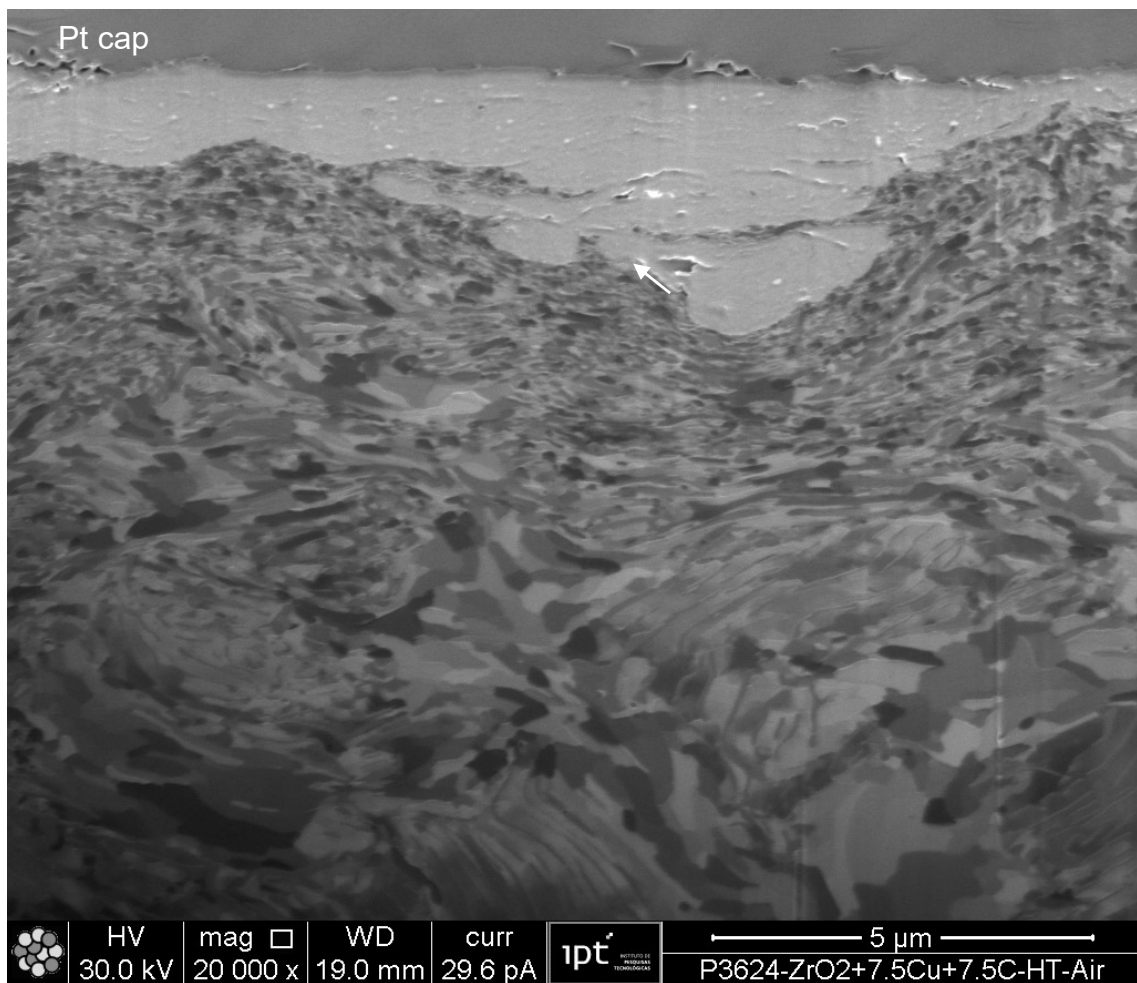


Figure 51 Pin, quaternary (Cu-graphite-ZrO<sub>2</sub>-Fe<sub>3</sub>O<sub>4</sub>) MM mixture tested at 400°C in air. FIB cross-section. The depth of the plastically deformed layer is ~ 5 μm thick, and the thickness of the compact smooth transfer ranges from 0.5 to 3.5 μm thick. The arrows show a sub-micron sized particle within the transfer layer (CoF ~0.56).

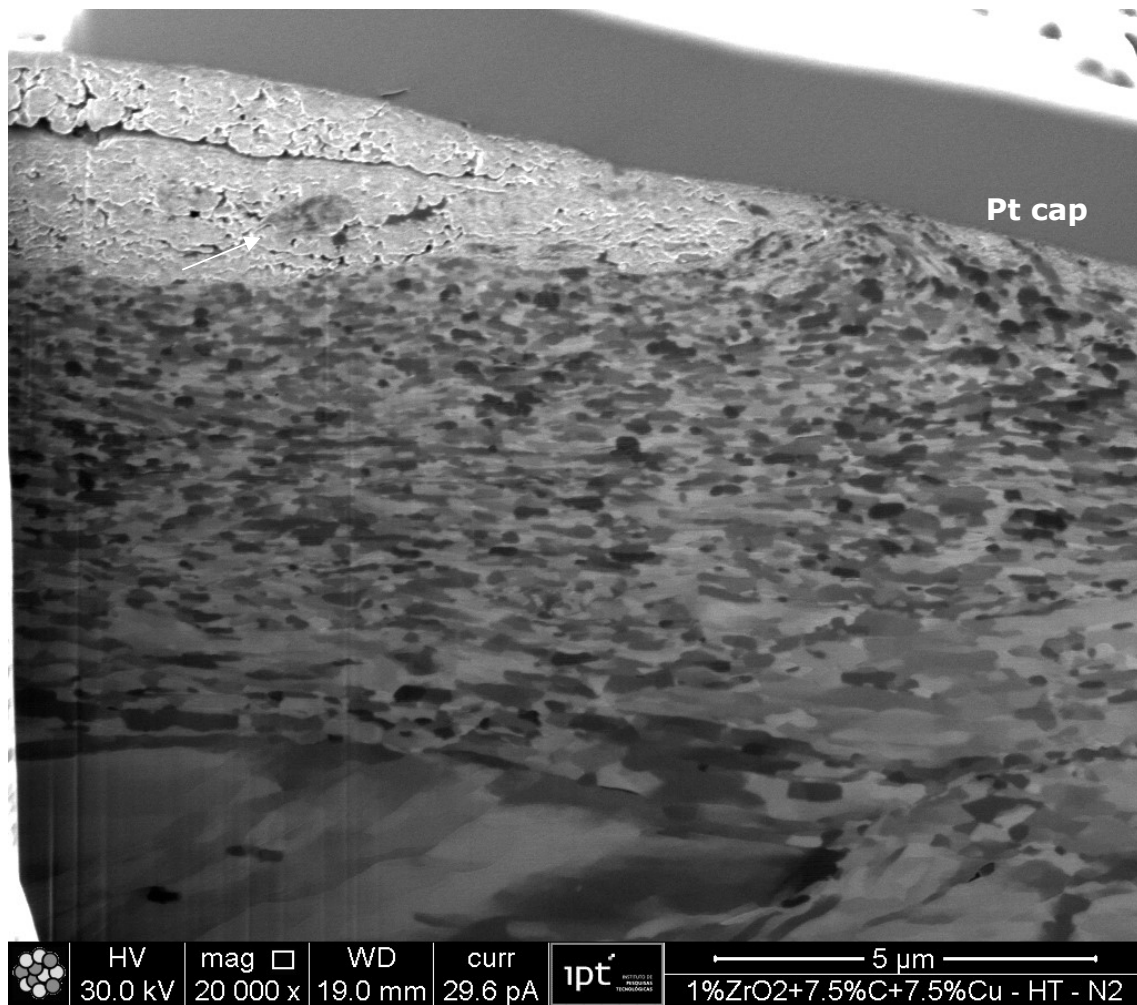


Figure 52 Pin, quaternary (Cu-graphite-ZrO<sub>2</sub>-Fe<sub>3</sub>O<sub>4</sub>) MM mixture tested at 400°C in N<sub>2</sub>. FIB cross-section. The depth of the plastically deformed layer is ~ 5 μm thick, and the thickness of the transfer layer ranges from 0.5 to 3.5 μm thick, lacking compaction. (CoF ~0.56).

### 5.8.2 Quaternary BM ZrO<sub>2</sub>- Cu-graphite-Fe<sub>3</sub>O<sub>4</sub> mixture characterization

Figure 53 shows a FIB cross-sections of the disc's tribosurface, tested with quaternary ZrO<sub>2</sub>-Cu-graphite-Fe<sub>3</sub>O<sub>4</sub> BM addition at **23°C in air**. The compact transfer layer seems to have undergone a tribosintering process, and ranges between 1.5 and 5 μm thick. However compact, the oxide transfer layer features discontinuities and longitudinal cracks throughout the section. EDS elemental mapping showed the presence of Zr-rich particles within the transfer layer (see circles). The arrows point at metallic debris, originated on the plastically deformed tribolayer of the first bodies, now trapped within the third body transfer layer. The plastically deformed layer ranges from 1.5 to 7 μm in thickness.

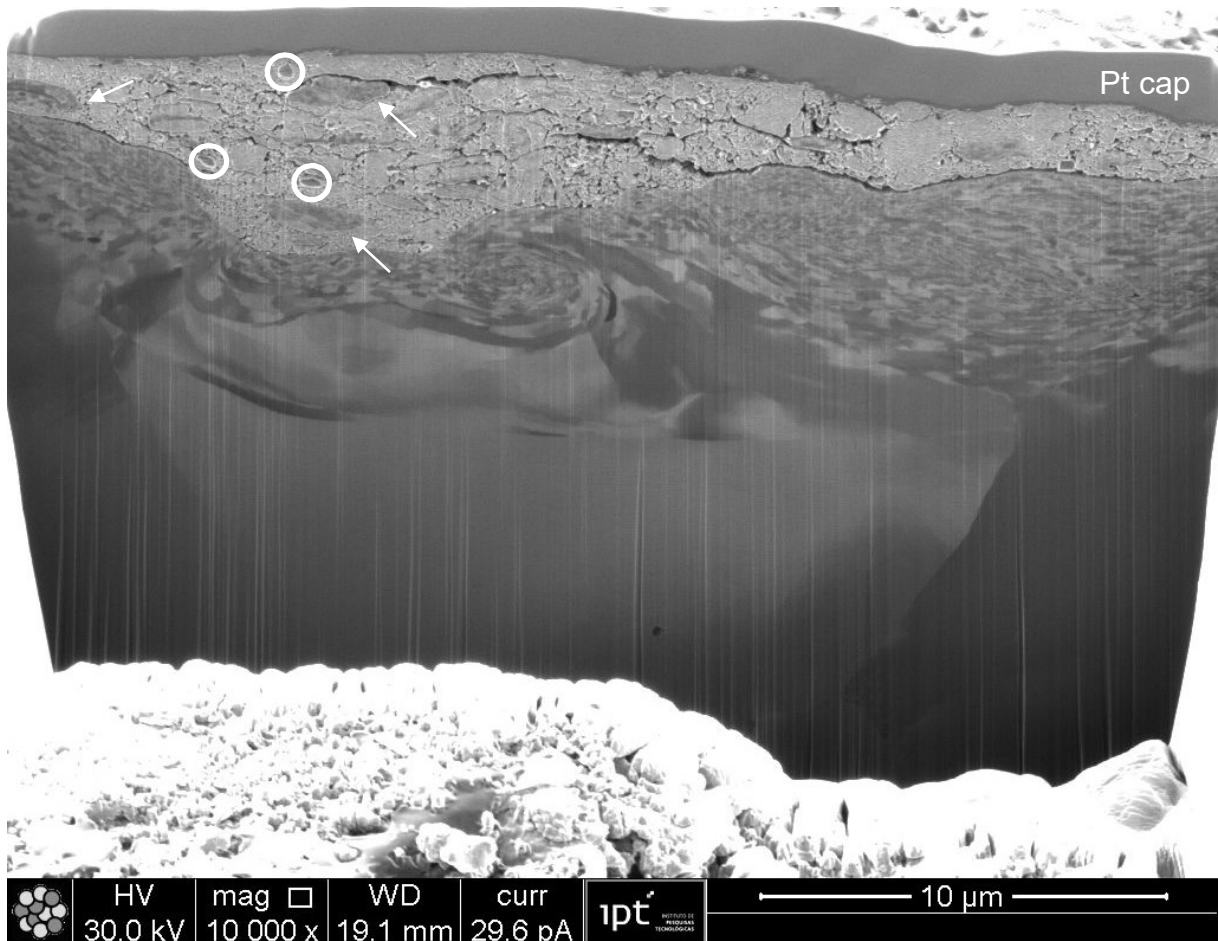


Figure 53 Disc, quaternary ZrO<sub>2</sub>-Cu-graphite-Fe<sub>3</sub>O<sub>4</sub> BM mixture tested at 23°C in air. FIB cross-section. The tribosintered transfer layer ranges from 1.5 to 5 μm thick. The plastically deformed layer ranges from 1.5 to 7 μm in thickness. Metallic debris are visible within the transfer layer (arrows), alongside with longitudinal cracks and discontinuities. Zr-rich particles are identified with circles. (CoF ~0.54).

Figure 54 shows a FIB cross-sections of the pin's tribosurface, tested with quaternary  $ZrO_2$ -Cu-graphite- $Fe_3O_4$  BM addition at 23°C in air. The compact oxide transfer layer is thin, under 1.5  $\mu m$  thick and present in the form of patches. In its thicker region, it has a coarse-grained aspect. The arrows point at a discontinuity region within the plastically deformed layer. Oxide third body is visible in the discontinuity, suggesting ploughing took place and created a fold on the material's surface. The plastically deformed layer is over 10  $\mu m$  thick.

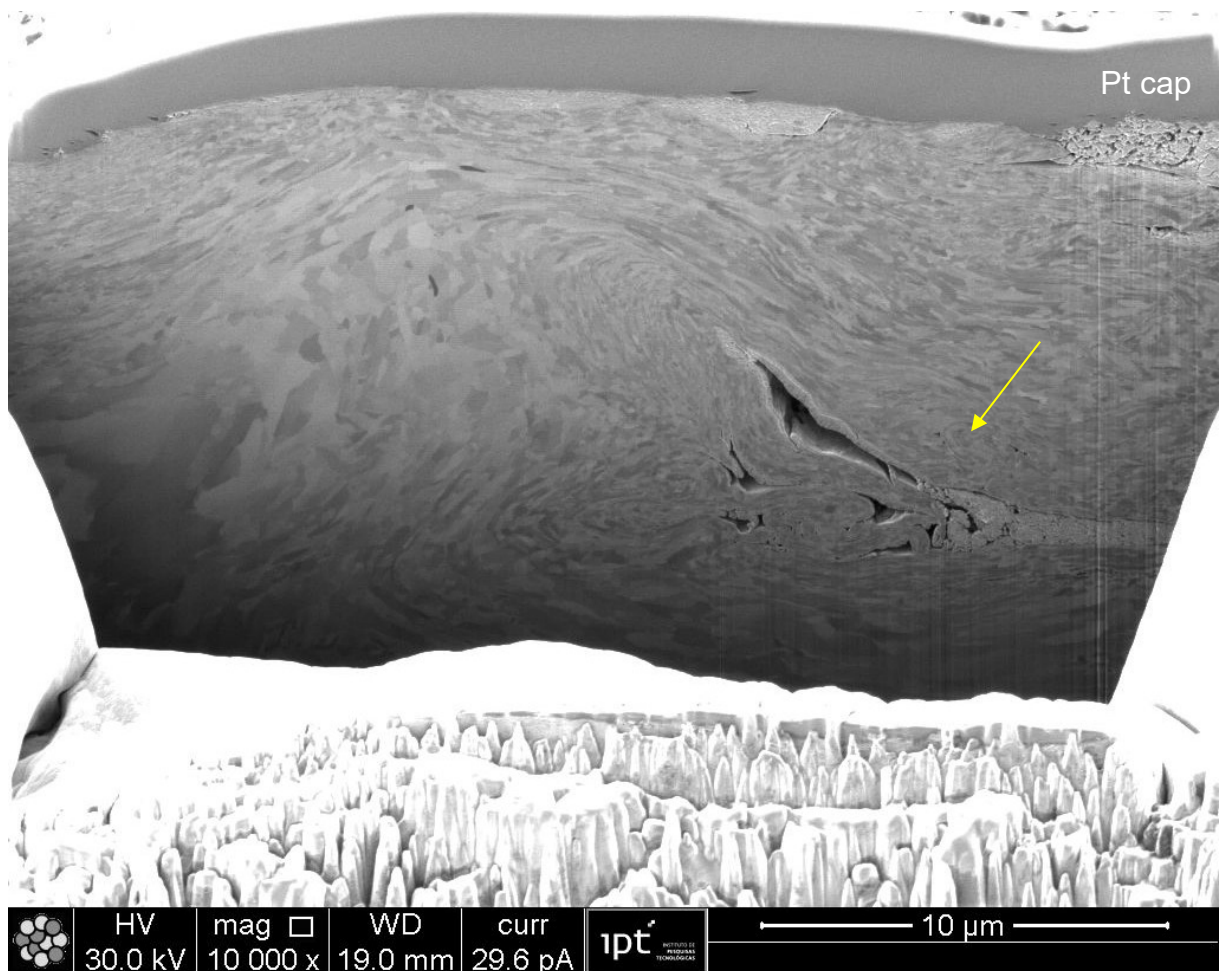


Figure 54 Pin, quaternary ( $ZrO_2$ -Cu-graphite- $Fe_3O_4$ ) BM mixture tested at 23°C in air. FIB cross-section. The plastically deformed layer is over 10  $\mu m$  thick. Compact smooth patches of oxide transfer layer are visible and are approximately 2  $\mu m$  thick. The arrow points to a discontinuity within the microstructure, and the presence of trapped oxide third body inside the tribologically transformed layer. (CoF ~0.54).

Figure 55 features a SEM-BEI topographical examination of the pin's tribosurface tested at 23°C in air with the quaternary ( $ZrO_2$ -Cu-graphite- $Fe_3O_4$ ) BM addition. EDS elemental mapping revealed Zr-rich particles encrusted on the pin's tribosurface (see arrows). A FIB cross-section was performed on the top of one of these Zr-rich particles, Figure 56 shows the image of the cross-section with the presence of a 5  $\mu m$  sized Zr-rich particle encrusted to the tribosurface. Around the Zr-rich area, EDS confirmed a O-rich region suggesting the presence of oxide third body trapped between the particle and the tribologically transformed surface.

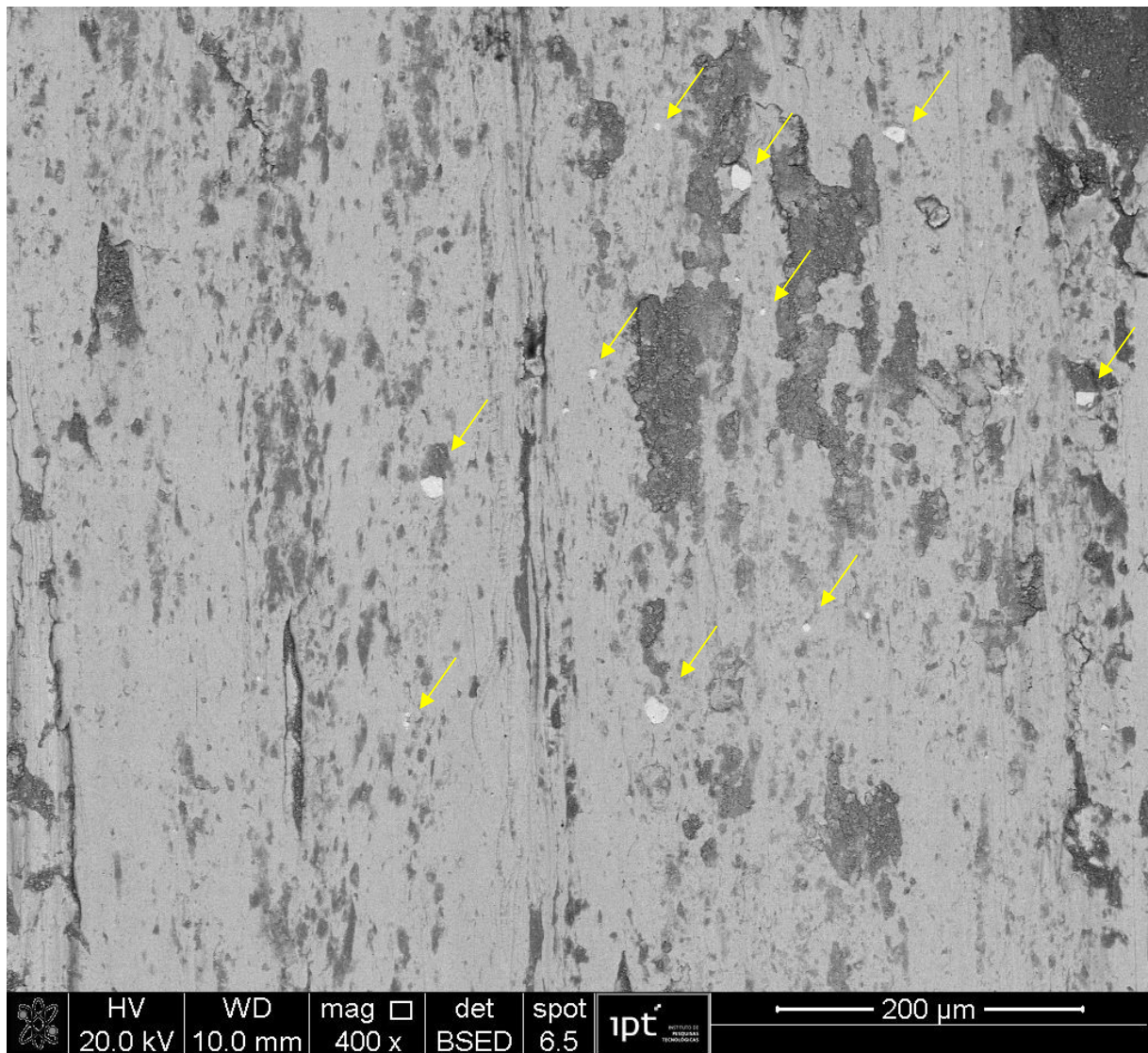


Figure 55 Pin, quaternary ( $ZrO_2$ -Cu-graphite- $Fe_3O_4$ ) BM mixture tested at 23°C in air. SEM-BEI image. The arrows point at Zr-rich particles (0.54).

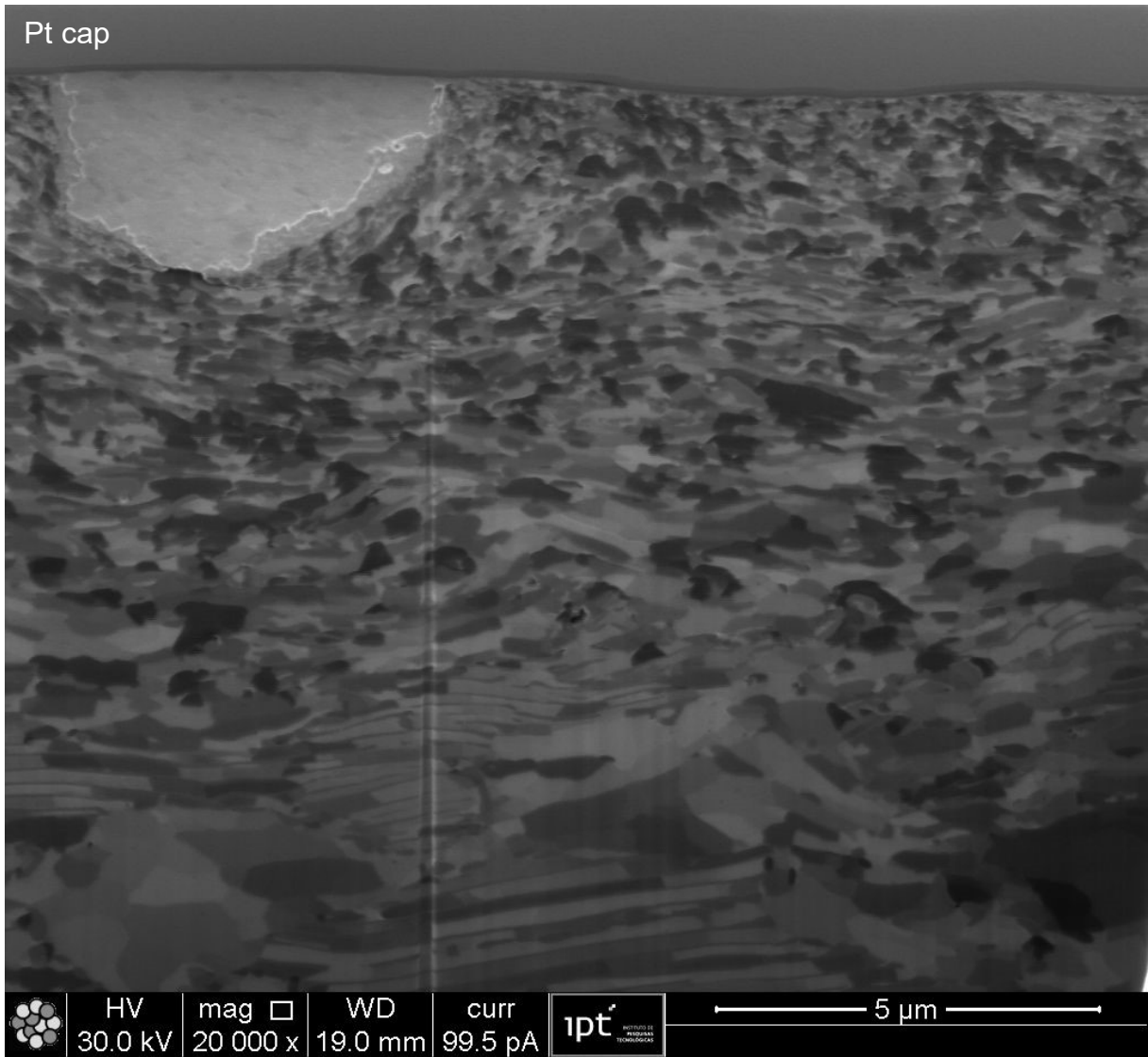


Figure 56 Pin, quaternary ( $\text{ZrO}_2\text{-Cu-graphite-Fe}_3\text{O}_4$ ) BM mixture tested at 23°C in air. FIB cross-section. The plastically deformed layer is approximately 5 μm thick. A Zr-rich inclusion is encrusted at the tribosurface. (CoF ~0.54).

Figure 57 displays the FIB cross-section of the quaternary Cu-graphite-ZrO<sub>2</sub>-Fe<sub>3</sub>O<sub>4</sub> BM mixtures tested at **400°C in N<sub>2</sub>**. EDS microanalysis confirmed the presence of Zr-rich sub-micron particles within the transfer layer (see arrows). A compact smooth oxide layer, with thickness of approximately 3.5 μm is observable in the image. Thea plastically deformed layer displays a depth between 2.5 and 5 μm and interfacial media addition is sandwiched by the plastically deformed layers.

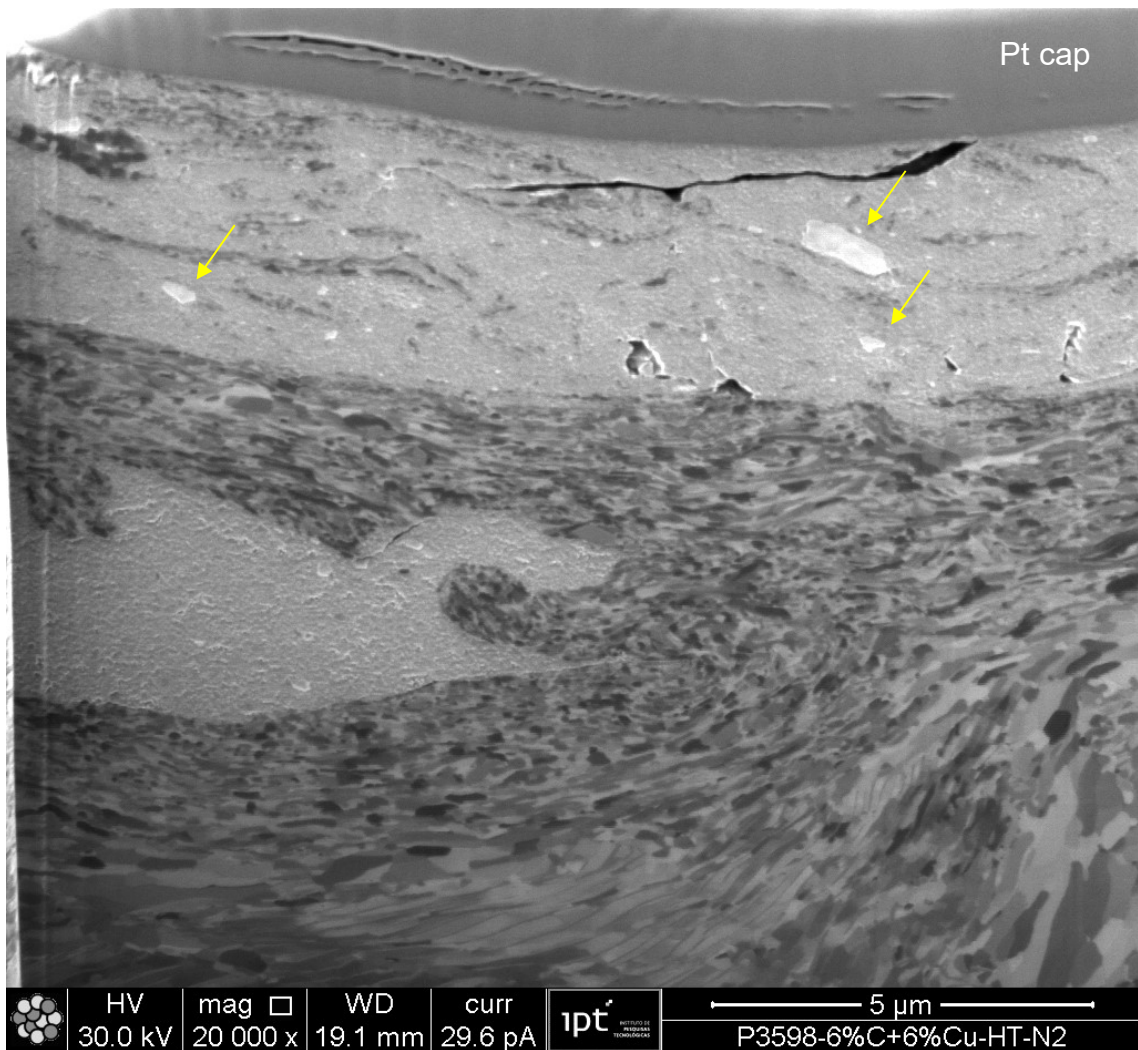


Figure 57 Pin, quaternary (Cu-graphite-ZrO<sub>2</sub>-Fe<sub>3</sub>O<sub>4</sub>) BM mixture tested at 400°C in N<sub>2</sub>, FIB cross-section. The depth of the plastically deformed layer ranges from 2 to 5 μm, and the thickness of the compact transfer layer is ~ 3.5 μm thick. The arrows point at Zr-rich areas, A region of the tribofilm is sandwiched by the plastically deformed region (CoF ~0.53).

FIB cross-section of the quaternary Cu-graphite-ZrO<sub>2</sub>-Fe<sub>3</sub>O<sub>4</sub> BM mixtures tested at **400°C in air** is presented in Figure 58. EDS microanalysis confirmed the presence of Zr-rich sub-micron particles within the transfer layer (see arrows). A compact smooth oxide layer, with thickness ranging from 1 to 3 μm is visible in Figure 58. The oxide transfer layer is smooth, compact, for both conditions, with the presence of a few cracks and sparse discontinuities (see circles). Figure 58 displays a plastically deformed layer with depth from 2 to 3 μm, whose microstructure orientation complies with the shape of the adhered oxide tribolayer.

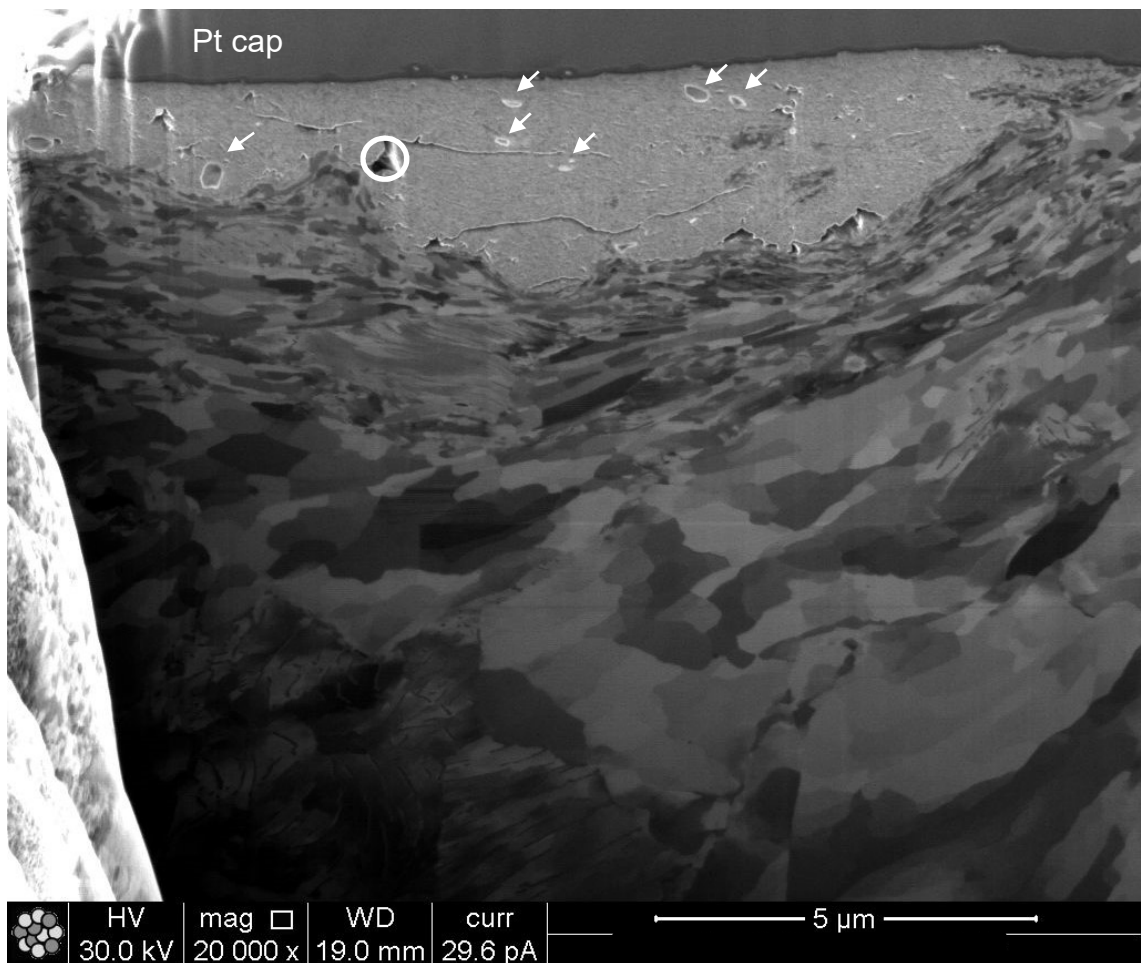


Figure 58 A) Pin, quaternary (Cu-graphite-ZrO<sub>2</sub>-Fe<sub>3</sub>O<sub>4</sub>) BM mixture tested at 400°C in air, FIB cross-section. The depth of the plastically deformed zone ranges from 2 to 3 μm, while the thickness of the compact transfer layer is between 1 and 3 μm thick and compact. The arrows point Zr-rich areas, while the circles show discontinuities in the transfer layer (CoF ~0.74).

Figure 59-a displays a STEM bright field image of the transfer layer lamella sampled from the surface of the pin tested at 400°C in air with the quaternary Cu-graphite-ZrO<sub>2</sub>-Fe<sub>3</sub>O<sub>4</sub> BM quaternary mixture. Figure 59-b show the C EDS elemental

mapping, respectively. The transfer layer does not feature the presence of C-rich agglomerates. Figures 58-c and 58-d feature the O and Cu EDS elemental mapping. The distribution of O is rather homogeneous, indicating the few Cu-rich areas in figure 58-d are likely associated with O.

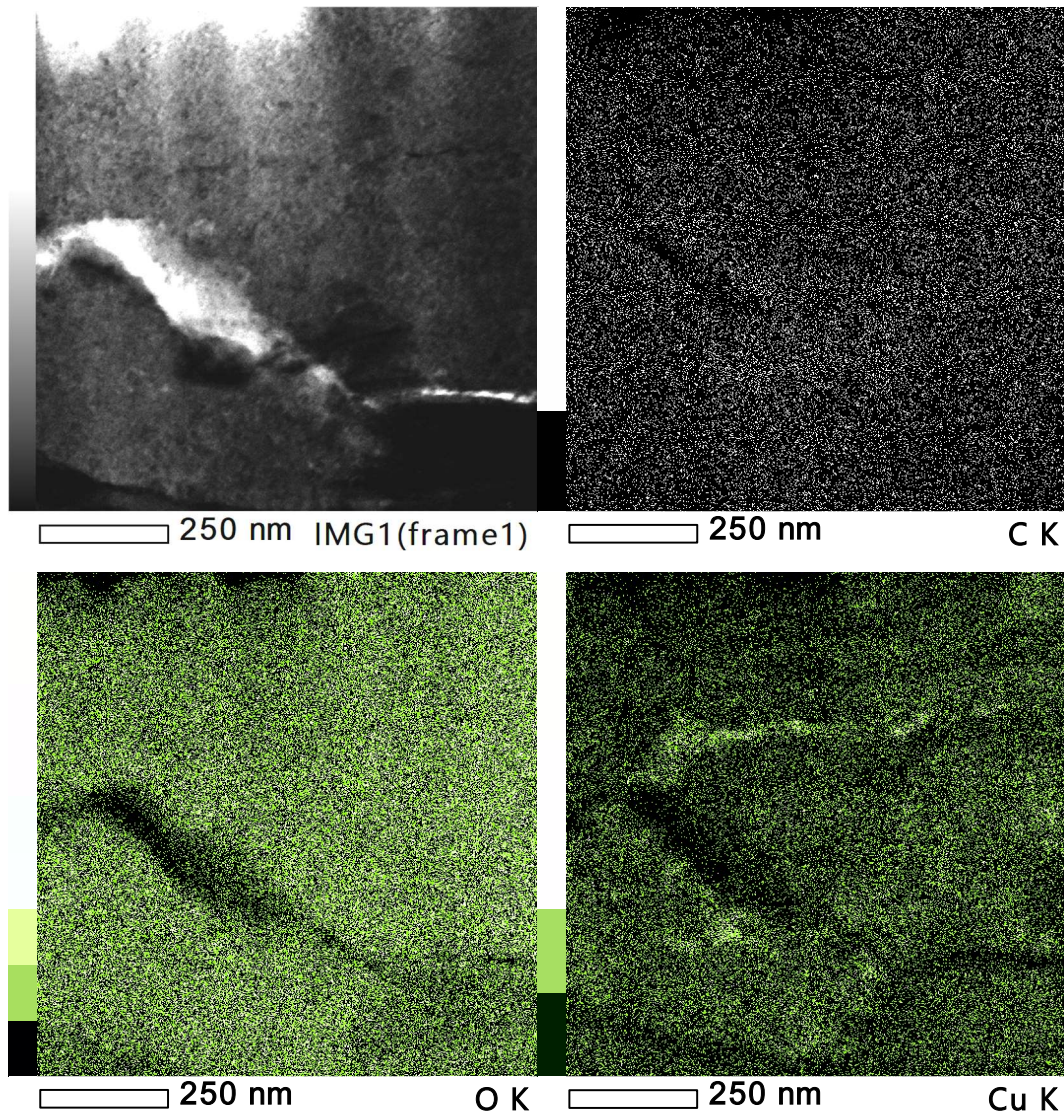


Figure 59 Pin, quaternary (Cu-graphite-ZrO<sub>2</sub>-Fe<sub>3</sub>O<sub>4</sub>) BM mixture tested at 400°C in air. (a) STEM, bright field image from a tribosurface lamella; (b) C EDS elemental mapping; (c) O EDS elemental mapping; (d) Cu EDS elemental mapping (CoF ~0.53).

Figure 59 features two TEM detail images of the tribofilm of sample (pin surface) tested at 400°C in air with the addition of the quaternary Cu-graphite-ZrO<sub>2</sub>-

Fe<sub>3</sub>O<sub>4</sub> BM mixture. Figure 59-a displays the Cu-rich nanocrystalline particles near the sample's surface, while figure 59-b shows the presence of curved lattice structures, characterized by Häusler et al. [90] as turbostratic graphite. They are nestled among other particles, indicating good homogenization of tribolayer in the nanoscale.

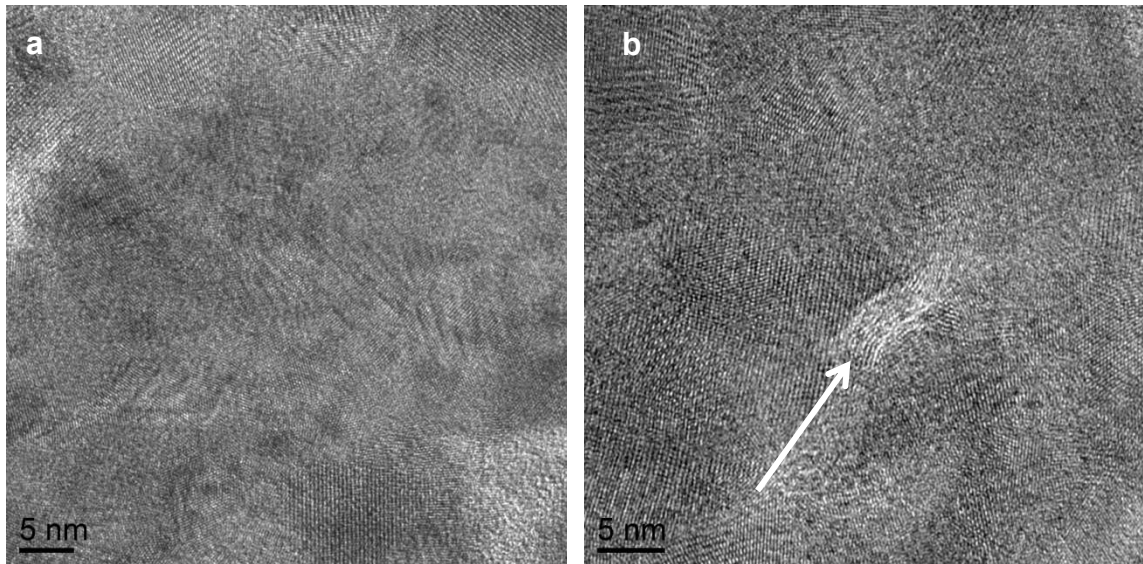


Figure 60 Pin, quaternary (Cu-graphite-ZrO<sub>2</sub>-Fe<sub>3</sub>O<sub>4</sub>) BM mixture tested at 400°C in air. TEM image from a tribosurface lamella. (a) Cu-rich area, Cu nanoparticles near the sample surface; (b) Graphite fibres amid the tribofilm (see arrows) (CoF ~0.53).

Furthermore, SAED energy filtered patterns are displayed with its EDS spectrum in Figure 61. They confirm the presence of Fe<sub>3</sub>O<sub>4</sub> and Fe<sub>2</sub>O<sub>3</sub>, thus corroborating that magnetite was, at least partially, transformed in hematite.

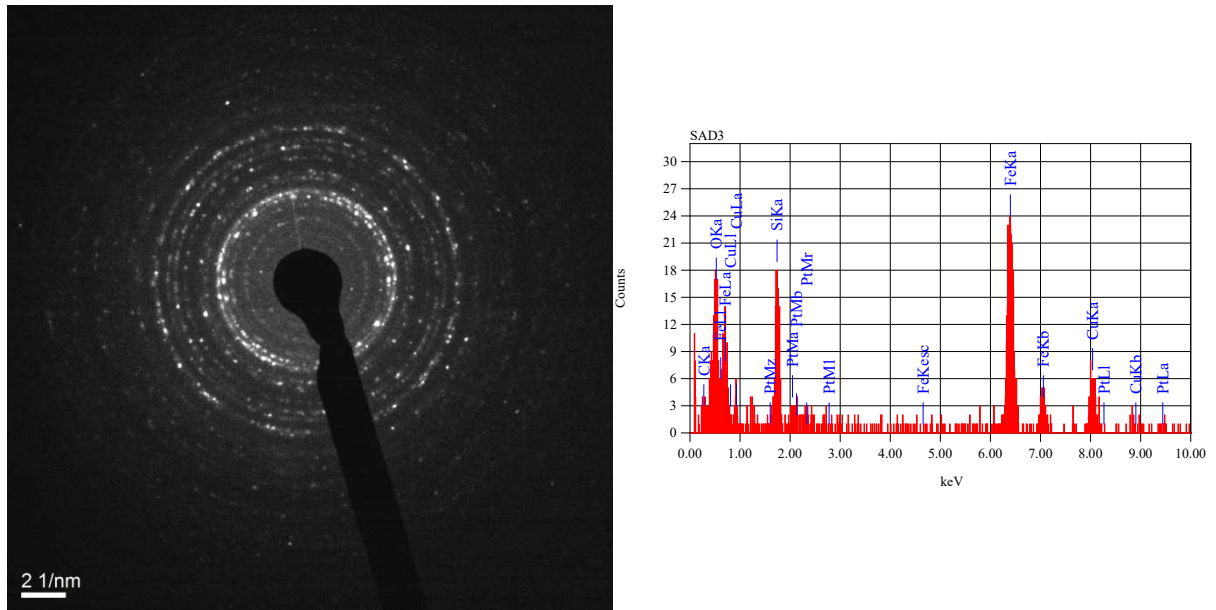


Figure 61 Pin, quaternary (Cu-graphite-ZrO<sub>2</sub>-Fe<sub>3</sub>O<sub>4</sub>) BM mixture tested at 400°C in air. a) Energy filtered SAED pattern; b) EDS spectrum for the same area. The pattern and spectrum confirm the presence of magnetite and hematite crystallographic phases.

### 5.8.3 Results summary for the quaternary ZrO<sub>2</sub>-Cu-graphite-Fe<sub>3</sub>O<sub>4</sub> system

The quaternary BM (ZrO<sub>2</sub>-Cu-graphite-Fe<sub>3</sub>O<sub>4</sub>) addition produced an average CoF value of 0.54 when tested at 23°C in air (see table 14). The CoF evolution curves for this condition featured an unstable behaviour. For tribotests performed at 400°C in air, this addition obtained the highest CoF value, 0.74, and the three tribotest repetitions were very unstable, resulting on high average CoF values (see Annex 6). Tribotests performed at 400° in N<sub>2</sub> produced an average CoF value of 0.53, that is very similar to the value obtained for the ternary BM (ZrO<sub>2</sub>-Cu-Fe<sub>3</sub>O<sub>4</sub>) addition tested in the same condition. For this condition, the CoF evolution curves were more a bit more stable than the same addition tested at 400°C in air, but still showed the presence of many cyclical peaks typical of a stick-slip mechanism.

The quaternary MM (ZrO<sub>2</sub>-Cu-graphite-Fe<sub>3</sub>O<sub>4</sub>) addition produced an average CoF value of 0.31 when tested at 23°C in air. This low CoF is comparable to the value (0.23) obtained for the binary MM (graphite- Fe<sub>3</sub>O<sub>4</sub>) and the ternary MM (Cu-graphite-Fe<sub>3</sub>O<sub>4</sub>). For tribotests performed at 400°C in air, this addition produced a CoF value of 0.56, that is comparable to the values obtained for the binary MM (Cu- Fe<sub>3</sub>O<sub>4</sub>)

additions. Lastly, tribotests performed at 400° in N<sub>2</sub> produced an average CoF value of 0.46, that is equal the value obtained for the ternary MM (Cu-graphite-Fe<sub>3</sub>O<sub>4</sub>) addition tested in the same condition.

Graphite's lubricant behaviour was minimized as the temperature increased, from 23°C to 400°C. Moreover, the use of N<sub>2</sub> atmosphere in tribotests performed at 400°C promoted a decrease in CoF, in comparison with tests carried out in air.

FIB cross-sections and TEM characterization showed BM prevented the selective transfer of graphite films to the tribosurface (see figures 53 to 61). Whereas MM was not able to prevent the formation of these graphite films, resulting on results comparable to the low values observed for the MM binary (graphite-Fe<sub>3</sub>O<sub>4</sub>) and the MM ternary (Cu-graphite-Fe<sub>3</sub>O<sub>4</sub>) additions (see figures 46 to 52).

In addition, the absence of significant copper patches within the transfer layer indicates the presence of ZrO<sub>2</sub> particles acted as micro or nano-scale grinding media within the transfer layer. And prevented the formation or larger metallic copper contacts in the tribosurface.

Lastly, the ZrO<sub>2</sub> particle size was observed in a diverse range of just under 5 to over 25 µm. Thus, the incorporation of ZrO<sub>2</sub> particles through high-energy ball milling features particle size control limitations.

Table 14 Results summary for the quaternary ZrO<sub>2</sub>-Cu-graphite-Fe<sub>3</sub>O<sub>4</sub> conditions

Result	MM ZrO <sub>2</sub> -Cu-graphite- Fe <sub>3</sub> O <sub>4</sub>		
	23°C in air	400° in air	400° in N <sub>2</sub>
Average CoF value	0.31	0.56	0.46
CoF evolution	Stable	Stable	Stable
Transfer layer thickness	1 to 2 μm*	0.5 to 3.5 μm*	0.5 to 3.5 μm*
Transfer layer homogenization	No	N.C.	N.A.
Transfer layer compaction	Compact, yet coarse-grained*	Compact and smooth*	Compact and smooth*
Probable magnetite-hematite transformation	No	Yes	No
Presence of Cu-patches/agglomerates	Yes nano-agglomerates	N.C.	N.A.
Presence of C-rich films	Yes	N.C.	Yes
Presence of Zr-rich particles	N.A.	N.C.	N.A.
Result	BM ZrO <sub>2</sub> -Cu-graphite- Fe <sub>3</sub> O <sub>4</sub>		
	23°C in air	400° in air	400° in N <sub>2</sub>
Average CoF value	0.54	0.74	0.53
CoF evolution			
Transfer layer thickness	1.5 to 5 μm**	2 to 3 μm*	~ 3.5 μm*
Transfer layer homogenization	N.A.	Yes, to the nanoscale	N.A.
Transfer layer compaction	Compact, yet coarse-grained**	Compact and smooth*	Compact and smooth*
Probable magnetite-hematite transformation	No	Yes	No
Presence of Cu-patches/agglomerates	No	No	No
Presence of C-rich films	No	No	No
Presence of Zr-rich particles	N.A.	N.A.	Yes

\* Result obtained with 1 cross-section. \*\* Result compiled from 3 cross-sections. N.C. = Not characterized by FIB. N.A. = Not available for this cross-section.

## 5.9 Results Summary

A total of 102 tribotests were performed in this study. An overview of the average values of the CoF results was presented in figure 14. Moreover, table 15 compiles the most important results herein observed. Regarding the average CoF results, the following behaviours were observed:

- The pure magnetite ( $\text{Fe}_3\text{O}_4$ ) tested at  $23^\circ\text{C}$  in air and  $400^\circ$  in air, produced average CoF values of 0.46 and 0.60 respectively.
- The binary MM ( $\text{Cu-Fe}_3\text{O}_4$ ) additions obtained average CoF values varying from 0.55 to 0.65 for tests performed at  $23^\circ\text{C}$  in air. At  $400^\circ$  in air, the average values observed were closer to the lower values at  $23^\circ\text{C}$ , and were approximately 0.56, whereas testes carried out at  $400^\circ\text{C}$  in  $\text{N}_2$  showed a decrease in the CoF, to approximately 0.50.
- The binary MM (graphite- $\text{Fe}_3\text{O}_4$ ) addition produced the lowest average CoF values for tests at  $23^\circ\text{C}$  in air, 0.23. Tribotests with the same addition at  $400^\circ\text{C}$  in air increased the CoF to 0.54.
- The ternary MM ( $\text{Cu-graphite-Fe}_3\text{O}_4$ ) addition tested at  $23^\circ\text{C}$  in air and at  $400^\circ\text{C}$  in air obtained CoF values of 0.23 and 0.55, respectively. These results are practically the same as those observed for the binary MM (graphite- $\text{Fe}_3\text{O}_4$ ) addition. Furthermore, testes performed at  $400^\circ$  in  $\text{N}_2$ , produced a CoF value of 0.46, which is lower than the value obtained for the binary MM ( $\text{Cu-Fe}_3\text{O}_4$ ) at the same condition.
- The ternary BM ( $\text{ZrO}_2\text{-Cu-Fe}_3\text{O}_4$ ) addition tested at  $23^\circ\text{C}$  in air produced an average CoF value of 0.62, while the same addition tested at  $400^\circ$  in  $\text{N}_2$  obtained a CoF value of 0.55.
- The ternary MM ( $\text{ZrO}_2\text{-Cu-Fe}_3\text{O}_4$ ) addition tested at  $23^\circ\text{C}$  in air produced an average CoF value of 0.66, while the same addition tested at  $400^\circ$  in  $\text{N}_2$  obtained a CoF value of 0.62. These values were slightly higher than those observed for the ternary BM ( $\text{ZrO}_2\text{-Cu-Fe}_3\text{O}_4$ ) addition tested in the same conditions.
- The quaternary BM ( $\text{ZrO}_2\text{-Cu-graphite-Fe}_3\text{O}_4$ ) addition produced an average CoF value of 0.54 when tested at  $23^\circ\text{C}$  in air. For tribotests

performed at 400°C in air, this addition obtained the highest CoF value, 0.74, amongst all other additions and conditions tested. Tribotests performed at 400° in N<sub>2</sub> produced an average CoF value of 0.53, that is very similar to the value obtained for the ternary BM (ZrO<sub>2</sub>-Cu-Fe<sub>3</sub>O<sub>4</sub>) addition tested in the same condition.

- The quaternary MM (ZrO<sub>2</sub>-Cu-graphite-Fe<sub>3</sub>O<sub>4</sub>) addition produced an average CoF value of 0.31 when tested at 23°C in air. This low CoF is comparable to the value (0.23) obtained for the binary MM (graphite-Fe<sub>3</sub>O<sub>4</sub>) and the ternary MM (Cu-graphite- Fe<sub>3</sub>O<sub>4</sub>). For tribotests performed at 400°C in air, this addition produced a CoF value of 0.56, that is comparable with the values obtained for obtained for the binary MM (Cu-Fe<sub>3</sub>O<sub>4</sub>) additions. Lastly, tribotests performed at 400°C in N<sub>2</sub> produced an average CoF value of 0.46, that is, a value equal the one obtained for the ternary MM (Cu-graphite-Fe<sub>3</sub>O<sub>4</sub>) addition tested in the same condition.

The nanoparticulate copper addition was observed in the form of micron-sized agglomerates in the MM mixtures and formed copper patches in the transfer layer. These copper patches promoted metallic contact on the tribosurfaces, and raised the CoF values for tests performed at 23°C. The presence of copper in the third body did not show greater compaction or outstanding smoothness of the oxide transfer layer for tests performed at 23°C. Instead, at 400°C copper acted as a soft copper. The increase in temperature was enough to promote recrystallization and change copper's behaviour within the transfer layer, lowering the CoF in comparison to tests performed at 23°C. Lastly, the instability in the CoF evolution curves and presence of peaks shows these metallic patches were responsible for the stick-slip mechanism in the dry sliding tests.

The addition of graphite to the third body mixtures was responsible for lowering the CoF values and stabilizing the curves. This behaviour was promoted by layers of graphite films, formed within the transfer layers of MM additions. The selective transfer of graphite dominated the transfer layer's response at 23°C for the MM additions because loose graphite was observed. Its lubricant aspect was compromised by the use of N<sub>2</sub> atmosphere, when tested at 400°C. Moreover, loose graphite will shear in the soft direction and produce low CoF. Whereas, when present in polymer pads,

graphite may show higher CoF values, due to the prevention of shear. Hinrichs et al. (2018) <sup>[91]</sup> showed the mechanism of fast amorphization of graphite during braking, and how tribotesting at full scale bench dynamometer for just one hour, is more effective on generating disorder generated in graphite's crystalline structure, than the amount of amorphization observed after 8h of high energy ball milling.

Adding ZrO<sub>2</sub> particles to the mixtures attenuated the development of copper patches amid the transfer layer. They have most likely acted as a grinding media, promoting greater homogenization of the tribolayer. Furthermore, the presence of these abrasive particles in the low volume percentages herein studied, did not promote a significant rise in the CoF values in comparison to additions without ZrO<sub>2</sub>.

The presence of abrasive particle (ZrO<sub>2</sub>) helped on producing a smooth compact layer, probably by comminution of the addition, where the ZrO<sub>2</sub> particles acted as the grinding media. Moreover, these systems also did not feature copper patches, observed in the tribosurface of previous studies with copper containing manually mixed interfacial media additions <sup>[61, 62, 92]</sup>. TEM characterization (figures 47 and 48), however, they showed the presence of selective transfer of graphite films, which created layers of graphite within the oxide tribolayer. This explains why quaternary MM mixtures produced lower CoF values for each temperature and atmosphere tested, when compared to the BM mixture, and suggests that the degradation of graphite took place only partially, and that this was enough to rise significantly the CoF of BM quaternary mixtures at 400°C in air, in comparison with N<sub>2</sub>. Furthermore, the lubricant role of these graphite patches within the quaternary MM transfer layers was likely minimized under N<sub>2</sub> atmosphere. Graphite is long known to lose its lubricant role in the absence of humidity and under vacuum <sup>[38]</sup>, and as cited before, a rise of CoF is expected as ball milling and tribotesting generate disorder in the graphite's crystalline structure<sup>[91]</sup>.

Varying the temperature affected the additions as follow:

1. It has most probably promoted magnetite-hematite transformation for tests performed at 400°C in air, and a subsequently rise in the CoF value in comparison with conditions tested at 400°C in N<sub>2</sub>.
2. The increase in temperature upheld and favoured the third body sintering. The compaction and smoothness of the oxide transfer layer

was visibly greater at 400°C, in comparison with tests carried out at 23°C.

3. Copper acted as soft copper when tested at 400°C, confirming its lubricant behaviour in higher temperature for greater contents of copper (15% Cu-Fe<sub>3</sub>O<sub>4</sub>).
4. Graphite's lubricating behaviour was minimized at 400°C. The oxidation of graphite and decrease of humidity played a major role in neutralizing graphite's lubricity.

The use of an inert N<sub>2</sub> atmosphere assisted the isolation of the temperature effect without the presence of oxidation, ruling out the hematite contribution to the CoF, allowing the identification of soft copper's behaviour for the 15% Cu-Fe<sub>3</sub>O<sub>4</sub> condition.

The mixing method played a dominant role in promoting homogenization of the third body within the transfer layer. Ball-milling was able to prevent graphite's selective transfer and therefore inhibit the formation of graphite films on the tribosurface. Moreover, BM and the incorporation of abrasive ZrO<sub>2</sub> particles were able to prevent copper patches adhesion to the tribolayer.

TEM characterization of the BM quaternary mixture tested at 400°C in air (figures 59 and 60) showed the presence of nanocrystalline copper and some graphite nestled and well mixed with other particles in the nanoscale. Most likely as a result of the formation of Cu-ZrO<sub>2</sub> clusters described in Menapace et al.<sup>[15]</sup>. This clustering behaviour is likely to have favoured a greater homogenization of the nanoparticulate copper, thus preventing the formation of copper patches observed in previous studies [61, 62].

Table 15 Results Summary

	Mixture (Systems)	Comp. (vol.%)	Mix. Meth.	Temp.	Atm.	Aver. CoF	Stand. Dev.	CoF evol. curve	Transfer layer thick. ( $\mu\text{m}$ )	Transfer layer homogen.	Transfer layer compaction	Fe <sub>3</sub> O <sub>4</sub> -Fe <sub>2</sub> O <sub>3</sub> transf.	Cu-patches	Carbon-rich film
<b>Pure Magnetite</b>	(Fe <sub>3</sub> O <sub>4</sub> )	100% Fe <sub>3</sub> O <sub>4</sub>	none	23°C	Air	0.46	0.12	Stable	~ 4	D.A.	Coarse-grained	No	D.A.	D.A.
			none	400°C	Air	0.60	0.06	Stable	0.5 to 5	D.A.	Smooth	Yes	D.A.	D.A.
<b>Binary</b>	(Cu-Fe <sub>3</sub> O <sub>4</sub> )	94% Fe <sub>3</sub> O <sub>4</sub> + 6% Cu	MM	23°C	Air	0.55	0.15	Peaks present	1 to 10	No	Coarse-grained	No	Yes	D.A.
			MM	400°C	Air	0.57	0.06	Peaks present	1 to 2	No	Smooth	Yes	Yes	D.A.
			MM	400°C	N <sub>2</sub>	0.50	0.11	Peaks present	2 to 7.5	No	Smooth	No	Yes	D.A.
	(graphite-Fe <sub>3</sub> O <sub>4</sub> )	85% Fe <sub>3</sub> O <sub>4</sub> + 15% Cu	MM	23°C	Air	0.65	0.13	Peaks present	1 to 10	No	Coarse-grained	No	Yes	D.A.
			MM	400°C	Air	0.56	0.06	Peaks present	1 to 2	No	Smooth	Yes	Yes	D.A.
			MM	400°C	N <sub>2</sub>	0.51	0.06	Peaks present	2 to 7.5	No	Smooth	No	Yes	D.A.
	(graphite-Fe <sub>3</sub> O <sub>4</sub> )	85% Fe <sub>3</sub> O <sub>4</sub> + 15% C	MM	23°C	Air	0.23	0.05	Stable	1.5 to 3	No	Coarse-grained	No	D.A.	Yes, continuous
			MM	400°C	Air	0.54	0.10	Peaks present	N.C.	N.C.	N.C.	Yes	D.A.	N.C.
MM			400°C	N <sub>2</sub>	0.46	0.06	Stable	~ 5	No	Mostly smooth	No	D.A.	Yes	
<b>Ternary</b>	(Cu-graphite-Fe <sub>3</sub> O <sub>4</sub> )	85% Fe <sub>3</sub> O <sub>4</sub> + 7.5% C + 7.5%Cu	MM	23°C	Air	0.23	0.09	Peaks present	0.5 to 1	No	Coarse-grained	No	Yes	Yes
			MM	400°C	Air	0.55	0.09	Few peaks	1 to 3	N.A.	Coarse-grained	Yes	N.C.	N.C.
			MM	400°C	N <sub>2</sub>	0.46	0.07	Stable	0.5 to 1	No	Smooth	No	Yes	Yes
	(ZrO <sub>2</sub> -Cu-Fe <sub>3</sub> O <sub>4</sub> )	89% Fe <sub>3</sub> O <sub>4</sub> + 10%Cu + ZrO <sub>2</sub>	BM	23°C	Air	0.62	0.12	Unstable	1 to 3	N.A.	Coarse-grained	No	N.A.	D.A.
BM			400°C	N <sub>2</sub>	0.55	0.07	Unstable	5 to 10	N.A.	Smooth	No	N.A.	D.A.	
<b>Quaternary</b>	(ZrO <sub>2</sub> -Cu-graphite-Fe <sub>3</sub> O <sub>4</sub> )	88% Fe <sub>3</sub> O <sub>4</sub> + 6%Cu + 6% C+ ZrO <sub>2</sub>	BM	23°C	Air	0.54	0.11	Unstable	1.5 to 5	N.A.	Coarse-grained	No	No	No
			BM	400°C	Air	0.74	0.18	Few peaks	2 to 3	Yes, to the nanoscale	Smooth	Yes	No	No
			BM	400°C	N <sub>2</sub>	0.53	0.06	Stable	~3.5	N.A.	Smooth	No	No	No
		MM	23°C	Air	0.31	0.06	Stable	1 to 2	No	Coarse-grained	No	Yes, nano-agglomerates	Yes	
		MM	400°C	Air	0.56	0.11	Stable	0.5 to 3.5	N.C.	Smooth	Yes	N.C.	N.A.	
		84% Fe <sub>3</sub> O <sub>4</sub> + 7.5% C + 7.5%Cu + 1%ZrO <sub>2</sub>	MM	400°C	N <sub>2</sub>	0.46	0.10	Stable	0.5 to 3.5	N.A.	Smooth	No	N.C.	Yes

D.A. = Does not apply. N.C. = Not characterized. N.A.= Not available

## 6 DISCUSSION

From the results summary, previously presented, the effects of the studied additions and the effects of these parameters will be presented individually. Moreover, the following comparisons are drawn from the results:

- Only MM mixtures containing graphite (graphite-Fe<sub>3</sub>O<sub>4</sub>, Cu-graphite-Fe<sub>3</sub>O<sub>4</sub> and ZrO<sub>2</sub>-Cu-graphite-Fe<sub>3</sub>O<sub>4</sub>), tested at 23°C, presented CoF values ranging from 0.23 to 0.31, therefore lower than pure magnetite at 23°C.
- Binary (Cu-Fe<sub>3</sub>O<sub>4</sub>) and ternary (ZrO<sub>2</sub>-Cu-Fe<sub>3</sub>O<sub>4</sub>) additions raised the CoF values in comparison to pure magnetite and graphite containing mixtures at 23°C.
- Binary (Cu-Fe<sub>3</sub>O<sub>4</sub>) and ternary (ZrO<sub>2</sub>-Cu-Fe<sub>3</sub>O<sub>4</sub>) additions, tested at 400°C, lowered slightly the CoF values obtained for pure magnetite. These systems showed lower CoF in tests performed at 400°C in N<sub>2</sub>.
- Ternary (ZrO<sub>2</sub>-Cu-Fe<sub>3</sub>O<sub>4</sub>) additions presented similar results for BM and MM mixtures.
- Quaternary (ZrO<sub>2</sub>-Cu-Fe<sub>3</sub>O<sub>4</sub>) mixtures differed significantly in function of the mixing method utilized. MM quaternary mixtures behaved similarly to the ternary (Cu-graphite-Fe<sub>3</sub>O<sub>4</sub>) mixtures, whereas the BM quaternary mixtures produced CoF results comparable to the binary (Cu-Fe<sub>3</sub>O<sub>4</sub>) and the ternary (ZrO<sub>2</sub>-Cu-Fe<sub>3</sub>O<sub>4</sub>) additions, thus, suggesting BM quaternary mixtures minimized the effect of graphite within the transfer layer.

The summary of the average values of the CoF shows that only the binary and ternary mixtures with graphite were able to produce CoF values lower than pure magnetite at room temperature. In this sense, Lee and Filip <sup>[13]</sup> showed that the good development of multiple friction layers lowered values of the friction level and wear of the material. Moreover, Fe<sub>3</sub>O<sub>4</sub> has already been reported as an important wear debris originated at the brake disc and adjusting conditions to produce a nano-structured

tribofilm containing about 10% of soft nanoinclusions, homogeneously distributed in the brittle  $\text{Fe}_3\text{O}_4$  matrix is considered influential on providing smooth sliding conditions [70, 93]. Therefore, the ability to create a homogeneous mixture in the magnetite can be used in the effort towards understanding the brake materials' third body behaviour.

### **6.1 Parameters acting in the transfer layer and friction coefficient**

This study was able to assess the effects of the parameters herein varied to the transfer layer formation, and the average CoF values. These studied parameters are as follows:

1. Varying the temperature
2. Varying the tribotest atmosphere
3. Adding graphite to the magnetite-based mixture
4. Adding copper to the magnetite-based mixture
5. The incorporation of  $\text{ZrO}_2$  particles to the magnetite-based mixture by manually mixing with a pestle and mortar.
6. The incorporation of  $\text{ZrO}_2$  particles to the magnetite-based mixture by high-energy ball milling.

### 6.1.1 Effect of temperature

As a general rule, tests performed at 400°C, produced smoother transfer layers when compared to the transfer layers observed for tests carried out at 23°C (see table 15). Individually, FIB cross-sections showed some smooth compact regions of the oxide transfer layers in conditions tested at 23°C (see figures 23, 24, 43 and 52). Yet, the overall observed aspect at 23°C was significantly coarse-grained, with some degree of tribo-sintering, but lacked compaction in comparison with conditions tested at 400°C. For tribotests performed at 400°C, thermo-induced sintering was responsible for producing compact smooth oxide transfer layers.

Regarding CoF values, the increase in temperature produced the opposite effect on copper and graphite. The copper containing mixtures without graphite, Cu-Fe<sub>3</sub>O<sub>4</sub> and Cu-ZrO<sub>2</sub>-Fe<sub>3</sub>O<sub>4</sub>, showed a decrease of CoF in tests performed at 400°C, in comparison with testes performed at 23°C. Whereas graphite containing mixtures, showed an increase in the CoF values at 400°C.

Furthermore, the increase of temperature facilitated ploughing of the first bodies' tribosurfaces, as observed in figures 29, 34 and 44. Since the oxide transfer layer is predominantly composed of the interfacial media addition, with some sparse metallic debris in it, but not representative, this effect shall not be discussed in this study.

The specific mechanisms acting on graphite and copper will be individually discussed further in this section. Lastly, both temperatures studied in this work are part of the service conditions spectra during the life of brake pads. <sup>[62]</sup>

### 6.1.2 Effect of atmosphere

Varying the atmosphere, allowed to isolate the magnetite-hematite transformation. As already mentioned, the presence of a  $\text{Fe}_3\text{O}_4$  matrix based friction film has been characterized within brake friction materials tribosurfaces and was reported as responsible for stabilizing the CoF and produce smooth dry sliding behaviour [16, 26, 82, 94]. In this sense, performing the tribotests at 400°C in air, introduced another composition variable to this study, as magnetite oxidized producing hematite.

Magnetite is not the only stable form of iron oxide at 400°C. If more oxygen is supplied to the system, in this case from atmospheric air, the oxidation of magnetite to hematite occurs at 400°C in air [95].

Supplementary to the indication of magnetite transformation to hematite visible in Figure 16, the CoF values obtained for pure  $\text{Fe}_3\text{O}_4$  at 400°C in air are in accordance with the results obtained by Kato (2003). He supplied  $\text{Fe}_3\text{O}_2$  particles in 4 different granulometries to pin-on-disc tribotests with a machined track. The CoF evolution curve observed in their study for nanoparticulate  $\text{Fe}_3\text{O}_2$  converged to approximately 0.6, the value same obtained in this study with the supply of magnetite particles at 400°C in air.

The rise in temperature under atmospheric air has also been shown to produce similar CoF increase for pin-on-disc tribotests of a brake material. Transfer layer characterization by means of EDS on the low-steel friction material pin showed that the iron oxide present for lower temperatures decreased with the rise of temperature, thus producing excessive wear of the grey cast iron disc at 350°C. The presence of more abrasive particles was considered responsible for this overall behaviour [96].

### 6.1.3 Effect of copper addition

Binary Cu-Fe<sub>3</sub>O<sub>4</sub> mixtures showed as general rule CoF higher than pure Fe<sub>3</sub>O<sub>4</sub> at 23°C and lower CoF values at 400°C . These results confirm the predictions of the model presented by Dmitriev et al. (2016) [60], in which copper would act as a soft constituent during the formation of a tribofilm. The third body addition considered in this model is similar to the Cu-Fe<sub>3</sub>O<sub>4</sub> mixtures investigated in this study. Their movable cellular automata (MCA) model used the mechanical properties of “soft” as entry parameters and they predicted that Cu addition would act as a solid lubricant (CoF values between 0.38 and 0.50) [60]. In addition, they consider the stress-strain response input, that of the homogenously distributed nanoparticulate copper at 500°C.

The experimental confirmation of copper acting as soft copper or as a solid lubricant at “high” temperatures corroborates the complex role copper assumes in the transfer layer formation and CoF response. For tests performed at 23°C, the CoF average values showed an increase, in relation to pure Fe<sub>3</sub>O<sub>4</sub>. Additionally, the presence of copper patches was observed in the cross-section characterization (see figures 23, 24 and 27), similar to those presented in previous works from this author [61, 62]. Rodrigues et al. [61, 62] had already interpreted the formation of copper patches as a possible reason for an increase of the CoF in comparison to the pure magnetite. These copper patches are schematically presented in figure 61.

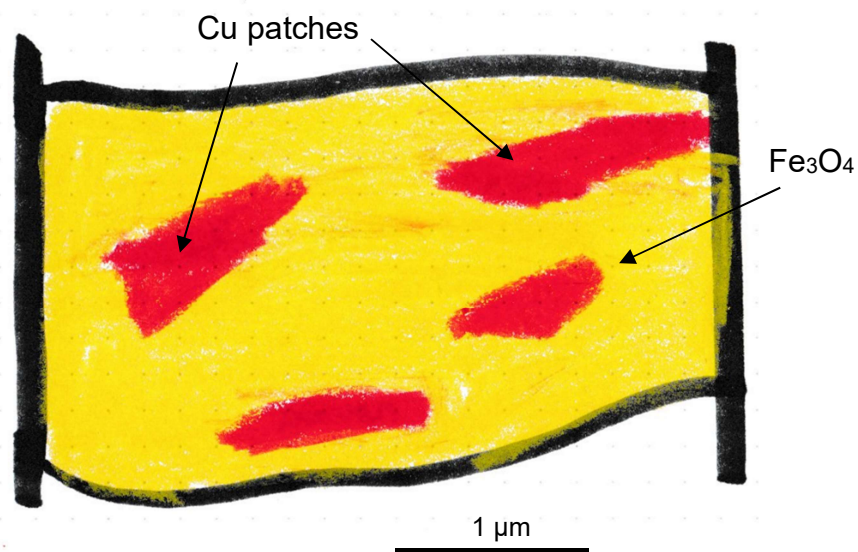


Figure 62 Schematic illustration of the oxide transfer layer with copper patches presence typically observed in Cu containing systems tested at 23°C.

Moreover, Aranganathan and Bijwe (2016) <sup>[11]</sup> have also confirmed that Cu inclusions are responsible for higher CoF in brake friction materials in comparison to Cu-free samples. In this sense, Su et al. (2015) <sup>[97]</sup> showed that exogenous copper increases the contact area. For low speeds (similar to the speed used in the present investigation), the copper third body lead to an increase in the values of the CoF, due to heavy adhesion and shearing. They also showed that higher speeds or increased pressure promoted a decrease in the values of the CoF lowers, due better fluidity, adhesive and ductility of the third body <sup>[97]</sup>.

Kumar and Bijwe (2013) used a full scale brake inertia dynamometer to investigate composite formulations of non-asbestos friction materials. They observed friction materials with copper and brass transferred a thin (most probably) metallic film to the tribosurfaces <sup>[77]</sup>.

Kumar and Bijwe affirmed that their observations showed consistency with those obtained by Jia and Ling (2004) which demonstrated that the formation of Cu films on the worn tribosurface may improve the contact state and present a more stable CoF with lower wear of the counter parts <sup>[98]</sup>. The promotion of a stable CoF is not contradictory to this study. Jia and Ling (2004) used a block on ring tribometer at a velocity of 1.05 m/s and an applied normal load of 294 N. These two parameters are, each, one order of magnitude order higher than those used in the pin-on-disc tribotests herein performed. At such higher velocity and normal load, the transfer layer obtained by them would most likely approximate to those obtained for tests performed at 400°C. As a matter of fact, these temperature spectra is relevant for brake materials investigation, for the pad contacts may reach up to 600°C. In addition, solid lubricants that should withstand these flash temperatures are the responsible for smooth and noiseless operation <sup>[16]</sup>.

Compiling the experimental results from this work, with the aforementioned copper film behaviour, the presence of copper patches may be considered responsible for both the increase of CoF values at 23°C and the decrease of the CoF at 400°C.

At 23°C, these copper films and agglomerates act as hard inclusions and patch structures similar to the primary *plateaus* described by Eriksson <sup>[10]</sup>. These patches rise the possible metal-metal contact, resulting on unstable CoF evolution curves, with the presence of peaks. Stick-slip mechanism takes a predominant role on the friction

coefficient behaviour and the average CoF values obtained are higher than those for the pure magnetite. Thus, not in resemblance with a solid's lubricant behaviour.

Whereas at 400°C, the behaviour of the same copper patches changes the described “soft” copper. Cu has a melting point of approximately 1060°C, and Gottstein et al. (1979) showed dynamic recrystallization of copper may take place at 530°C. Österle et al. (2012) presented, by means of TEM characterization, recrystallized copper nanoparticles (100 nm) were incorporated to the brake constituents transfer layers.

The characterization of the transfer layer of the binary Cu-Fe<sub>3</sub>O<sub>4</sub> system tested at 400°C attests a better distribution of copper in the micron-scale, within the transfer layer. TEM characterization was able to show that these copper agglomerates were still present for the copper containing systems at 400°C (see figures 30 and 31). Thus, the increase in temperature promoted the recrystallization of copper, a probable shearing effect in the patches and produced soft copper films within the oxide transfer layer. Figure 62 displays schematically how these copper films within the transfer layer for conditions tested at 400°C.

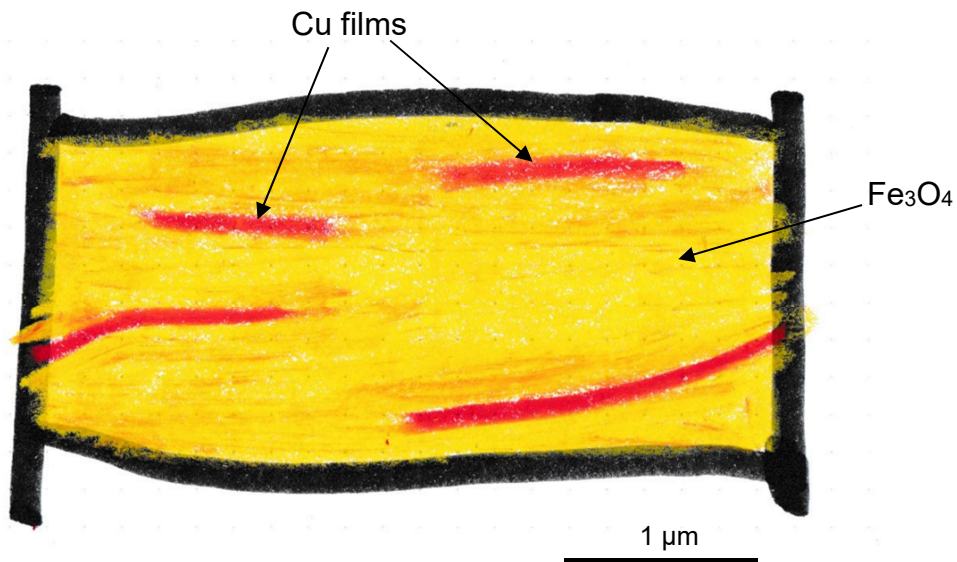


Figure 63 Schematic illustration of the oxide transfer layer with copper film presence typically observed in Cu containing systems tested at 400°C.

The microstructural characterization results of the transfer layer of the copper-magnetite system support understanding the different behaviour of the CoF at room temperature and at 400°C.

#### 6.1.4 Effect of graphite addition

In this study, all graphite MM containing mixtures tested at 23°C produced low CoF values (0.23 and 0.31), below those obtained for the pure Fe<sub>3</sub>O<sub>4</sub> tested at this temperature. These findings are in accordance with experimental and modelling results obtained by Österle et al. (2014) for similar testing methodology [83].

The characterization of the oxide transfer layers showed the presence of graphite films within the oxide third body. At 23°C, graphite's lubricant behaviour is endorsed by the presence of these films, explaining why CoF values and curves are low and stable for these systems. Figure 64 represents a schematic image to illustrate a transfer layer with graphite films, similar to those observed in this study.

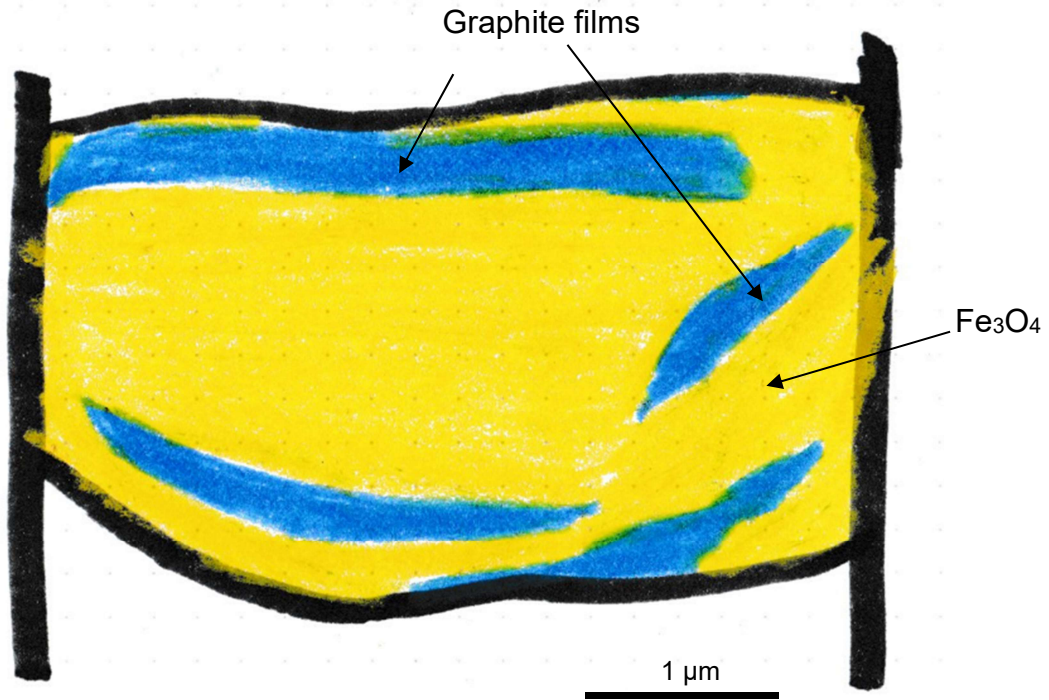


Figure 64 Schematic illustration of the oxide transfer layer with graphite film presence typically observed in graphite containing systems tested at 23°C.

Moreover, ternary MM Cu-graphite-Fe<sub>3</sub>O<sub>4</sub> mixture presented the same behaviour as binary graphite- Fe<sub>3</sub>O<sub>4</sub> mixture. The selective transfer of graphite films to this system's first bodies was imposed the prevailing of graphite effect as a solid lubricant over the previously measured effect of Cu additions at 23°C. In addition, the observation that aforementioned ternary mixture produced the same average CoF

values as the binary graphite-Fe<sub>3</sub>O<sub>4</sub> mixture at 400°C in air and in N<sub>2</sub>, and very similar results to those obtained for MM binary Cu- Fe<sub>3</sub>O<sub>4</sub> mixtures at the same temperature. The aforementioned effects make it overall hard to elect a predominant responsible for the mixtures tested at 400°C, and it also draws the attention to the fact that at these temperatures, copper and graphite produce very similar results regarding friction coefficient.

Graphite's loss of lubricity at higher temperatures was shown by Cho et al. [37] to induce rough friction at the tribosurface with temperature rise. At 700°C, the lubricant effect of graphite was reported to lose its efficiency rapidly, once oxidation took place and decomposed it into gases [37]. The oxidation of graphite was also observed by Sliney [89], in coatings and self-lubricating composite bearings. The oxidation took place at 400°C, leading to the conclusion that graphite may be serviceable up to 400°C, but past this temperature only for very short application times. Though the high temperature tribotests in this study have a nominal temperature of 400°C, this temperature reflects only on a bulk measurement of the disc surface. As a result, the flash temperature at the contact may reach much higher values.

These results indicate copper's lubricant role at high temperature is only comparable to a layer lattice lubricant such as graphite, for the condition in which graphite's lubrication properties are decreased. Once graphite loses its slid lubricant role, the "soft" copper behaviour at 400°C was not able to compensate it, thus producing higher CoF values than those observed at 23°C, but in accordance with both copper and graphite behaviours at 400°C.

Graphite has been proposed in literature as a solution for producing copper-free brake pads. Aranganathan and Bijwe (2016) varied amounts of thermo-graphite on tribological properties of a braking friction material. Thermo-graphite consists of graphite with higher thermal conductivity. They observed the ideal addition amount of thermo-graphite was around 10% [12]. In another study, Aranganathan and Bijwe compared the properties of natural and thermo graphites for braking application. They confirmed the overall properties (thermal conductivity and fade performance improvement allied with a tendency to reduce wear) of the thermo-graphite are more suitable in the quest towards copper's suppression from brake pads [39].

The results obtained in this work for tests performed at 400°C indicate experimentally that graphite and soft copper behave similarly in terms of CoF, as

investigated by Österle et al. [60] with MCA modelling. They suggested graphite and copper would act very similarly at the transfer layer and produce similar effects on the third body transfer layer.

On the other hand, characterization of the brake pads debris generated by full scale inertial bench dynamometer indicated iron from the brake disc and that graphite may form cementite, which was observed to induce erratic CoF behaviour and avoid smooth braking from occurring [94]. Thus, suggesting the replacement of copper by graphite may not be so trivial.

Lastly, these results show the presence of graphite films on the transfer layer play prevail over other additions when it comes to CoF behaviour. At 400°C the lubricant effect of graphite is affected and its effects on the CoF become very similar to those of copper.

### 6.1.5 Effect of ZrO<sub>2</sub> particles

The addition of such small percentages of ZrO<sub>2</sub> particles (1 to 4% in vol) in this study was enough to differ significantly on the homogenization of the oxide transfer layer. The addition of ZrO<sub>2</sub> nanoparticles in MM mixtures promoted better homogenization and contributed with the formation of smoother compact oxide layers, in comparison to interfacial additions from previous studies [88, 92],

ZrO<sub>2</sub> particles contributed to the homogenization of the transfer layer to the nanoscale, by preventing the selective transfer of copper patches to the first bodies from occurring, as previously described in this section.

A visual scheme of the different effects of adding ZrO<sub>2</sub> to the third body addition is presented in figures 64. ZrO<sub>2</sub> nanoparticles manually mixed in the third body acted similarly to a nano-grinding media within the transfer layer, helping to break copper micron-sized agglomerates. Figure 65 shows the transfer layer produced with a quaternary MM mixture, graphite films are present amid the transfer layer, whereas copper patches described previously are not visible, as observed in the TEM results for this condition (see figures 48 and 49).

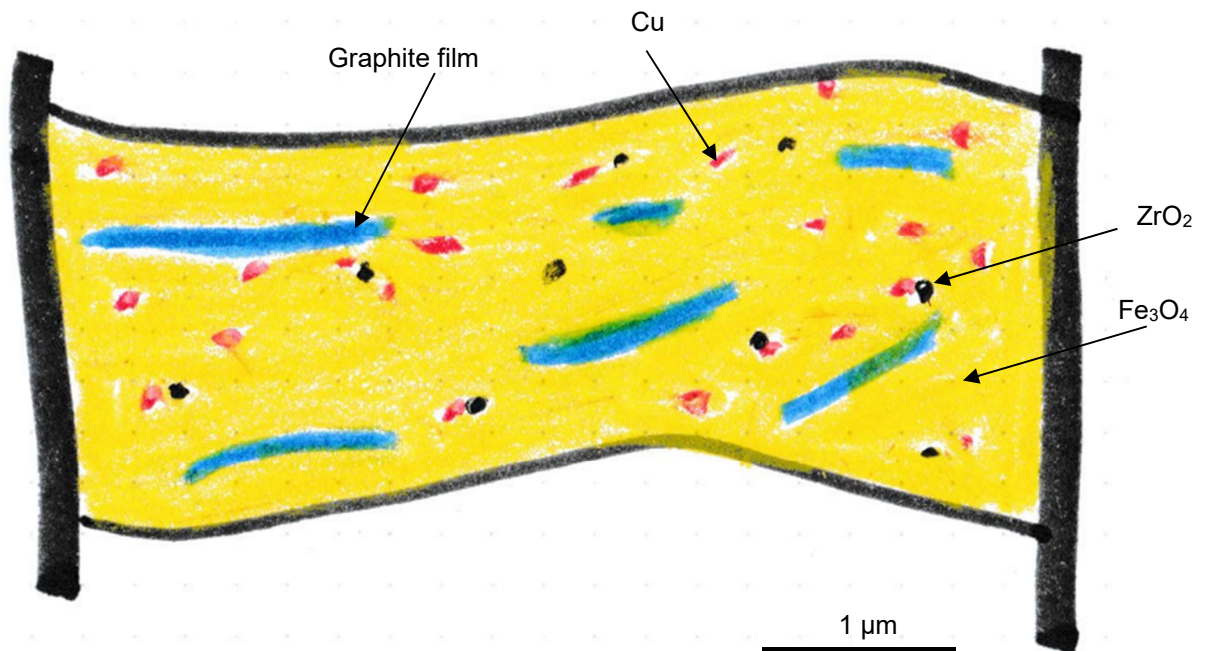


Figure 65 Schematic illustration of the oxide transfer layer of the MM quaternary system, with graphite film presence, nano-sized copper agglomerates and ZrO<sub>2</sub> particles.

### 6.1.6 Effect of high-energy ball milling

Both quaternary BM conditions, tested at 23°C in air and 400°C in N<sub>2</sub> ( figures 42 and 43) showed the presence of compact smooth oxide layers adhered to the first body's surface. This differs from the general observations of transfer layers formed at 23°C for the other mixtures. In addition, the incorporation of ZrO<sub>2</sub> particles by means of high-energy ball milling, was also able to prevent the selective transfer of graphite continuous films to the tribosurfaces. Figure 66 displays a scheme of the BM quaternary mixture, the characterization in this work showed the selective transfer from both copper patches and graphite continuous films were not observed for this system. In this sense, Hinrichs et al. (2018), showed that BM and full scale dynamometer tribotests are responsible for the amorphization of graphite <sup>[91]</sup>. The amorphization of graphite in this study is the most likely reason for the loss of lubricity for all graphite containing BM conditions, especially those tested at 23°C, in comparison to the MM conditions.

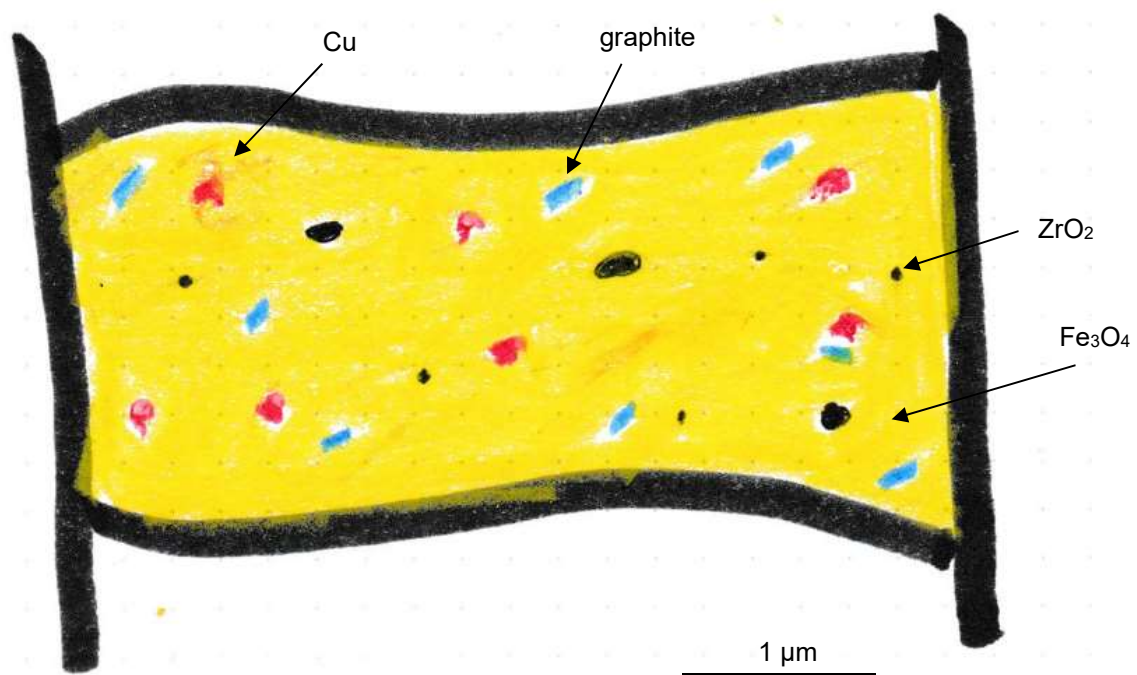


Figure 66 Schematic illustration of the oxide transfer layer of the BM quaternary system, with nano-seized graphite and copper, alongside with ZrO<sub>2</sub> particles from the ball mill grinding media.

High-energy ball milling has already been shown to produce better modelling of a real brake tribofilm formation, while manually mixed additions simulate early stage

brake debris formation [83]. The presence of abrasive particles in brake friction materials was proved to decrease squealing noise [47, 48] and constitutes part of real commercial brake pads. The present study shows very similar interfacial media additions produce dissimilar tribological behaviour according to the degree of homogenization in the nanoscale. These results indicate that high-energy ball milling may, as suggested by Menapace et al. [15] may be used as an ally to control and enhance the friction materials properties, and therefore produce copper free brake pads. Moreover, the additions showed significant differences at 400°C and room temperature, but kept the aforementioned mixing properties.

The incorporation of ZrO<sub>2</sub> particles through the use of zirconia balls in the high-energy BM, produced a wide range of particle size (see Figure 39). Modelling results from Österle and Dmitriev (2012) had already demonstrated that the addition of hard inclusions to the third body should present a smaller size than the actual transfer layer thickness, otherwise, the hard inclusions may “rip off” the friction transfer layer [75]. Finally, to exert better control over the ZrO<sub>2</sub> particle size and mixture composition, an option would be to add ZrO<sub>2</sub> to the mixture before milling, and change the grinding media material. The option to add ZrO<sub>2</sub> and mill it with ZrO<sub>2</sub> balls may also be a choice for different milling times. Characterizing the BM mixture sampled with different milling times should help to shed a light on this matter.

### 6.1.7 Final considerations

As the deadline for producing copper-free brake pads in the USA is approached and the awareness to copper airborne emissions risks is risen worldwide, industrial and academic research seems to consolidate the paths to achieve it. The growth of copper-free brake pad patents' applications worldwide,<sup>[52–54, 99]</sup> indicates this issue is of particular industrial interest.

Some of the solutions to copper's suppression in brake pads consider graphite<sup>[11, 39, 40]</sup> as a possible replacement. Another study proposes stainless steel swarfs as a replacement option.<sup>[100]</sup> Yet, the list of solutions and studies extends greatly as they align with the interests of a particular group or country. And counter-intuitive solutions are proposed, such as replacing copper by rare earth  $\text{La}_2\text{O}_3$  in polymeric matrix<sup>[101]</sup>.

How copper acts on the transfer layer, and the synergic effects of copper and the other additions herein studied, contribute to a better definition of copper's complex properties that a replacement should mimic.

The comprehensive characterization with FIB and TEM, combined with EDS micro analysis showed the same copper agglomerates that are responsible for increasing the CoF at 23°C are also responsible for producing soft films within the oxide transfer layer, at 400°C, and decrease the CoF results. Thus, contributing for smooth sliding behaviour.

## 7 CONCLUSIONS

The present study sought to investigate the role of the interfacial media addition (nanoparticulate copper, graphite and zirconia amid a magnetite based-matrix) on the transfer layer generated in pin-on-disc tribotests at 23°C and 400°C, and under air and N<sub>2</sub> atmosphere. Combining the CoF results with the characterization results, the following conclusions are drawn:

i. Patches of metallic copper were observed on the transfer layer of the MM Cu-Fe<sub>3</sub>O<sub>4</sub>, Cu-graphite-Fe<sub>3</sub>O<sub>4</sub> systems. At 23°C, these patches were responsible for rising the CoF values, whereas at 400°C, these patches went through recrystallization, and produced soft copper films. Thus, confirming Cu lubricant feature at 400°C.

ii. Selective transfer of graphite-films to the first bodies tribosurfaces for MM graphite containing systems, promoted the lowest CoF values observed in the systems herein studied (0.23 and 0.31). At 400°C, the lubricity of graphite was minimized and the behaviour became similar to the MM copper additions tested 400°C. Therefore, suggesting the existence of similarities between the behaviours of soft copper and graphite with minimized lubricity.

iii. Selective transfer of copper patches may be prevented by adding an abrasive particle (ZrO<sub>2</sub>) to the third body, which destroys the lubricating films, promoting the formation of a homogeneous mixture of the solid lubricant particles in the magnetite film.

iv. The mixing method of friction materials interfered significantly on the transfer layer nature and consequently on the CoF behaviour. From this, the authors draw the following conclusions:

v. The presence of abrasive particle (ZrO<sub>2</sub>) helped on producing a smooth compact layer within the quaternary MM mixture, probably by comminution of the third body within the tribolayer.

vi. Selective transfer of graphite films were only prevented by the incorporation of ZrO<sub>2</sub> particles by means of high-energy ball milling. Adding ZrO<sub>2</sub> nanoparticles manually was not able to prevent the formation of these graphite films within the transfer layer.

## 8 FUTURE WORK SUGGESTIONS

- Investigate the formation of carbon-rich film for graphite additions with different particle size, graphene addition, coke addition and other types of graphite.
- Study the effect of the  $ZrO_2$  particle size on the transfer layer homogenization.
- Vary the amount of  $ZrO_2$  particle in volume to find an optimal value of transfer layer homogenization and CoF behaviour.
- Perform tribotests with first bodies more similar real braking friction materials by producing pins (for the tribotests) by incorporating the investigated additions to commercial brake pad matrix formulations. In addition, performing the tribotests with grey cast iron discs.
- Ask for brake pad formulations from the Brazilian industry, and therefore adapt the efforts of the investigation to the national reality.

## 9 REFERENCES

1. GORZ, A. **Lettre à D.** Paris: Galilée, 2006.
2. JOST, H. P. Tribology — Origin and future. **Wear**, v. 136, n. 1, p. 1–17, fev. 1990.
3. DOWSON, D. **History of Tribology.** 1st. ed. [s.l.] Longman, 1979.
4. JACKO, M. G.; TSANG, P. H. S.; RHEE, S. K. Automotive friction materials evolution during the past decade. **Wear**, v. 100, n. 1–3, p. 503–515, 1984.
5. BLAU, P. J. **Compositions , Functions , and Testing of Friction Brake Materials and Their Additives.** [s.l: s.n.].
6. KUKUTSCHOVÁ, J. et al. On airborne nano/micro-sized wear particles released from low-metallic automotive brakes. **Environmental Pollution**, v. 159, n. 4, p. 998–1006, 2011.
7. WAHLSTRÖM, J. **A study of airborne wear particles from automotive disc brakes.** [s.l: s.n.].
8. DENIER VAN DER GON, H. A. C. et al. A revised estimate of copper emissions from road transport in UNECE-Europe and its impact on predicted copper concentrations. **Atmospheric Environment**, v. 41, n. 38, p. 8697–8710, 2007.
9. ÖSTERLE, W. et al. Chemical and microstructural changes induced by friction and wear of brakes. **Wear**, v. 251, p. 1469–1476, 2001.
10. ERIKSSON, M. **Friction and Contact Phenomena of Disc Brakes Related to Squeal.** [s.l.] Uppsala University, 2000.
11. ARANGANATHAN, N.; BIJWE, J. Development of copper-free eco-friendly brake-friction material using novel ingredients. **Wear**, v. 352–353, p. 79–91, abr. 2016.
12. ARANGANATHAN, N.; BIJWE, J. Special grade of graphite in NAO friction materials for possible replacement of copper. **Wear**, v. 330–331, p. 515–523, 2014.
13. LEE, P. W.; FILIP, P. Friction and wear of Cu-free and Sb-free environmental friendly automotive brake materials. **Wear**, v. 302, n. 1–2, p. 1404–1413, 2013.

14. YUN, R.; FILIP, P.; LU, Y. Tribology International Performance and evaluation of eco-friendly brake friction materials. **Tribology International**, v. 43, n. 11, p. 2010–2019, 2010.
15. MENAPACE, C. et al. Pin-on-disc study of brake friction materials with ball-milled nanostructured components. **Materials and Design**, v. 115, p. 287–298, 2017.
16. ÖSTERLE, W.; DMITRIEV, A. The Role of Solid Lubricants for Brake Friction Materials. **Lubricants**, v. 4, n. 1, p. 5, 2016.
17. KATO, H. Severe–mild wear transition by supply of oxide particles on sliding surface. **Wear**, v. 255, n. 1–6, p. 426–429, ago. 2003.
18. KATO, H.; KOMAI, K. Tribofilm formation and mild wear by tribo-sintering of nanometer-sized oxide particles on rubbing steel surfaces. **Wear**, v. 262, n. 1–2, p. 36–41, 2007.
19. KATO, H. Effects of supply of fine oxide particles onto rubbing steel surfaces on severe-mild wear transition and oxide film formation. **Tribology International**, v. 41, n. 8, p. 735–742, 2008.
20. CZICHOS, H. Systems approach to wear problems. In: **Wear control handbook**. New York: American Society of Mechanical Engineers, 1980. p. 17–34.
21. KATO, K. Wear in relation to friction - A review. **Wear**, v. 241, n. 2, p. 151–157, 2000.
22. BLAU, P. **Friction Science and Technology**. [s.l.] CRC Press, 2008. v. 20084465
23. GODET, M. The third-body approach: A mechanical view of wear. **Wear**, v. 100, n. 1–3, p. 437–452, 1984.
24. BLAU, P. J.; MCLAUGHLIN, J. C. Effects of water films and sliding speed on the frictional behavior of truck disc brake materials. **Tribology International**, v. 36, n. 10, p. 709–715, 2003.
25. ERIKSSON, M.; LORD, J.; JACOBSON, S. Wear and contact conditions of brake pads: Dynamical in situ studies of pads on glass. **Wear**, v. 249, n. 3–4, p. 272–278, 2001.

26. ÖSTERLE, W. et al. A comprehensive microscopic study of third body formation at the interface between a brake pad and brake disc during the final stage of a pin-on-disc test. **Wear**, v. 267, n. 5–8, p. 781–788, 2009.
27. DMITRIEV, A. I.; ÖSTERLE, W. Modeling of brake pad-disc interface with emphasis to dynamics and deformation of structures. **Tribology International**, v. 43, n. 4, p. 719–727, 2010.
28. BETTGE, D.; STARCEVIC, J. Topographic properties of the contact zones of wear surfaces in disc brakes. **Wear**, v. 254, n. 3–4, p. 195–202, 2003.
29. KUKUTSCHOVÁ, J. et al. Wear mechanism in automotive brake materials , wear debris and its potential environmental impact. v. 267, p. 807–817, 2009.
30. SANDERS, P. G. et al. Airborne Brake Wear Debris: Size Distributions , Composition , and a Comparison of Dynamometer and Vehicle Tests. **Environmental Science Technology**, v. 37, n. 18, p. 4060–4069, 2003.
31. GARG, B. D. et al. Brake Wear Particulate Matter Emissions. **Environmental Science Technology**, v. 34, n. 21, p. 4463–4469, 2000.
32. SANDERS, P.G. DALKA, T.M. XU, N. MARICQ, M.M. BASCH, R. H. Brake Dynamometer Measurement of Airborne Brake Wear Debris. **SAE paper**, v. 01, n. 2180, 2002.
33. KUKUTSCHOVÁ, J. et al. Wear performance and wear debris of semimetallic automotive brake materials. **Wear**, v. 268, n. 1, p. 86–93, 2010.
34. COPPER DEVELOPMENT ASSOCIATION INC. **No Title**.
35. POPE, C. A. et al. Lung cancer, cardiopulmonary mortality, and long-term exposure to fine particulate air pollution. **Journal of the American Medical Association**, v. 287, n. 9, p. 1132–1141, 2002.
36. VON UEXKÜLL, O. et al. Antimony in brake pads-a carcinogenic component? **Journal of Cleaner Production**, v. 13, n. 1, p. 19–31, jan. 2005.
37. CHO, M. H. et al. Tribological properties of solid lubricants (graphite, Sb<sub>2</sub>S<sub>3</sub>, MoS<sub>2</sub>) for automotive brake friction materials. **Wear**, v. 260, n. 7–8, p. 855–860, 2006.

38. SAVAGE, R. H. Graphite Lubrication. **Journal of Applied Physics**, v. 19, n. 1, p. 1–10, jan. 1948.
39. ARANGANATHAN, N.; BIJWE, J. Comparative performance evaluation of NAO friction materials containing natural graphite and thermo-graphite. **Wear**, v. 358–359, p. 17–22, 2016.
40. KOLLURI, D. K. et al. Effect of Natural Graphite Particle size in friction materials on thermal localisation phenomenon during stop-braking. **Wear**, v. 268, n. 11–12, p. 1472–1482, 12 maio 2010.
41. JANG, H.; KIM, S. J. The effects of antimony trisulfide ( $Sb_2S_3$ ) and zirconium silicate ( $ZrSiO_4$ ) in the automotive brake friction material on friction characteristics. **Wear**, v. 239, n. 2, p. 229–236, 2000.
42. SASADA, T.; OIKE, M.; EMORI, N. Effect of Abrasive Grain Size on the Transition Between Abrasive and Adhesive Wear. **Wear**, v. 97, n. 3, p. 291–302, 1984.
43. CHO, M. H. et al. The role of transfer layers on friction characteristics in the sliding interface between friction materials against gray iron brake disks. **Tribology Letters**, v. 20, n. 2, p. 101–108, 2005.
44. LEE, E. J. et al. Morphology and toughness of abrasive particles and their effects on the friction and wear of friction materials: A case study with zircon and quartz. **Tribology Letters**, v. 37, n. 3, p. 637–644, 2010.
45. CHO, K. H. et al. The size effect of zircon particles on the friction characteristics of brake lining materials. **Wear**, v. 264, n. 3–4, p. 291–297, 2008.
46. MATĚJKA, V. et al. Effects of silicon carbide in semi-metallic brake materials on friction performance and friction layer formation. **Wear**, v. 265, n. 7–8, p. 1121–1128, 2008.
47. LAZIM, A. R. M. et al. Squealing characteristics of worn brake pads due to silica sand embedment into their friction layers. **Wear**, v. 358–359, p. 123–136, 2016.
48. KCHAOU, M. et al. Experimental studies of friction-induced brake squeal: Influence of environmental sand particles in the interface brake pad-disc. **Tribology International**, v. 110, n. November 2016, p. 307–317, 2017.

49. KIM, S. S. et al. Friction and vibration of automotive brake pads containing different abrasive particles. **Wear**, v. 271, n. 7–8, p. 1194–1202, 2011.
50. NOSONOVSKY, M.; BHUSHAN, B. Green tribology: Principles, research areas and challenges. **Philosophical Transactions of the Royal Society A: Mathematical, Physical and Engineering Sciences**, v. 368, n. 1929, p. 4677–4694, 2010.
51. ANAND, A. et al. Role of Green Tribology in Sustainability of Mechanical Systems: A State of the Art Survey. **Materials Today: Proceedings**, v. 4, n. 2, p. 3659–3665, 2017.
52. TROMBOTTO, F. **Friction Material**, 2014. Disponível em: <<http://www.google.com/patents/WO2014024152A1?cl=en>>
53. XIAOHUA LU et al. **Copper-free ceramic type friction material and preparation method thereof** CHINA, 2013.
54. CHEN, H.; PAUL, H.-G. **COPPER-FREE FRICTION MATERIAL FOR BRAKE PADS**, 2013.
55. STRAFFELINI, G. et al. Present knowledge and perspectives on the role of copper in brake materials and related environmental issues: A critical assessment. **Environmental Pollution**, v. 207, p. 211–219, 2015.
56. HIRATSUKA, K.; MURAMOTO, K. Role of wear particles in severe-mild wear transition. **Wear**, v. 259, n. 1–6, p. 467–476, 2005.
57. JIANG, J.; STOTT, F. H.; STACK, M. M. The role of triboparticulates in dry sliding wear. **Tribology International**, v. 31, n. 5, p. 245–256, 1998.
58. BERTHIER, Y. Background on friction and wear. **Handbook of materials behavior models**, p. 676–699, 2001.
59. DMITRIEV, A. I.; ÖSTERLE, W. Modelling the Sliding Behaviour of Tribofilms Forming During Automotive Braking: Impact of Loading Parameters and Property Range of Constituents. **Tribology Letters**, v. 53, n. 1, p. 337–351, 1 jan. 2014.
60. DMITRIEV, A.; ÖSTERLE, W. **Sliding Simulations With Variable Amounts of Copper and Graphite Mixed With Magnetite** .EuroBrake Proceedings. **Anais...**2016

61. RODRIGUES, A. C. P. et al. Effect of Cu particles as an interfacial media addition on the friction coefficient and interface microstructure during ( steel / steel ) pin on disc tribotest. **Wear**, v. 331, p. 70–78, 2015.
62. RODRIGUES, A. C. P. et al. Pin-on-disc tribotests with the addition of Cu particles as an interfacial media: Characterization of disc tribosurfaces using SEM-FIB techniques. **Tribology International**, v. 100, p. 351–359, 2016.
63. LIBSCH, T. A.; RHEE, S. K. Friction and wear testing ‘ Metallographic examination. **Wear**, v. 46, p. 203–212, 1978.
64. ÖSTERLE, W.; URBAN, I. Third body formation on brake pads and rotors. **Tribology International**, v. 39, n. 5, p. 401–408, 2006.
65. ÖSTERLE, W.; URBAN, I. Friction layers and friction films on PMC brake pads. v. 257, n. April 2003, p. 215–226, 2004.
66. SCIESKA, S. F. Tribological phenomena in steel-composite brake material friction pairs. **Wear**, v. 64, p. 367–378, 1980.
67. INGO, G. M. et al. Thermal and microchemical investigation of automotive brake pad wear residues. **Thermochimica acta**, v. 418, p. 61–68, 2004.
68. MOSLEH, M.; BLAU, P. J.; DUMITRESCU, D. Characteristics and morphology of wear particles from laboratory testing of disk brake materials. **Wear**, v. 256, p. 1128–1134, 2004.
69. ÖSTERLE, W.; PRIETZEL, C.; DMITRIEV, A. I. Investigation of surface film nanostructure and assessment of its impact on friction force stabilization during automotive braking. **International Journal of Materials Research**, v. 101, n. 5, p. 669–675, 2010.
70. ÖSTERLE, W. et al. Towards a better understanding of brake friction materials. **Wear**, v. 263, n. 7- 12 SPEC. ISS., p. 1189–1201, 2007.
71. CHANDRA VERMA, P. et al. Braking pad-disc system: Wear mechanisms and formation of wear fragments. **Wear**, v. 322–323, p. 251–258, 2015.
72. FILIP, P.; WEISS, Z.; RAFAJA, D. On friction layer formation in polymer matrix

composite materials for brake applications. **Wear**, v. 252, p. 189–198, 2002.

73. ÖSTERLE, W.; DMITRIEV, A. I.; KLOSS, H. Does ultra-mild wear play any role for dry friction applications, such as automotive braking? **Faraday Discussions**, v. 156, p. 159, 2012.

74. ÖSTERLE, W. et al. Verification of nanometre-scale modelling of tribofilm sliding behaviour. **Tribology International**, v. 62, p. 155–162, 2013.

75. ÖSTERLE, W.; DMITRIEV, A. I. I.; KLOSS, H. Possible impacts of third body nanostructure on friction performance during dry sliding determined by computer simulation based on the method of movable cellular automata. **Tribology International**, v. 48, p. 128–136, abr. 2012.

76. ÖSTERLE, W. et al. On the role of copper in brake friction materials. **Tribology International**, v. 43, n. 12, p. 2317–2326, dez. 2010.

77. KUMAR, M.; BIJWE, J. Optimized selection of metallic fillers for best combination of performance properties of friction materials: A comprehensive study. **Wear**, v. 303, n. 1–2, p. 569–583, 2013.

78. ROUBICEK, V. et al. Wear and environmental aspects of composite materials for automotive braking industry. **Wear**, v. 265, p. 167–175, 2008.

79. JACKO, M. G. Physical and chemical changes of organix disc pads in service. **Wear**, v. 46, p. 163–175, 1978.

80. JACKO, M. G.; TSANG, P. H. S.; RHEE, S. K. Wear debris compaction and friction film formation of polymer composites. **Wear**, v. 133, n. 1, p. 23–38, 1989.

81. YI, G.; YAN, F. Mechanical and tribological properties of phenolic resin-based friction composites filled with several inorganic fillers. **Wear**, v. 262, p. 121–129, 2007.

82. HINRICHS, R. et al. A TEM snapshot of magnetite formation in brakes: The role of the disc's cast iron graphite lamellae in third body formation. **Wear**, v. 270, n. 5–6, p. 365–370, 2011.

83. ÖSTERLE, W. et al. Tribological screening tests for the selection of raw materials for automotive brake pad formulations. **Tribology International**, v. 73, p. 148–155,

2014.

84. SILVA, T. F. et al. Elemental mapping of large samples by external ion beam analysis with sub-millimeter resolution and its applications. **Nuclear Instruments and Methods in Physics Research Section B: Beam Interactions with Materials and Atoms**, v. 422, n. March, p. 68–77, maio 2018.

85. RAJPUT, N. S.; LUO, X. FIB Micro-/Nano-fabrication. In: **Micromanufacturing Engineering and Technology**. Second Edi ed. [s.l.] Elsevier, 2015. p. 61–80.

86. EMGE, A. et al. The effect of sliding velocity on the tribological behavior of copper. **Wear**, v. 263, n. 1- 6 SPEC. ISS., p. 614–618, 2007.

87. VOLKERT, C. A.; MINOR, A. M. Focused Ion Beam Microscopy and Micromachining. **MRS Bulletin**, v. 32, n. 05, p. 389–399, 2007.

88. RODRIGUES, A. C. P. et al. **EFFECT OF THE TEMPERATURE ON TRIBOFILM GENERATED FROM COPPER , GRAPHITE AND MAGNETITE MIXTURES ASEuroBrake Proceedings. Anais...2018**

89. SLINEY, H. E. Solid lubricant materials for high temperatures-a review. **Tribology International**, v. 15, n. 5, p. 303–315, 1982.

90. HÄUSLER, I. et al. Comprehensive characterization of ball-milled powders simulating a tribofilm system. **Materials Characterization**, v. 111, p. 183–192, 2016.

91. HINRICHS, R. et al. Amorphization of Graphite Flakes in Gray Cast Iron Under Tribological Load. **Materials Research**, v. 21, n. 4, 28 maio 2018.

92. RODRIGUES, A. C. P. et al. Impact of copper nanoparticles on tribofilm formation determined by pin-on-disc tests with powder supply: Addition of artificial third body consisting of Fe<sub>3</sub>O<sub>4</sub>, Cu and graphite. **Tribology International**, v. 110, 2017.

93. ÖSTERLE, W.; DMITRIEV, A. I. Functionality of conventional brake friction materials - Perceptions from findings observed at different length scales. **Wear**, v. 271, n. 9–10, p. 2198–2207, 2011.

94. HINRICHS, R. et al. Phase characterization of debris generated in brake pad

coefficient of friction tests. **Wear**, v. 270, n. 7–8, p. 515–519, 2011.

95. SUNDMAN, B. An assessment of the Fe-O system. **Journal of Phase Equilibria**, v. 12, n. 2, p. 127–140, abr. 1991.

96. VERMA, P. C. et al. Role of the friction layer in the high-temperature pin-on-disc study of a brake material. **Wear**, v. 346–347, p. 56–65, 2016.

97. SU, L. et al. Effect of copper powder third body on tribological property of copper-based friction materials. **Tribology International**, v. 90, p. 420–425, 2015.

98. XIAN, J.; XIAOMEI, L. Friction and wear characteristics of polymer-matrix friction materials reinforced by brass fibers. **Journal of Materials Engineering and Performance**, v. 13, n. 5, p. 642–646, 2004.

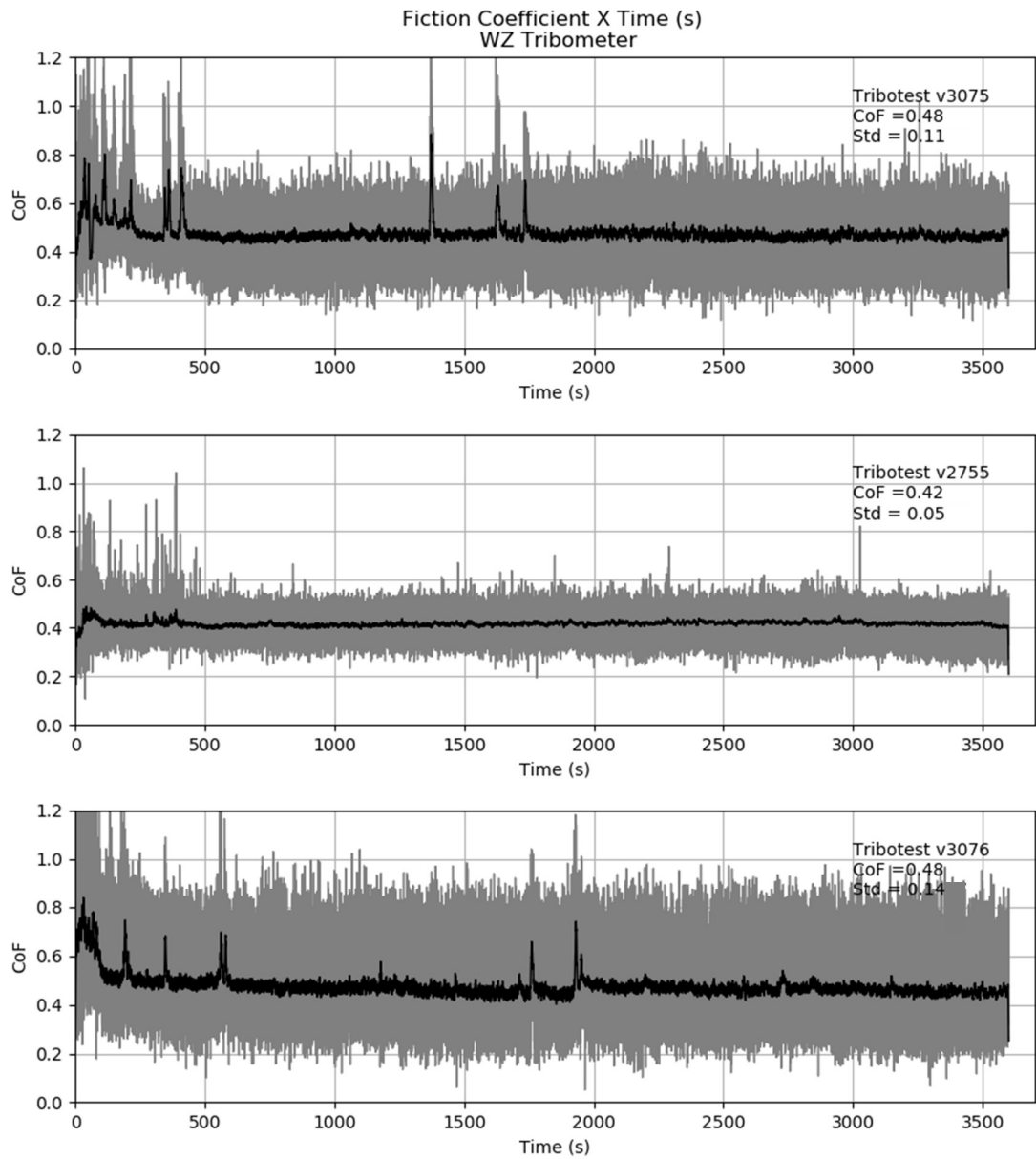
99. SHI, Y. et al. ( 12 ) Patent Application Publication ( 10 ) Pub . No . : US 2013 / 0203888 A1. v. 1, n. 19, 2013.

100. MAHALE, V.; BIJWE, J.; SINHA, S. A step towards replacing copper in brake-pads by using stainless steel swarf. **Wear**, v. 424–425, p. 133–142, abr. 2019.

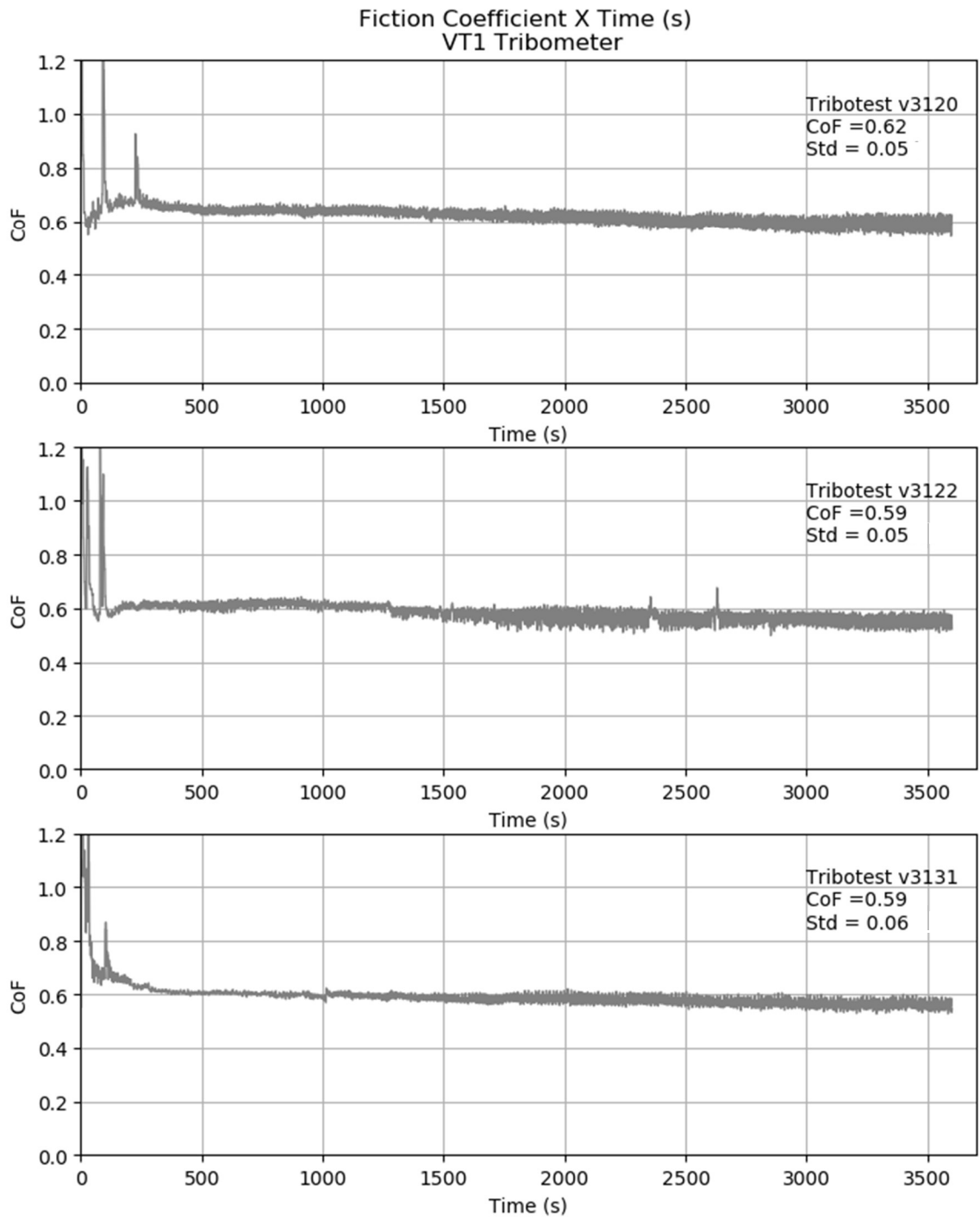
101. ZHENG, K. et al. The Role of Rare Earth Lanthanum Oxide in Polymeric Matrix Brake Composites to Replace Copper. **Polymers**, v. 10, n. 9, p. 1027, 2018.

## ANNEX 1

Tribotests performed with addition of pure  $\text{Fe}_3\text{O}_4$  at 23°C in air

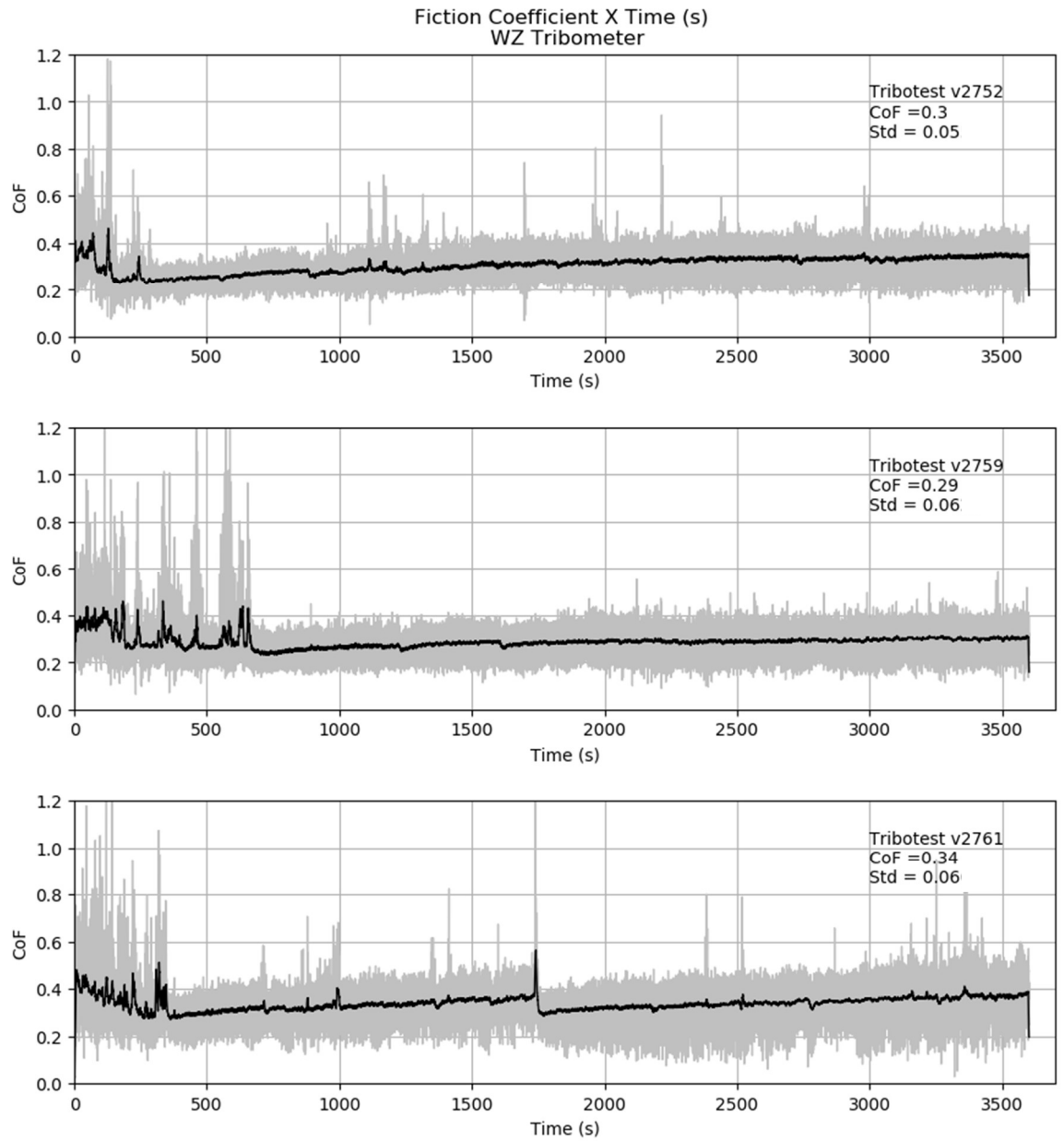


Tribotests performed with addition of pure Fe<sub>3</sub>O<sub>4</sub> at 400°C in air

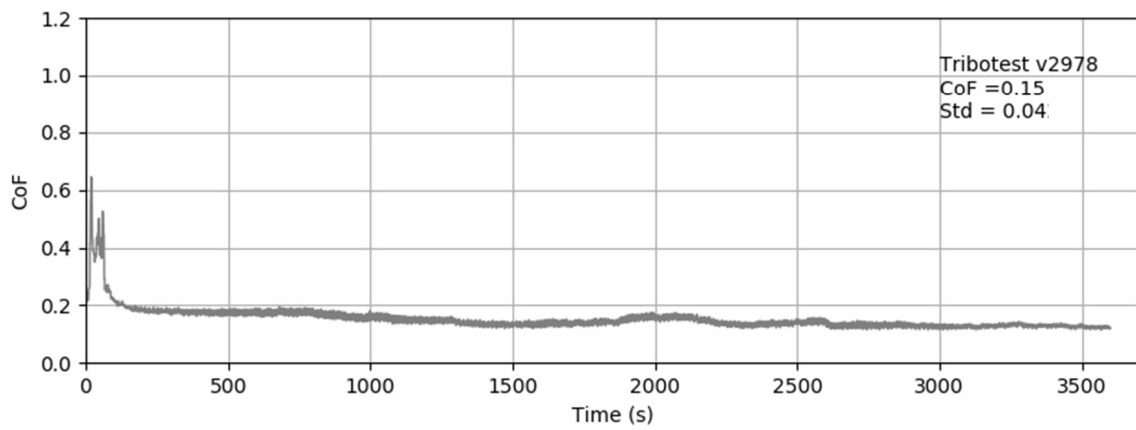
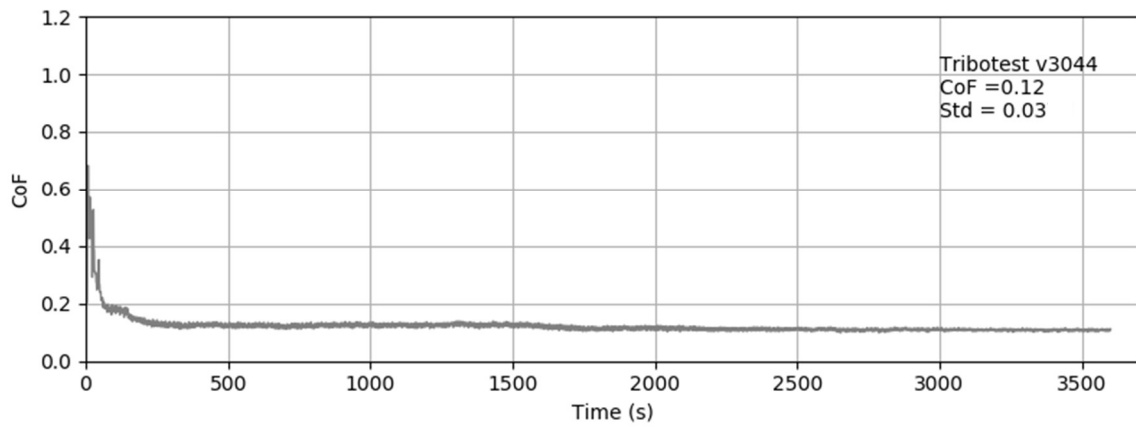
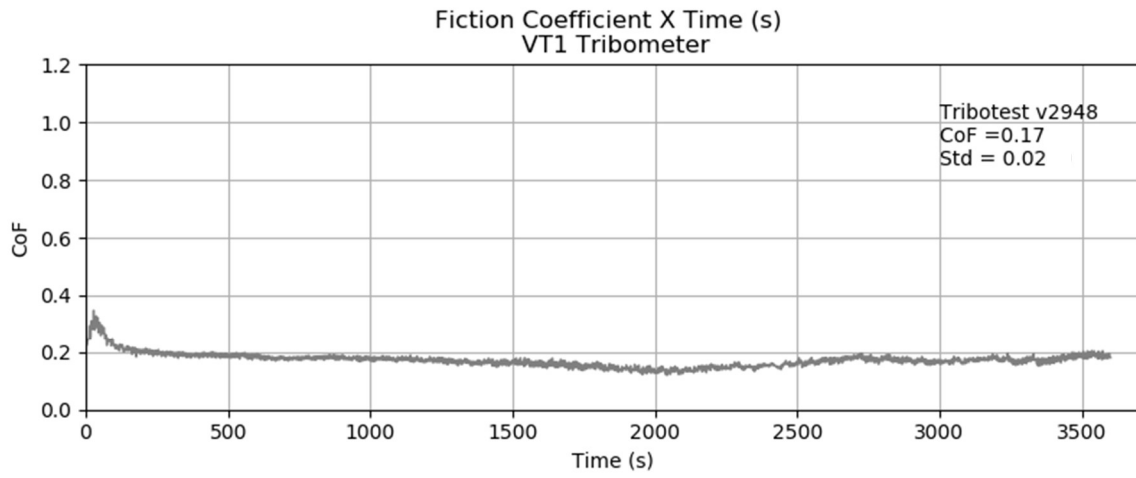


## ANNEX 2

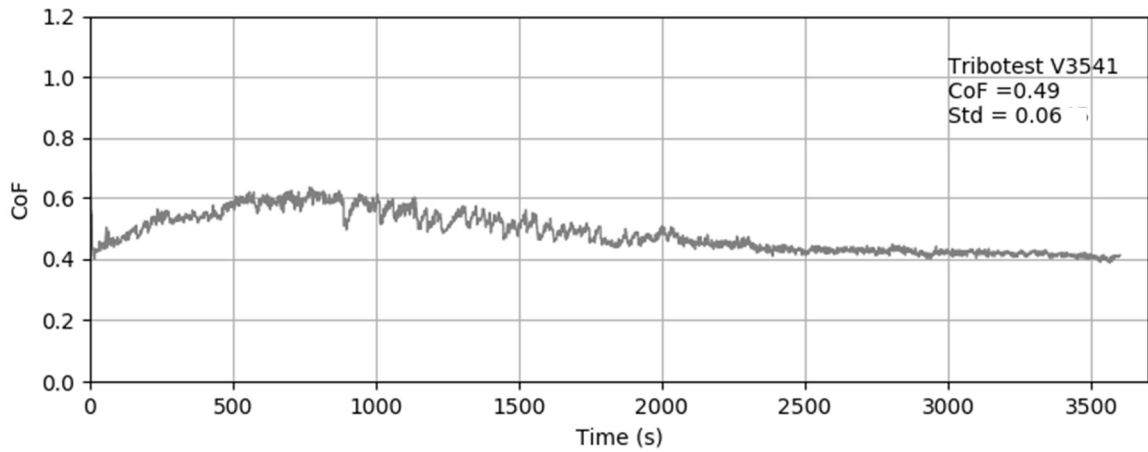
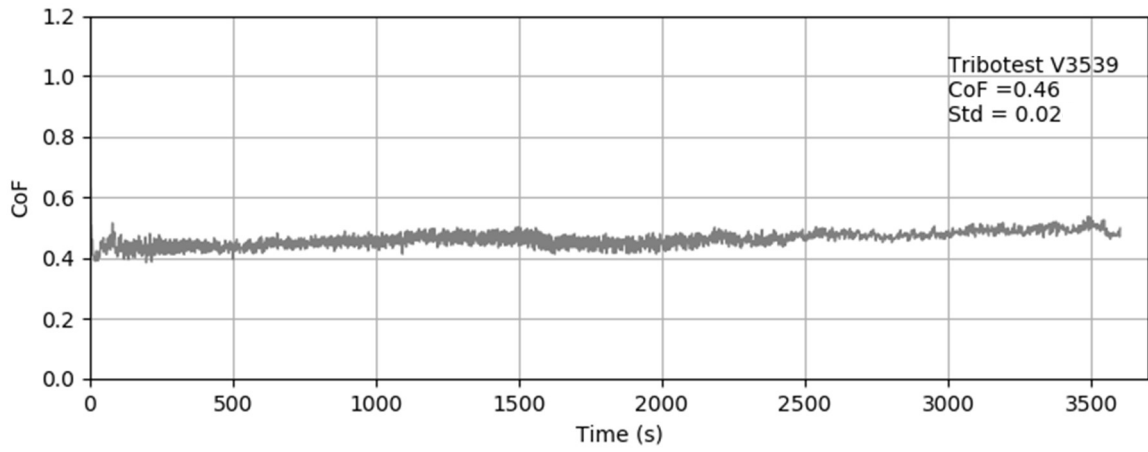
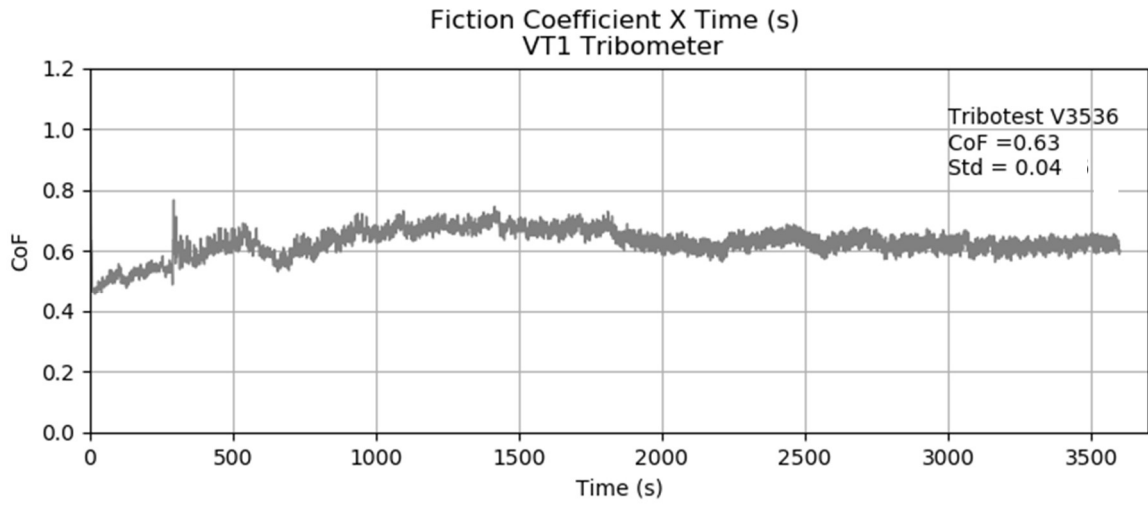
Tribotests performed with addition of binary graphite-Fe<sub>3</sub>O<sub>4</sub> at 23°C in air



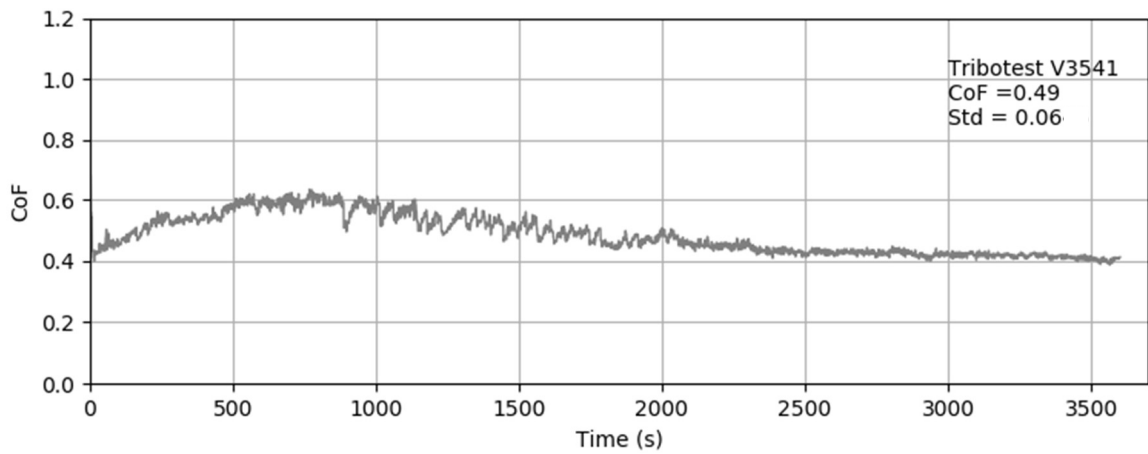
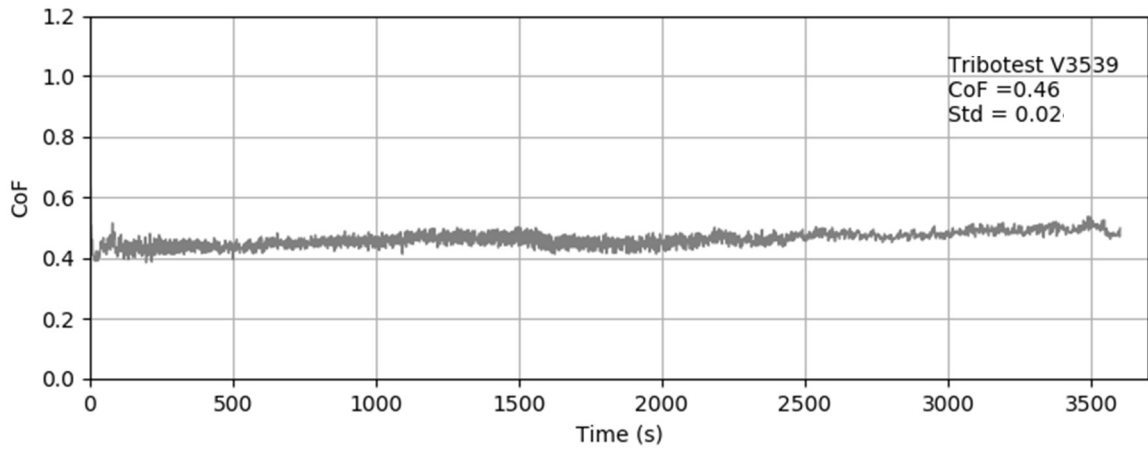
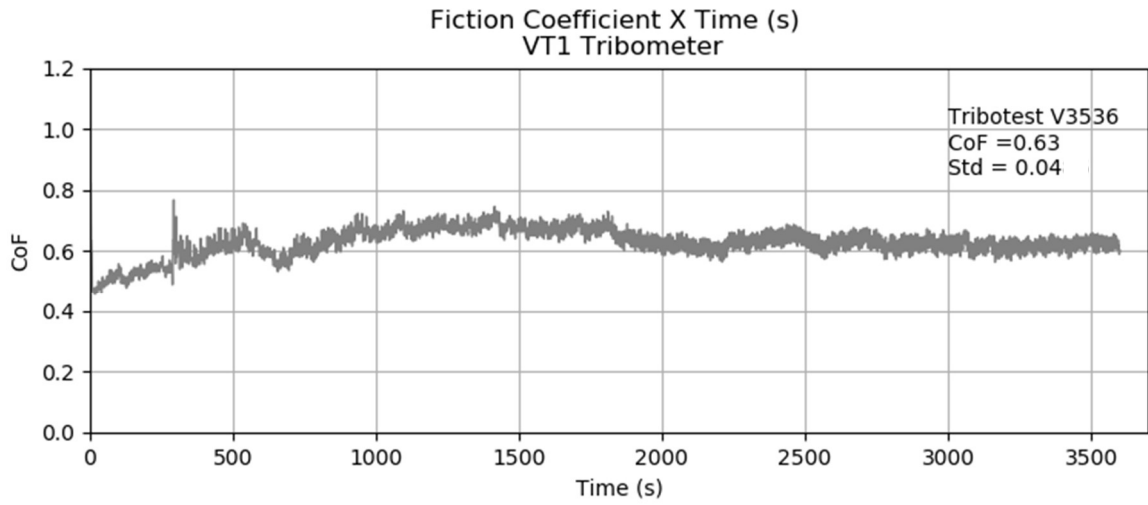
Tribotests performed with addition of binary graphite-Fe<sub>3</sub>O<sub>4</sub> at 23°C in air



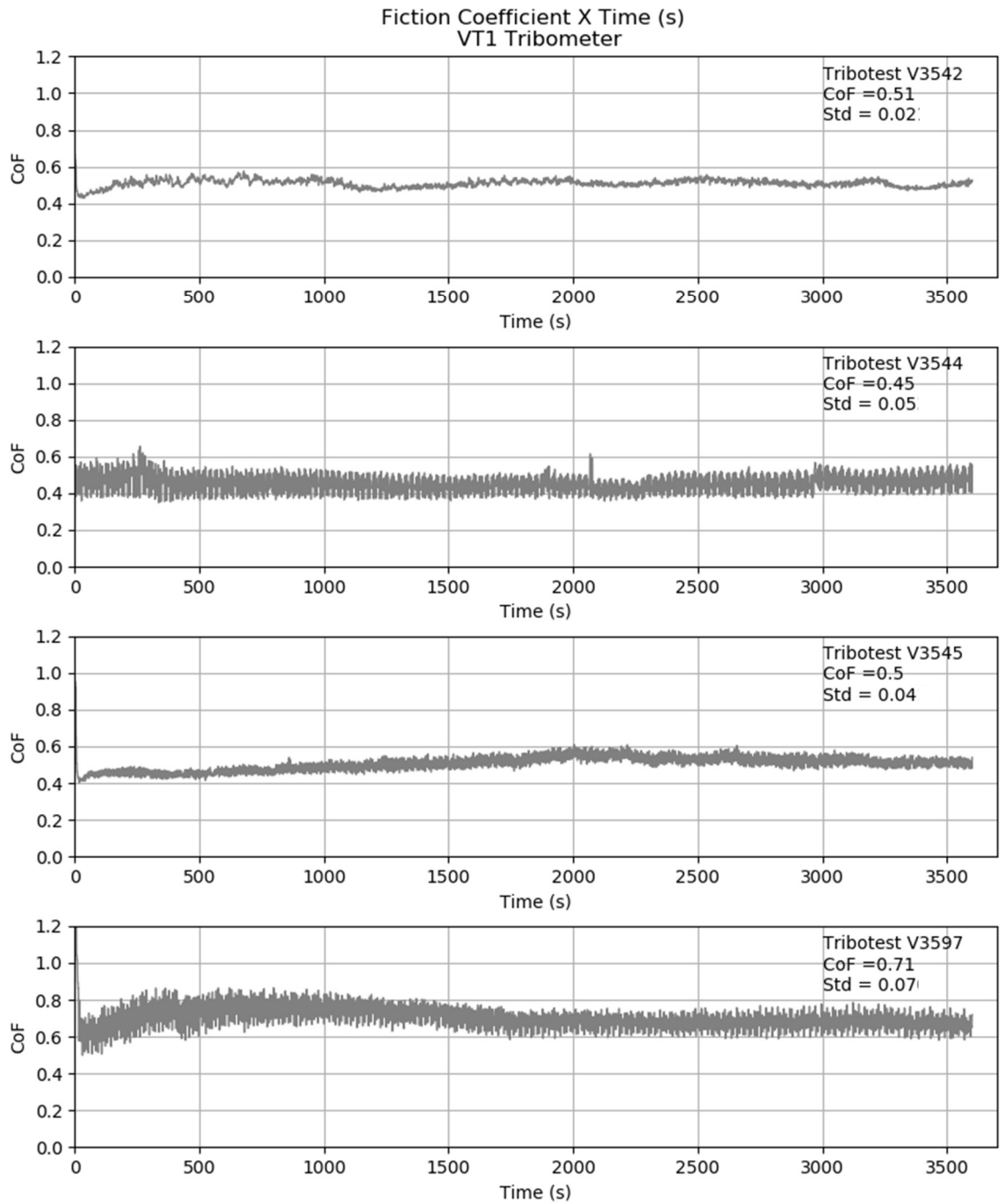
Tribotests performed with addition of binary graphite-Fe<sub>3</sub>O<sub>4</sub> at 400°C in N<sub>2</sub>



Tribotests performed with addition of binary graphite-Fe<sub>3</sub>O<sub>4</sub> at 400°C in air

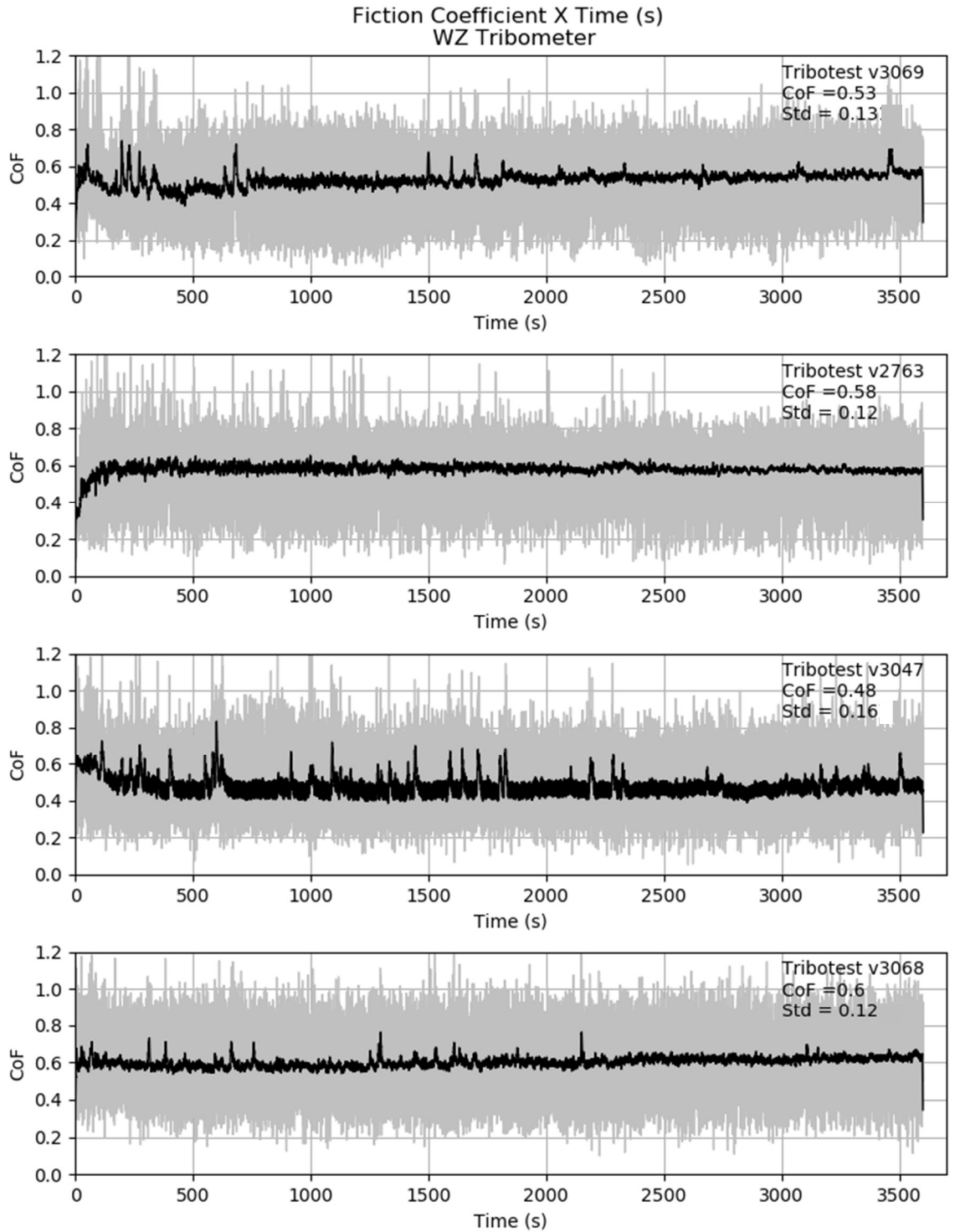


Tribotests performed with addition of binary graphite-Fe<sub>3</sub>O<sub>4</sub> at 400°C in air

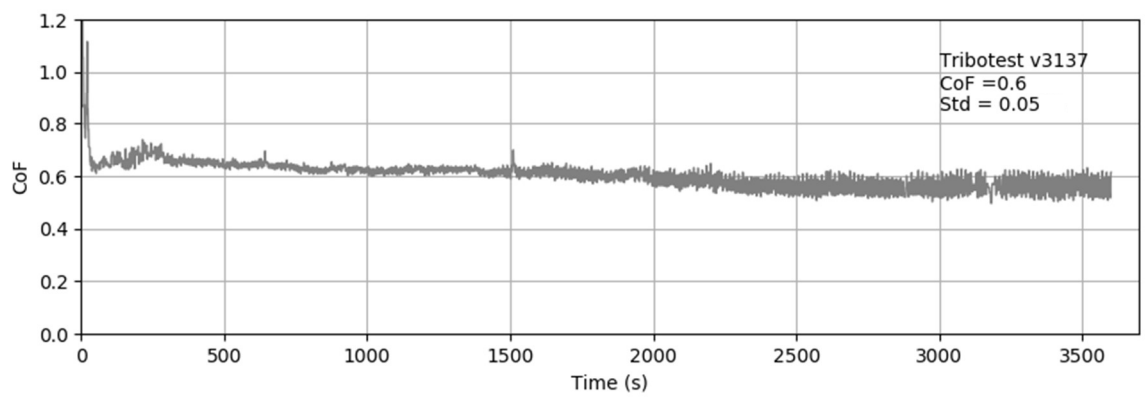
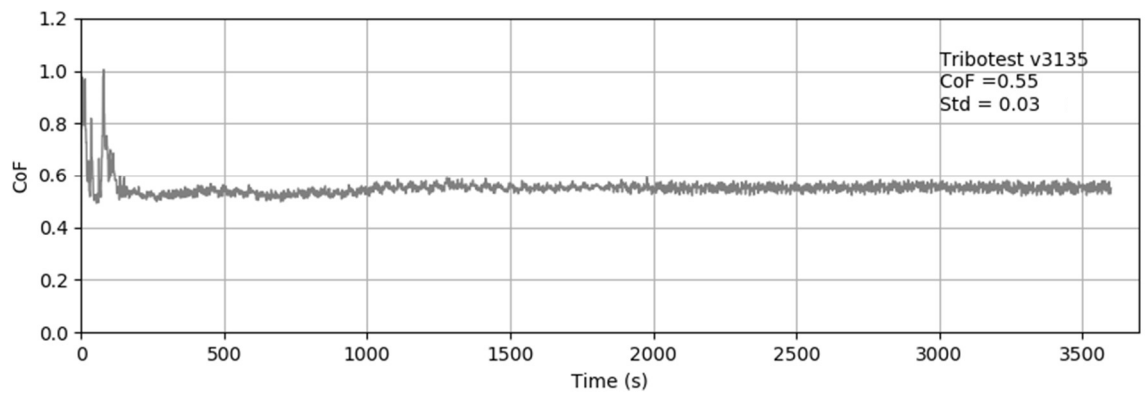
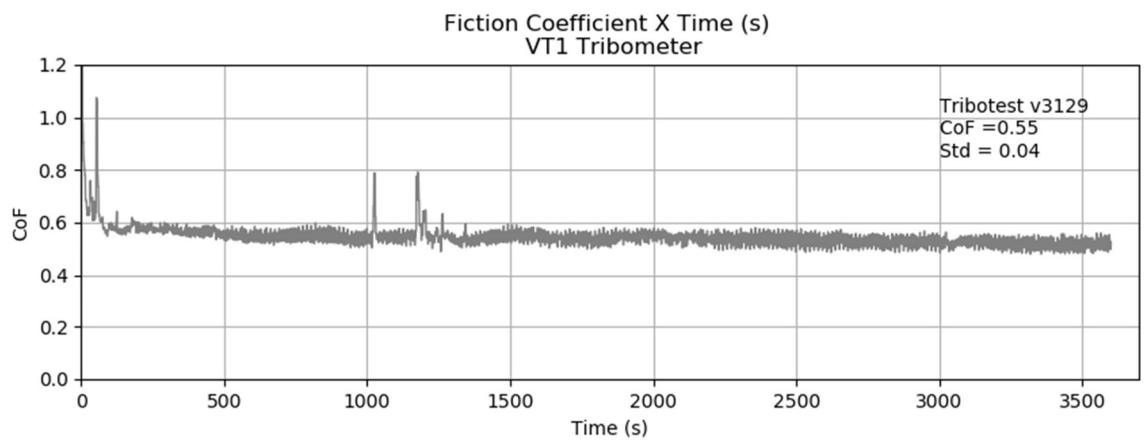


### ANNEX 3

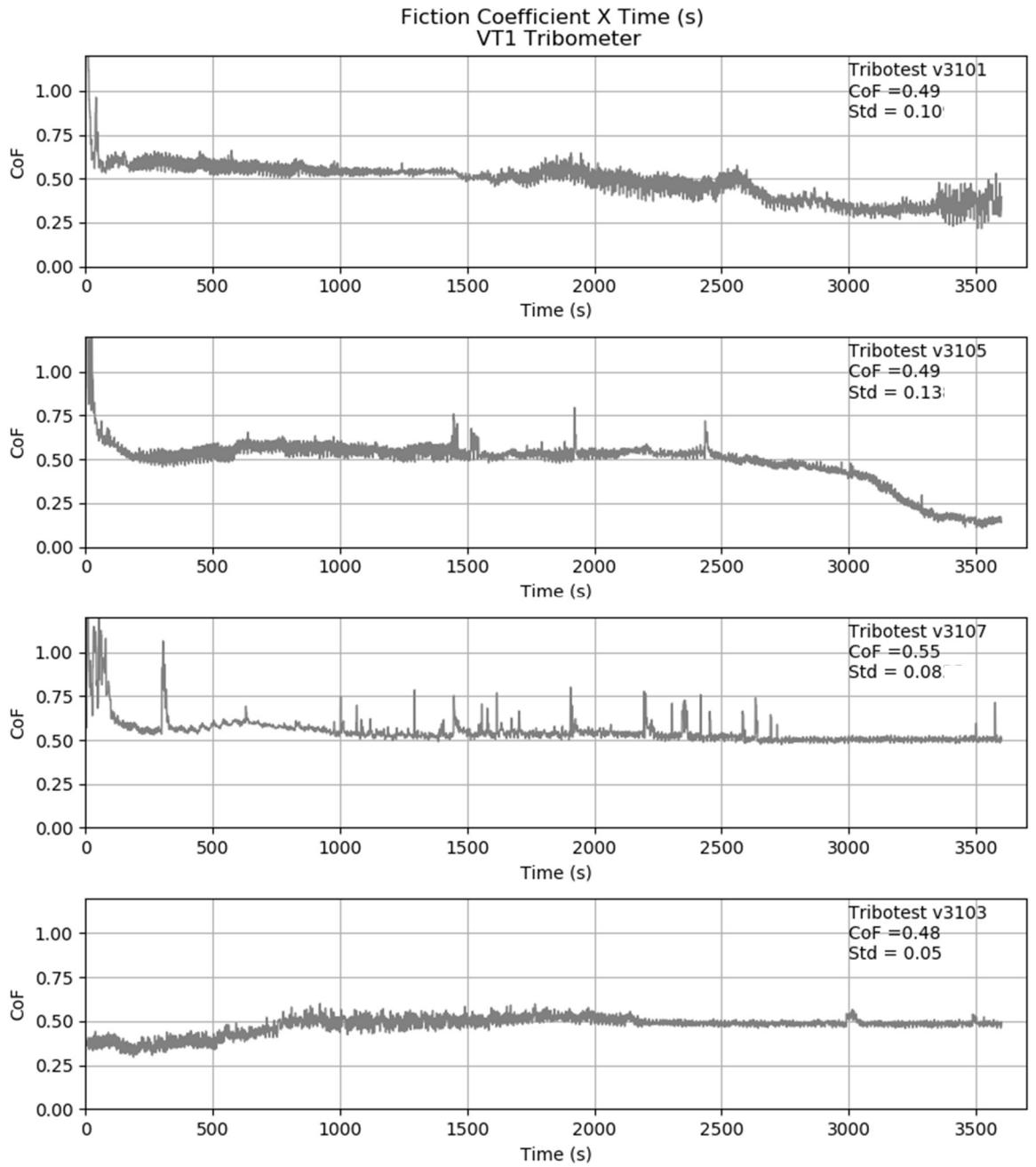
Tribotests performed with addition of binary 6%Cu-Fe<sub>3</sub>O<sub>4</sub> at 23°C in air



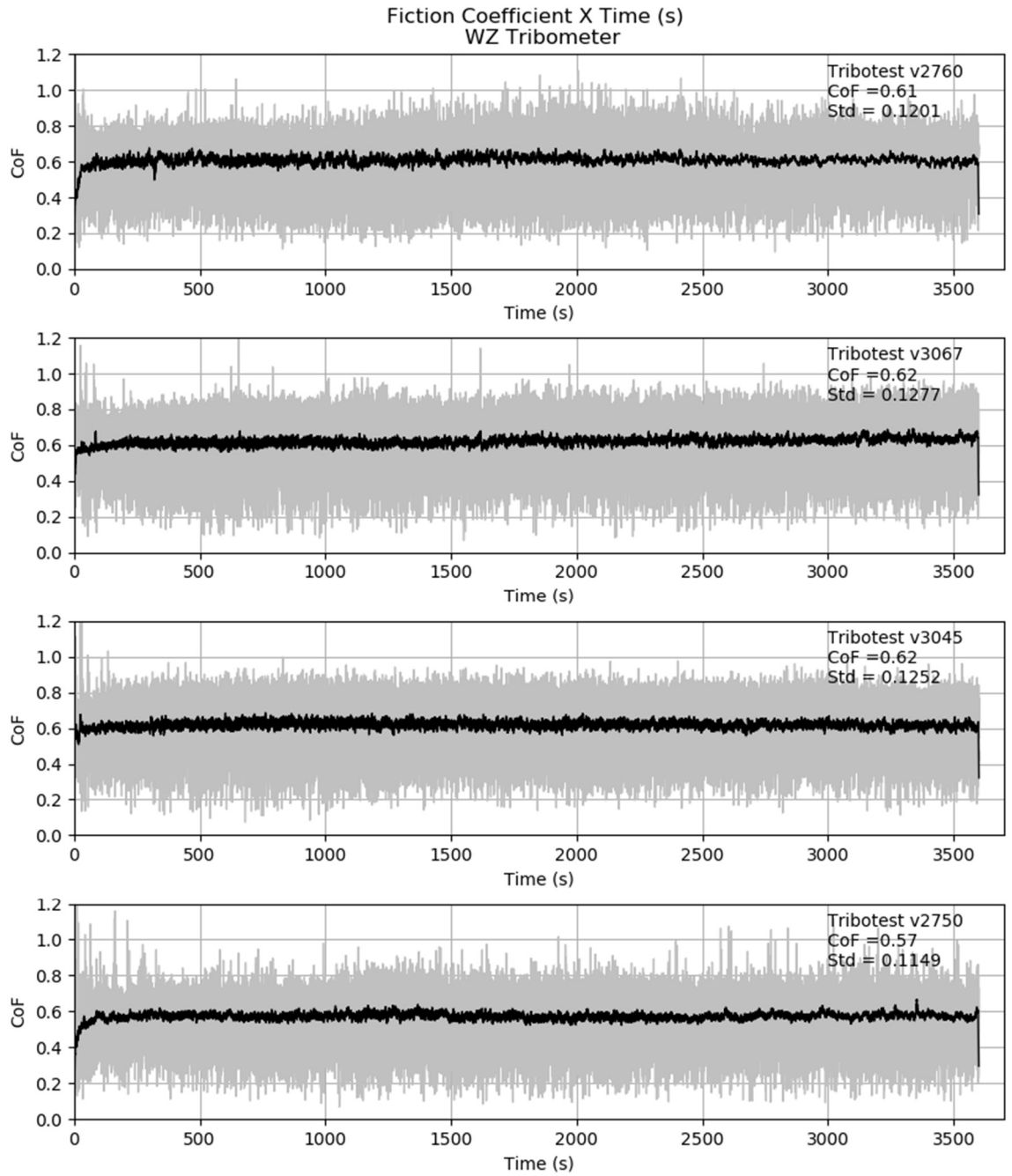
Tribotests performed with addition of binary 6%Cu-Fe<sub>3</sub>O<sub>4</sub> at 400°C in air



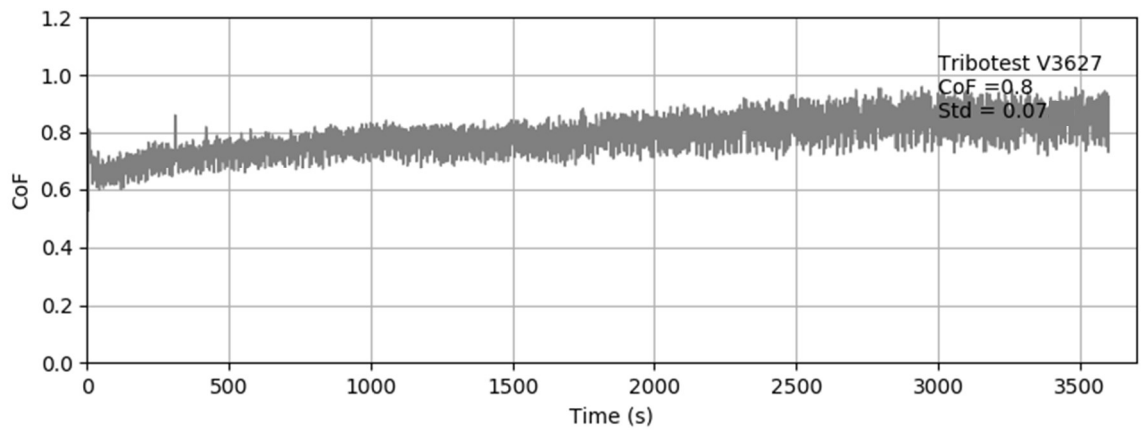
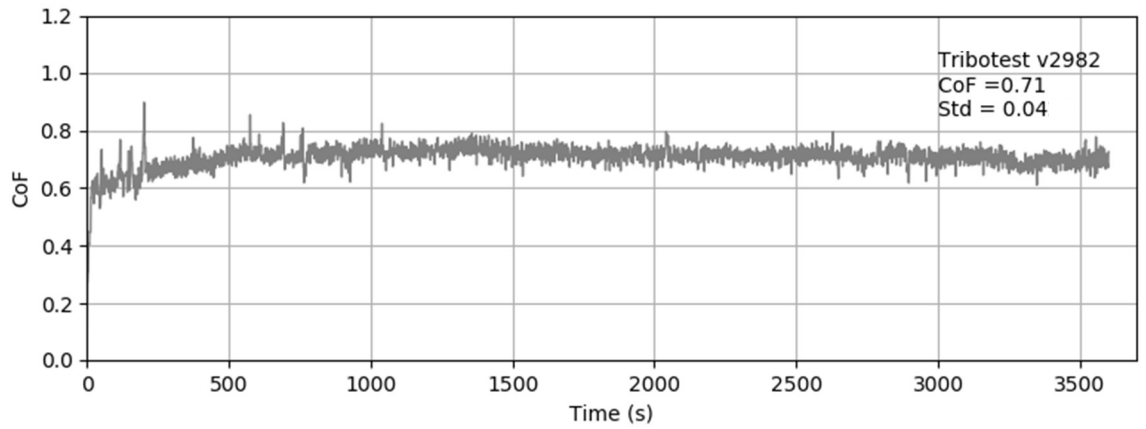
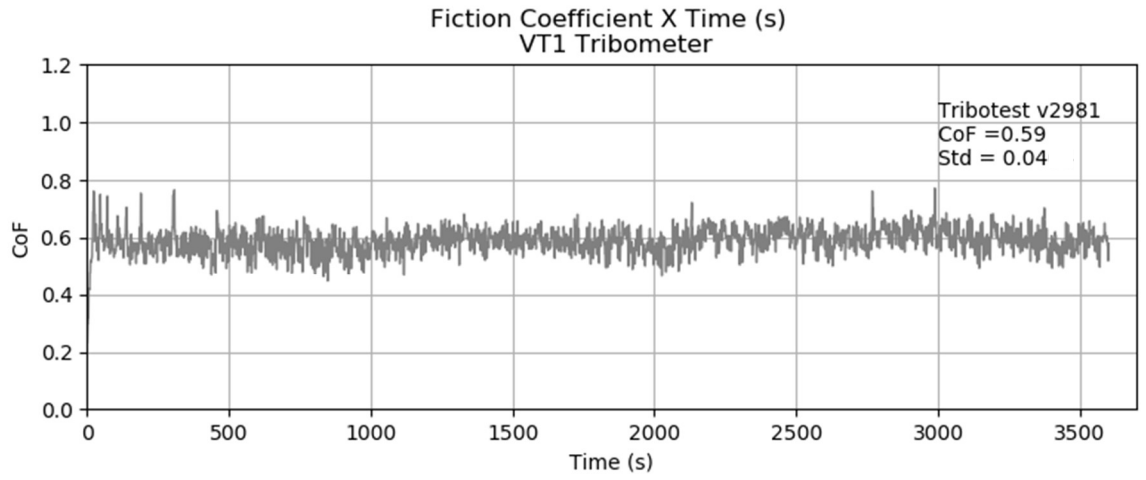
Tribotests performed with addition of binary 6%Cu-Fe<sub>3</sub>O<sub>4</sub> at 400°C in N<sub>2</sub>



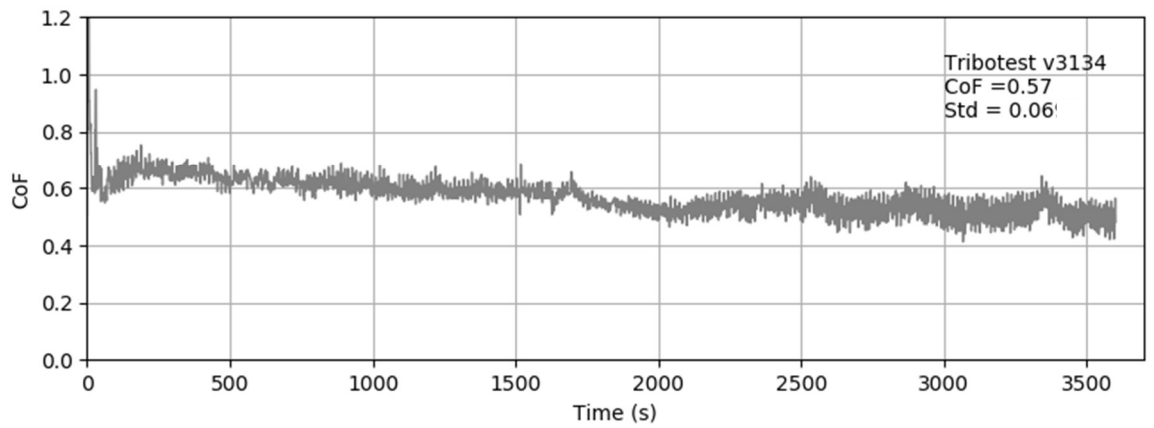
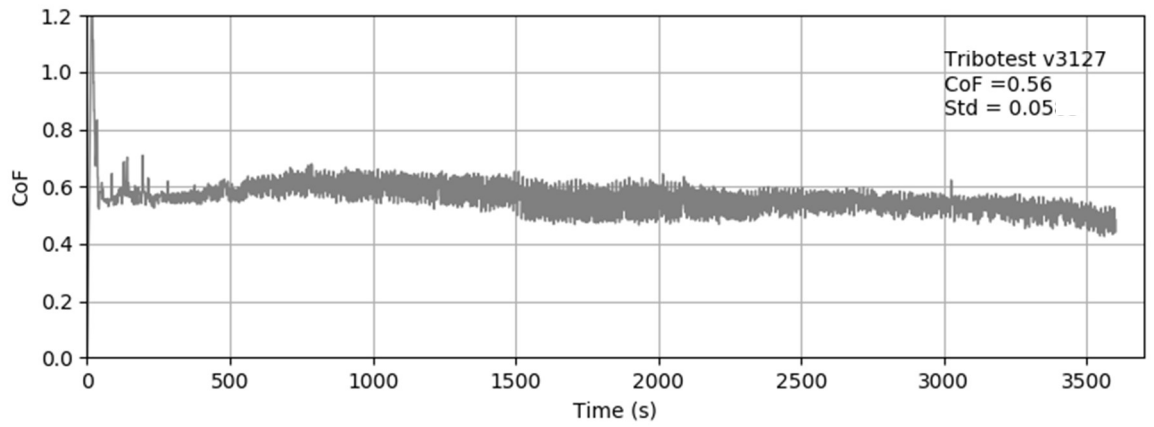
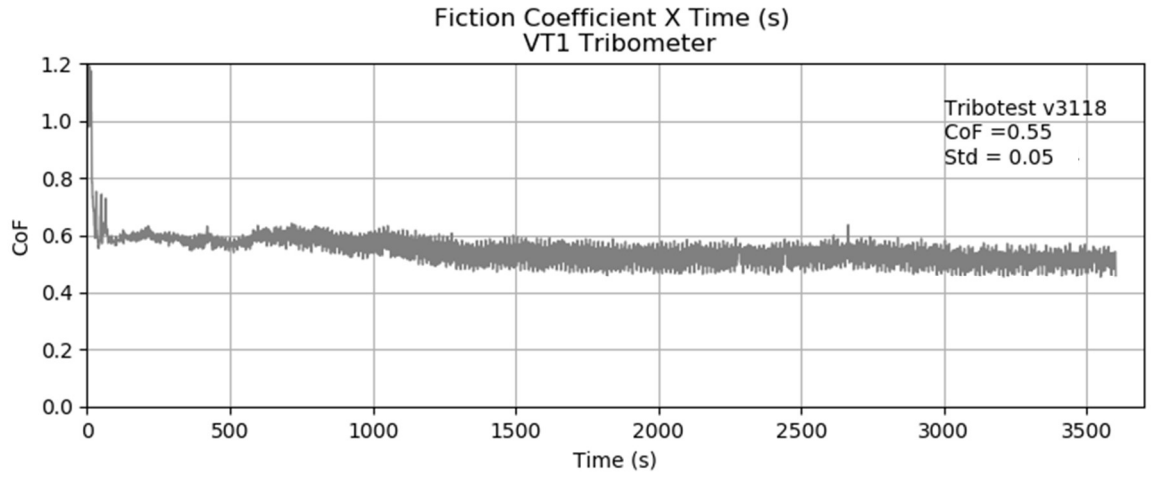
Tribotests performed with addition of binary 15%Cu-Fe<sub>3</sub>O<sub>4</sub> at 23°C in air



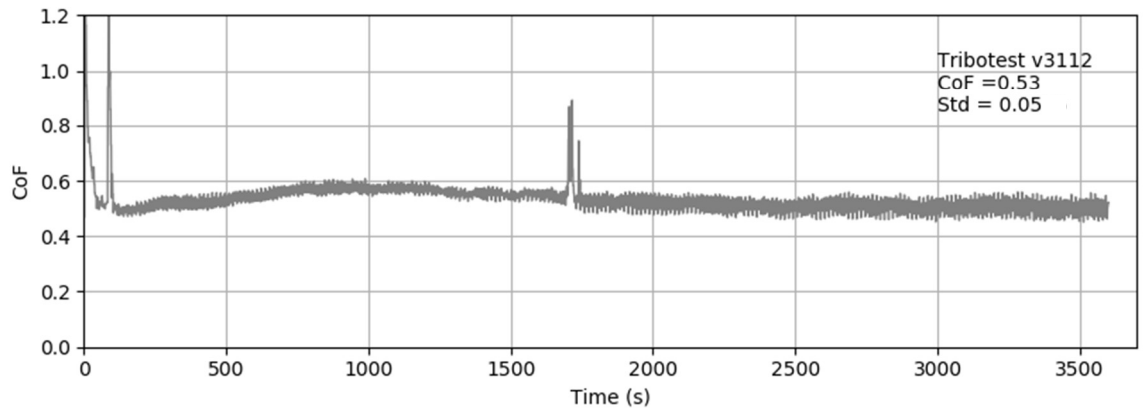
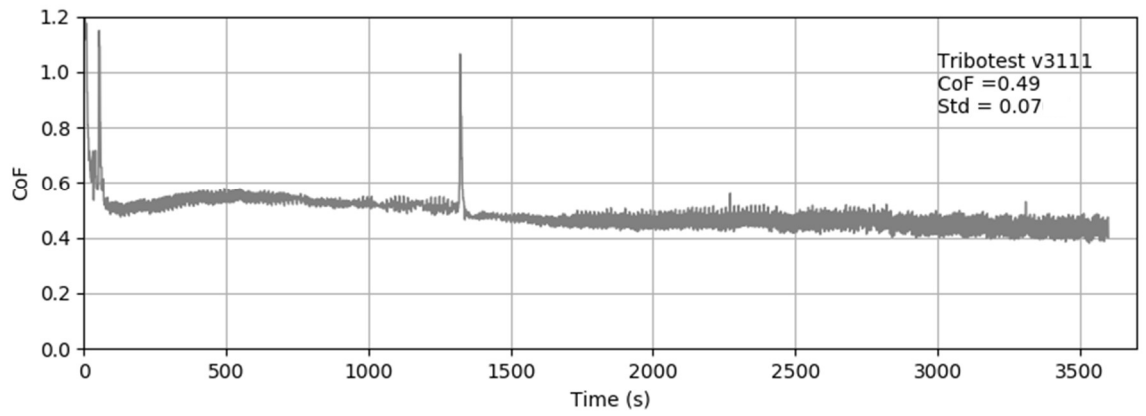
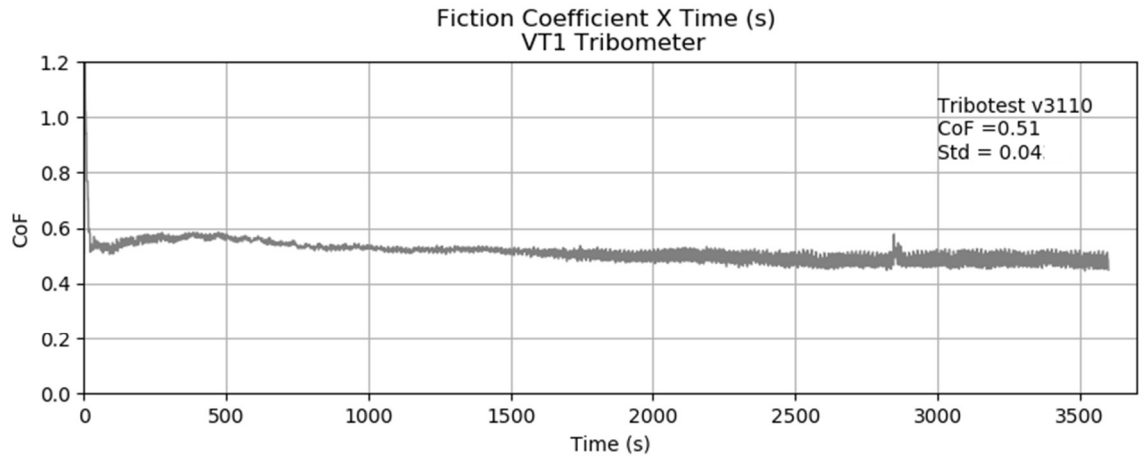
Tribotests performed with addition of binary 15%Cu-Fe<sub>3</sub>O<sub>4</sub> at 23°C in air



Tribotests performed with addition of binary 15%Cu-Fe<sub>3</sub>O<sub>4</sub> at 400°C in air

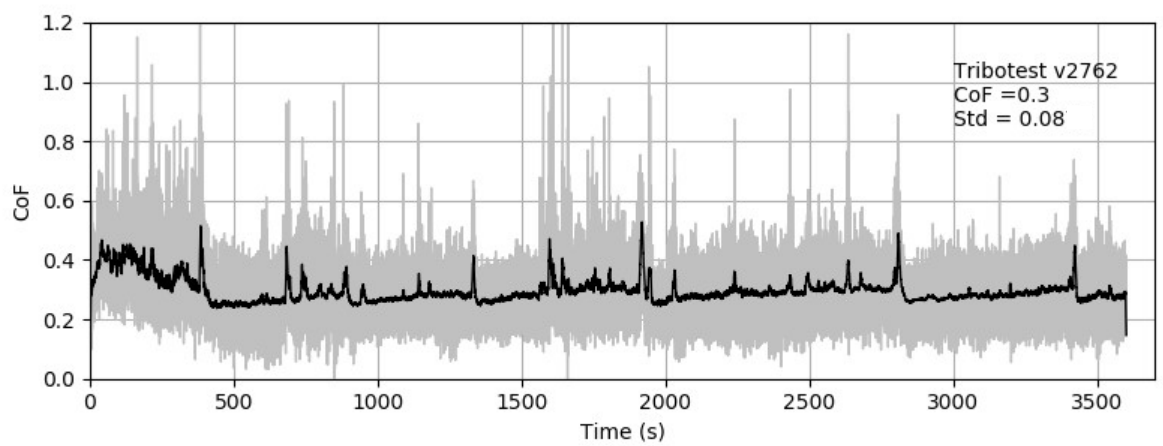
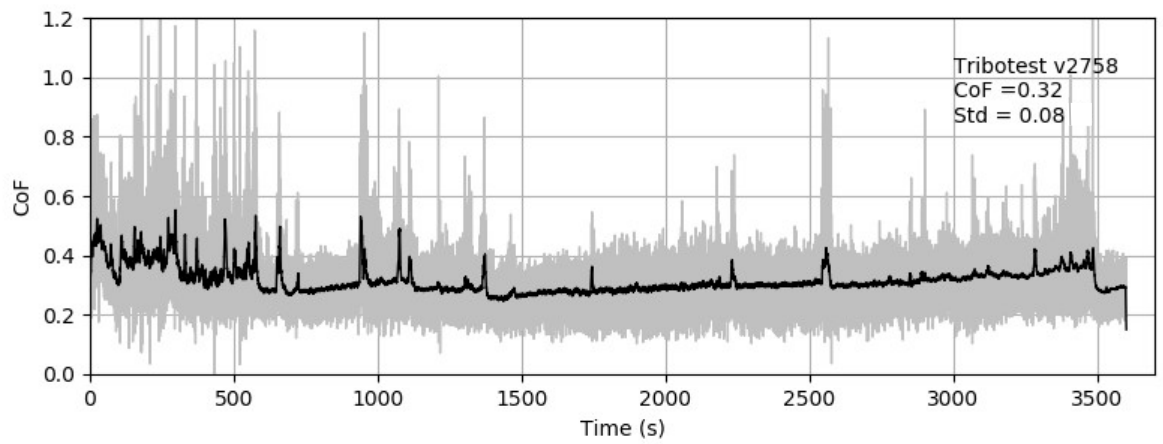
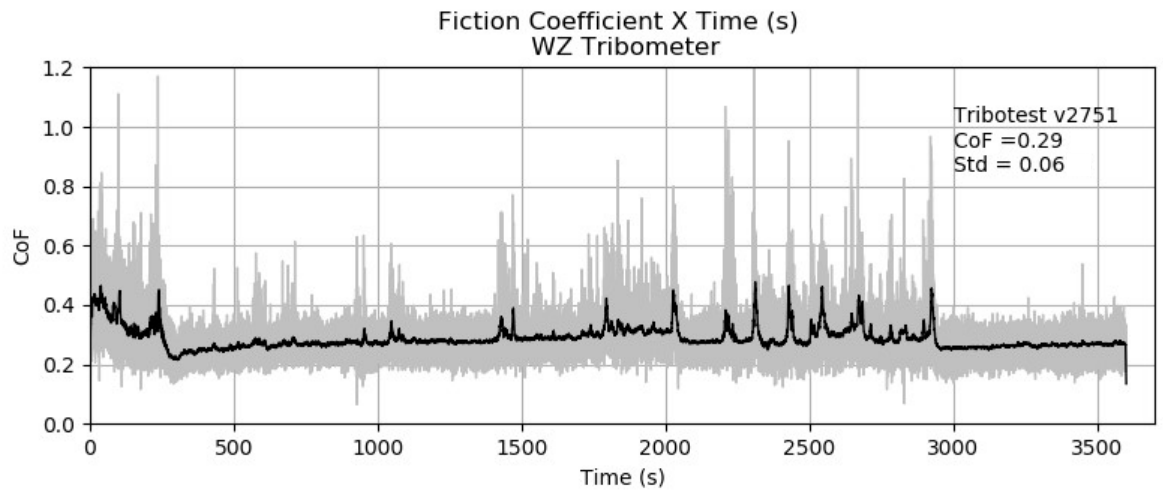


Tribotests performed with addition of binary 15%Cu-Fe<sub>3</sub>O<sub>4</sub> at 400°C in N<sub>2</sub>

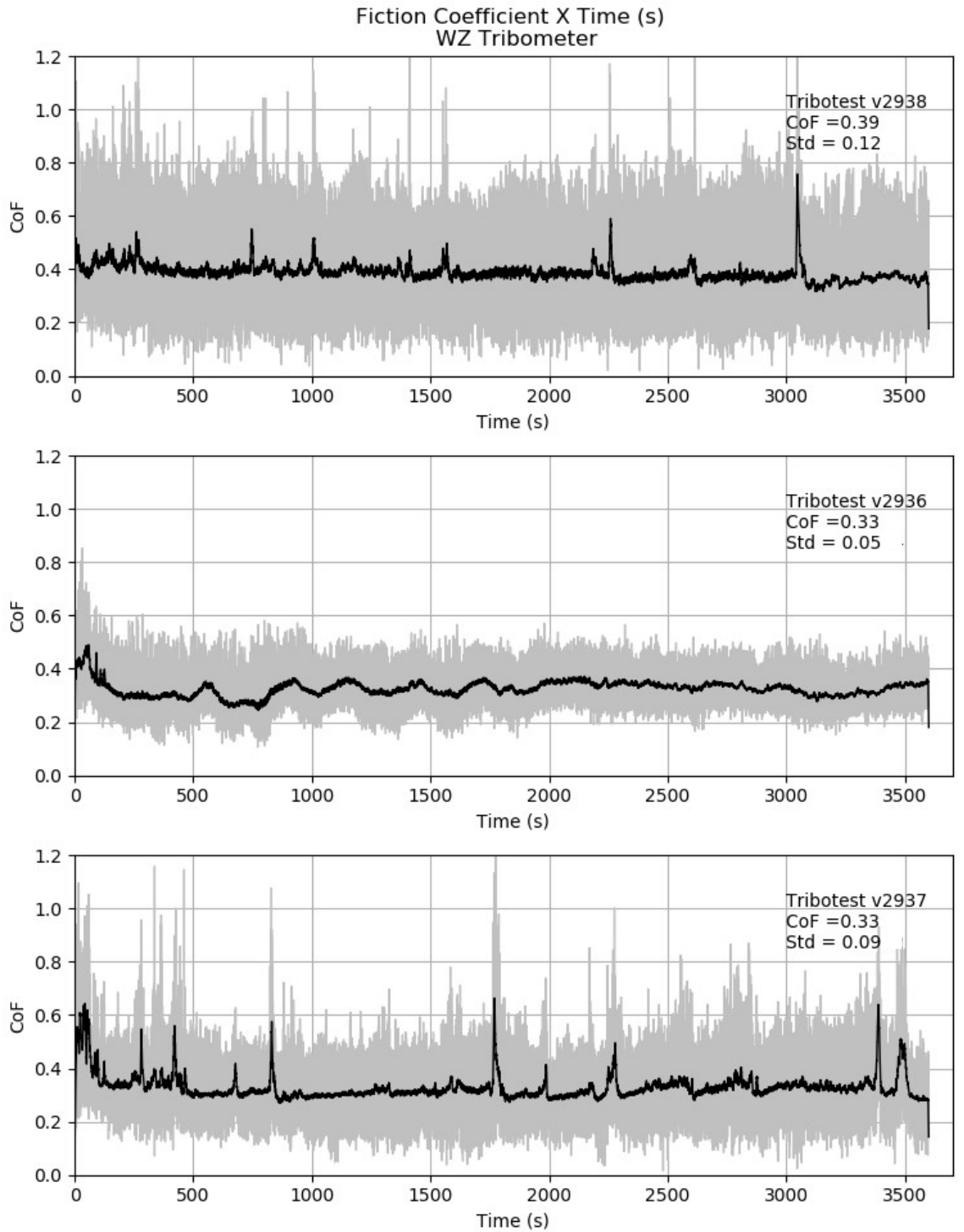


## ANNEX 4

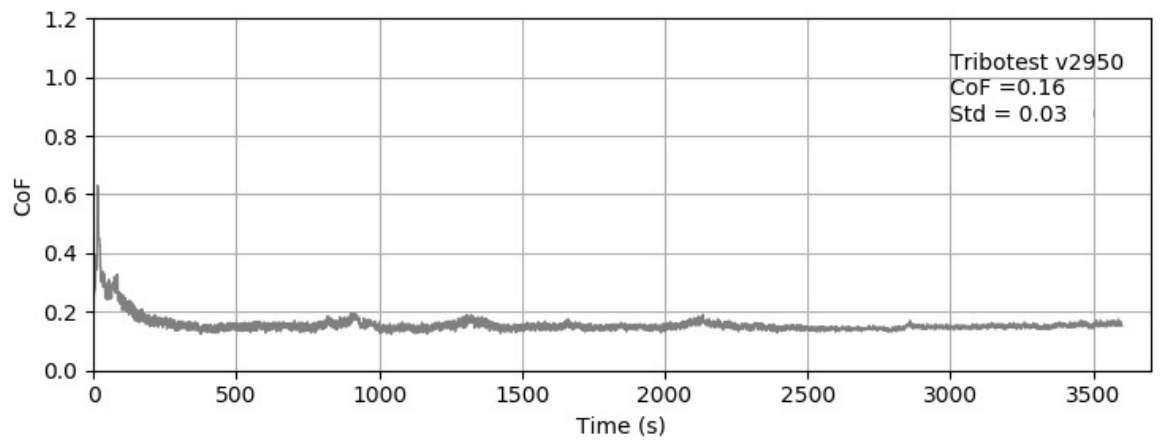
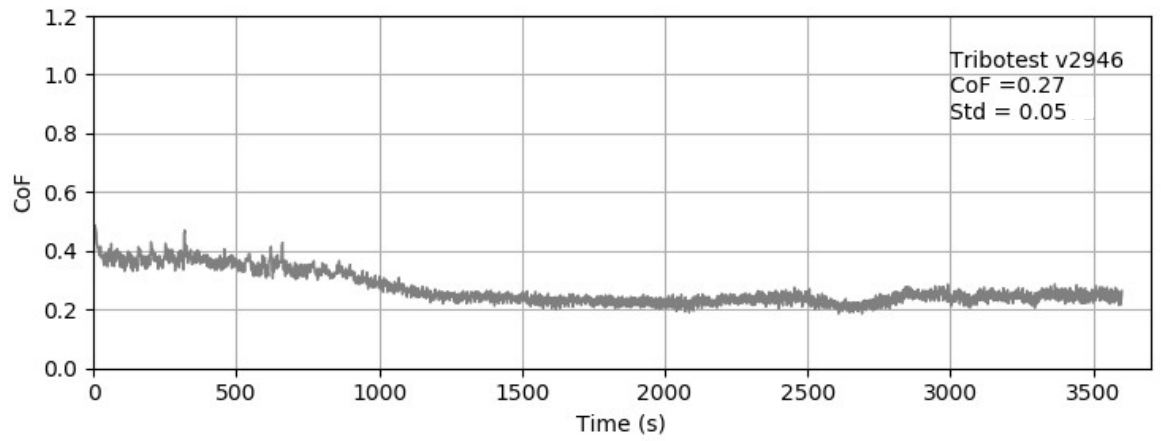
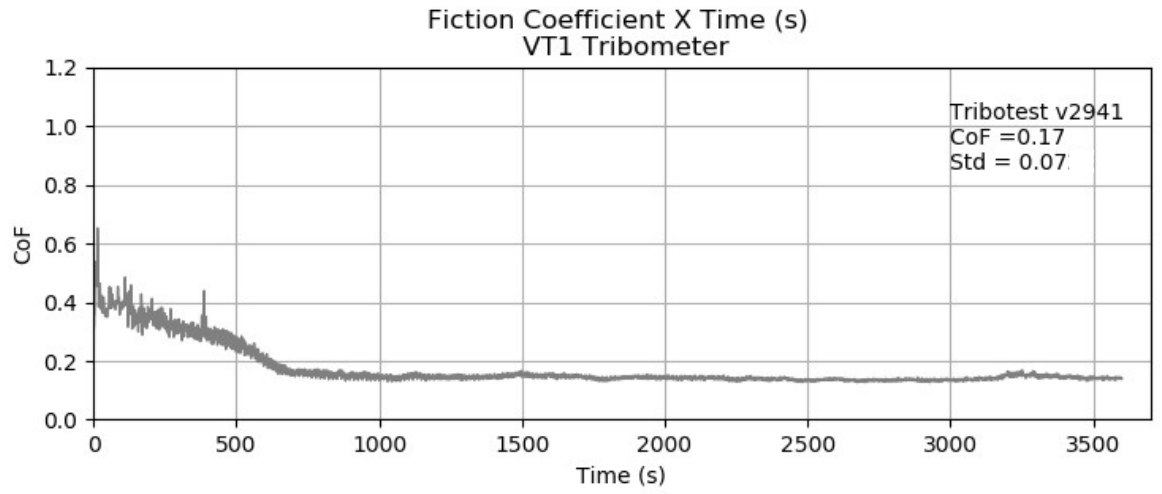
Tribotests performed with addition of ternary MM Cu-graphite- $\text{Fe}_3\text{O}_4$  at 23°C in air



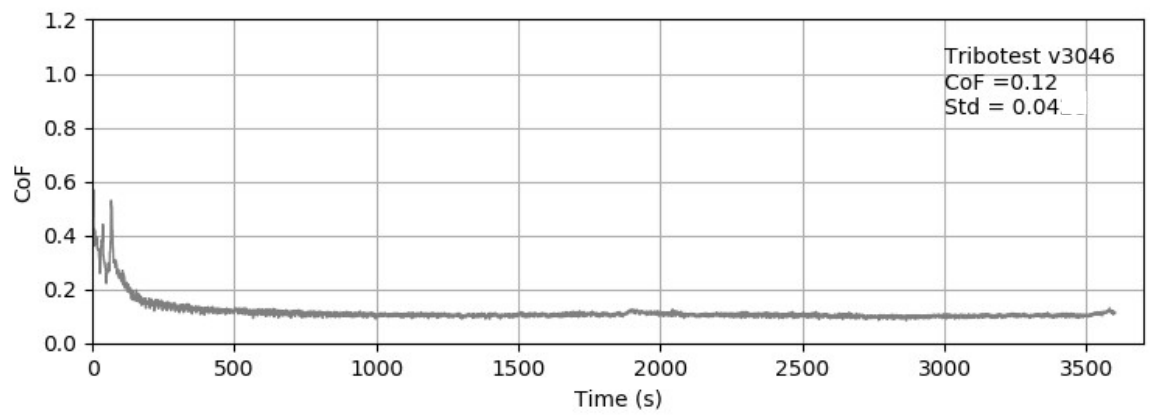
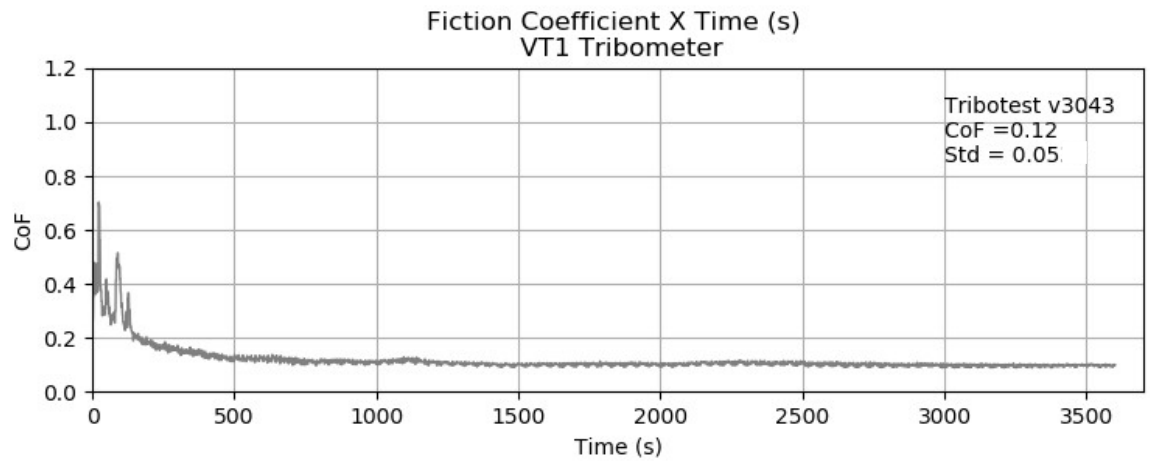
Tribotests performed with addition of ternary MM Cu-graphite-Fe<sub>3</sub>O<sub>4</sub> at 23°C in air



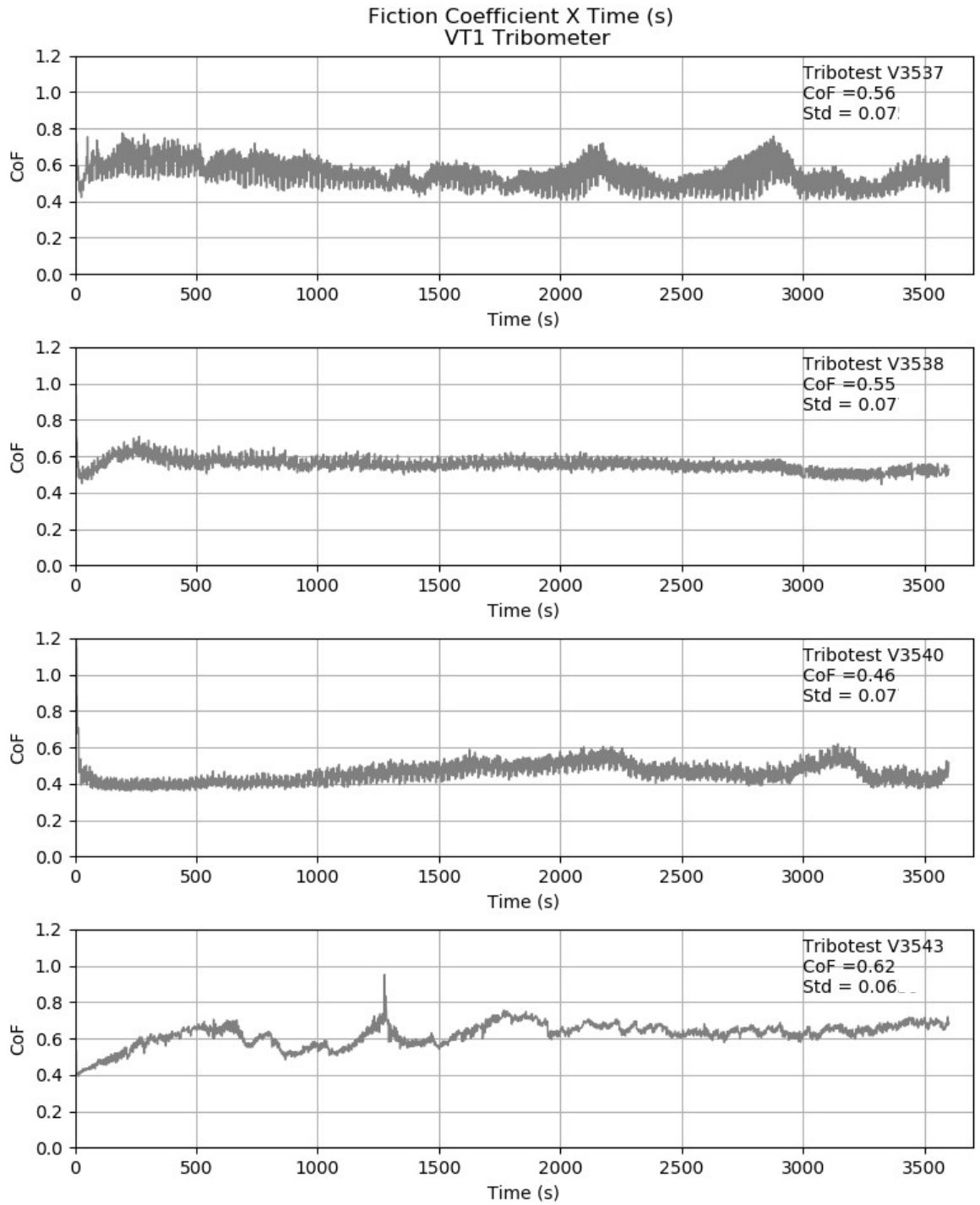
Tribotests performed with addition of ternary MM Cu-graphite-Fe<sub>3</sub>O<sub>4</sub> at 23°C in air



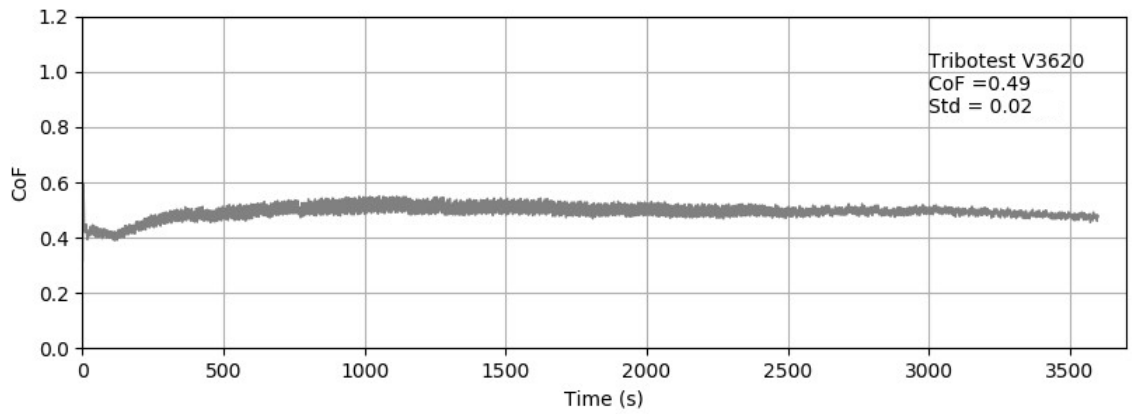
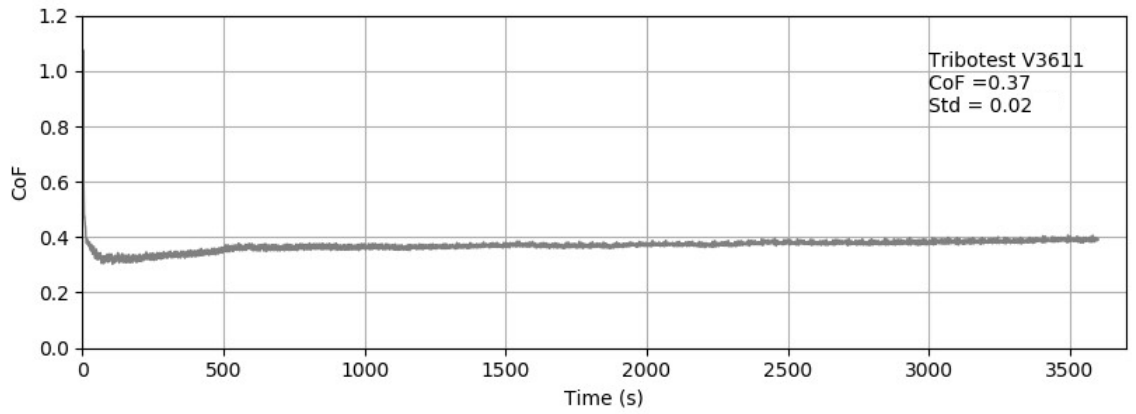
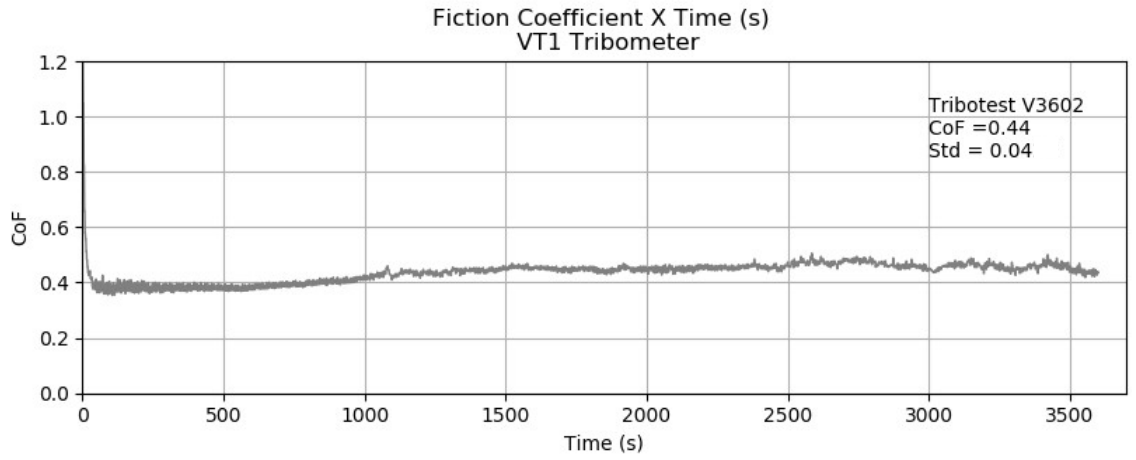
Tribotests performed with addition of ternary MM Cu-graphite-Fe<sub>3</sub>O<sub>4</sub> at 23°C in air



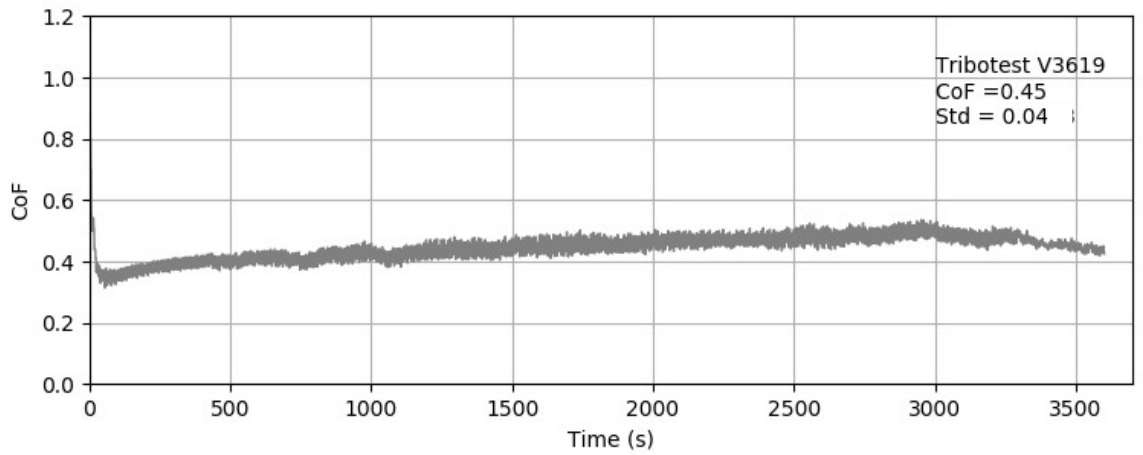
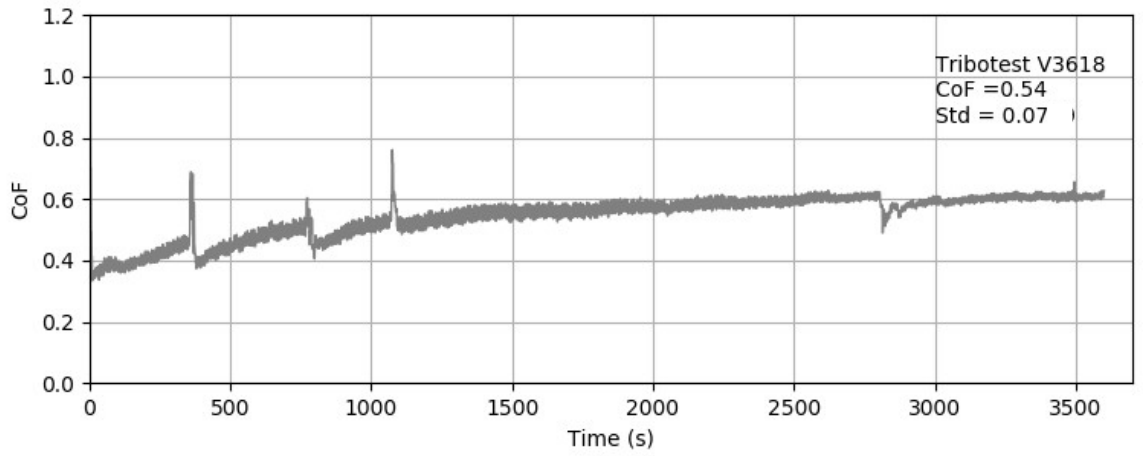
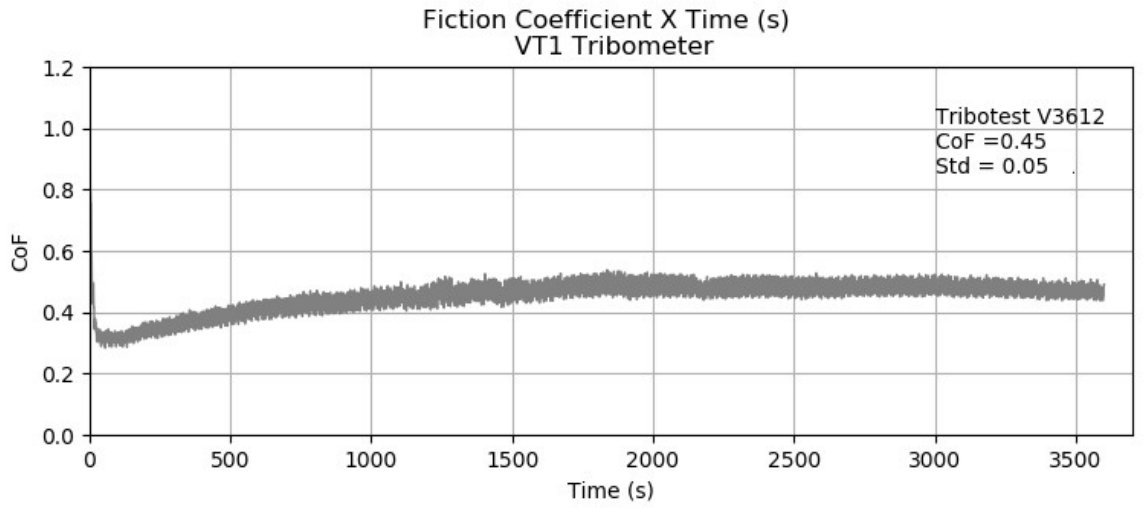
Tribotests performed with addition of ternary MM Cu-graphite-Fe<sub>3</sub>O<sub>4</sub> at 400°C in air



Tribotests performed with addition of ternary MM Cu-graphite-Fe<sub>3</sub>O<sub>4</sub> at 400°C in N<sub>2</sub>

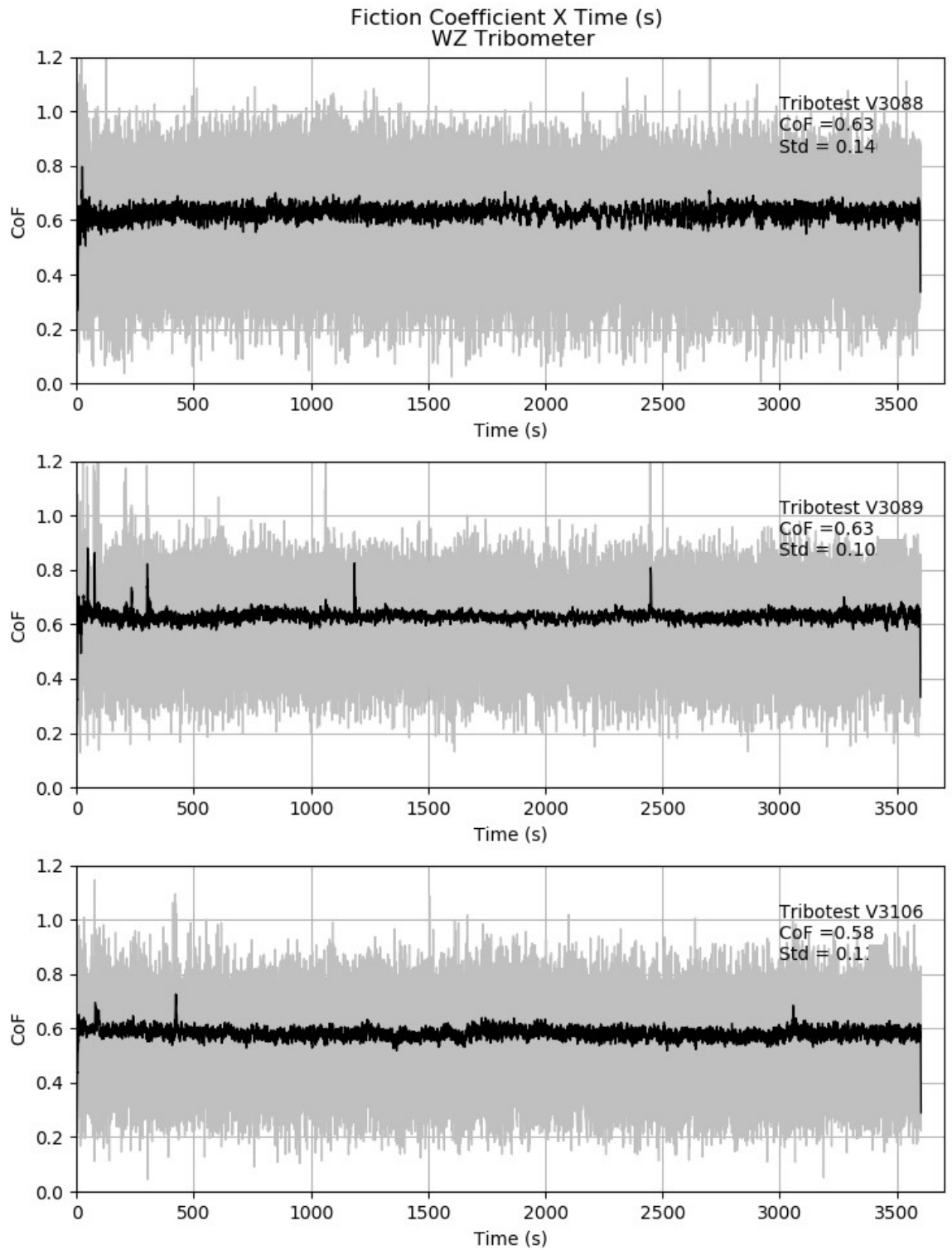


Tribotests performed with addition of ternary MM Cu-graphite-Fe<sub>3</sub>O<sub>4</sub> at 400°C in N<sub>2</sub>

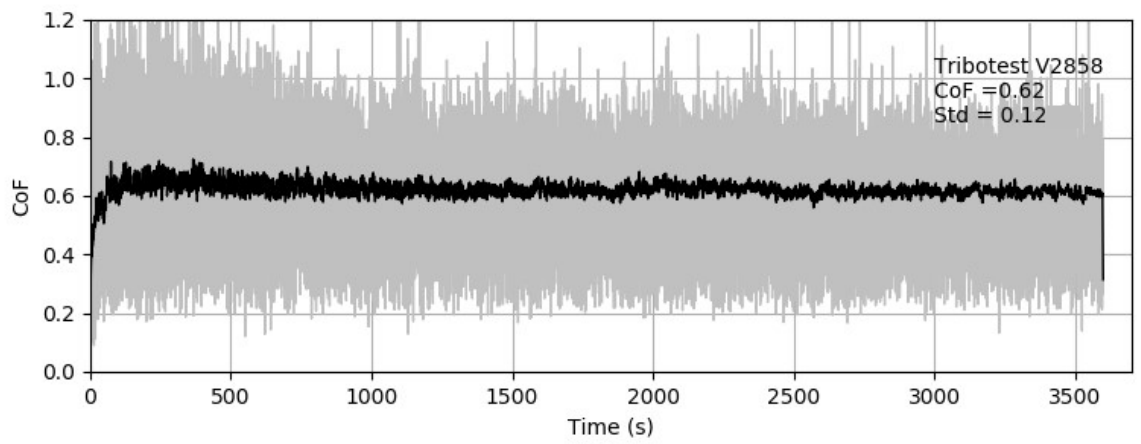
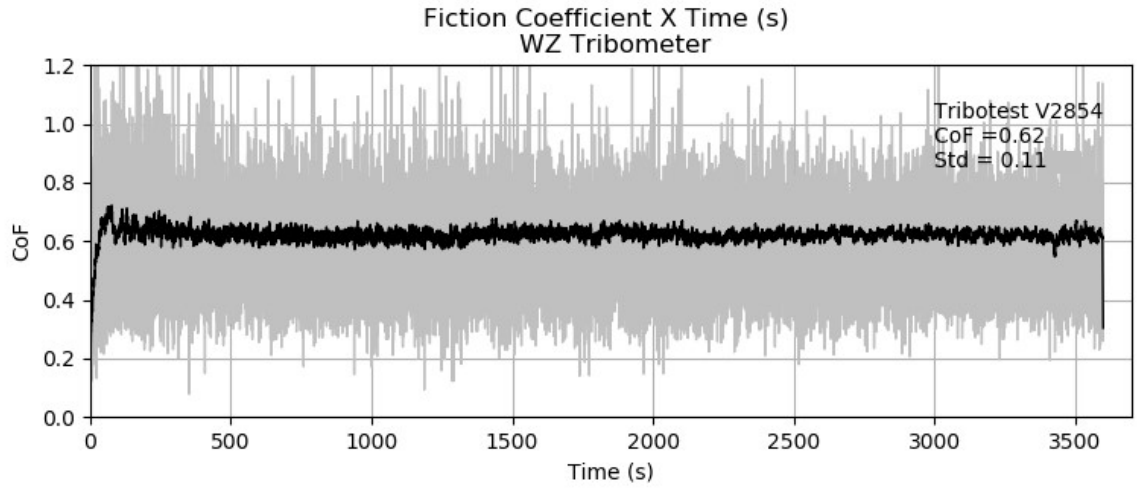


## ANNEX 5

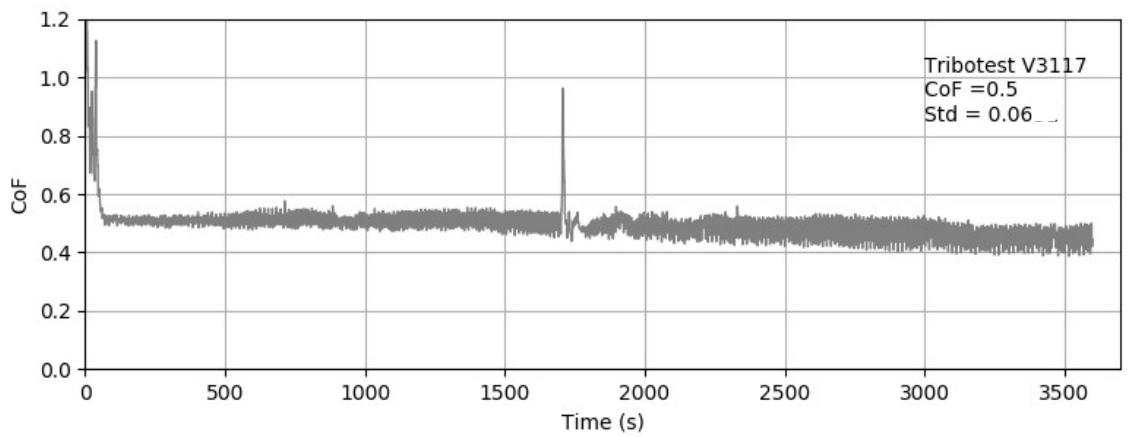
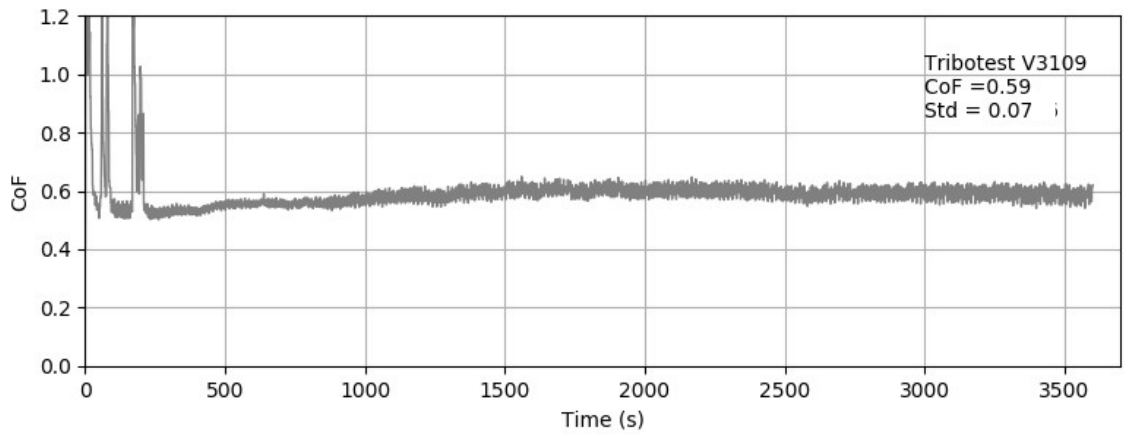
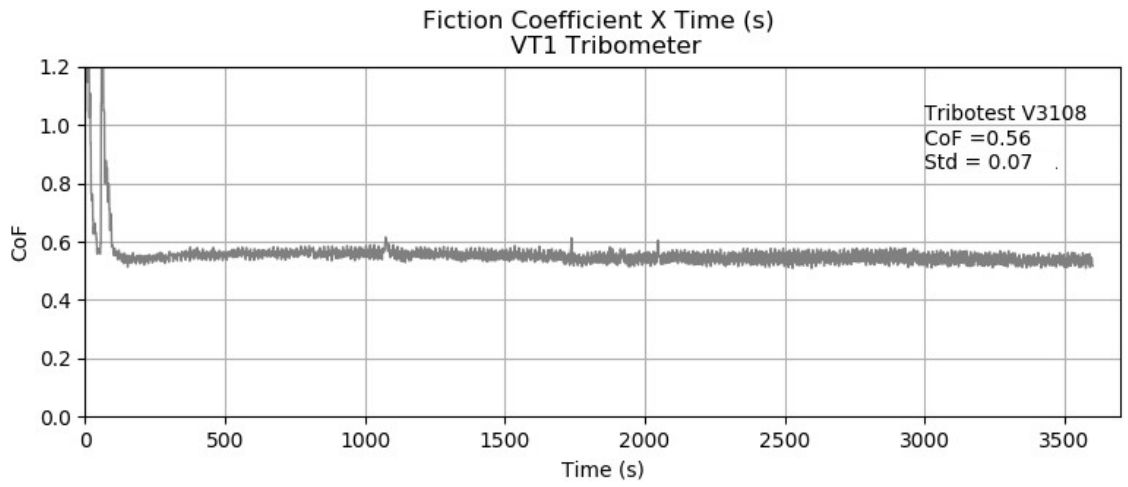
Tribotests performed with addition of ternary BM  $ZrO_2-Cu-Fe_3O_4$  at 23°C in air



Tribotests performed with addition of ternary BM  $ZrO_2-Cu-Fe_3O_4$  at 23°C in air

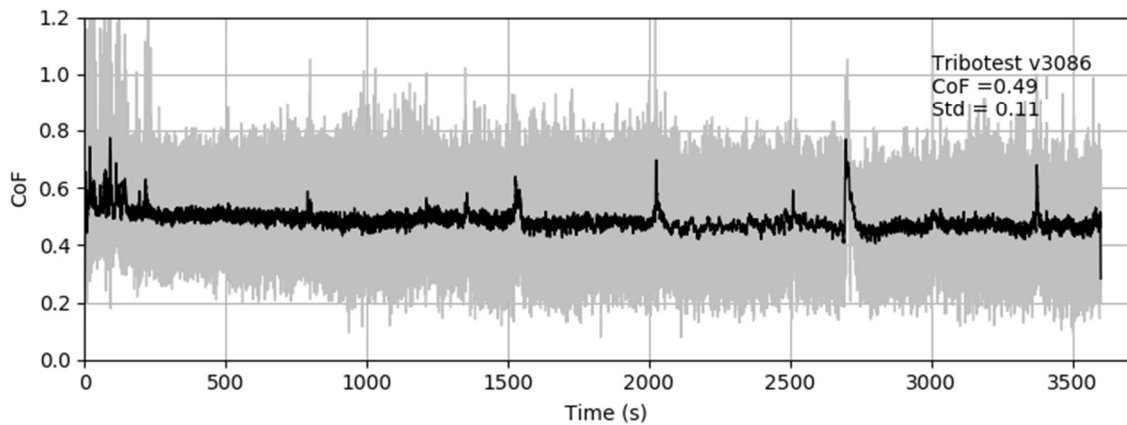
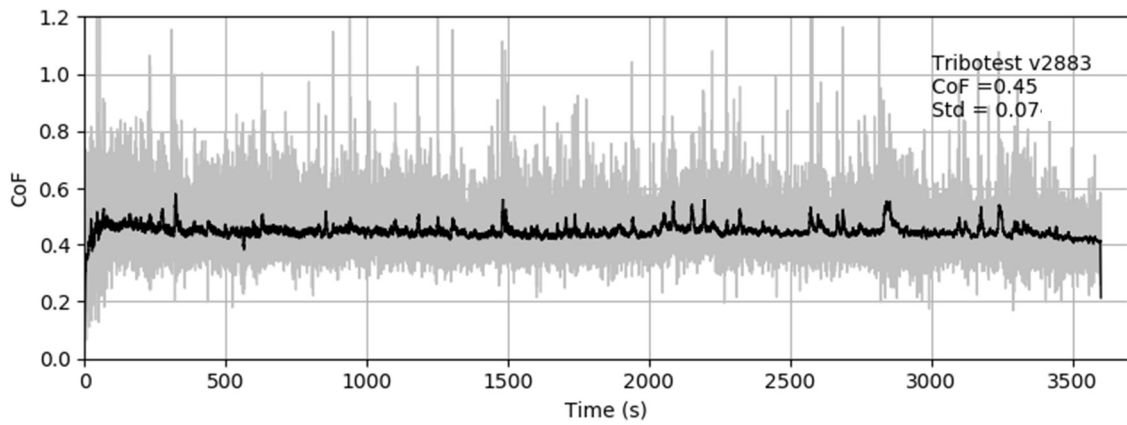
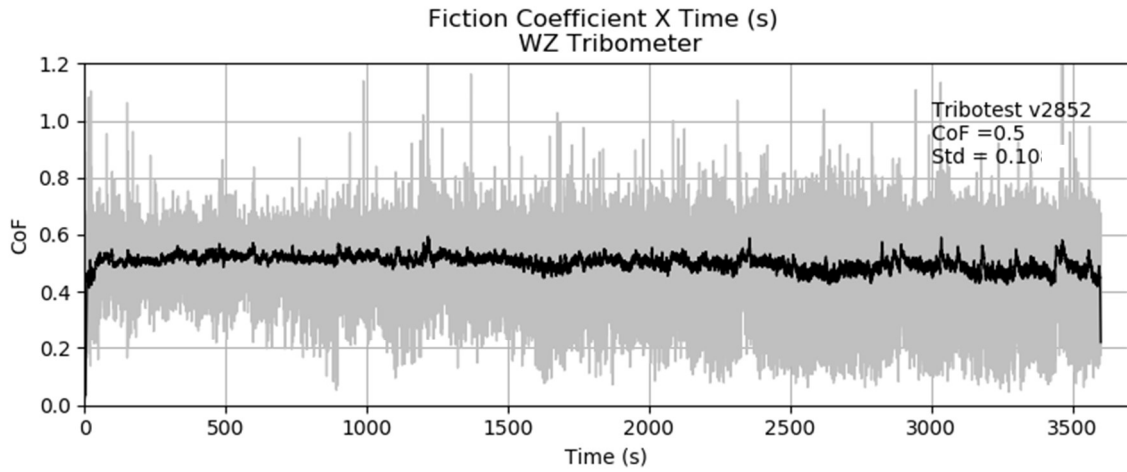


Tribotests performed with addition of ternary BM  $ZrO_2-Cu-Fe_3O_4$  at  $400^\circ C$  in  $N_2$

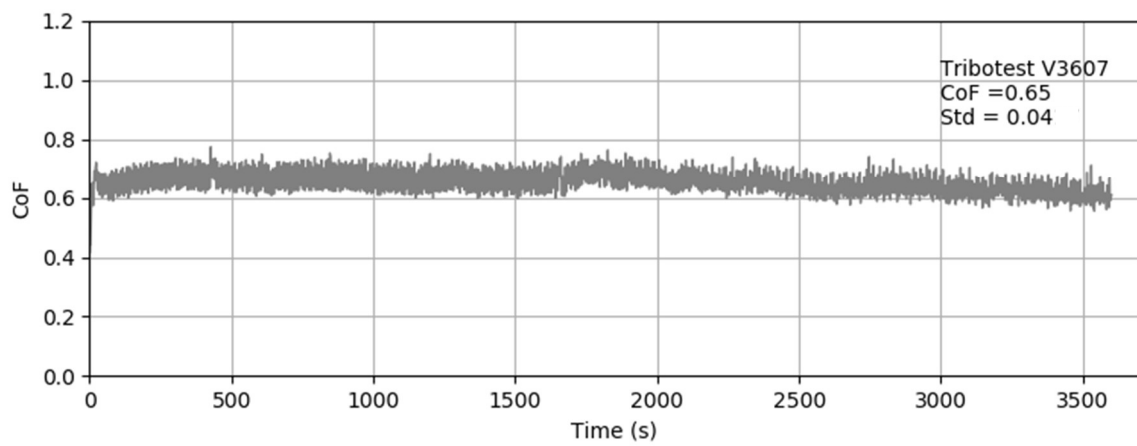
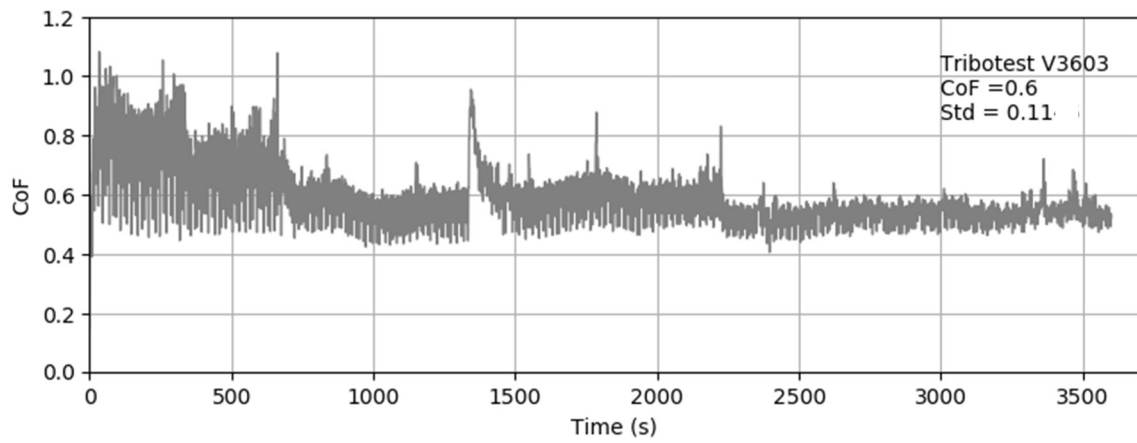
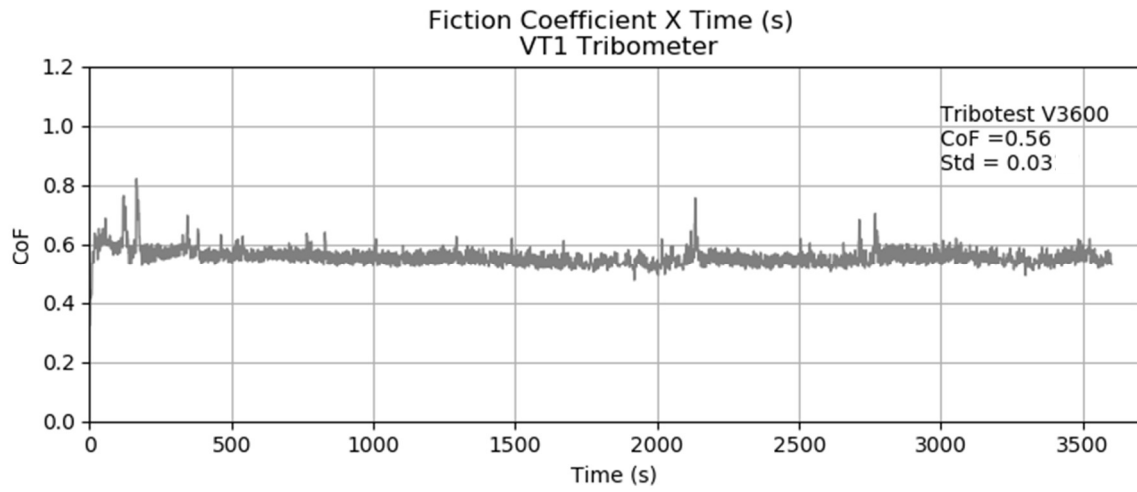


## ANNEX 6

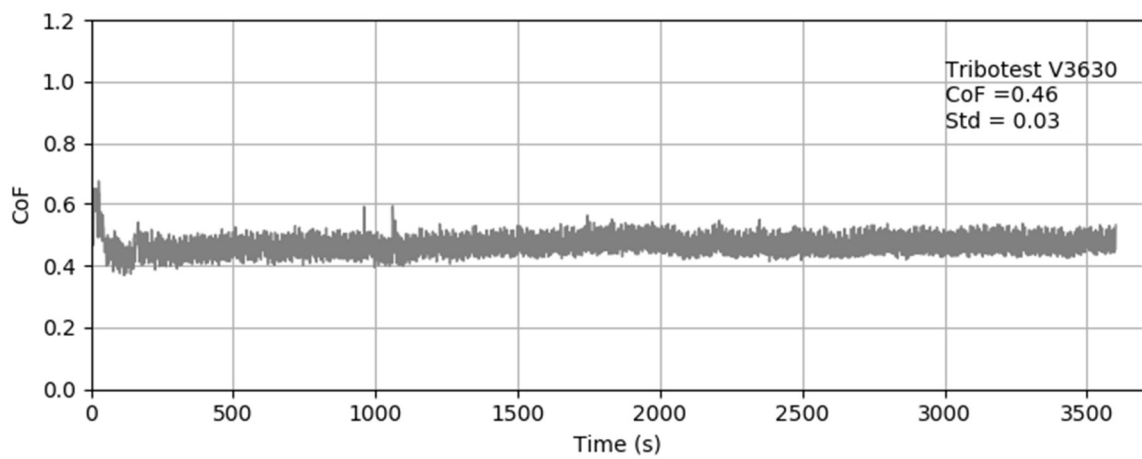
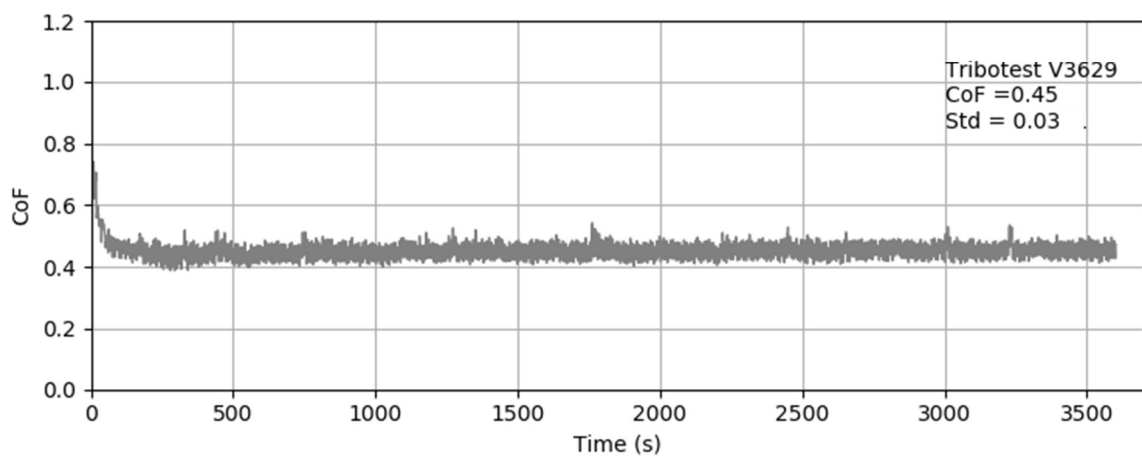
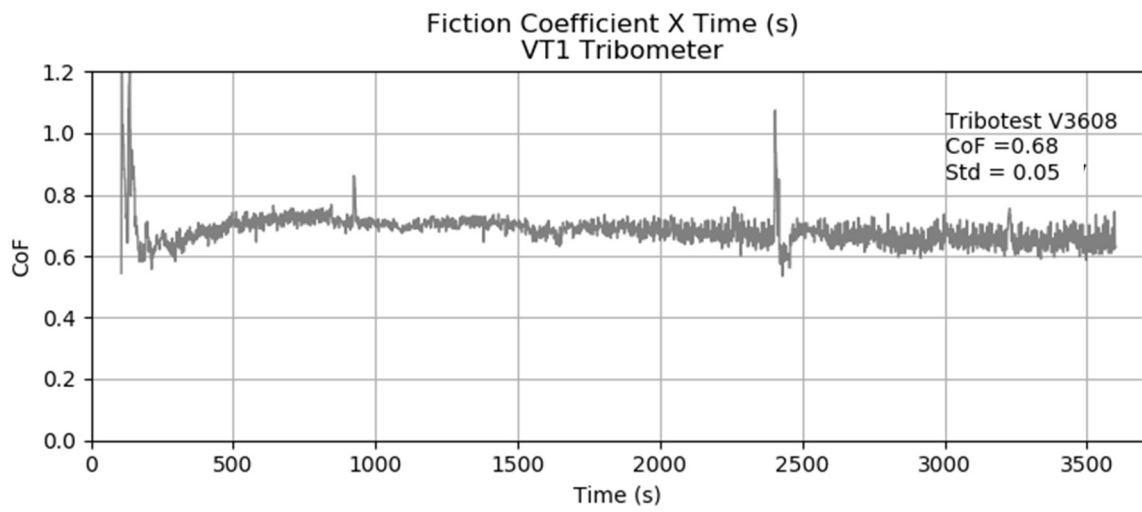
Tribotests performed with addition of quaternary BM  $ZrO_2$ -Cu-graphite- $Fe_3O_4$  at 23°C in air



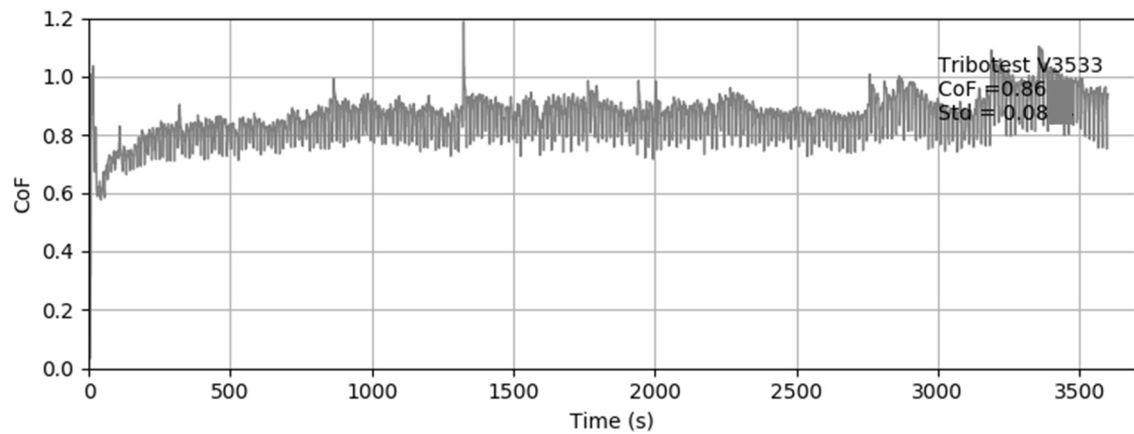
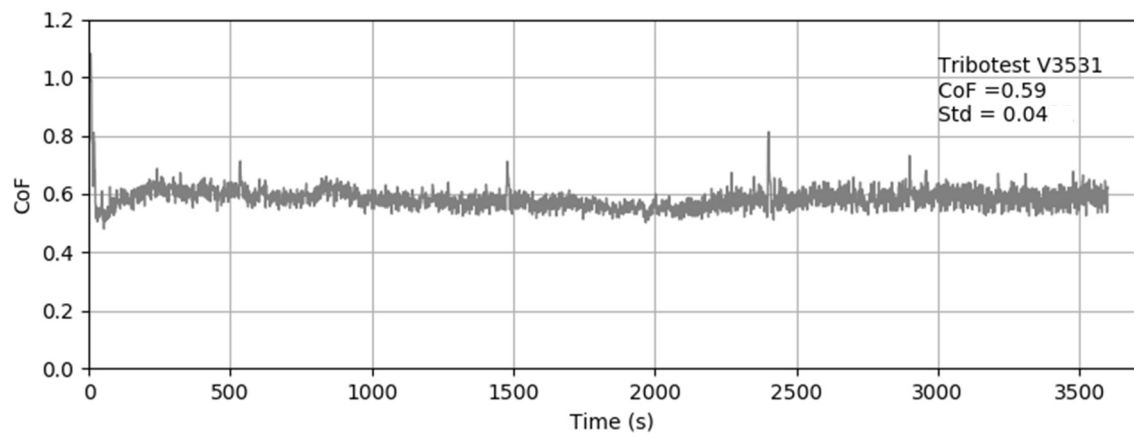
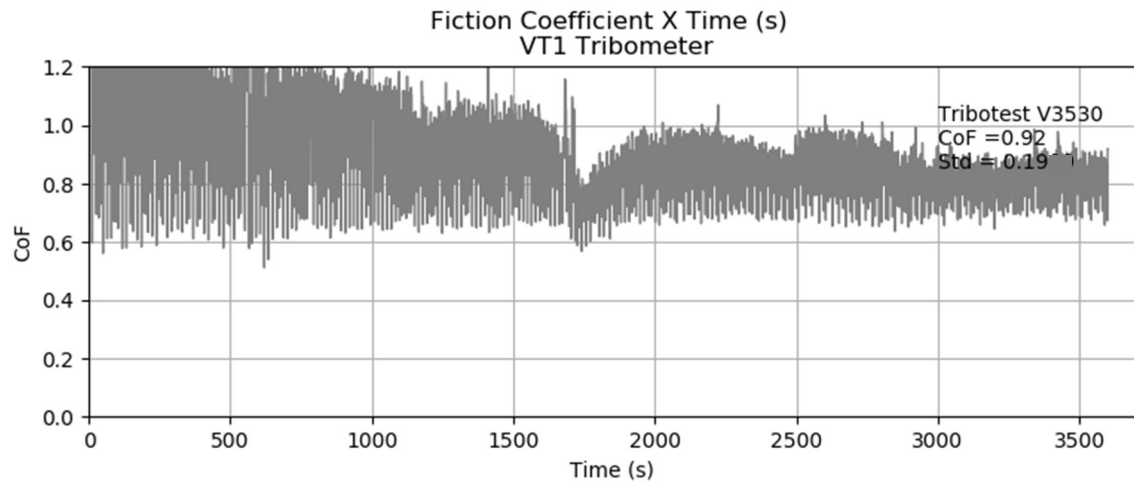
Tribotests performed with addition of quaternary BM  $ZrO_2$ -Cu-graphite- $Fe_3O_4$  at 23°C in air



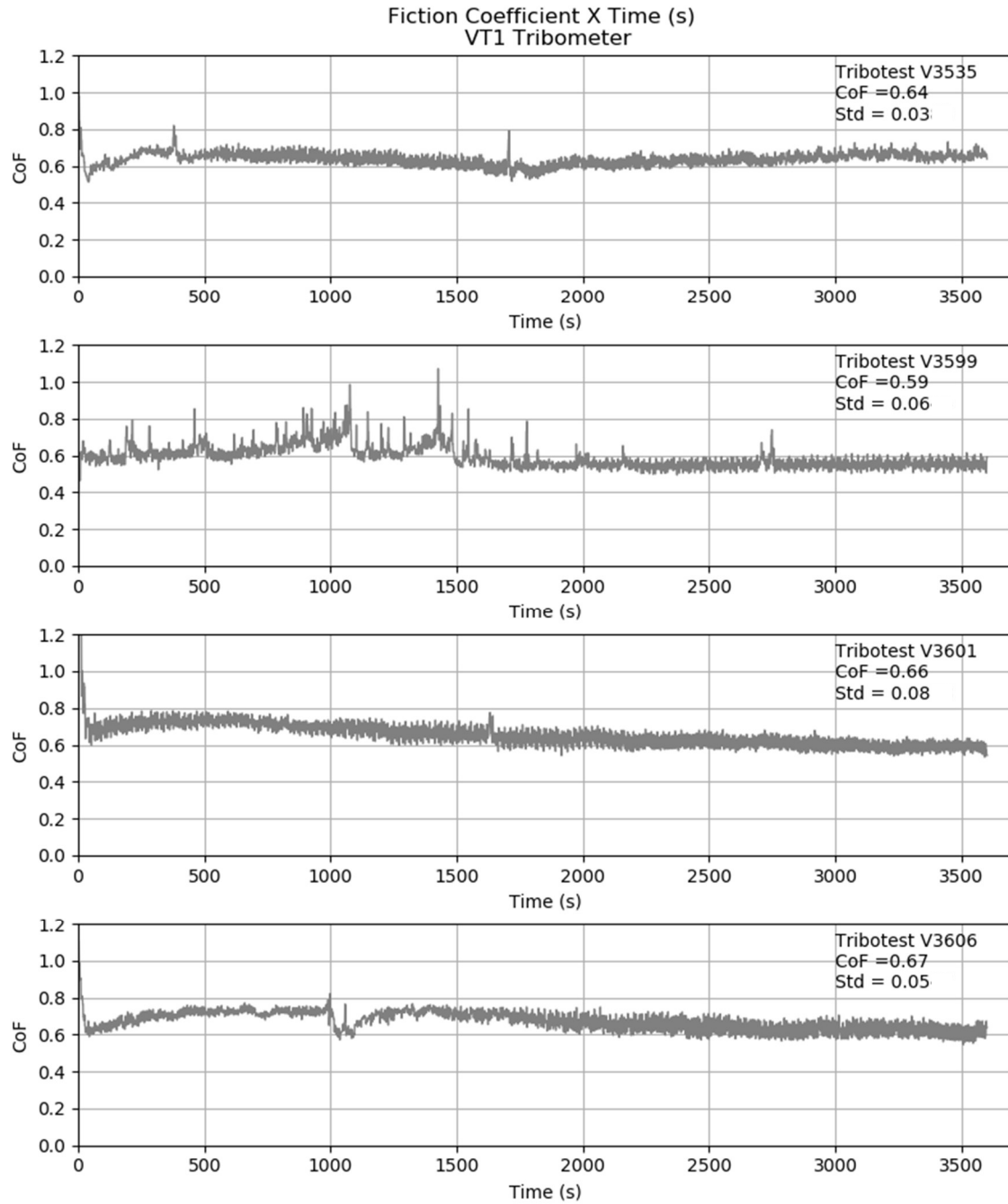
Tribotests performed with addition of quaternary BM  $ZrO_2$ -Cu-graphite- $Fe_3O_4$  at 23°C in air



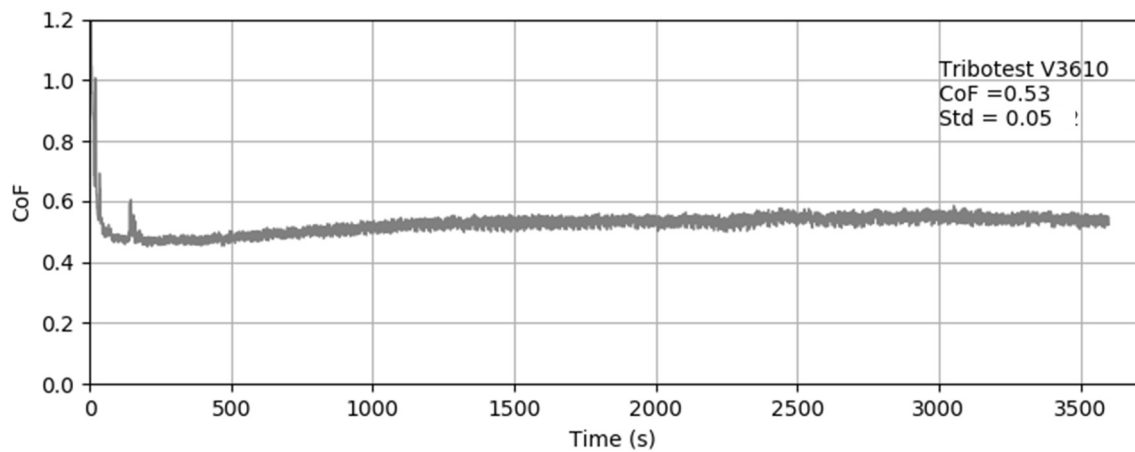
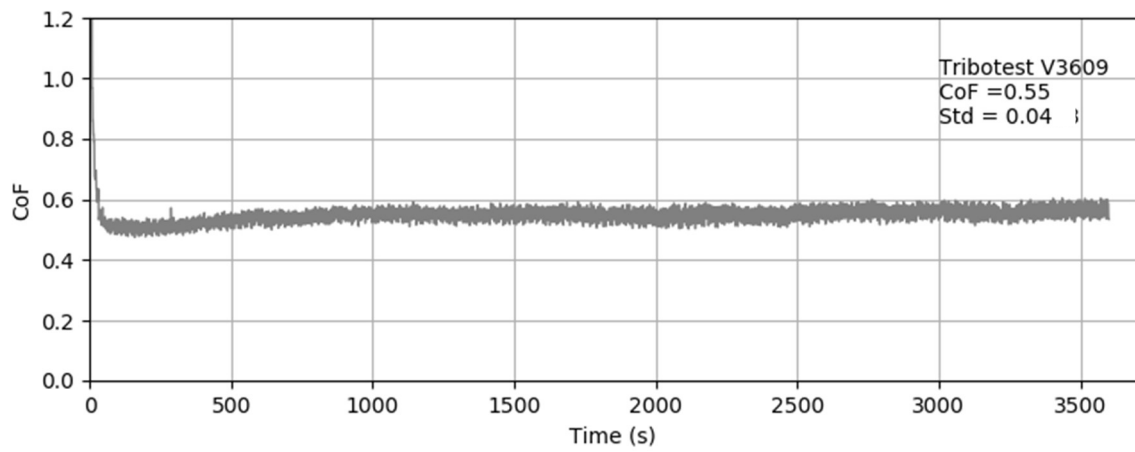
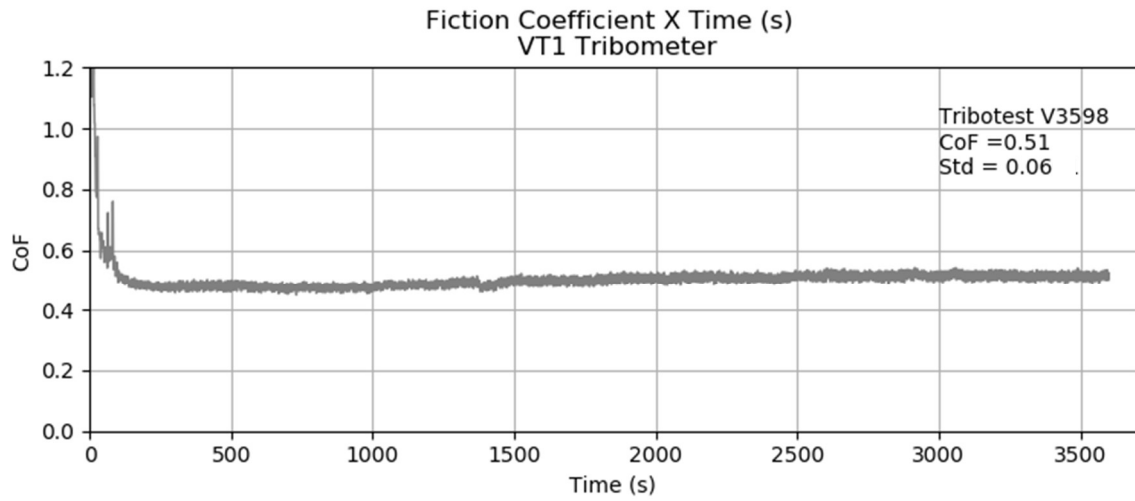
Tribotests performed with addition of quaternary BM  $ZrO_2$ -Cu-graphite- $Fe_3O_4$  at  $400^\circ C$  in air  $N_2$



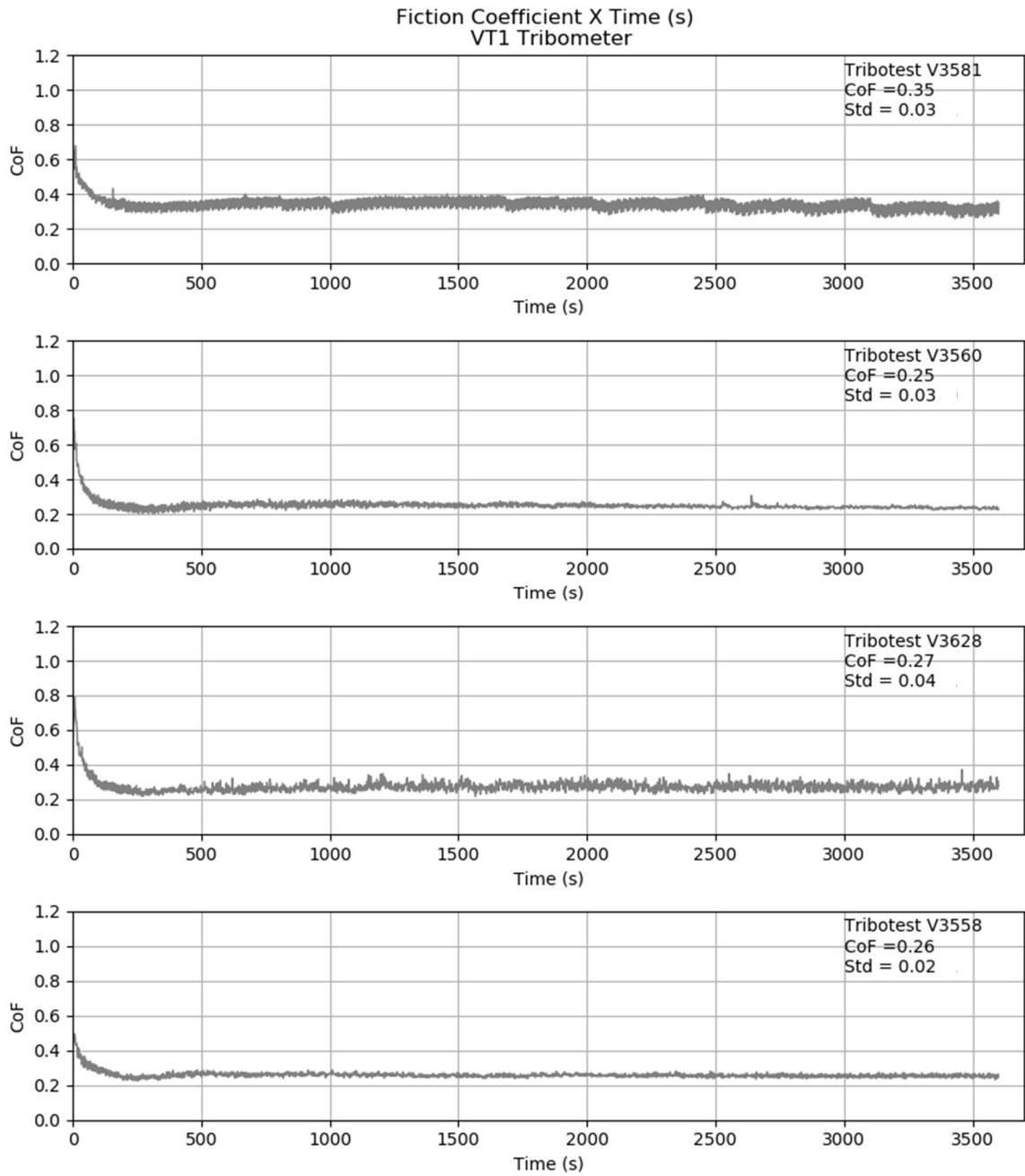
Tribotests performed with addition of quaternary BM  $ZrO_2$ -Cu-graphite- $Fe_3O_4$  at 400°C in air



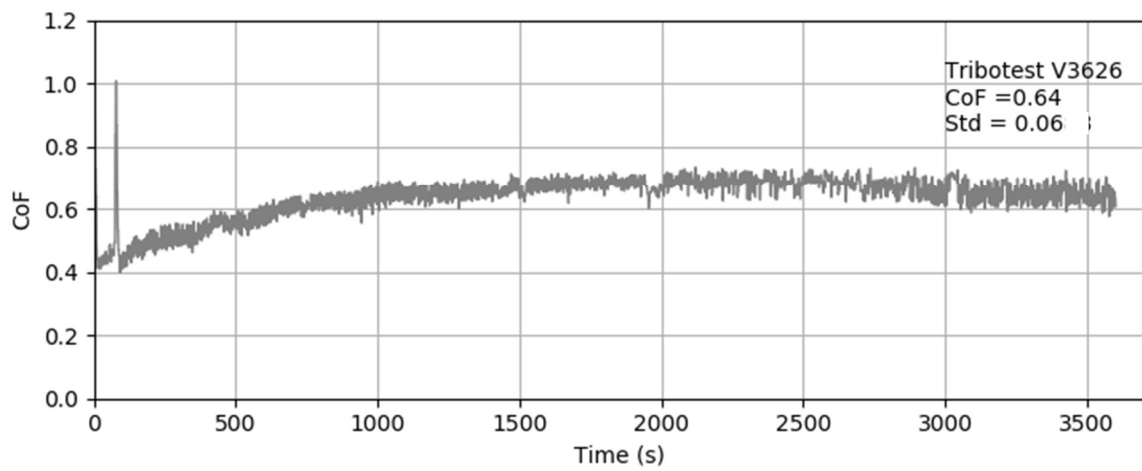
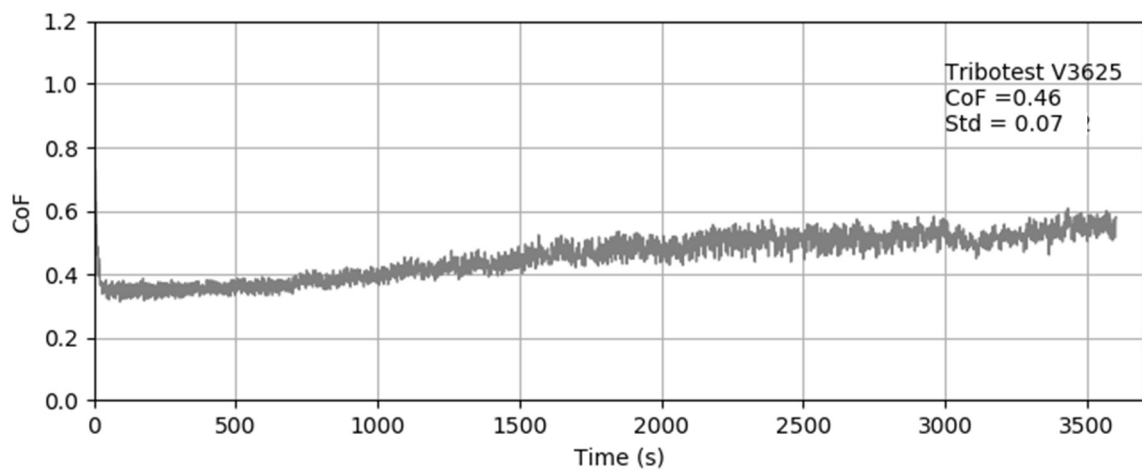
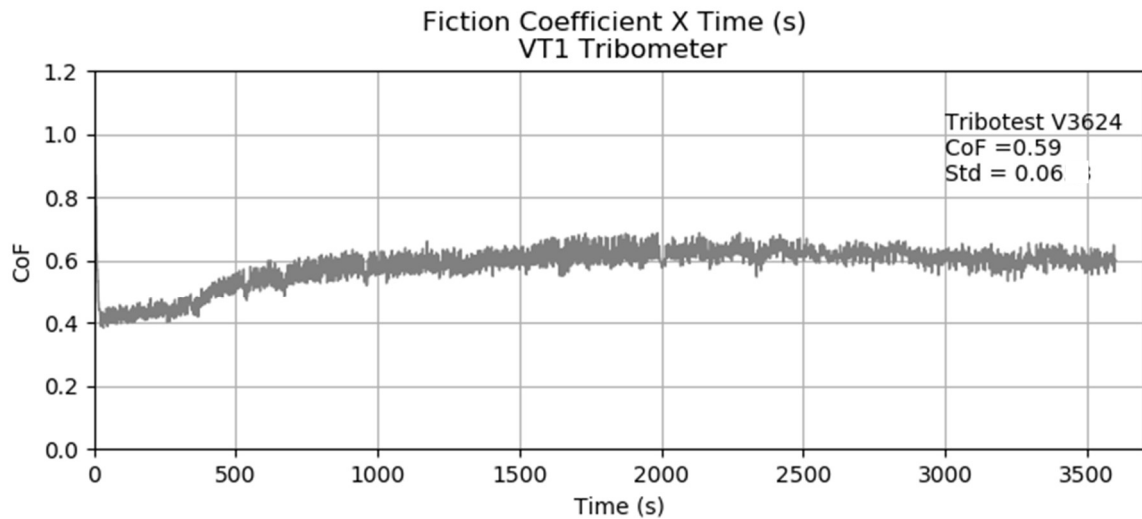
Tribotests performed with addition of quaternary BM  $ZrO_2$ -Cu-graphite- $Fe_3O_4$  at  $400^\circ C$  in  $N_2$



Tribotests performed with addition of quaternary MM ZrO<sub>2</sub>-Cu-graphite-Fe<sub>3</sub>O<sub>4</sub> at 23°C in air



Tribotests performed with addition of quaternary MM  $ZrO_2$ -Cu-graphite- $Fe_3O_4$  at  $400^\circ C$  in air



Tribotests performed with addition of quaternary MM ZrO<sub>2</sub>-Cu-graphite-Fe<sub>3</sub>O<sub>4</sub> at 23°C in N<sub>2</sub>

